Nanoparticle Interventions for Colorectal Cancer: Delivery of Polymer Encapsulated SN-38

Usman Arshad

04/02/2021

Thesis submitted in accordance with the requirements of the University of Liverpool for the degree of Doctor in Philosophy

Declaration

This thesis is the result of my own work unless otherwise stated. The material contained within this thesis has not been presented, nor is currently being presented, wholly, or in part, for any other degree or qualification.

The research was undertaken within the Department of Molecular and Clinical Pharmacology at the University of Liverpool.

Abstract

Colorectal cancer remains a significant cause of morbidity and mortality worldwide. Half of all patients develop liver metastases, presenting unique challenges for their treatment. Irinotecan is a topoisomerase I inhibitor used to treat metastatic colorectal cancers. Its use is limited by severe dose-limiting toxicities and heterogeneity in its clinical response. Moreover, the clinical use of the active metabolite (7-Ethyl-10-hydroxycamptothecin, SN-38) is significantly limited due to poor solubility, instability and a short elimination half-life. Thus, the shortcomings of conventional chemotherapy have encouraged the exploration of nanomedicines; the application of nanotechnology in the diagnosis and treatment of disease.

This thesis describes the development of SN-38 loaded nanoparticles for use in the treatment of colorectal cancer, particularly advanced stage metastatic disease, to improve both the safety and effectiveness of available therapies. For screening purposes, a robust and sensitive liquid chromatography-tandem mass spectrometry assay for the detection of irinotecan, SN-38 and SN-38 glucuronide was developed and colorectal cancer spheroids were characterised for their use in assessing cytotoxicity. Several polymer nanomaterials were thereafter screened for drug release, cytotoxicity and macrophage uptake. Subsequently, the pharmacokinetic profiles of the best candidates were compared to free SN-38 and irinotecan *in vivo*. In the final year of the PhD, the world was afflicted by the COVID-19 pandemic, which resulted in a change of focus towards assessing potential drug repurposing opportunities for SARS-CoV-2 antivirals.

As demonstrated in chapter 2 the liquid chromatography-tandem mass spectrometry assay was fully validated to FDA guidelines in PBS and mouse plasma. In chapter 3 the physiological relevance of spheroids was shown, with their ability to mimic the *in vivo*/clinical environment better than monolayer cultures. In particular, drug sensitivity and uptake differed between culture systems, due to the arrangement of cancer cells in spheroids i.e. the outer rim of actively proliferating cells, a middle viable layer of quiescent cells and an internal necrotic core. Therefore, such properties of spheroids meant they would represent a more robust tool for drug screening purposes. A panel of polymer nanomaterials were screened in chapter 4. Formulations SB1 and CA16 were selected on the basis that they showed a slower sustained release profile, adequate cytotoxicity against colorectal cancer cells and minimal macrophage uptake. However, when given *in vivo* both formulations did not lead to the prolonged circulation of SN-38. In comparison to irinotecan, significantly lower concentrations of SN-38 released from nanoparticles were present in the plasma ($p \leq 0.001$ for SB1 or CA16 versus irinotecan). The data indicated possible non-specific uptake of the nanoparticles within other organs. The analysis for drug repurposing to target COVID-19, included in appendix A, highlighted the importance of taking into account the achievable plasma pharmacokinetics as an indicator of antiviral activity. Several drug candidates were identified (13 drugs showed plasma exposures above that required for an antiviral activity) and were recommended for further investigation.

In conclusion, despite promising *in vitro* data SN-38 loaded nanoparticles did not display better pharmacokinetic properties (AUC and C_{max}) over the parent drug irinotecan *in vivo*. However, areas warranting further investigation to improve translation, such as nanoparticle biodistribution and potential toxicity, were demonstrated. Furthermore, to address the challenges of targeting metastatic tumours with nanotechnology, it is necessary to combine the rational design of nanoparticles with the fundamental understanding of tumour biology.

Acknowledgements

Firstly I would like to thank my supervisors Professor Andrew Owen and Professor Chris Goldring for all their advice, guidance and support throughout my PhD. I would also like to thank other members of the supervisory team Professor Steve Rannard, Neil Kitteringham, Marianne Ashford, Kevin Treacher and Paul Sutton, for all their ideas and valuable input towards the project.

I am also grateful to all team members in the Centre for Drug Safety Science, H Block and Materials Innovation Factory who assisted me in various aspects of the project. I would like to thank Helen and Jo for their help in carrying out the *in vivo* studies. Thanks to Paul, Marco, Lee and Hannah for their assistance with the LC-MS/MS. Thanks also to the chemist's Claire and Sarah for producing all the materials that were tested. I would also like to extend my gratitude to members of the office Brian, Lucia, Chris, Amy and Marc. Additionally, I wish to thank Cancer Research (UK) who funded me and this work.

I would like to thank my family for their support and encouragement. Special thanks go to Mum, Dad, Omar, Iqrah, Habibah and little Khadijah. Without your support, none of this would be possible. Lastly thanks to Saba for her invaluable love, help and support.

Publications

Rajoli, R. K., Pertinez, H., **Arshad, U.,** Box, H., Tatham, L., Curley, P., Neary, M., Sharp, J., Liptrott, N. J., Valentijn, A., David, C., Rannard, S. P., Aljayyoussi, G., Pennington, S. H., Hill, A., Boffito, M., Ward, S. A., Khoo, S. H., Bray, P. G., O'Neill, P. M., … Owen, A. (2020). Dose prediction for repurposing nitazoxanide in SARS-CoV-2 treatment or chemoprophylaxis. medRxiv: the preprint server for health sciences, 2020.05.01.20087130. DOI: https://doi.org/10.1101/2020.05.01.20087130

Arshad, U., Pertinez, H., Box, H., Tatham, L., Rajoli, R.K.R., Curley, P., Neary, M., Sharp, J., Liptrott, N.J., Valentijn, A., David, C., Rannard, S.P., O'Neill, P.M., Aljayyoussi, G., Pennington, S.H., Ward, S.A., Hill, A., Back, D.J., Khoo, S.H., Bray, P.G., Biagini, G.A. and Owen, A. (2020), Prioritization of Anti-SARS-Cov-2 Drug Repurposing Opportunities Based on Plasma and Target Site Concentrations Derived from their Established Human Pharmacokinetics. *Clinical Pharmacology & Therapeutics*. DOI:10.1002/cpt.1909

Arshad, U., Sutton, P.A., Ashford, M.B., Treacher, K.E., Liptrott, N.J., Rannard, S.P., Goldring, C.E. and Owen, A., (2020). Critical considerations for targeting colorectal liver metastases with nanotechnology. *Wiley Interdisciplinary Reviews: Nanomedicine and Nanobiotechnology*, 12(2), p.e1588.

Un Nahar, N., **Arshad, U.,** Goldring, C.E. and Sutton, P.A. (2018). I04 An *in vitro* model of HIPEC: Facilitating pharmacological assessment in colorectal peritoneal metastases II.i).*Translational research, Pleura and Peritoneum*, 3(s1), A416-A442. DOI: https://doi.org/10.1515/pp-2018-7024

David, R., Talbot, E., Allen, B., Wilson, A., **Arshad, U.,** & Doherty, A. (2018). The development of an in vitro Pig-a assay in L5178Y cells. *Archives of toxicology*, 92(4), 1609-1623.

Conference Talk titled "Nanotechnology in Cancer" at the Nanomedicine: Diagnostics and Treatment of Cancer and Other Diseases (BSNM-UKIERI, 2019)

Newsletter; "The Promise and Challenges of Nanomedicines in Fighting Cancer" for Advanced Science News. (2019) https://www.advancedsciencenews.com/the-promise-and-challenges-of-nanomedicines-in-fighting-cancer/

Contents

Declaration I

Abstract II

Acknowledgements III

Publications IV

Contents V

List of Figures X

List of Abbreviations XIII

Chapter 1: General Introduction 1

1.1 Introduction 1

1.2 Colorectal Cancer and its Treatments 2

1.2.1 Surgery 2

1.2.2 Radiotherapy 3

1.2.3 Chemotherapy 3

1.2.4 Targeted Therapy 4

1.3 Nanomedicine in Cancer Therapy 6

1.3.1 Advantages of Nanotechnology in Drug Delivery 8

1.3.2 The Mononuclear Phagocytic System 11

1.3.3 Targeting Approaches; Active and Passive Targeting 12

1.4 Irinotecan: A Key Chemotherapeutic Drug for Colorectal Cancer 17

1.4.1 Discovery 17

1.4.2 Pharmacokinetics 17

1.4.3 Distribution 18

1.4.4 Metabolism 18

1.4.5 Elimination 20

1.4.6 Mechanism of Action 20

1.4.7 Toxicity 23

1.5 Nanomedicine for Colorectal Cancer 25

1.5.1 Irinotecan-based Nanocarriers 26

1.5.1.1 Onivyde 26

1.5.1.2 Etirinotecan pegol 27

1.5.1.3 DEP irinotecan 28

1.5.1.4 NK012 28

1.6 Hyperbranched Polydendrons 30

1.7 Aims and Objectives 31

Chapter 2: Development and Validation of an LC-MS/MS Assay for the Quantification of Irinotecan and its Key Metabolites: *In Vivo* Assessment of Irinotecan Metabolism 32
2.1 Introduction 33
2.2 Methods and Materials 35
2.2.1 Materials 35
2.2.2 Tuning for Irinotecan, SN-38, SN-38G and IS 35
2.2.3 Chromatographic Separation 35
2.2.4 Preparation of Standards and Controls 36
2.2.5 Extraction Procedure 36
2.2.6 Assay Validation 37
2.2.7 Linearity 37
2.2.8 Recovery 37
2.2.9 Selectivity 37
2.2.10 Accuracy & Precision 37
2.2.11 Stability 38
2.3 Application of the Method 38
2.3.1 Animals 38
2.3.2 Pharmacokinetic Study 38
2.3.3 Statistics 38
2.4 Results 39
2.4.1 Method Development 39
2.4.2 Chromatographic Separation 40
2.4.3 Method Validation 41
2.4.3.1 Linearity 41
2.4.3.2 Extraction Recovery 42
2.4.3.3 Selectivity 43
2.4.3.4 Accuracy & Precision 43
2.4.3.5 Stability 48
2.4.4 Method Application 48
2.5 Discussion 50
2.6 Conclusion 51
Chapter 3: Monolayer (2D) and Spheroid (3D) Colorectal Cancer Models as a Tool for Assessing and Understanding Chemotherapeutic Effectiveness during Pre-Clinical Development 52
3.1 Introduction 54
3.2 Materials and Methods 59
3.2.1 Materials 59

3.2.2 Cell Lines and Maintenance 59
3.2.3 Monolayer (2D) Culture 60
3.2.4 Spheroid (3D) Culture 60
3.2.5 Analysis of Spheroid Growth 60
3.2.6 Histological Analysis 61
3.2.6.1 Spheroid Processing and Embedding 61
3.2.6.2 Spheroid Sectioning and Staining 62
3.2.6.3 Monolayer Staining 62
3.2.6.4 Imaging 62
3.2.7 Drug Treatment 63
3.2.7.1 Drugs 63
3.2.7.2 Monolayer Experiments 63
3.2.7.3 Spheroid Experiments 63
3.2.7.4 Determination of Cell Viability Following Treatment 64
3.2.8 Western Blotting 65
3.2.8.1 Cell Lysis 65
3.2.8.2 Tissue Lysis 65
3.2.8.3 Protein Determination 66
3.2.8.4 Immunoblotting 66
3.2.9 Immunofluorescence 67
3.2.9.1 Monolayer 67
3.2.9.2 Spheroid Sections 68
3.2.9.3 Whole-mount spheroids 68
3.2.10 Statistical Analysis 69
3.3 Results 70
3.3.1 Analysis of Spheroid Growth Kinetics - Spheroid Formation and Cultivation 70
3.3.2 Immunohistological Characterisation of Spheroids 73
3.3.3 Chemosensitivity of Monolayer and Spheroids Following Drug Treatment 76
3.3.4 Monitoring the Effect of Repeated Chemotherapeutic Exposure in Spheroids 78
3.3.5 Effect of Drug Treatment on Spheroid Histology 82
3.3.6 Detection of Topoisomerase I-DNA Covalent Complexes 85
3.3.7 Differential Expression of Proteins in Monolayer Cell Cultures 88
3.3.8 Investigating Protein Expression in Monolayer Cultures Compared to Spheroids 90
3.3.9 Differential Protein Expression in Human Tissues and Cell Cultures 92
3.4 Discussion 94
3.5 Conclusion 101

Chapter 4: Nanomedicines for Colorectal Cancer Therapy: *In Vitro* and *In Vivo* Assessment of SN-38 Encapsulated Nanoparticles 102
4.1 Introduction 103
4.2 Materials and Methods 109
4.2.1 Materials 109
4.2.2 Animals 109
4.2.3 SN-38 Nanoparticles Preparation and Characterisation 109
4.2.4 Cell Culture 111
4.2.4.1 Monolayer (2D) Culture 111
4.2.4.2 Spheroid (3D) Culture 111
4.2.5 *In vitro* Assessment of SN-38 Release 111
4.2.6 *In Vitro* Cytotoxicity 112
4.2.6.1 Monolayer (2D) Experiments 112
4.2.6.2 Spheroid (3D) Experiments 112
4.2.6.3 Determination of Cell Viability Following Treatment 113
4.2.7 Macrophage Uptake 113
4.2.8 *In Vivo*: Pharmacokinetic Evaluation 113
4.2.9 Statistical Analysis 114
4.3 Results 115
4.3.1 Characterisation and Selection of NPs 115
4.3.1.1 Drug Release 115
4.3.1.2 Cytotoxicity Studies 120
4.3.1.3 Macrophage Uptake 125
4.3.2 Candidate Selection 126
4.3.3 *In Vivo* Plasma Pharmacokinetics 127
4.4 Discussion 131
4.5 Conclusion 135
Chapter 5: General discussion 136
5.1 Introduction 136
5.2 LC-MS/MS Method Development 137
5.3 The Establishment and Characterisation of Colorectal Cancer Spheroids 138
5.4 Preclinical Assessment of SN-38 Loaded Nanoparticles 141
5.5 Future Considerations 145
5.5.1 Improving Translation 145
5.5.2 Vascularisation and Perfusion 147
5.5.3 The Tumour Microenvironment 150

5.5.4 Active Targeting 153
5.6 Perspectives and Conclusion 155
References 159
Appendix A Prioritisation of Anti-SARS-Cov-2 Drug Repurposing Opportunities Based on Plasma and Target Site Concentrations Derived from their Established Human Pharmacokinetics 186
A.1 Introduction 187
A.2 Methods 190
A.2.1 Candidate Analysis 190
A.2.2 Lung Accumulation Prediction 190
A.2.3 Data Analysis and Interpretation 191
A.3 Results 193
A.3.1 Identified Papers and Methods 193
A.3.2 Identification of Candidates Achieving Plasma Concentrations Expected to Exert Antiviral Activity (C_{max}/EC_{50} Ratio) 193
A.3.3 Identification of Candidates Achieving Plasma Concentrations Exceeding the SARS-Cov-2 EC_{90} (C_{max}/EC_{90} Ratio) 196
A.3.4 Detailed Interrogation of the Plasma Pharmacokinetics in Relation to Reported Anti-SARS-Cov-2 Activity 198
A.3.5 Simulated Exposure Relative to Reported Anti-SARS-Cov-2 Activity in Lung and Other Tissues 202
A.4 Discussion 206
A.5 Conclusion 214
Appendix B 215

List of Figures

Figure 1.2 Schematic representation of passive and actively targeted NP delivery systems. 14
Figure 2.1 Chemical structures of irinotecan, SN-38, SN-38G and SN-38-d3 33
Figure 2.2 Representative MS/MS chromatograms of Irinotecan, SN-38, SN-38G and, SN-38-d3 at 500ng/ml. 40
Figure 2.3 Representative LC-MS/MS chromatogram of Irinotecan, SN-38, SN-38G and the internal standard SN-38-d3. 41
Figure 2.4 Standard curve generated from extracted mouse plasma standards for Irinotecan, SN-38 and SN-38G. 42
Figure 2.5 The percentage recovery for Irinotecan, SN-38 and SN-38G at low, medium and high QCs in various matrices. 43
Figure 2.6 The plasma concentration-time curves of irinotecan, SN-38, and SN-38G following administration of irinotecan to BALB/c mice. 49
Figure 3.1 Schematic diagram of a spheroid. 56
Figure 3.2 Time table for setting up and performing spheroid-based drug assays with established tumour cell lines. 64
Figure 3.3 Effect of cell density on HCT116 spheroid formation 71
Figure 3.4 Effect of cell density on CT26 spheroid formation 72
Figure 3.5 Immunohistological assessment of HCT116 spheroids. 74
Figure 3.6 Immunohistological assessment of CT26 spheroids 75
Figure 3.7 Concentration-response curves for cells grown in 2D. 76
Figure 3.8 Concentration-response curves for HCT116 cells grown in 2D vs. 3D. 77
Figure 3.9 Concentration-response curves for CT26 cells grown in 2Dvs. 3D. 77
Figure 3.10 The effect of repeated drug treatment on HCT116 spheroids 80
Figure 3.11 The effect of repeated drug treatment on CT26 spheroids 81
Figure 3.12 Histological assessment of HCT116 spheroids following drug treatment 83
Figure 3.13 Histological assessment of CT26 spheroids following drug treatment 84
Figure 3.14 Detection of topoisomerase I-DNA covalent complexes by fluorescence microscopy following irinotecan treatment in 2D 86
Figure 3.15 Detection of topoisomerase I-DNA covalent complexes by fluorescence microscopy following SN-38 treatment in 2D 86
Figure 3.16 Detection of topoisomerase I-DNA covalent complexes by fluorescence microscopy following SN-38 treatment in 3D.. 87
Figure 3.17 Western blotting of proteins in CRC cancer cell lines grown in 2D 89
Figure 3.18 Comparison of CRC cells cultured in 2D vs. 3D. 91
Figure 3.19 Comparison of human tissue vs. CRC cells cultured in vitro. 93
Figure 4.1 An overview of the equilibrium dialysis method 112
Figure 4.2 Drug release profiles of free SN-38 and SN-38 loaded SB polymer nanoparticles, in phosphate-buffered saline at pH 7.4, over 48 hours 116
Figure 4.3 Drug release profiles of free SN-38 and SN-38 loaded SB polymer nanoparticles, in phosphate-buffered saline at pH 7.4, for the first 8 hours. 117
Figure 4.4 Drug release profiles of free SN-38 and SN-38 loaded CA polymer nanoparticles, in phosphate-buffered saline at pH 7.4, over 48 hours.. 118
Figure 4.5 Drug release profiles of free SN-38 and SN-38 loaded CA polymer nanoparticles, in phosphate-buffered saline at pH 7.4, for the first 8 hours. 119
Figure 4.6 The ten best nanoparticles identified from the in vitro drug release screen 120
Figure 4.7 Potency of SN-38 encapsulated nanoparticles compared to free SN-38 and irinotecan in monolayer colorectal cancer cell lines 121
Figure 4.8 Potency of SN-38 encapsulated nanoparticles compared to free SN-38 and irinotecan in spheroid colorectal cancer cell lines 122
Figure 4.9 Cytotoxicity of SB1 NPs in spheroids. 123
Figure 4.10 Cytotoxicity of CA16 NPs in spheroids 124

Figure 4.11 Uptake of nanoparticles by macrophages 125
Figure 4.12 Summary of candidates from the in vitro tiered screen. 126
Figure 4.13 Plasma concentration-time profiles of SN-38 following intravenous administration of irinotecan, free SN-38, SB1 and CA16 in BALB/c mice. 128
Figure 4.14 Plasma concentration-time profiles of SN-38 glucuronide following intravenous administration of irinotecan, SB1 and CA16 in BALB/c mice. 130
Figure 5.1 Overview of nanoparticle drug delivery to colorectal cancer liver metastases. 144
Figure 5.2 Overview of several key interactions involving NPs within the tumour 147
Figure A.1 Assessment of the variation in reported EC_{50} values for SARS-CoV-2 across the drugs for which more than one value was available in the literature. 195
Figure A.2 A bar chart displaying C_{max}/EC_{90} ratio for compounds studied for in vitro antiviral activity against SARS-CoV-2 for which data were available to recalculate an EC_{90} 197
Figure A.3 Digitised pharmacokinetic interrogation of all drugs calculated to have a C_{max}/EC_{50} ratio above 1. 199
Figure A.4 A bar chart displaying the simulated lung C_{max}/EC_{50}. 203
Figure A.5 A heatmap displaying the simulated tissue C_{max}/EC_{50} values for all drugs with available data. 205
Figure B.1 Morphology and appearance of colorectal cancer cell lines in monolayer (2D). 215
Figure B.2 Morphology of monolayer cells following drug treatment. 216
Figure B.3 Concentration-response curves for LoVo and DLD-1 cells grown in 2D vs. 3D 217
Figure B.4 Detection of topo I-DNA covalent complexes by fluorescence microscopy in HCT116 cells (2D). 217
Figure B.5 Detection of topo I-DNA covalent complexes by fluorescence microscopy in CT26 cells (2D) 218
Figure B.6 Detection of topo I-DNA covalent complexes by fluorescence microscopy in microscopy following irinotecan treatment in 3D 219
Figure B.7 Histological assessment of human tissue samples 219
Figure B.8 Drug release profiles SN-38 loaded nanoparticles, SB1 and CA16, in phosphate-buffered saline at pH 5.5. 220
Figure B.9 Concentration-response curves for monolayer cells treated with select polymer nanomaterial's. . 226
Figure B.10 Concentration-response curves for spheroids treated with select polymer nanomaterial's.. 230
Figure B.11 Reported EC_{50} and EC_{90} derived from in vitro anti-SARS-CoV-2 activity data 234
Figure B.12 Analysis of predicted and measured lung Kp. 235

List of Tables

Table 2.1 The operating chromatographic conditions 36
Table 2.2 Optimised tuning setting for the detection of the compounds 39
Table 2.3 The parent mass, product ion and collision energy for each of the compounds 39
Table 2.4 Intra-day and Inter-day accuracy and precision for irinotecan, SN-38 and SN-38G in mouse plasma . 45
Table 2.5 Intra-day and Inter-day accuracy and precision for irinotecan, SN-38 and SN-38G in DMEM 46
Table 2.6 Intra-day and Inter-day accuracy and precision for SN-38 in PBS 47
Table 2.7 Stability of the working solutions of Irinotecan, SN-38 and SN-38G stored at -40°C over 6 weeks 48
Table 3.1 Summary of the differences in two-dimensional vs. three-dimensional cell culture models 54
Table 3.2 Details of Cell Lines 59
Table 3.3 Antibodies for western blotting 67
Table 3.4 Antibodies for immunofluorescence 69
Table 3.5 The comparative IC_{50} values calculated from cell lines treated with irinotecan and SN-38 in 2D and 3D cell culture 78
Table 3.6 The comparative IC_{50} values following repeated exposures with irinotecan and SN-38 in 3D cell culture 79
Table 4.1 SN-38 based nanoformulations currently in development 105
Table 4.2 Nanoparticle formulations differing in the monomer composition 110
Table 4.3 Nanoparticle formulations differing in the polymer composition 110
Table 4.4 Pharmacokinetic parameters of irinotecan, free SN-38, SB1 and CA16 after intravenous administration in BALB/c mice 128
Table A.1 Summary of the top leads identified 200
Table B.1 Origin, genetic and mutational characteristics of investigated human colorectal cancer cell lines .. 215
Table B.2 SN-38 pharmacokinetic parameters after intravenous administration of irinotecan in BALB/c mice 231
Table B.3 SN-38 pharmacokinetic parameters after intravenous administration of SN-38 in BALB/c mice 231
Table B.4 SN-38 pharmacokinetic parameters after intravenous administration of SB1 in BALB/c mice 231
Table B.5 SN-38 pharmacokinetic parameters after intravenous administration of CA16 in BALB/c mice 232
Table B.6 SN-38 glucuronide pharmacokinetic parameters after intravenous administration of irinotecan in BALB/c mice 232
Table B.7 SN-38 glucuronide pharmacokinetic parameters after intravenous administration of SB1 in BALB/c mice 233
Table B.8 SN-38 glucuronide pharmacokinetic parameters after intravenous administration of CA16 in BALB/c mice 233
Table B.9 Data used for deriving predicted Kp and KpU tissue concentrations 236
Table B.10 Drugs investigated for SARS-CoV-2 antiviral activity and experimental overview 238

List of Abbreviations

Name	Abbreviation	Definition/function
2D	Two Dimensional	
3D	Three Dimensional	
5-FU	5-Fluorouracil	A chemotherapeutic agent that prevents cell proliferation by inhibiting thymidine formation
ABC	ATP-Binding Cassette	A transport system superfamily
ACE2	Angiotensin-Converting Enzyme 2	An enzyme attached to the cell membranes of cells in various organs that regulate Angiotensin 2 signalling
ACN	Acetonitrile	An organic solvent used for mobile phases
ANOVA	Analysis of Variance	
APC	Adenomatous Polyposis Coli	A protein that is a negative regulator that controls beta-catenin concentrations and is involved in cell adhesion
ATP	Adenosine-Triphosphate	Unit of energy in cells
AUC	Area Under the Curve	A measure of total systemic exposure to a drug
BCA	Bicinchoninic Acid	Assay to measure protein
BSA	Bovine Serum Albumin	Protein standard used in assays measuring protein levels
CAR	Cellular Accumulation Ratio	The ratio of intracellular to extracellular concentration
CES	Carboxylesterase	An enzyme that catalyses the hydrolysis of a carboxylic ester
CID	Chemotherapy-Induced Diarrhoea	Changes in intestinal absorption accompanied by excessive electrolyte and fluid secretion
CIMP	CpG Island Methylator Phenotype	A subset of colorectal cancers that happen through an epigenetic instability pathway and that are characterized by vast hypermethylation of promoter CpG island sites
CIN	Chromosomal Instability	A higher than normal rate of missegregation of chromosomes or parts of chromosomes during mitosis, resulting in copy number alterations (or aneuploidy.
CLM	Colorectal Liver Metastases	Colon cancer that has spread to the liver
C_{max}		The maximum concentration or maximum systemic exposure
COVID-19	Coronavirus 2019	An infectious disease caused by a newly discovered coronavirus.
COX	Cyclooxygenase	Responsible for converting arachidonic acid to prostaglandins
CPT	Camptothecin	A cytotoxic topoisomerase I specific quinoline alkaloid inhibitor
CRC	Colorectal Cancer	Development of cancer from the colon or large intestine
DAB	3,3'-Diaminobenzidine	An organic compound that is used in the staining of nucleic acids and proteins
dH20	Deionised Water	Water that has been treated to remove all ions
DMEM	Dulbecco's Modified Eagle Medium	Cell culture medium
DMSO	Dimethyl Sulfoxide	A colourless organosulfur solvent, which dissolves both polar and non-polar compounds
DNA	Deoxyribonucleic Acid	A double-stranded polymer containing four bases tethered to a sugar-phosphate backbone
DTT	Dithiothreitol	A reducing agent
ECM	Extracellular Matrix	A three-dimensional network of extracellular macromolecules that provides structural and biochemical support
EGFR	Epidermal Growth Factor Receptor	A type of receptor tyrosine kinase involved in cell signalling pathways that control cell division and survival

EMA	European Medicines Agency	A decentralized agency of the EU responsible for the scientific evaluation, supervision and safety monitoring of medicines
EPR	Enhanced Permeability and Retention Effect	A phenomena governing the transport of macromolecules and drug-delivery systems to the tumour site
FA	Folinic Acid	A form of folic acid that acts as a chemoprotective agent and a type of chemosensitising agent
FAP	Familial Adenomatous Polyposis	An autosomal-dominant, precancerous condition of the colon
FBS	Foetal Bovine Serum	Growth medium additive
FDA	Food and Drug Administration	An agency of the United States Department of Health and Human Services whose principal purpose is to enforce the Federal Food, Drug and Cosmetic Act
Fu	Fraction Unbound	The fraction of drug in plasma that is not bound to a carrier protein or other molecule, which generally is pharmacologically active
H&E	Haematoxylin and Eosin	Staining technique
HGF	Hepatocyte Growth Factor	A protein that regulates cell growth, cell motility and morphogenesis
HSC	Hepatic Stellate Cells	Liver-specific mesenchymal cells that play vital roles in liver physiology and fibrogenesis
HTS	High Throughput Screening	A drug discovery process that allows automated testing of large numbers of chemical and/or biological compounds for a specific biological target
IC_{50}	Half Maximal Inhibitory Concentration	The concentration of a chemical required to exert an inhibitory effect on 50% of the population
IF	Immunofluorescence	A technique that uses a detector antibody or an antigen labelled with fluorescent dyes
IS	Internal Standard	A chemical substance that is added in a constant amount to samples
IV	Intravenous	Solutions administered directly into the venous circulation
KC	Kupffer Cells	A macrophage present within the liver sinusoids
LC-MS/MS	Liquid Chromatography Coupled with Tandem Mass Spectrometry	Analytical chemistry technique
LDS	Lithium Dodecyl Sulphate	Sample buffer used to prepare proteins
LLOQ	Lower Limit of Quantification	Lowest analyte concentration that can be quantitatively detected
LSEC	Liver Sinusoidal Endothelial Cells	Form the wall of the liver sinusoids
LYVE-1	Lymphatic Vessel Endothelial Hyaluronan Receptor	A type I integral membrane glycoprotein that binds to hyaluronan
MCRC	Metastatic Colorectal Cancer	Cancer cells which have spread beyond the colon to other organs
MMR	Mismatch Repair	Repairs mismatches induced during replication
MOI	Multiplicity of Infection	Number of virions that are added per cell during infection
MPS	Mononuclear Phagocytic System	Class of cells that occur in widely separated parts of the human body and that have in common the property of phagocytosis
MRM	Multiple Reaction Monitoring	A highly specific and sensitive mass spectrometry technique used to selectively quantify compounds
MSI	Microsatellite Instability	A change that occurs in certain cells in which the number of repeated DNA bases is different from what it was when inherited
MW	Molecular Weight	The sum of the atomic masses of all atoms in a molecule

NK	Natural Killer Cells	A type of immune cell that has granules with enzymes that can kill tumour cells or cells infected with a virus
NME	New Molecular Entity	An active ingredient that contains no active moiety that has been previously approved
NO	Nitric Oxide	A toxic compound that acts as a vasodilator
NP	Nanoparticles	A wide class of materials that are smaller than 1000nm
NPC	Non-parenchymal cells	Specialised cells that interact with hepatocytes to form a functional hepatic unit
NSAID	Non-Steroidal Anti-Inflammatory Drugs	A class of drugs that are widely used to relieve pain and reduce inflammation
OS	Overall Survival	The length of time from either the date of diagnosis or the start of treatment for a disease
OTC	Over-The-Counter	A drug classified safe and effective for use by the general public without a doctor's prescription
PBPK	Physiologically Based Pharmacokinetics	A mathematical modelling technique for predicting the absorption, distribution, metabolism and excretion of drugs
PBS	Phosphate-Buffered Saline	A buffer solution
PCR	Polymerase Chain Reaction	A technique that enables the amplification of small amounts of DNA
PEG	Polyethylene glycol	A linear synthetic polyether
PFA	Paraformaldehyde	Tissue fixative
PPI	Protease and Phosphatase Inhibitor	A reagent used for protein sample protection for cell and tissue lysates
QC	Quality control	
RIPA	Radioimmunoprecipitation Assay	A lysis buffer used to lyse cells and tissues
ROS	Reactive Oxygen Species	A type of unstable molecule that contains oxygen and that easily reacts with other molecules in a cell
RPMI	Roswell Park Memorial Institute	Growth medium
RT	Room Temperature	
SARS-CoV-2	Severe Acute Respiratory Syndrome Coronavirus 2	The strain of coronavirus that causes coronavirus disease 2019
SD	Standard Deviation	
SDS	Sodium Dodecyl Sulfate	Anionic surfactant
SN-38G	SN-38 Glucuronide	Metabolite of irinotecan
$T_{1/2}$		The time required to reduce the plasma concentration to half of its initial value
T_{max}		The time taken to reach the maximum concentration
TNM	Tumour Node Metastases	Cancer staging system
TOP I	Topoisomerase I	An enzyme that reduces supercoiling in DNA
UGT	Uridine Diphosphate Glucuronosyltransferase	An enzyme responsible for the formation of glucuronides
VEGF	Vascular Endothelial Growth Factor	A signalling protein that promotes the growth of new blood vessels

Chapter 1: General Introduction

1.1 Introduction

Cancer is one of the foremost causes of death globally. According to the World Health Organization's World Cancer Report, in 2018 there were an estimated 18 million new cases of cancer with a reported 10 million deaths worldwide. The predicted global burden is expected to double to about 29–37 million new cancer cases by 2040 (World Health Organization, 2020). Cancer is a complex disease that arises from the transformation of normal cells into tumour cells in a multistage process. The complexity of cancer pathophysiology requires much efforts to identify the best approach for its successful management. Despite attempts to mitigate risk factors, the prevalence of cancer is continuing to increase. Over the next decade, cancer will be diagnosed in about 200 million people who will require care (World Health Organization, 2020). Treatment must, therefore, be improved and capacity scaled up.

Current standards of care combine precise staging of cancer with chemotherapy, radiotherapy and/or surgical resection. Radiotherapy and chemotherapy are known for significant adverse effects, with most methods targeting non-specifically any rapidly dividing cells irrespective of whether they are tumourous or not. Furthermore, poor pharmacokinetic characteristics of anticancer drugs arising from poor solubility, stability and metabolism pose challenges relating to toxicity, inefficacy and limited bio-distribution. Thus, it is imperative to develop effective therapies that can address these challenges and provide selective targeting of tumour sites. In particular, nanomedicines are being studied to achieve effective drug delivery, establish novel *in vitro* diagnostics, and develop nano-based implants. In the past decade, approximately 12,000 reports on the topic of nanomaterials as drug carriers in cancer treatment have been published (Z. Li, Tan, Li, Shen, & Wang, 2017). The design and synthesis of a library of nanomaterials, precise control over their physicochemical properties and ease of their surface functionalisation, has brought nano-based formulations to the forefront of medical research, emerging as potential tools for cancer treatment and its management.

1.2 Colorectal Cancer and its Treatments

Colorectal cancer (CRC) is the third most common cancer worldwide, with more than 1.8 million new cases diagnosed in 2018 (10.2% of the total number of cancers diagnosed; (Bray et al., 2018). In the United Kingdom, CRC is the fourth most common cancer amongst men and women with over 41,000 people being diagnosed annually, a trend that has gradually increased over the last 50 years (Cancer Research UK, 2018). Metastatic disease often occurs for patients with CRC and the lungs, liver, peritoneum and brain are primarily involved. For instance, at diagnosis, 14–20% of patients present with hepatic metastases (synchronous), and up to a third of patients will subsequently develop hepatic metastases (metachronous) during their disease (Adam et al., 2015). Survival is greatly dependent on the stage of cancer and the five-year overall survival (OS) for metastatic CRC (mCRC) remains low; less than 10% in recent reports (Cancer Research UK, 2018). This results in CRC being a leading cause of cancer deaths and represents a significant burden on patients, families and the healthcare system.

Metastatic disease often occurs for patients with CRC and the lungs, liver, peritoneum and brain are primarily involved. For instance, at diagnosis, 14–20% of patients present with hepatic metastases (synchronous), and up to a third of patients will subsequently develop hepatic metastases (metachronous) during their disease (Adam et al., 2015). Survival is greatly dependent on the stage of cancer and the five-year OS for metastatic CRC (mCRC) remains low; less than 10% in recent reports (Cancer Research UK, 2018). This results in CRC being a leading cause of cancer deaths and represents a significant burden on patients, families and the healthcare system.

1.2.1 Surgery

In general, patients with mCRC who go untreated have a median survival of 5–6 months. Several treatment options are available for patients with colorectal liver metastases (CLM), with chemotherapy and surgical resection forming the backbone of treatment in these patients. Surgical resection is the only treatment that offers a potential chance of cure and long-term survival with 5-year survival reported to be over 50% in recent studies (Aloia et al., 2006; Donadon, Ribero, Morris-

Stiff, Abdalla, & Vauthey, 2007; Fernandez et al., 2004). The overall median survival following liver resection in patients with CLM is reported to be 3.6 years. Patient selection is fundamental and several factors must be considered, including medical tolerability and technical/oncologic feasibility. Only 20% to 30% of patients with CLM are suitable for hepatic resection (Folprecht, Grothey, Alberts, Raab, & Kohne, 2005; Nordlinger et al., 2009).

Not all patients undergoing resection experience long-term benefit – around 30% develop recurrence and 15% succumb to their disease a year after surgery (Jones et al., 2012). This is because surgery leaves small clusters of tumour cells that cannot be removed or detected on scans or other tests. Some months after surgery, these cancer cells can proliferate again. Hence, long term survival is still only possible in a small minority of patients with mCRC. Therefore, to increase OS in this setting, several licensed agents are normally used to complement surgery.

1.2.2 Radiotherapy

Radiotherapy uses ionising radiation to eliminate cancer cells and is often used as a palliative treatment. Radiotherapy is less common for colon cancers but is utilised for rectal cancers. The indications for radiation in rectal cancer are to reduce the risk of local recurrence and to shrink locally advanced tumours to facilitate successful resection. In a Cochrane review, it was concluded that preoperative radiotherapy reduces the risk of local recurrence compared with surgery alone and overall mortality is marginally improved (R. K. S. Wong, Tandan, De Silva, & Figueredo, 2007).

1.2.3 Chemotherapy

The use of chemotherapy for advanced and mCRC was introduced by Charles Heidelberger with the discovery of 5-fluorouracil (5-FU), an antimetabolite that interferes with deoxyribonucleic acid (DNA) biosynthesis through the inhibition of thymidylate synthase (Heidelberger et al., 1957). It was later detected that the addition of folinic acid (FA) potentiated the effects of 5-FU, by stabilising the binding of 5-FU to thymidylate synthase to further enhance its inhibitory effect (Ullman, Lee, Martin, & Santi, 1978). Hence 5-FU/FA regimens gained acceptance in the early nineties in both the adjuvant and

metastatic setting (Poon et al., 1989). However, major advances in the evolution of chemotherapy for CRC were not achieved until the early 2000s when irinotecan (topoisomerase I inhibitor), oxaliplatin (a platinum-based alkylating agent) and the 5-FU prodrug capecitabine were introduced and combination therapies were formed (Gustavsson et al., 2015). Combination regimens have since become standard practice following their introduction and include;

- FOLFOX (folinic acid, 5-fluorouracil and oxaliplatin)
- FOLFIRI (folinic acid, 5-fluorouracil, irinotecan)
- FOLFIRINOX (folinic acid, 5-fluorouracil, irinotecan and oxaliplatin)
- XELOX (capecitabine, oxaliplatin) followed by FOLFIRI.

Both combination therapies (FOLFOX, FOLFIRI) have become standard cytotoxic combination regimens for the treatment of mCRC. Several trials (GERCOR and GOIM studies) showed similar efficacy for the FOLFIRI and FOLFOX regimens in patients with advanced CRC (Colucci et al., 2005; Tournigand et al., 2004). Both FOLFIRI and FOLFOX have been stated to enable a resection rate of 9-40% amongst patients with initially unresectable CRC liver metastases (Nordlinger et al., 2007). Combination chemotherapy, however, is not indicated as a first-line systemic treatment in all patients. A preference of combination or single-agent therapy as first-line treatment is dependent on patient and tumour-related factors and the fundamental aim of the therapy. Combination treatment choice is further based on differences in toxicity profiles between these regimens i.e. additional gastrointestinal side effects with FOLFIRI, whereas increased thrombocytopenia and neurotoxicity are present with FOLFOX (Colucci et al., 2005).

1.2.4 Targeted Therapy

In recent years, the development of novel pharmacological agents targeting molecular pathways known to play a vital role in carcinogenesis has shown significant improvement to the clinical outcome of mCRC patients. Vascular endothelial growth factor (VEGF) is a crucial mediator of angiogenesis.

Upon binding to its associated receptor on endothelial cells, VEGF activates cascades of signalling pathways to promote the growth and migration of endothelial cells. This leads to the formation of new blood vessels to supply oxygen, growth factors and cytokines to the tumour site (Ferrara, 2004). In 2004, Hurwitz et al. were the first to demonstrate that the addition of bevacizumab, a humanized monoclonal antibody that targets VEGF, to first-line FOLFIRI resulted in an improved OS (20.3 versus 15.6 months) (Hurwitz et al., 2004). Epidermal growth factor receptors (EGFR) are also involved in promoting the proliferation of malignant cells during carcinogenesis. Upon activation by its ligands, activation of two signalling pathways (RAS/RAF-MAPK for proliferation and PI3K-Akt/mTOR for survival) facilitate the growth of tumours (Normanno et al., 2006). Cetuximab, a chimeric monoclonal antibody, and panitumumab, a humanized monoclonal antibody, are two monoclonal antibodies targeting EGFR to reduce or delay the growth of cancer. These monoclonal antibodies extended the median OS to 20–30 months (7-8%) when used in combination with first-line FOLFOX or FOLFIRI chemotherapy regimens (Bokemeyer et al., 2011; Douillard et al., 2013; Van Cutsem et al., 2011). However, their use is limited to patients with wild-type KRAS. More recently, additional agents with antian¬giogenic effects such as aflibercept and regorafenib have been developed in attempts to maximise anti-VEGF targeting. Despite this, they have only displayed small survival benefits and treatment led to significant toxicities (Phase III CORRECT trial and Phase III VELOUR trial) (Grothey et al., 2013; Van Cutsem et al., 2011). Nevertheless, the efficacy of these newer approaches remains very limited against mCRC and novel treatment strategies are needed to reduce metastasis-related CRC mortality.

1.3 Nanomedicine in Cancer Therapy

Nanotechnology involves the use of nanometer-scale materials and systems by controlling the matter on the nanometre length scale. The applications of such approaches in various disciplines are becoming increasingly common. In particular, the medical application of nanotechnologies termed nanomedicine was defined by the National Institutes of Health of the United States and the European Science Foundation, as the "science that uses nanomaterials to the development of diagnosis, treatment and prevention of specific medical application" (Foundation, 2004; Oberdorster, 2010). An extensive variety of nanocarriers or nanoparticulate systems, composed of different materials have been proposed in the biomedical field. As current advances in biotechnology and related areas are aiding the discovery and rational design of many new classes of drugs, it is crucial to improve specific drug delivery methods by utilising nanotechnology, to turn these new advances into clinical effectiveness.

Nanoparticles (NP) are submicron-sized particles with diameters ranging from 10 – 1000nm (Parveen & Sahoo, 2008). NP-based systems possess unique physicochemical properties and their size, shape and surface properties can be tuned to modify the fate of both the NP and loaded drug (Shi, Kantoff, Wooster, & Farokhzad, 2017). Hence, the application of NPs in cancer therapy has been explored more widely than in any other disease, and their potential for optimising the pharmacokinetics of chemotherapeutics and selectively accumulating high concentrations of cytotoxic agents within tumours have been reported (Cheng et al., 2007; Jain & Stylianopoulos, 2010; Koo et al., 2011; Senapati, Mahanta, Kumar, & Maiti, 2018).

Drugs including small molecules, peptides, proteins and nuclear acids can be loaded in/onto NPs by various means, such as physical entrapment (encapsulating anti-cancer drugs within their cores), covalent linking or surface attachment i.e. polymeric micelles and polymer conjugates. As such, NPs designed to preserve the drug in its active conformation could provide significant clinical benefit as it has the potential to overcome problems such as insolubility of hydrophobic drugs, protecting a drug

from degradation in harsh physiological environments, enabling control of drug release kinetics and increasing drug uptake by cancer cells. Their surfaces can be additionally modified to incorporate specialised coatings or long-chain polymers (polyethylene glycol; PEG) to impart increased stability and an enhanced circulatory half-life (Knop, Hoogenboom, Fischer, & Schubert, 2010). Attaching targeting moieties including antibodies, nucleic acids, peptides, recombinant proteins and aptamers can further improve their selective accumulation (Rosenblum, Joshi, Tao, Karp, & Peer, 2018). On top of the mentioned physiological advantages of NPs, the tumour's pathophysiology offers ample opportunity for NP-based drug delivery. In comparison to healthy tissues, solid tumours exhibit a morphologically irregular and abnormally acidic microenvironment. As a result, NPs due to their small size tend to preferentially accumulate and localise within the tumour microenvironment, due to the hyper permeable vasculature and dysfunctional lymphatic drainage within tumours - referred to as the enhanced permeability and retention (EPR) effect which is discussed in more detail in section 1.3.3 (Kobayashi, Watanabe, & Choyke, 2014; Matsumura & Maeda, 1986). Therefore, the unwanted side effects and the toxicity of the therapeutic agent is reduced and the therapeutic efficacy is enhanced (Yih & Al-Fandi, 2006). NPs are opening new therapeutic opportunities for therapeutic agents that cannot be utilised effectively as conventional drug formulations because of poor bioavailability or drug instability. The various advantages of NPs are summarised in the table below.

Table 1.1 Summary of the advantages of NPs

Increase the aqueous solubility of the drug
Protect the drug from degradation
Produce a prolonged release of the drug
Improve the bioavailability of the drug
Provide a targeted delivery of the drug
Decrease the toxic side effects of the drug
Offer appropriate form for all routes of administration
Allow rapid-formulation development

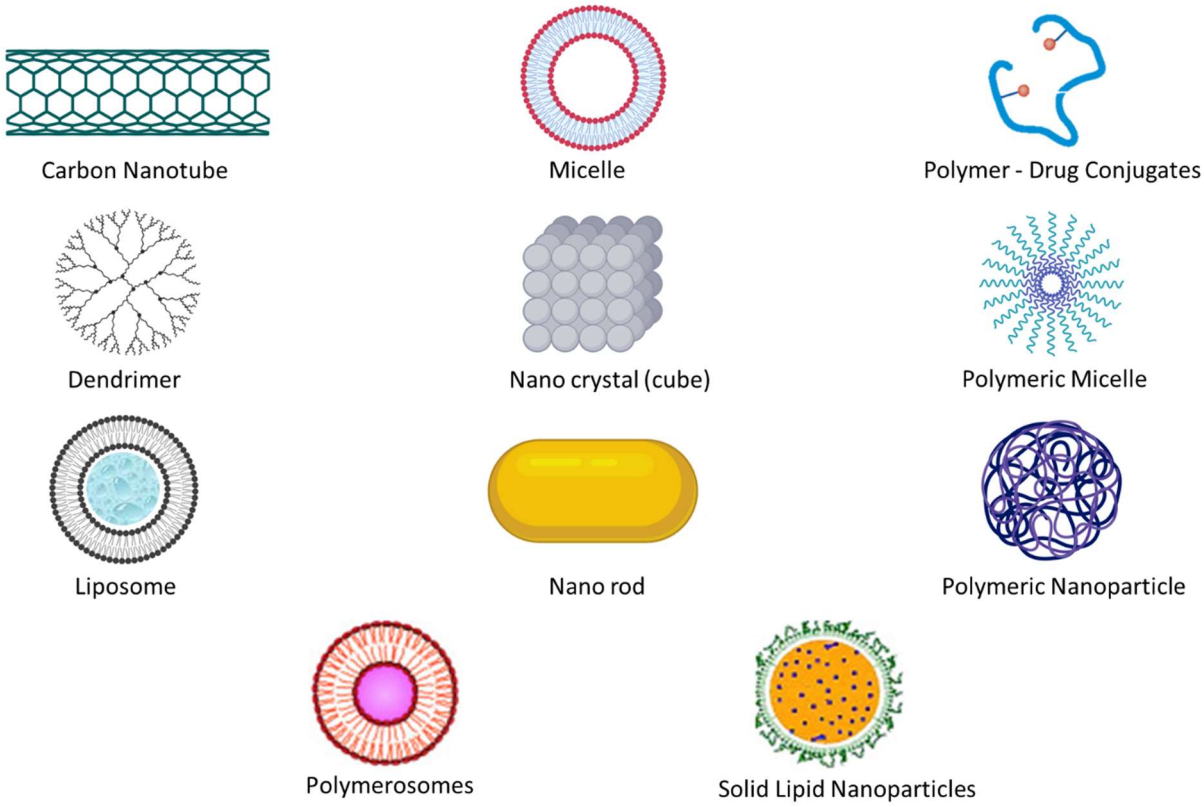

Figure 1.1 Schematic diagrams of several nanotechnology-based nanocarriers

1.3.1 Advantages of Nanotechnology in Drug Delivery

Nanotechnology in medicine is increasingly being viewed as a promising tool that will eventually surpass conventional chemotherapy. Several different nanocarriers are being investigated as controlled drug delivery vehicles for cancer therapy. These include carbon nanotubes, dendrimers, liposomes, micellar systems, NPs, and synthetic polymers (Mody, Tekade, Mehra, Chopdey, & Jain, 2014). These nano-sized drug carriers offer a versatile platform to which many properties can be added and modified, with the overall aim of improving therapeutic effectiveness and specificity. Several of these nanomedicines have been approved for use in clinical practice (see Table 1.2).

Table 1.2 Selected nanomedicines that have been approved or are in clinical development

Name	Particle type / Drug	Application / Indication	Approval Year / Phase	Advantages	
Doxil® /Caelyx® (Janssen)	Liposomal Doxorubicin (PEGylated) ~100nm	Ovarian cancer HIV associated Kaposi's - sarcoma Multiple myeloma	FDA (1995) EMA (1996)	Enhanced circulation time and up to six times more effective than free Dox	(Barenholz, 2012)
Myocet® (Teva UK)	Liposomal Doxorubicin (non-PEGylated) 150-250nm	Metastatic breast cancer	EMA (2000)	Better toxicity profile than free Dox (decreased occurrence of cardiac events and congestive heart failure)	(Anselmo & Mitragotri, 2016; Teva UK, 2019)
Onivyde® (Ipsen Biopharmaceuticals)	Liposomal Irinotecan (PEGylated) 80-140nm	Metastatic pancreatic cancer	FDA (2015)	Prolonged circulation and reduced gastrointestinal toxicity	(Ipsen Pharma, 2019; Tran, DeGiovanni, Piel, & Rai, 2017)
Genexol® PM (Samyang Biopharmaceuticals)	Polymeric micelle formulated – Paclitaxel (PEG-PLA) 20-50nm	Breast cancer Lung cancer Ovarian cancer	South Korea (2007)	Enhanced tumour distribution Reduced toxicity present Cremophor-free	(K. S. Lee et al., 2008; Samyang Biopharm, 2019)
VYXEOS® (Jazz Pharmaceuticals)	Liposomal Cytarabine–Daunorubicin (non-PEGylated) ~100nm	Acute myeloid leukaemia	FDA (2017) EMA (2018)	Improved overall survival	(Jazz Pharmaceuticals, 2019)
NK012 (Nippon Kayaku)	Polymeric micelle of SN-38 (PEG–PGA) ~20nm	Small cell lung cancer Metastatic colorectal cancer	Phase II		(Kayaku, 2019; Nakajima, Yasunaga, et al., 2008; Takahashi et al., 2010)
CPX-1 (Jazz Pharmaceuticals)	Liposomal formulation of Irinotecan and Floxuridine 110nm	Colorectal cancer Advanced solid tumours	Phase II		(Batist et al., 2009)
Onzeald™ Etirinotecan Pegol (Nektar)	Polymer drug conjugate of Irinotecan (PEGylated)	Metastatic breast cancer Ovarian cancer Colorectal cancer	Phase III		(Hoch, Staschen, Johnson, & Eldon, 2014; Nektar, 2019)
NLG207 formerly CRLX101 (NewLink Genetics)	Nanoparticle-Drug Conjugate Containing Camptothecin (Cyclodextrin–PEG)	Ovarian cancer Renal cancers Small cell lung cancer	Phase II		(Svenson, Wolfgang, Hwang, Ryan, & Eliasof, 2011)

	~20 to 30nm			
AZD2811 (AstraZeneca)	Polymeric nanoparticle containing an aurora kinase B inhibitor (PEG-PLA) 80-130nm	Advanced solid tumours Haematological tumours	Phase II	(Ashton et al., 2016; AstraZeneca, 2019)
MTL-CEBPA (MiNA Therapeutics)	SMARTICLES® based liposomal nanoparticle encapsulating CEBPA-targeting saRNA	Liver cancer	Phase I	(MiNA Therapeutics, 2019)
Promitil® (LipoMedix Pharmaceuticals)	Liposomal Mitomycin-C (PEGylated) 100nm	Advanced colon cancer Solid tumours	Phase I/II	(LipoMedix, 2019; Tahover et al., 2018)

1.3.2 The Mononuclear Phagocytic System

Systemic delivery via intravenous injection is the only route that has been successfully employed to deliver therapeutic NPs for cancer. Generally, complex NP therapies involving nanocarrier systems are difficult to deliver via other routes because they do not readily cross biological barriers in an intact form. Intravenous delivery is generally considered to be reliable and minimally invasive for cancer therapy, but NPs are subject to numerous physiological barriers within the circulatory system itself. The mononuclear phagocytic system (MPS), consisting of phagocytic cells located within organs including the bone marrow, spleen, liver and lymph nodes, sequesters and clears NPs from the systemic circulation (W. Jiang et al., 2017). Numerous serum proteins, in particular, opsonisation by complement factors (C3, C4 and C5), fibrinogen, albumin, apolipoprotein and immunoglobulins, are adsorbed onto the surface of circulating NPs (Nguyen & Lee, 2017). This typically triggers the recognition of opsonised NPs by specialised receptors, resulting in NP clearance from circulation by the MPS. Examples of phagocytic cells comprising the MPS include blood circulating monocytes, splenic red pulp and marginal zone macrophages, hepatic Kupffer cells (KC) and liver sinusoidal endothelial cells (LSEC), along with bone marrow macrophages (Davies, Jenkins, Allen, & Taylor, 2013; Y. N. Zhang, Poon, Tavares, McGilvray, & Chan, 2016). Given that premature elimination from the circulation obstructs NPs from accumulating in tumours, research has focussed on the design of NP surface chemistries to minimise clearance via the MPS.

The most common technique involves functionalisation of the NP surface with PEG, through a process called PEGylation. PEG molecules form a closely associated hydrating layer around the NP, impeding protein adsorption and subsequent clearance. In doing so, NPs are said to gain a “stealth” attribute and can remain in circulation for longer periods, increasing their chances of reaching target sites. This feature was best demonstrated by Doxil, whereby PEGylation extended the half-life from minutes to hours (Gabizon, Shmeeda, & Barenholz, 2003). The impact of PEGylation varies for NPs differing in shape, size and surface charge. PEGylation of smaller NPs results in a higher surface PEG density (larger hydrodynamic volume), meaning they are more readily able to evade clearance by the MPS (Alexis,

Pridgen, Molnar, & Farokhzad, 2008; Walkey, Olsen, Guo, Emili, & Chan, 2012). To specifically study the effect of surface charge on MPS uptake, Xiao *et al.* were able to demonstrate that NPs with high negative or positive charges were taken up by murine macrophages *in vitro* as well as *in vivo* (K. Xiao et al., 2011). Other surface modifications have included zwitterionic ligands, hydrophilic sugar coatings (dextran10) and the use of biological proteins (Abraxane® and INNO-206), but PEG remains the most widely used conjugation technique. Several PEGylated NPs loaded with chemotherapeutic agents have displayed selective tumour accumulation and enhanced inhibition in various xenografted models of CRC liver metastases (B. L. Chen et al., 2016; Luo et al., 2018; Pohlen, Buhr, & Berger, 2011; H. Zhang et al., 2015). Such results demonstrate the advantages of PEGylated over non-PEGylated drug delivery systems for cancer therapy. Of note, EZN-2208 is a PEGylated prodrug loaded with SN-38 that showed prolonged circulation in various preclinical tumour xenograft models in comparison to free drug. PEG was attached in a manner that stabilised the drug, maintaining its active conformation (Gritli et al., 2016; Sapra et al., 2008). However, when given to patients with advanced CRC in a randomised clinical study, EZN-2208 did not demonstrate superior efficacy in terms of OS in comparison to irinotecan (Garrett et al., 2013). Possible reasons for this were thought to be due to poor tumour drug distribution and pharmacokinetics. Therefore, even after NPs have successfully evaded clearance by the MPS, they still need to be able to effectively extravasate towards and penetrate the tumour microenvironment.

1.3.3 Targeting Approaches; Active and Passive Targeting

Alongside the MPS, both passive and active targeting plays a key role in assisting NP delivery to tumour sites - as depicted in Figure 1.2. Large fenestrae of 100–200nm (increases to 400-600nm in some liver diseases) and an absence of an organised basement membrane are features of the liver sinusoids (Aird, 2007). Hence, they can facilitate passive liver targeting through the widely reported EPR effect. This effectively builds up a high local concentration of NPs in the perisinusoidal space of Disse, whereby diffusion towards the malignant tumour cells can occur. Since the EPR effect is evident within tumours, it results in the preferential uptake and retention of NPs (Maeda, Wu, Sawa, Matsumura, &

Hori, 2000). Excessive pro-angiogenic signalling within the tumour microenvironment leads collectively to the production of immature blood vessels that are heterogeneous, poorly perfused and disorganised. The lymphatic systems of tumours are also abnormal, causing fluid retention and high interstitial pressure whilst leakage results from large inter-endothelial cell junctions, all of which favour the retention of NPs. These mechanistic features underpin the EPR effect and have been greatly exploited as a strategy to passively deliver NPs into tumours. It was established that NK012, a polymeric micelle formulation of SN-38, enhances its anti-tumour activity through the EPR effect. By using a VEGF-secreting tumour model, significantly enhanced accumulation of NK012 within tumours was demonstrated, augmented by the hypervascularity and hyperpermeability induced by VEGF (Koizumi et al., 2006). Similarly, in a phase II clinical trial the accumulation of the liposome, CPX-1, in CRC lesions was attributed to EPR-based accumulation (Batist et al., 2008; S. Goel et al., 2011; Golombek et al., 2018). Despite the benefits of passive targeting, major limitations still exist. Heterogeneity within tumours and between the primary and metastatic tumours often causes the non-uniform delivery of NPs (Adua et al., 2017). Additionally, passive delivery of NPs can result in drug exposure to healthy tissues and cells i.e. passively targeted NPs release their payload into the tumour microenvironment rather than within tumour cells. This can reduce therapeutic effectiveness, promote drug resistance, and promote off-target toxicity (W. Jiang et al., 2017). A possible solution to overcome such drawbacks is through the application of actively targeted NPs.

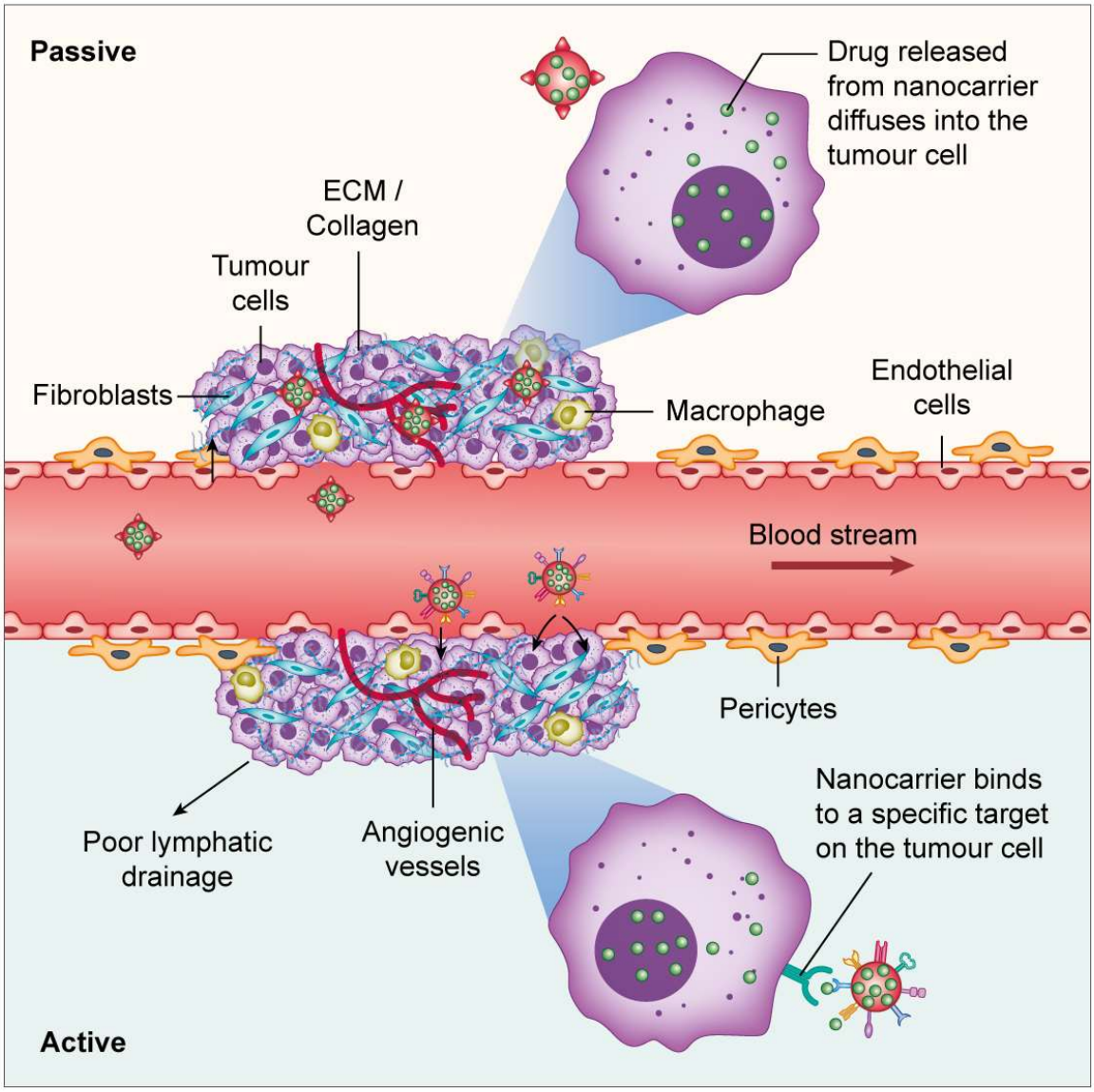

Figure 1.1 Schematic representation of passive and actively targeted NP delivery systems. By taking advantage of the EPR effect, non-targeted NPs can passively extravasate through the leaky vasculature and accumulate within the tumour (upper). Alternatively, the surface of NPs can be conjugated with targeting moieties to actively bind with a cell-specific target (lower). This allows for enhanced cellular uptake inside the tumour.

As mentioned earlier the limitations for chemotherapeutic treatments in mCRC are many, with the most common being the non-specific distribution of chemotherapeutic drugs. This poor specificity leads to a plethora of toxicological problems as well as drug resistance, which are the major concern and the primary reason for the failure of chemotherapy (C. Liu et al., 2009). A targeted approach may therefore be applied, to advance the pharmacological properties and reduce the toxicities associated

with the treatment of mCRC. Active targeting requires the conjugation of recognition molecules that can promote retention of NPs specifically at the tumour site. It is generally achieved by targeting surface molecules or receptors overexpressed on either the tumour cells, microenvironment or its vasculature. Careful selection of the targeting moiety is needed, and the target should be highly and preferentially expressed at the tumour site. Moreover, the targeting moiety should have strong and specific binding affinity to the intended target and be well suited to chemical modification by conjugation. However, to take advantage of this increased affinity, actively targeted NPs must first reach the target site. Effective passive targeting is therefore essential for these NPs to increase their accumulation and distribution at the tumour site. Recently, Sharma *et al.* demonstrated that NPs functionalised with folic acid displayed preferential *in vivo* uptake in colon tissue (Cisterna et al., 2016). Similarly in an mCRC experimental model, folate conjugated pRNA NPs were found to be specifically retained in liver metastases, without any untargeted uptake in other organs (Rychahou et al., 2013). Other investigations have shown that using hyaluronic acid as a targeting ligand on the surface of NPs, resulted in increased CRC targeting when compared to the non-targeted NPs (B. Xiao et al., 2015). Further, widely explored cellular targets for CRC include CD44, ASGPR, VEGFR, EGFR, TfR1, DR-5 carcinoembryonic antigens, TAG-72, integrin α5β1 and A54 peptide surface markers (Cohen & Margel, 2012; Schmid et al., 2014; Y. N. Zhang et al., 2016). Presently, methods to prime the tumour microenvironment are being reviewed to enhance NP delivery by normalising the tumour microenvironment (Jain & Stylianopoulos, 2010; Khawar, Kim, & Kuh, 2015; Stylianopoulos, Munn, & Jain, 2018). Despite the enhanced efficacy demonstrated in various studies, factors including; immunogenicity and stability of the targeting moiety leading to premature NP clearance, uneven exposure to chemotherapy - bringing about tumour recurrence, drug resistance and loss of activity due to receptor mediated endocytosis, severely hinder the application of targeted NPs. Research conducted by Wilhelm *et al.* highlighted this point, as they showed that active targeting only slightly improves the number of NPs that are efficiently delivered to tumours (Wilhelm et al., 2016).

A hallmark of cancer cells is their ability to activate invasion and metastasis (Hanahan & Weinberg, 2011). Metastasis, a multistage process, concerns the spread of malignant cells from a primary tumour to distant organs. Joseph Claude Récamier in 1829 was the first to reference and document metastasis - “métastase”, which he described as the haematogenous spread of disease (Pienta, Robertson, Coffey, & Taichman, 2013). This profound observational study initiated investigations into the mechanisms of metastasis in cancer (Talmadge & Fidler, 2010). Stephen Paget's seed and soil theory of metastases, stating that a permissive microenvironment (the soil) promotes the growth of the disseminated tumour cell (the seed), remains the basis of research to date and is widely accepted to explain the mechanism of metastasis (Paget, 1989). In a complementary hypothesis, James Ewing proposed in 1928 that cancer cells were directed to that site by the direction of lymphatic and circulatory systems (Ewing, 1928). Recent advances in our understanding of the metastatic process have led to the development of the concept of “pre-metastatic niche formation”. Here, changes at the cellular and molecular level are thought to occur in target tissues before the tumour cells leave the primary site. As a result, this renders the target site susceptible to metastatic cells (Psaila & Lyden, 2009). Continuous efforts to uncover the metastatic process will ultimately provide unprecedented potential for the improvement and development of effective adjuvant therapies.

1.4 Irinotecan: A Key Chemotherapeutic Drug for Colorectal Cancer

1.4.1 Discovery

Irinotecan (Camptothecin-11, CPT-11, Campto®, and Camptosar®) is a semisynthetic water-soluble derivative of the natural alkaloid camptothecin (CPT). The origin of irinotecan dates back to the late 1950s when a screening program of natural products was conducted by the United States Department of Agriculture (Wall & Wani, 1995). An extract of Camptotheca acuminate (family Nyssaceae), a plant native to China and Tibet was shown to have cytotoxic anti-tumour activity against lymphoid leukaemia cells, L-1210. Subsequent studies conducted at the National Cancer Institute demonstrated that CPT was the active constituent. CPT has a pentacyclic structure (rings A-E) and is insoluble in virtually all organic compounds except dimethyl sulfoxide (DMSO) in which it exhibits moderate solubility (Wall & Wani, 1996). The first soluble derivative was a sodium carboxylate form, but this achieved only low response rates and high toxicities (Moertel, Schutt, Reitemeier, & Hahn, 1972). It was, therefore, necessary to develop a soluble analogue able to exist in the active lactone (closed ring) form. Irinotecan, developed jointly by Daiichi Pharmaceuticals and Yakult Honsha in Japan, was the first water soluble CPT analogue to undergo extensive clinical evaluation and obtain regulatory approval. Irinotecan became commercially available in Japan for the treatment of ovarian, cervical, gastric, and lung cancers in 1994. In the mCRC setting, irinotecan obtained FDA monotherapy approval as a second-line treatment in 1996 (for patients refractory to 5-FU monotherapy), and in combination with 5-FU and folinic acid (as in the FOLFIRI regimen) as a first-line treatment for mCRC in 2000 (Cunningham, Falk, & Jackson, 2002; Douillard et al., 2000; Rougier et al., 2002; Vanhoefer et al., 2001). By 2006, the drug was approved in more than 100 countries and sold in 88.

1.4.2 Pharmacokinetics

Irinotecan is the prodrug for SN-38, which inhibits topoisomerase I (TOP I), an enzyme involved in DNA replication. SN-38 is 100- to 1000-fold more cytotoxic than irinotecan, and its exposure is highly variable. SN-38 is inactivated by further enzymatic conversion into SN-38 glucuronide (SN-38G).

1.4.3 Distribution

Irinotecan is a hydrophilic compound with an estimated volume of distribution up to 400L/m^2 at steady state. At physiological pH, the lactone-rings of irinotecan and SN-38 can be hydrolysed into a carboxylate isoform. As a result, a pH-dependent equilibrium exists such that, an acidic pH promotes the formation of the active non-ionic lactone form, while a more basic pH favours the inactive anionic carboxylate form. As only the lactone form has antitumour activity, a small change in pH could adjust the pharmacokinetics and efficacy of irinotecan and SN-38. Additionally, the lactone and carboxylate forms express distinctive affinities for transporters and disparities are seen in pharmacokinetic profiles in animals versus humans. Within plasma the carboxylate form of irinotecan and the lactone form of SN-38 dominate (Sasaki et al., 1995). Studies have shown this to be due to a higher tissue distribution of irinotecan lactone and the preferential binding of SN-38 lactone to plasma proteins (M.-C. Haaz, Rivory, Riché, & Robert, 1997; Xie, Mathijssen, Sparreboom, Verweij, & Karlsson, 2002). Both irinotecan (30-68%) and SN-38 (~95%) are highly bound to albumin (Burke & Mi, 1994). In blood, SN-38 is almost completely bound, with two-thirds located in platelets and, predominantly, red blood cells (Combes et al., 2000).

1.4.4 Metabolism

The carboxylesterases (CES1 and 2) and butyrylcholinesterase enzymes can hydrolyse the prodrug irinotecan into its active metabolite SN-38. CES1 and CES2 are localised in liver, colon, kidney and blood cells, while butyrylcholinesterase is predominantly found in plasma (Rudakova, Boltneva, & Makhaeva, 2011). Conversion by these esterases mainly occurs intra-hepatically and is a relatively slow and inefficient process as only 2–5% of irinotecan converted into SN-38 (G. Chabot et al., 1995; J Greg Slatter, Su, Sams, Schaaf, & Wienkers, 1997). The affinity of CES2 for irinotecan is 12.5-fold greater than CES1, whilst in the blood, butyrylcholinesterase has a 6-fold higher activity than CES (Bencharit et al., 2002; Laurent P Rivory, Bowles, Robert, & Pond, 1996; Rudakova et al., 2011). Following this conversion, SN-38 is actively transported into the liver by OATP1B1 (SLCO1B1), ABCB1,

MRP1 (ABCC1), MRP2 (ABCC2), and MXR (ABCG2). In particular, ATP-binding cassette (ABC) transporter ABCB1 located on the bile membrane is involved in the secretion of SN-38 into the liver.

Irinotecan is also metabolised by intrahepatic cytochrome P450 (CYP) enzymes, i.e. CYP3A4 and CYP3A5, into inactive metabolites — APC (7-ethyl-10-[4-N-(5-aminopentanoic acid)-1-piperidino] carbonyloxycamptothecin) and NPC (7-ethyl-10-[4-(1-piperidino)-1-amino] carbonyloxycamptothecin) (Santos et al., 2000). NPC can further be metabolised into SN-38 by CES1 and CES2 in the liver, but to a lower degree as compared to irinotecan (Dodds, Haaz, Riou, Robert, & Rivory, 1998). APC is poorly converted to SN-38 by CES2 and is also at least 100-fold less active than SN-38.

SN-38 is detoxified in the liver to SN-38G by uridine diphosphate glucuronosyltransferase (UGT) enzymes and excreted into the intestinal lumen via the bile duct (M. C. Haaz, Rivory, Jantet, Ratanasavanh, & Robert, 1997). This inactivation route involves the transfer of the glucuronic acid from the cofactor UDP-glucuronic acid to the SN-38, causing the formation of 10-O-glucuronyl-SN-38 (SN-38G), an inactive water-soluble and glucuronidated metabolite. SN-38G is formed directly after SN-38 formation, hence accounting for the short half-life of SN-38. Moreover, SN-38G can be deconjugated into SN-38 by (bacterial) β-glucuronidases produced by intestinal bacteria, which could result in the enterohepatic circulation of SN-38 and its reabsorption (Cole, Fuller, Mallet, & Rowland, 1985; Fujisawa & Mori, 1997; Sperker, Backman, & Kroemer, 1997; Younis, Malone, Friedman, Schaaf, & Petros, 2009). Several UGT subtypes are involved in the hepatic (UGT1A1, UGT1A9) and extrahepatic (UGT1A1, UGT1A7, UGT1A10) conversion of SN-38, of which UGT1A1, UGT1A7 and UGT1A9 are the major isoenzymes (Ciotti, Basu, Brangi, & Owens, 1999; Hanioka et al., 2001; L. Iyer et al., 1998; Strassburg, Oldhafer, Manns, & Tukey, 1997; Tallman, Ritter, & Smith, 2005). Reports have shown the UGT1A7 isoform to be approximately 20 times more active at physiological pH when compared to UGT1A1 (Ciotti et al., 1999). Furthermore, patients genetically predisposed with decreased UGT1 activity (Gilbert's syndrome) have an increased risk of irinotecan-associated adverse events

(Wasserman et al., 1997). The most common *UGT1A1* polymorphisms are *UGT1A1*6* and *UGT1A1*28*. Both polymorphisms produce increased systemic exposure to irinotecan and SN-38 in patients homozygous for these variants (Lalitha Iyer et al., 1999; Y. Wang et al., 2012).

1.4.5 Elimination

The clearance of irinotecan is mainly biliary (66%) with the remainder undergoing urinary excretion (32%) (Mathijssen et al., 2001). Irinotecan is transported into the bile by several ABC transporters (i.e. ABCB1, ABCC2, and ABCG2). All metabolites, except SN-38G (primarily excreted in urine), are predominately excreted in faeces, although they are also detectable in urine.

1.4.6 Mechanism of Action

The primary therapeutic target of SN-38 is DNA TOP I. TOP I is critical for cell growth proliferation and repair, as it makes a transient single-stranded break in the DNA duplex, which allows for the unwinding of supercoiled DNA, enabling the replication fork to process in duplicating the DNA. When inhibiting TOP I, SN-38 triggers several events, interfering with the replication fork and the nicking-ligation reaction of TOP I. After TOP I-mediated DNA cleavage, SN-38 binds to and stabilises the TOPI-DNA cleavable complex, thereby preventing re-ligation of the DNA strand. Subsequent accumulation of cleavable complexes results in double-stranded DNA breaks that inhibit DNA replication, triggering apoptotic cell death and transient cell cycle arrest (Pommier, Pourquier, Fan, & Strumberg, 1998). SN-38 is considered an S-phase-specific antitumour drug since it needs ongoing DNA synthesis to exert its cytotoxic effects.

Two recent publications suggest that SN-38 may not uniquely target TOP I. One study refers to the interaction of SN-38 with the E3 ligase MDM2 (a ligase of tumour suppressor protein p53) and the anti-apoptotic protein Bcl-xL (B. Lee et al., 2019). This suggests that SN-38 acts as a selective protein binding inhibitor. Another study put forward the idea that SN-38 inhibits human FUBP1 (Far Upstream Element (FUSE) Binding Protein 1) activity. FUBP1 is a multifunctional DNA- and RNA-binding protein and SN-38 prevents binding of FUBP1 to its single-stranded DNA target. This induced deregulation of

FUBP1 target genes in hepatocarcinoma cells (Khageh Hosseini et al., 2017). Nevertheless, these different studies suggest that SN-38 may have targets other than TOP I, which is a plausible hypothesis because it is known that other CPT analogues can regulate gene expression independent of TOP I function (Mabb et al., 2016).

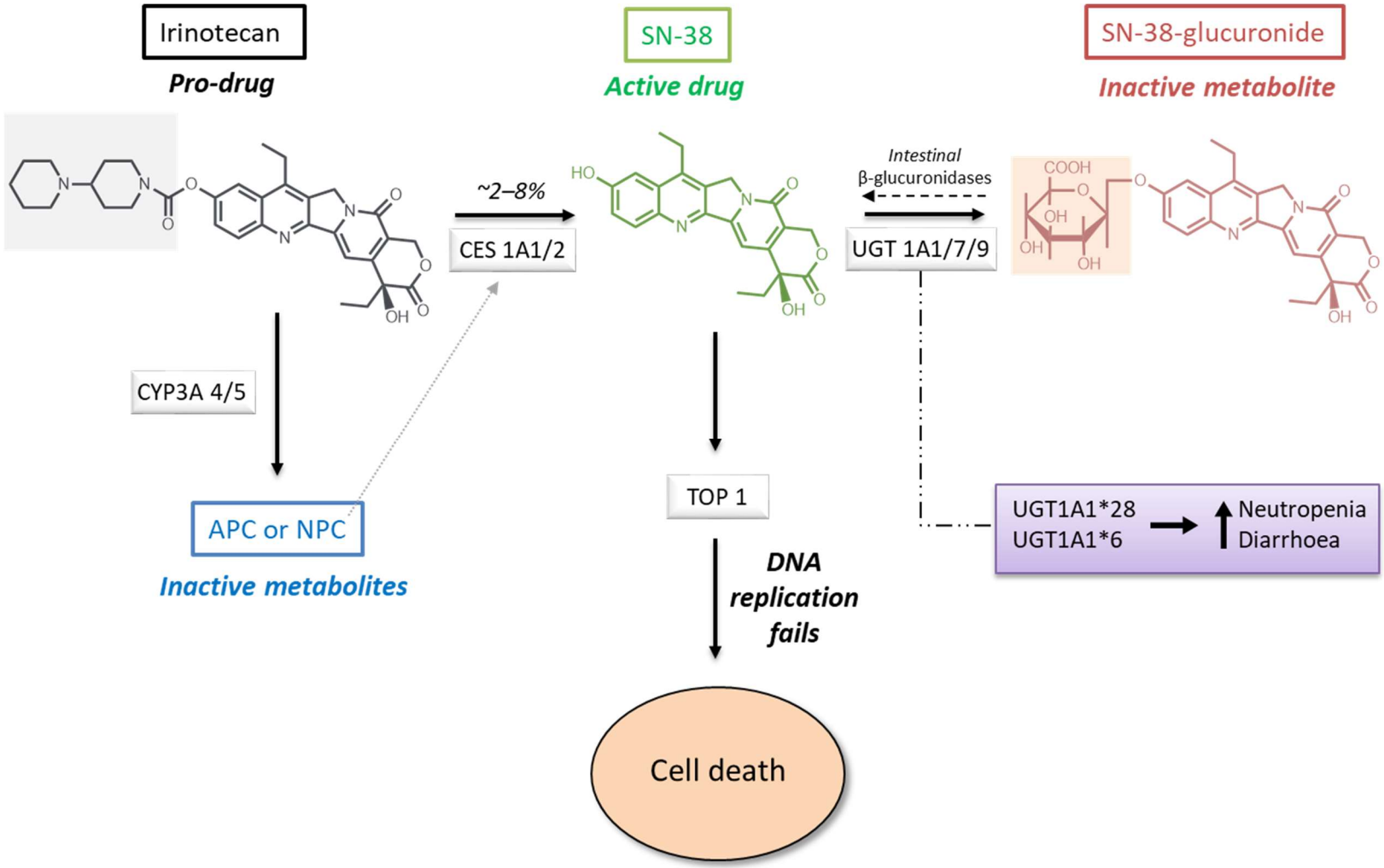

Figure 1.3 Schematic summarising the metabolism of Irinotecan

Irinotecan is metabolised into its active metabolite SN-38 via carboxylesterases. SN-38 is then inactivated into its glucuronide conjugate, SN-38G, by the uridine diphosphate glucuronosyltransferases. Hepatobiliary excretion occurs then SN-38G is reconverted into active SN-38 by bacterial β-glucuronidases. A second irinotecan detoxification pathway is the CYP3A mediated oxidation of irinotecan into APC and NPC. Carboxylesterases (CES2) also facilitate the conversion of NPC into SN-38.

1.4.7 Toxicity

Administration of irinotecan is limited by severe dose-limiting toxicities with distinct inter-individual and inter-ethnic variability. The most common being chemotherapy-induced diarrhoea (CID) and myelosuppression; ~35% of the treated patients reported grade 3/4 diarrhoea and ~14–47% reported grade 3/4 neutropenia (Hoskins, Goldberg, Qu, Ibrahim, & McLeod, 2007; Richardson & Dobish, 2007). Such toxicities decrease therapeutic benefit by preventing dose intensification and efficacy in up to 40% of treated patients (Maroun et al., 2007). The manifestation of both severe diarrhoea and neutropenia (~10%) is associated with a greater risk of death (~3.5%) for patients (Ducreux, Kohne, Schwartz, & Vanhoefer, 2003; Rothenberg, Meropol, Poplin, Van Cutsem, & Wadler, 2001). Moreover, acute CID occurs following 1–24 h of administration. It can be life-threatening when it is prolonged, owing to the risk of dehydration, imbalance of electrolytes, hemodynamic collapse or severe sepsis due to bacterial translocation (Rothenberg et al., 2001).

Irinotecan acutely damages the intestinal mucosa, causes the mitotic arrest of crypt cells and increases apoptosis. The severity of irinotecan-induced gastrointestinal toxicity and histological damage is associated with the intestinal β-glucuronidase activity, the rate of biliary excretion of SN-38 and the reconversion of SN-38 from the enteric SN-38G. If the rate of SN-38 glucuronidation in the intestines is low, active SN-38 is exposed to the epithelial cells for a lengthier period, resulting in severe diarrhoea due to the loss of colonic absorptive capacity. Thus, the glucuronidation of SN-38 is imperative for limited gastrointestinal toxicity. The rate of metabolic conversion to the water-soluble derivative SN-38G depends on polymorphs of the UGT1A1 enzyme and is highly variable among individuals. For instance, individuals with the UGT1A1*28 allele have been reported to have a higher risk of neutropenia caused by limited metabolism of SN-38. This is due to the reduced expression of UGT1A1 leading to impaired clearance and increased toxicity (Innocenti et al., 2009; Wiseman & Markham, 1996).

Other common toxicities observed following irinotecan administration are nausea, vomiting, abdominal pain, constipation, anorexia, asthenia, fever, decrease in body weight and alopecia (Bast, 2016). Rare, but life-threatening non-haematological toxicities include interstitial lung disease and hypersensitivity reactions. Oxidative metabolic pathways, CYP2B6 and CYP3A4, create inactive irinotecan metabolites and increase the potential for drug-drug interactions. Hepatotoxicity is also reported, with several observational clinical studies having reported that the inclusion of irinotecan in preoperative chemotherapy regimens is associated with the risk to develop steatohepatitis in up to 50% of cases (Mahli et al., 2018). Furthermore, there is significant evidence that the presence of chemotherapy-induced steatohepatitis is associated with increased morbidity and possibly mortality following hepatic resection as a result of hepatic insufficiency (Morris-Stiff, Tan, & Vauthey, 2008). Details of the mechanisms of irinotecan induced hepatotoxicity remain unclear. However, it is thought to involve hepatic changes brought about by liver inflammation, oxidative stress, mitochondrial dysfunction and fibrosis.

1.5 Nanomedicine for Colorectal Cancer

The number of patients with CRC has increased markedly over the past 20 years and will continue to increase in the future. Despite recent advances in chemotherapy, chemotherapeutic treatments for CRC are not as effective as for some other cancers, because of the difficulty of delivering drug at effective concentrations to the target site. To maintain therapeutic concentrations at the tumour site, chemotherapeutic drugs must be administered at high doses and this causes serious toxicity to normal (non-cancerous) tissues and organs i.e. due to the non-specific distribution of chemotherapeutic drugs. In many cases, the failure to achieve effective doses at the tumour site leads to the failure of chemotherapy, cancer recurrence and reduced patient survival.

As discussed above irinotecan has several well-established limitations. Although SN-38 is up to a 1000-fold more potent than irinotecan, its clinical use is limited by its poor solubility and chemical instability of its pharmacologically active lactone ring (G. G. Chabot, 1997). It is practically insoluble in water (11–38μg/ml) and is not solubilised at 0.5% (w/w) in most pharmaceutically acceptable solvents and oils, limiting the direct formulation as a solution dosage form (Williams et al., 2003). The active, closed-ring structure (lactone) of SN-38 is stable at pH ≤ 4.5 and hydrolyses completely to form the open-ring structure (carboxylate) at pH > 9.0 (L. P. Rivory, Chatelut, Canal, Mathieu-Boue, & Robert, 1994). At pH 6.7 both forms are in equilibrium. The instability of the active drug molecule at physiological pH (pH 7.4) is a major hurdle in attaining effective therapy with SN-38, as the open carboxylate form of SN-38 has no therapeutic effect resulting in low anti-tumour activity. Other limitations include fast reversal of the trapped TOPI-DNA cleavage complex following drug removal and drug resistance mediated by the ABC transporters. In addition, the conversion of irinotecan into SN-38 is often inefficient in humans and leads to variability in SN-38 exposure (Hsiang et al., 1989). Alongside this, the narrow therapeutic index of irinotecan presents further challenges for its use as an anti-cancer therapeutic in the clinic.

The transport of drugs by NPs has shown great promise in terms of improving drug distribution and bioavailability, increasing tissue half-life and concentrating anticancer molecules in the tumour mass, providing optimal drug delivery to tumour tissue, and minimising drug toxicity, including those effects associated with pharmaceutical excipients. Similarly, NPs may interact with key drug-resistance molecules to prevent a reduction in intracellular drug levels. Recently published data have provided convincing pre-clinical evidence regarding the potential of active-targeted nanotherapeutics in CRC therapy, although, unfortunately, only a few of these therapies have been translated into early-phase clinical trials. Thus, incorporating SN-38 into a pharmaceutical formulation with an adequate solubility and stability profile might be attractive for cancer therapy. As a result, some of the limitations and challenges mentioned may be overcome by using a nanomedicine-based approach, leading to a more efficient chemotherapeutic option.

Various polymer-based structures have been used in cancer treatment and established excellent therapeutic potential at both preclinical and clinical development stages. The high rate of irinotecan toxicity has prompted the development of alternative treatment strategies to reduce the drug's serious side effects. This includes the use of encapsulated drug delivery by various nanocarriers, including liposomes (Onivyde), polymeric nano-conjugates (NKTR102) and micellar formulations (NK012).

1.5.1 Irinotecan-based Nanocarriers

1.5.1.1 Onivyde

The liposomal carrier, Onivyde (also known as PEP02 or MM-398), was approved in 2015 for combination with 5-FU and folic acid as a second-line therapeutic option for patients with metastatic pancreatic ductal adenocarcinoma, after disease progression following gemcitabine-based therapy (H. Zhang, 2016). Onivyde liposomes are unilamellar lipid bilayer vesicles with a mean diameter of ~110 nm. The vesicle is composed of distearoyl phosphatidylcholine, cholesterol and DSPE-PEG2k in the ratio of 3:2:0.015, which encapsulates more than 90% of the drug (X. Liu, Tang, Wainberg, & Meng,

2020; Tran et al., 2017). This liposomal encapsulation helps protect irinotecan from early conversion into its active metabolite SN-38. Onivyde displayed a much slower clearance, a prolonged terminal $t_{1/2}$ of circulating total irinotecan (25.8 hours), and more favourable pharmacokinetics of SN-38 were observed in comparison to free drug-treated patients (Chiang, Chang, Shan, & Chen, 2016; Roy et al., 2013). The dose-normalised $AUC_{0-\infty}$ value of active SN-38 was approximately five times higher for Onivyde than that of irinotecan (Chiang et al., 2016; Roy et al., 2013). However, Onivyde's approval was accompanied by a "black box" safety warning from the FDA, referring to the likelihood of severe diarrhoea (grades 3–4, 13%) and severe and life-threatening neutropenia (grades 3–4, 27%) (Barenholz, 2012). Although Onivyde demonstrated antitumor efficacy and improved safety in a subcutaneous CRC model in nude mice (Wolfram et al., 2015), the advantages of encapsulated drug delivery could not be demonstrated in CRC patients in a phase II clinical trial, and the effort was abandoned. Despite this, Onivyde is currently being investigated in a variety of solid tumour types, including lung and breast cancer.

1.5.1.2 Etirinotecan pegol

Etirinotecan pegol (NKTR-102 or Onzeald), is a long-acting topoisomerase-I inhibitor that was designed to improve the pharmacokinetics of irinotecan. Structurally, etirinotecan pegol contains a large-chain PEG core to which four molecules of irinotecan are attached via a cleavable ester-based linker (Hoch et al., 2014). This linker is slowly hydrolysed *in vivo* to subsequently release irinotecan. The high molecular weight of etirinotecan pegol (22 kDa) limits its ability to freely cross intact vasculature into healthy tissues, but promotes extravasation via the EPR effect. In an initial phase 1 study, the mean half-life of SN-38 was prolonged from 2 days following administration of conventional irinotecan to 50 days with etirinotecan pegol. Additionally, fewer cases of early-onset cholinergic diarrhoea and neutropenia were seen (Jameson et al., 2013). A randomised phase 2 study assessing two schedules of etirinotecan pegol (145 mg/m^2 every 14 or 21 days) reported that the drug produced substantial antitumour activity in patients (Awada et al., 2013). Subsequent phase 3 clinical studies in patients with advanced metastatic breast cancer (Tripathy et al., 2019) and advanced breast cancer with brain

metastases (Perez et al., 2015), did not achieve statistical significance. No improvement in overall survival was present in patients receiving etirinotecan pegol, and, as a result, development activities came to an end.

1.5.1.3 DEP irinotecan

Starpharma's DEP irinotecan is a PEGylated polylysine dendrimer with SN-38 conjugated to the surface via a hydrolytically labile linker. The incorporation of the active metabolite, SN-38 avoids the need for hepatic conversion and thereby minimises variability in SN-38 levels. In preclinical studies, DEP irinotecan has shown to be well tolerated in animals (Kelly et al., 2020). Efficacy assessments have been conducted, using a range of xenograft cancer models (SW620, HT-29, MDA-MB-231 and CAPAN-1). These studies demonstrated significant efficacy and survival benefits of DEP irinotecan compared to standard irinotecan. DEP irinotecan, alone and in combination with Lynparza, showed significant anti-tumour efficacy and synergy compared with standard irinotecan and Lynparza (olaparib) in an irinotecan-refractory human colon cancer model (Starpharma, 2019). Treatment with DEP irinotecan provided a significantly greater level of inhibition – 62% for low dose and 97% for high dose. DEP irinotecan is currently in a phase 1/2 adaptive trial to evaluate its safety, tolerability and pharmacokinetics, and to determine anti-tumour efficacy in various tumour types.

1.5.1.4 NK012

NK012 is an SN-38-loaded polymeric micelle formulation constructed in an aqueous milieu by the self-assembly of an amphiphilic block copolymer, consisting of PEG and partially SN-38–bound polyglutamate (Koizumi et al., 2006). PEG is hydrophilic and forms the outer shell of the micelle, whilst SN-38–bound polyglutamate is hydrophobic and forms the inner core of the micelle. The ester bond between glutamic acid and SN-38 is gradually cleaved by hydrolysis under physiological conditions. Hence the release of SN-38 is not dependent on metabolic conversion by enzymes. NK012 has a particle size of 20 nm and shows high colloidal stability due to the hydrophobicity of SN-38, as well as

π–π stacking of the drugs inside the micelle (Y. Li, Zhang, Liu, & He, 2019). It is thought that NK012 accumulates in tumour tissue by utilising the EPR effect.

NK012 is proposed to be a promising agent for clinical applications given that its ability to suppress tumour cell growth *in vitro* and its antitumor effects in animal models are greater than those of irinotecan in various cell types, including several human tumours. In addition, NK012 has been found to accumulate in high concentrations in tumourous mouse models (Nakajima, Yanagihara, et al., 2008; Sumitomo et al., 2008)**.** A phase I study was launched to evaluate the tolerability, pharmacokinetics, safety, and recommended phase II dose of NK012 in 38 patients with advanced cancer. Accordingly, the recommended dose was determined to be 28 mg/m^2. In a second phase I study, NK012 showed high plasma levels with a terminal $t_{1/2}$ of approximately 210 hours (Hamaguchi et al., 2010). NK012 was well tolerated, and the antitumor activity showed partial responses and several occurrences of prolonged stable disease condition, such as a reduction of tumour size. In addition, a multicentre open-label phase II study was launched to evaluate the efficacy and safety of NK012 in 58 patients with unresectable metastatic CRC. In this trial, the presence of febrile neutropenia and grade ≥ 3 neutropenia, indicated that NK012 at 28 mg/m^2 may be too high for CRC patients pretreated with oxaliplatin (Hamaguchi et al., 2018). Since November 2017, no further reports of development have been presented within the literature.

Therefore, the polymers employed in NP formulations make them ideal drug delivery systems, and they could play an important role in improving the bioavailability of the anticancer drugs and the subsequent therapeutic effect in CRC treatment.

1.6 Hyperbranched Polydendrons

When developing a highly efficient therapeutic, many issues need to be considered. The ideal system should be able to overcome the biological barriers, distinguish the tumour tissues from the normal cells, target specific sites and release an efficacious dose. The advantages of using polymeric nanostructures are based upon the flexibility of their modified structures. This yields materials with various compositions, sizes and surfaces, thereby allowing for tuneable properties.

Hyperbranched polydendrons are dendrimer-like materials that mimic the surface functionality of a dendrimer (repetitively branched monomers with a large number of adjustable peripheral groups) with a much greater molecular weight and size than conventional dendrimers (Hatton et al., 2015). This technology allows drug encapsulation within polymer NPs and henceforth the dispersion of poorly water soluble compounds. These novel materials are intended to offer benefits as nanomedicines through their increased stability, encapsulation properties, enhanced bioavailability and decreased drug toxicity structure. They also present high densities of surface functionality that could be applied for a more targeted approach.

The materials which were made use of in this thesis comprised of a branched polymer and either a block copolymer or a linear dendritic hybrid. It is useful to be able to control the properties of such materials including for example their size, size distribution, surface functionality (active targeting and incorporation of acid degradable branching units to saturate drug at tumour site), hydrophobicity/hydrophilicity (i.e. hydrophobic core for encapsulation of hydrophobic drugs), variety of drug loadings and behaviour in systems of use, e.g. in aqueous systems in the case of biological applications. Hyperbranched polydendrons offer enormous flexibility in the customisation of NPs in drug delivery, and thereby represent a promising opportunity for the *in vivo* diagnosis and treatment of CRC liver metastases. However, with so many parameters capable of being altered, a process of optimisation is initially required.

1.7 Aims and Objectives

This thesis aimed to characterise bespoke polymeric NP formulations loaded with SN-38 and evaluate their prospective use in the treatment of CRC liver metastases. It was hypothesised that incorporating SN-38 into these nanomaterial's could improve the treatment outcomes of CRC by augmenting drug retention and enhancing SN-38's bioavailability. The experimental objectives for which the chapters are based are as follows: Chapter 2 details the development and optimisation of a liquid chromatography-mass spectrometry assay for the detection of irinotecan, SN-38 and SN-38G in various matrices. Chapter 3 outlines the development and characterisation of CRC spheroids using both human and mouse cell lines. Responses to both irinotecan and free SN-38 are investigated. Chapter 4 describes the analysis of various polymer nanomaterial's using an *in vitro* tiered screening system to select out the most effective candidates. Properties such as drug release and retention, disposition, cytotoxicity and pharmacodynamics were investigated. The plasma pharmacokinetic profiles of the best NP candidates were investigated *in vivo* and compared with both free SN-38 and irinotecan.

Chapter 2: Development and Validation of an LC-MS/MS Assay for the Quantification of Irinotecan and its Key Metabolites: *In Vivo* Assessment of Irinotecan Metabolism

Abstract

Irinotecan is a chemotherapeutic agent used in the treatment of metastatic colorectal cancer. The work presented throughout this thesis required the development of a liquid chromatography-tandem mass spectrometer bioanalytical assay. A method was therefore optimised to quantify irinotecan, its active metabolite SN-38 and SN-38 glucuronide (SN-38G) in different matrices (mouse plasma, PBS and DMEM growth medium). A 100µL of the sample was prepared after protein precipitation with centrifugal evaporation and analysed on a C18 column (Synergi^{TM} Hydro-RP 80A) using 0.1% formic acid in water and 0.1% formic acid in acetonitrile as mobile phases. The mass spectrometer worked with multiple reaction monitoring in positive scan mode with a 5.50-minute analytical run time. The method was validated according to the bioanalytical guidelines defined by the Food and Drug Administration. The standard curves were linear ($R^2 \geq 0.99$) over a concentration range of 4-1024ng/mL for irinotecan, 2-512ng/mL for SN-38 and 2-512ng/mL for SN-38G across all matrices. Intra-day and inter-day variations (precision and accuracy) observed during the validation for all analytes, were found to be within the set limit of 15%. The developed method was successfully used to quantify irinotecan, SN-38, and SN-38G and applied to a pharmacokinetic study in BALB/c mice. Results from plasma concentration-time profiles suggested the rapid elimination of irinotecan and SN-38 from the plasma.

2.1 Introduction

Irinotecan (Camptosar®, CPT-11) is a chemotherapeutic drug used in the treatment of colorectal cancer, most often in combination with other chemotherapeutics (folinic acid and 5-fluorouracil) or targeted (cetuximab and bevacizumab) therapies. Irinotecan is cleaved into the primary active metabolite SN-38 (7-ethyl-10-hydroxycamptothecin), primarily by liver carboxylesterases (CES) (Senter, Beam, Mixan, & Wahl, 2001). SN-38 is 100–1000 times more potent than its parent drug, but as it's poorly soluble it cannot be administered systemically, hence irinotecan is currently used as a prodrug in clinical applications (Humerickhouse, Lohrbach, Li, Bosron, & Dolan, 2000; Kaneda, Nagata, Furuta, & Yokokura, 1990; Marangon, Posocco, Mazzega, & Toffoli, 2015). It is necessary to simultaneously monitor for the prodrug and its main metabolites to resolve the issues around the inter-individual variability in the pharmacokinetics and pharmacodynamics of irinotecan, and thus to improve colorectal cancer treatment.

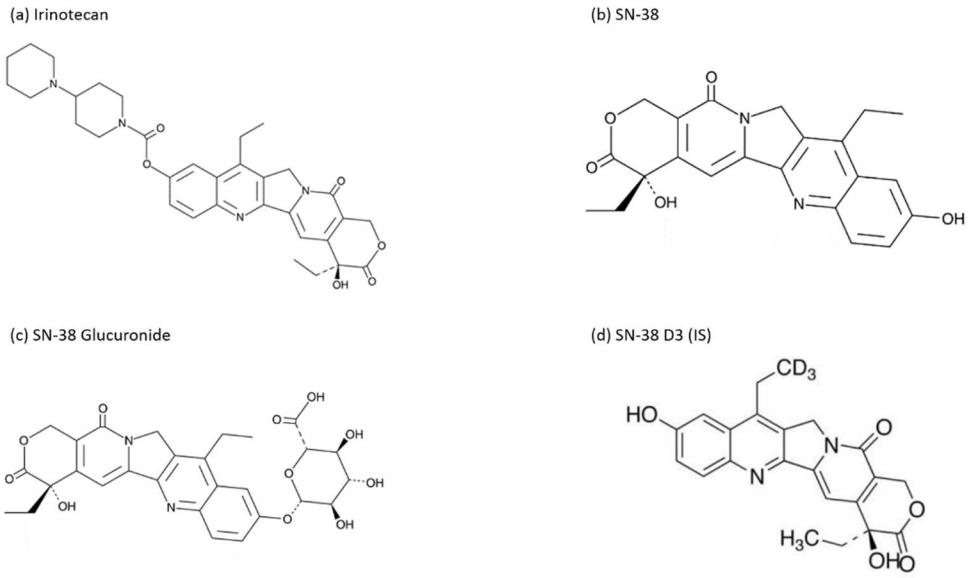

Figure 2.1 Chemical structures of irinotecan, SN-38, SN-38G and SN-38-d3 (internal standard)

The availability of a plethora of completely validated bioanalytical methods has paved the way for the characterisation of the pharmacokinetic profile of irinotecan in various preclinical species and human subjects. Previously researchers have utilised HPLC coupled parallel to both fluorescence and LC-MS detectors, due to the similarity of excitation and emission spectra between irinotecan and its

metabolites (de Bruijn et al., 1997; Kurita & Kaneda, 1999; Owens, Dodds, Fricke, Hanna, & Crews, 2003; X. Yang et al., 2005). For instance, Sai *et al* set the excitation at 368 nm and emission at 432 nm for and irinotecan, SN-38G, APC, NPC and for SN-38 the excitation and emission were set at 368 and 535 nm, respectively (Sai, Kaniwa, Ozawa, & Sawada, 2002). However, these fluorescence methods suffer from several drawbacks such as lengthy preparation times i.e. the need for specific pH, limited sensitivity, longer run times, limited dynamic ranges due to saturation and high sample volumes. Moreover, fluorescence detection cannot yet provide the required analytical sensitivity and specificity for SN-38G.

Recently, liquid chromatography coupled with tandem mass spectrometry (LC-MS/MS) has become a favoured analytical tool for the rapid and efficient quantification of drugs, metabolites, and biomarkers in different biological matrices due to the unique combination of high specificity, sensitivity, and the high throughput of samples. Several methods are currently employed for the determination of irinotecan and its metabolites, but only a few methods are available to quantify irinotecan, SN-38 (Bardin et al., 2005; M. Chen et al., 2017; Ghazaly, Perry, Kitromilidou, Powles, & Joel, 2014; Ramesh, Ahlawat, & Srinivas, 2010) and in particular, SN-38G (Atasilp et al., 2018; Basu, Zeng, Yin, Gao, & Hu, 2016; Marangon et al., 2015; Prijovich, Burnouf, & Roffler, 2014) with a high degree of sensitivity. Published methods for the direct determination of all three metabolites suffer from laborious sample preparation, complicated extraction procedures and long run times (Kurita & Kaneda, 1999; Owens et al., 2003; Poujol et al., 2003; Sparreboom et al., 1998). Therefore, we have developed and validated an LC-MS/MS method, in accordance with the bioanalytical guidelines defined by the Food and Drug Administration (FDA, 2016), for quantifying the levels of irinotecan and its metabolites SN-38 and SN-38G in a range of biological materials. The developed method was thereafter applied in a pharmacokinetic study using the plasma of BALB/c mice.

2.2 Methods and Materials

2.2.1 Materials

Irinotecan and SN-38 were purchased from Hangzhou J&H chemical company (J&H Chemical, Shanghai, China). SN-38G and the internal standard (IS) SN-38-d3 were purchased from Toronto Research Chemicals, (Toronto, Canada). Drug-free mouse plasma was purchased from BioIVT (West Sussex, UK). All other consumables were purchased from Sigma Aldrich (Dorset, UK) and were of LC-MS grade or the highest analytical grade commercially available.

2.2.2 Tuning for Irinotecan, SN-38, SN-38G and IS

Detection of all compounds was conducted using a TSQ Endura™ Triple Quadrupole Mass Spectrometer (Thermo Fisher Scientific, UK). Tuning was performed using direct infusion (20µl/minute) of a 500ng/mL stock of each compound with 50% mobile phase A (100% H_2O with 0.1% formic Acid, LC-MS/MS grade), 50% mobile phase B (100% acetonitrile (ACN) with 0.1% formic acid) at a flow rate of 300µl/minute. Ionisation was achieved via heated electron spray ionization in the Multiple Reaction Monitoring (MRM) positive mode, at a spray voltage of 3800V. The following parameters were optimised to achieve the highest signal intensity: spray voltage, sheath gas and auxiliary gas.

2.2.3 Chromatographic Separation

Chromatographic separation was achieved using a multistep gradient (Table 2.1) with a Synergi™ 4 µm Hydro-RP 80 (150*2mm) obtained from Phenomenex (Macclesfield, UK). The assay was conducted over 5.50 minutes at a flow rate of 400µl/minute. Data acquisition and chromatographic analysis were carried out using Xcalibur 2.2 from Thermo Fisher Scientific, UK.

Table 2.1 The operating chromatographic conditions

Time (minutes)	Mobile Phase A (%)	Mobile Phase B (%)
0.0	90	10
0.1	90	10
0.5	14	86
3.0	8	92
3.1	5	95
4.0	5	95
4.0	90	10
5.5	90	10

2.2.4 Preparation of Standards and Controls

Irinotecan and SN-38 stock solutions were prepared at a concentration of 1mg/ml in dimethyl sulfoxide (DMSO). A stock solution of SN-38G was prepared at a concentration of 0.5mg/mL and stored in glass vials at −40°C. Working standards of SN-38 and SN-38G were prepared in the appropriate matrix via serial dilution ranging from 2 to 512ng/ml; whilst final irinotecan concentrations ranged from 5 to 1024ng/ml. Quality control samples (QC) of 5, 100 and 500ng/ml were prepared for SN-38 and SN-38G and 10, 200, and 1000ng/mL for irinotecan from their respective working solutions. The IS working solution (500ng/mL) was prepared by diluting its stock solution with DMSO. All stock solutions were stored at −30°C.

2.2.5 Extraction Procedure

Extraction was performed using a protein precipitation method. A total volume of 100µl of either sample, standards or QCs was transferred to glass vials where 800µl of 100% ACN containing 0.75% FA and 500ng/ml of IS was added. Following mixing, samples were centrifuged at 4000 × g for 10 minutes at 4°C. The supernatant fraction was transferred to a fresh glass vial and evaporated to dryness using a rotary vacuum centrifuge, Jouan RC 10.22 (Thermo Fisher Scientific, UK). The pelleted residue was reconstituted with 100µL solution of H_2O: ACN (90:10) and vortexed. Subsequently, 80µl of the sample was then transferred into 200µl chromatography vials. Thereafter 5µl of each sample was injected into the LC-MS/MS system for analysis.

2.2.6 Assay Validation

The assay was validated according to the most recent FDA guidelines (FDA, 2016). The following criteria were assessed: linearity, recovery, selectivity, accuracy, precision and inter-assay as well as intra-assay variability.

2.2.7 Linearity

Linearity was assessed by three independent preparations of a calibration standard curve for each analyte. The calibration curve was obtained by plotting the ratio of peak area of the analyte to the peak area of IS. Maximum allowed deviation of standards was set at 15% of the stated value, excluding the lower limit of quantification (LLOQ) where deviation was set at no more than 20%.

2.2.8 Recovery

Recovery experiments were performed by comparing the results for extracted samples of each compound at three concentrations (same as high, medium, and low QCs) with non-extracted standards that were taken to represent 100% recovery.

2.2.9 Selectivity

The degree of interference from the matrix (due to potential interfering substances including endogenous matrix components, metabolites, and decomposition products) was assessed via comparison of extracted blank samples with the lowest point of the standard curve, the LLOQ. The LLOQ was a minimum of five-times greater than the background signal.

2.2.10 Accuracy & Precision

The intra-day and inter-day precision and accuracy of the method were determined with QC samples at three different concentrations (three injections for each concentration) on the same day and three different days. The calculated average concentration relative to the nominal concentration was used to express accuracy (% variability of accuracy = error/stated value*100). The relative standard

deviation was calculated from the QC values and used to estimate the precision (%variation of precision = standard deviation/average assay value*100). Acceptable variation for accuracy and precision was set at 15% and 20% for the lower concentrations.

2.2.11 Stability

Stability of irinotecan, SN-38 and SN-38G stock solutions were evaluated by repeated injection of standards (low, medium, and high) after 3 freeze-thaw cycles. Each analyte was considered stable at each concentration when the differences between the freshly prepared samples and the stability of testing samples did not deviate more than 15% from the nominal concentrations.

2.3 Application of the Method

2.3.1 Animals

All animal experiments were performed in accordance with criteria outlined in a Home Office UK approved project licence (PPL 70/8563/OWEN) granted under the Animals (Scientific Procedures) Act 1986 and approved by the Animal Ethics Committee at the University of Liverpool. Male BALB/c mice weighing between 20-25g were purchased from Charles River Laboratories (Margate, UK) and housed in a licenced specified pathogen-free establishment. Mice were given free access to food and water and housed at a temperature between 19°C and 23°C under a 12-hour light-dark cycle.

2.3.2 Pharmacokinetic Study

The developed LC-MS/MS method was used to study the plasma concentration-time profile in mice. Mice (n=3) were injected intravenously (tail vein) with irinotecan at a dose of 40mg/kg and blood was collected in heparinised tubes following cardiac puncture at 0.083, 0.25, 0.5, 2, 2.5, 3, 4 and 5 hours after dose administration. Samples were centrifuged at 10,000 rpm for 10 minutes to separate plasma and stored at −40°C until analysis.

2.3.3 Statistics

Statistical analysis was performed on SigmaPlot 14.0 and results are presented as the average ± SD.

2.4 Results

2.4.1 Method Development

Various preliminary experiments were carried out to develop the analytical method for the detection of irinotecan, SN-38 and SN-38G. LC-MS/MS conditions were optimised so that good symmetrical peaks and resolution were achieved. The optimised global settings were positive ion 3800V, sheath gas 50, aux gas 30 and sweep gas 0. Mass parameters were fine-tuned for maximum sensitivity, and parent ion transitions (MRM mode) were selected to afford the best response for the spectrum analysis as shown in Table 2.2.

Table 2.2 Optimised tuning setting for the detection of the compounds

Parameter	Optimised Setting
Positive Ion (V)	3800*
Sheath Gas	50
Aux Gas	30
Sweep Gas	0
Ion Transfer Tube Temperature (°C)	375
Vaporiser Temperature (°C)	375

*The spray voltage was time-dependent – divert valve was switched on between 2.2 to 3.2 minutes

To improve the specificity, the MRM scan type was used. The MRM transitions from precursor ions to product ions were optimised based on their most abundant precursor ions and corresponding product ions. These parameters for irinotecan, SN-38, SN-38G and the IS are summarised in Table 2.3 and Figure 2.2.

Table 2.3 The parent mass, product ion and collision energy for each of the compounds

Compound	Precursor (m/z)	Product (m/z)	Collision Energy (V)
Irinotecan	587.226	316.097	48.174
		502.151	30.781
		543.226	26.584
SN-38	393.087	349.111	24.056
SN-38G	569.104	393.111	24.056
		349.111	38.77
SN-38-d3	396.104	352.111	24.107

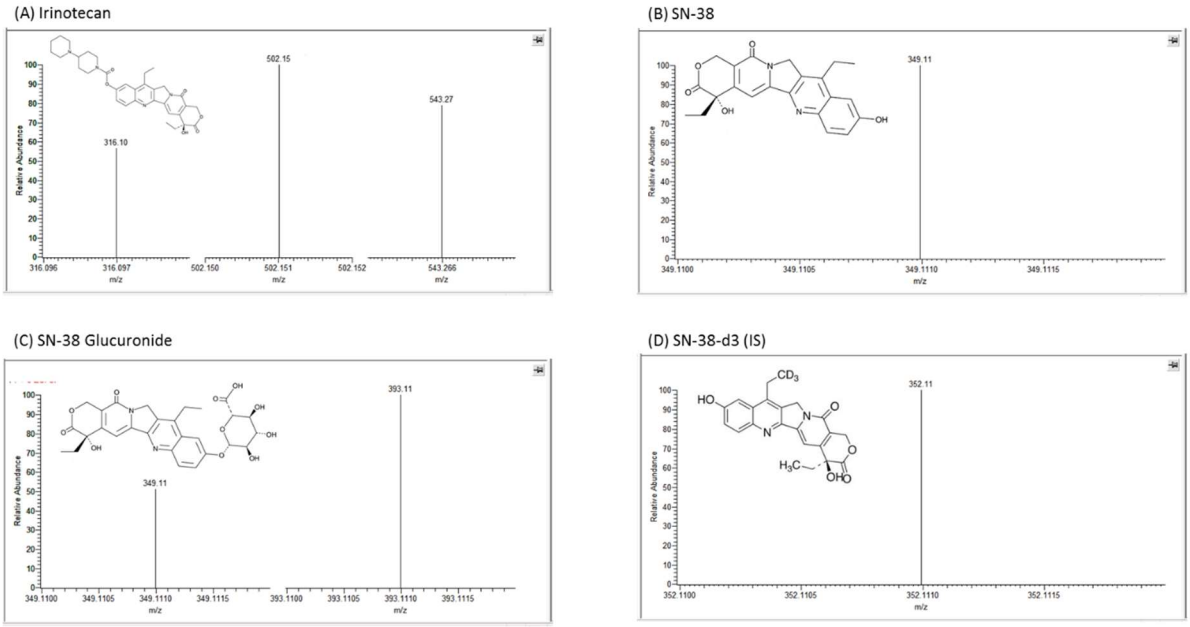

Figure 2.2 Representative MS/MS chromatograms of (A) Irinotecan (B) SN-38 (C) SN-38G and (D) SN-38-d3 at 500ng/ml.

2.4.2 Chromatographic Separation

The elution of the analytes was rapid and selective with adequate separation of all the peaks within a period of 5.5 minutes. Irinotecan, SN-38, SN-38G and the IS were eluted at approximately 2.78, 2.85, 2.66 and 2.85 minutes, respectively. No interfering peaks were observed at these retention times, plus the peaks were well separated and did not display any interference from other compounds.

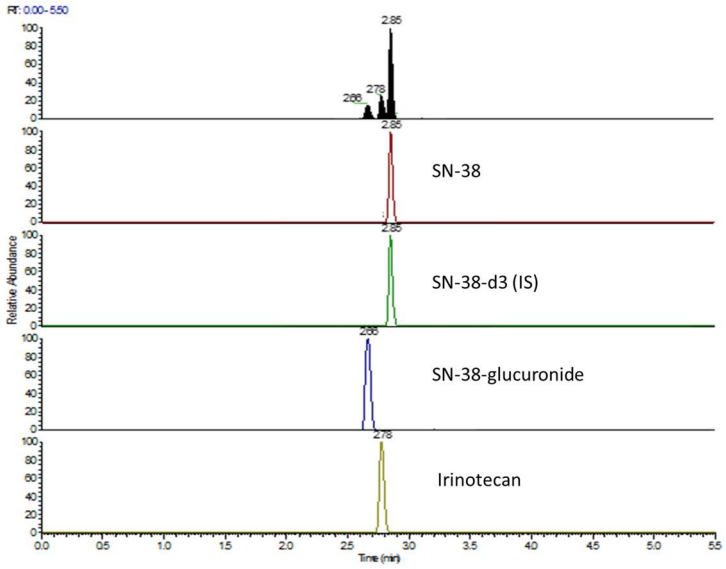

Figure 2.3 Representative LC-MS/MS chromatogram of Irinotecan (retention time: 2.78 mins), SN-38 (retention time: 2.85 mins), SN-38G (retention time: 2.66 mins) and the internal standard SN-38-d3 (retention time: 2.85 minutes).

2.4.3 Method Validation

2.4.3.1 Linearity

Method validation was conducted in blank mouse plasma, phosphate-buffered saline (PBS) and Dulbecco's modified Eagle medium (DMEM) growth media. The nine-point standard curves were linear in the concentration range for all matrices between 4-1024ng/mL for irinotecan, 2-512ng/mL for SN-38 and 2-512ng/mL for SN-38G. Mouse plasma calibration curves for each analyte are shown in Figure 2.4. The average correlations of the calibration curve were found to be acceptable (Pearson's coefficient of determination R^2>0.99). The peak area ratio (analyte to IS; variation of IS was <15% in each run) was proportional to the stated concentration ranges, as seen in Figure 2.4D.

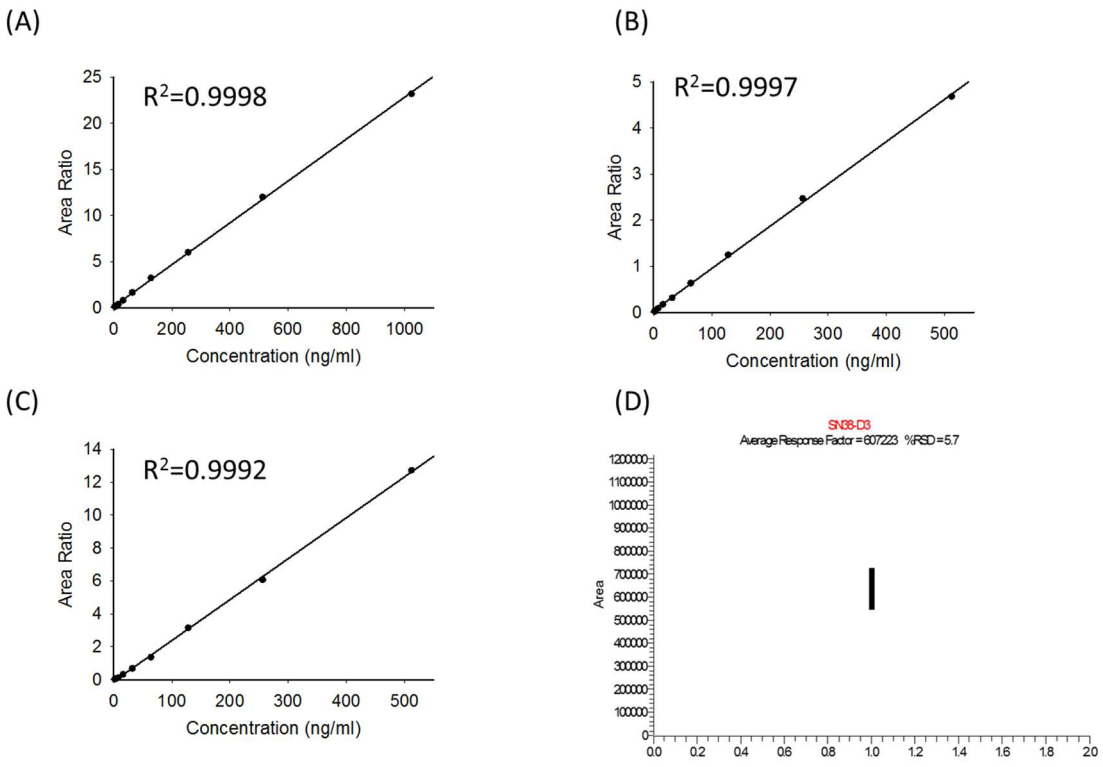

Figure 2.4 Standard curve generated from extracted mouse plasma standards for **(A)** Irinotecan, **(B)** SN-38 and **(C)** SN-38G. Variation in the IS response area used to create the calibration curves is displayed in **(D)**.

2.4.3.2 Extraction Recovery

The recovery was evaluated using three replicates of QC samples at three concentration levels (the same concentrations as QC sample) in mouse plasma, PBS and DMEM. The results showed (Figure 2.5) that the recoveries were not less than 70% for all the analytes. The average recovery was in the range 80.4–90.48% for irinotecan, 90.16–106.05% for SN-38 and within 72.79–85.41% for SN-38G.

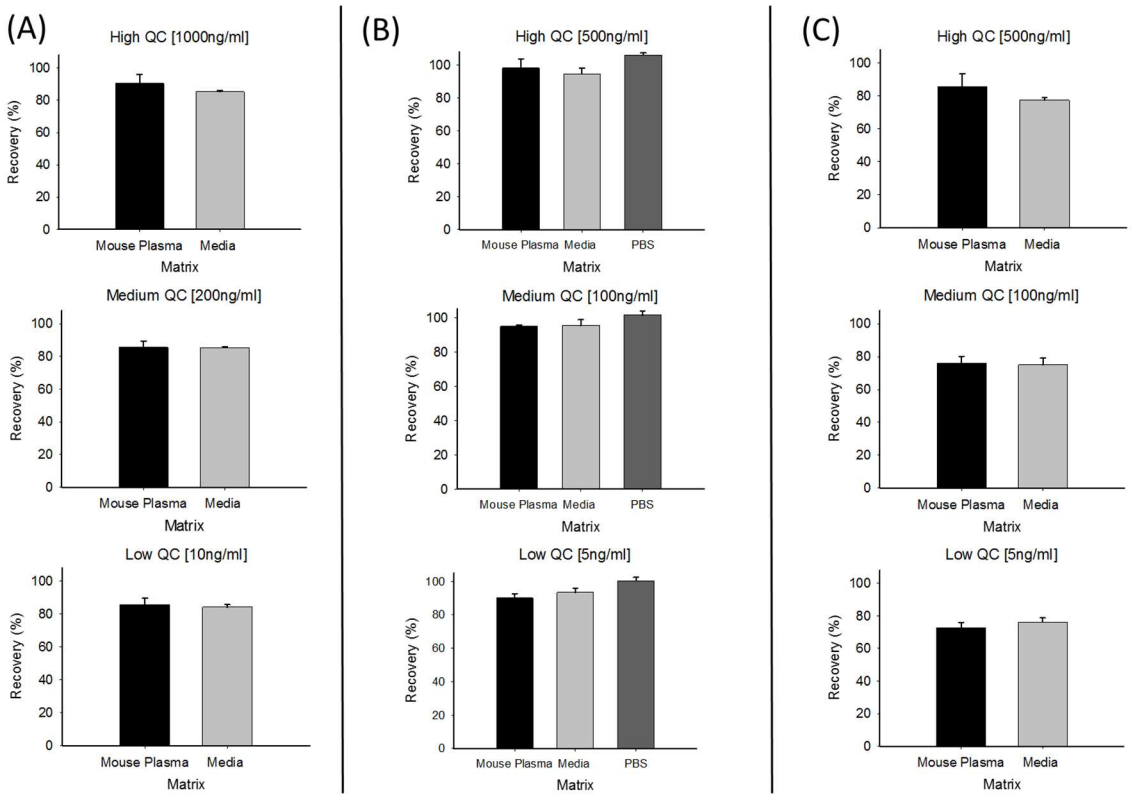

Figure 2.5 The percentage recovery for **(A)** Irinotecan, **(B)** SN-38 and **(C)** SN-38G at low, medium and high QCs in various matrices. Data is shown as an average percentage of unextracted standards ± SD (n=3).

2.4.3.3 Selectivity

FDA guidelines require the LLOQ produce a peak area of at least five-fold greater than that observed in the blank matrix. The acceptable LLOQ of irinotecan, SN-38 and SN-38G were determined to be 4, 2, and 2ng/mL respectively and was validated through the analysis of three replicates. Additionally, the signal produced by the IS showed no interference with any of the analytes.

2.4.3.4 Accuracy & Precision

The variability within and between assays was calculated to demonstrate that the method maintained accuracy and precision across repetitions. Table 2.4, Table 2.5 and Table 2.6 shows the variance of accuracy and precision calculated from average values of three repetitions of the assay (low QC, medium QC and high QC) either from the same experiment (intra-day) or an average of three separate experiments (inter-day). For FDA guidance, these results demonstrated that the precision and accuracy values were in the acceptance range (<15%). Across all matrices, the intra and inter-day

precision consisted of ≤6.49% and ≤11.47% for irinotecan, ≤10.16% and ≤9.24% for SN-38, and ≤8.27% and ≤6.68% for SN-38G. Across all matrices, the intra and inter-day accuracy consisted of ≤10.71% and ≤11.49% for irinotecan, ≤9.02% and ≤9.24% for SN-38, and ≤6.72 and ≤5.86% for SN-38G.

Table 2.4 Intra-day and Inter-day accuracy and precision for irinotecan, SN-38 and SN-38G in mouse plasma (n=3)

Compound		Average ±SD (ng/ml)	Intra-day		Average ± SD (ng/ml)	Inter-day	
			Variance of accuracy (%)	Variance of precision (%)		Variance of accuracy (%)	Variance of precision (%)
Irinotecan	High (1000ng/ml)	1034.29 ± 15.45	3.43	1.49	1004.09 ± 28.23	0.41	2.81
	Medium (200ng/ml)	221.42 ± 14.38	10.71	6.49	203.67 ± 15.54	1.83	11.47
	Low (10ng/ml)	10.68 ± 0.51	6.82	4.77	11.15 ± 0.81	11.49	7.29
SN-38	High (500ng/ml)	488.15 ± 9.96	-4.66	2.04	475.59 ± 24.69	-1.42	3.14
	Medium (100ng/ml)	101.26 ± 0.53	1.26	0.53	106.72 ± 4.49	1.05	8.26
	Low (5ng/ml)	5.14 ± 0.22	7.06	10.16	4.64 ± 0.38	-2.37	4.27
SN-38G	High (500ng/ml)	475.59 ± 24.69	-4.88	5.19	486.69 ± 15.72	-2.66	3.23
	Medium (100ng/ml)	106.72 ± 4.49	6.72	4.21	104.80 ± 2.72	4.80	2.59
	Low (5ng/ml)	4.64 ± 0.38	-7.18	8.27	4.72 ± 0.11	-5.64	2.31

Table 2.5 Intra-day and Inter-day accuracy and precision for irinotecan, SN-38 and SN-38G in DMEM (n=3)

Compound		Intra-day			Inter-day		
		Average ± SD (ng/ml)	Variance of accuracy (%)	Variance of precision (%)	Average ± SD (ng/ml)	Variance of accuracy (%)	Variance of precision (%)
Irinotecan	High (1000ng/ml)	1012.6 ±31.2	1.3	3.1	995.4 ± 17.1	-0.5	1.7
	Medium (200ng/ml)	196.2 ± 6.1	-1.9	3.1	199.3 ± 2.9	-0.3	1.5
	Low (10ng/ml)	10.4 ± 0.32	3.9	3.1	10.3 ± 0.1	6.4	3.1
SN-38	High (500ng/ml)	498.6 ± 4.9	-0.3	1.0	500.4 ± 0.3	0.1	0.6
	Medium (100ng/ml)	100.2 ± 0.8	0.2	0.8	98.1 ± 2.5	-1.9	2.5
	Low (5ng/ml)	5.0 ± 0.1	0.5	1.6	4.7 ± 2.8	-5.8	5.9
SN-38G	High (500ng/ml)	500.7 ± 4.4	0.1	0.9	500.5 ± 2.6	0.1	0.5
	Medium (100ng/ml)	98.8 ± 2.1	-1.2	2.1	103.4 ± 4.9	3.4	4.8
	Low (5ng/ml)	4.9 ± 0.2	-0.6	3.8	5.3 ± 0.4	5.9	6.7

Table 2.6 Intra-day and Inter-day accuracy and precision for SN-38 in PBS (n=3)

	Average ± SD (ng/ml)	**Intra-day**		**Average ± SD (ng/ml)**	**Inter day**	
		Variance of accuracy (%)	Variance of precision (%)		Variance of accuracy (%)	Variance of precision (%)
High (500ng/ml)	500.0 ± 2.6	0.1	0.5	502.6 ± 2.5	0.5	0.5
Medium (100ng/ml)	100.2 ± 0.7	0.4	0.7	100.8 ± 0.4	0.8	0.4
Low (5ng/ml)	5.1 ± 0.16	9.0	7.3	5.2 ± 0.1	9.2	2.1

2.4.3.5 Stability

Analyte stock solutions were found to be stable following 3 freeze-thaw cycles at −40°C. As seen in Table 2.7, a concentration difference of less than 15% was observed across all analytes. The analytical method was therefore proved to be applicable for routine analysis over this period.

Table 2.7 Stability of the working solutions of Irinotecan, SN-38 and SN-38G stored at -40°C over 6 weeks

		After 3 freeze-thaw cycles		
Analyte	**Nominal Concentration (ng/mL)**	**Average ± SD**	**Variance of Precision (%)**	**Variance of Accuracy (%)**
Irinotecan	High (1000ng/ml)	981.8 ± 20.1	0.2	-1.8
	Medium (200ng/ml)	198.3 ± 7.7	3.9	-0.8
	Low (10ng/ml)	10.8 ± 1.4	13.1	7.5
SN-38	High (500ng/ml)	500.1 ± 16.6	3.6	0.1
	Medium (100ng/ml)	101.0 ± 3.9	3.8	0.9
	Low (5ng/ml)	4.9 ± 0.3	5.8	-0.4
SN-38G	High (500ng/ml)	501.8 ± 18.1	3.6	0.4
	Medium (100ng/ml)	96.1 ± 8.7	9.1	3.9
	Low (5ng/ml)	4.5 ± 0.6	14.1	-9.6

2.4.4 Method Application

The validated method was applied to determine irinotecan, SN-38 and SN-38G content in mouse plasma after intravenous administration of 40mg/kg irinotecan in male BALB/C mice. Average plasma concentrations of irinotecan, SN-38 and SN-38G as a function of time after administration are shown in Figure 2.6. As seen from Figure 2.6A, a sharp decline in the plasma concentration of irinotecan was observed with time and irinotecan was found to be mostly eliminated from plasma within 5 hours of dose administration. The concentration of SN-38 was found to increase initially in the first 30 minutes

followed by its gradual elimination from plasma over time (Figure 2.6B). The extent of SN-38 glucuronidation in mice was assessed by the direct measurement of SN-38G and its levels seemed to be maintained (Figure 2.6C).

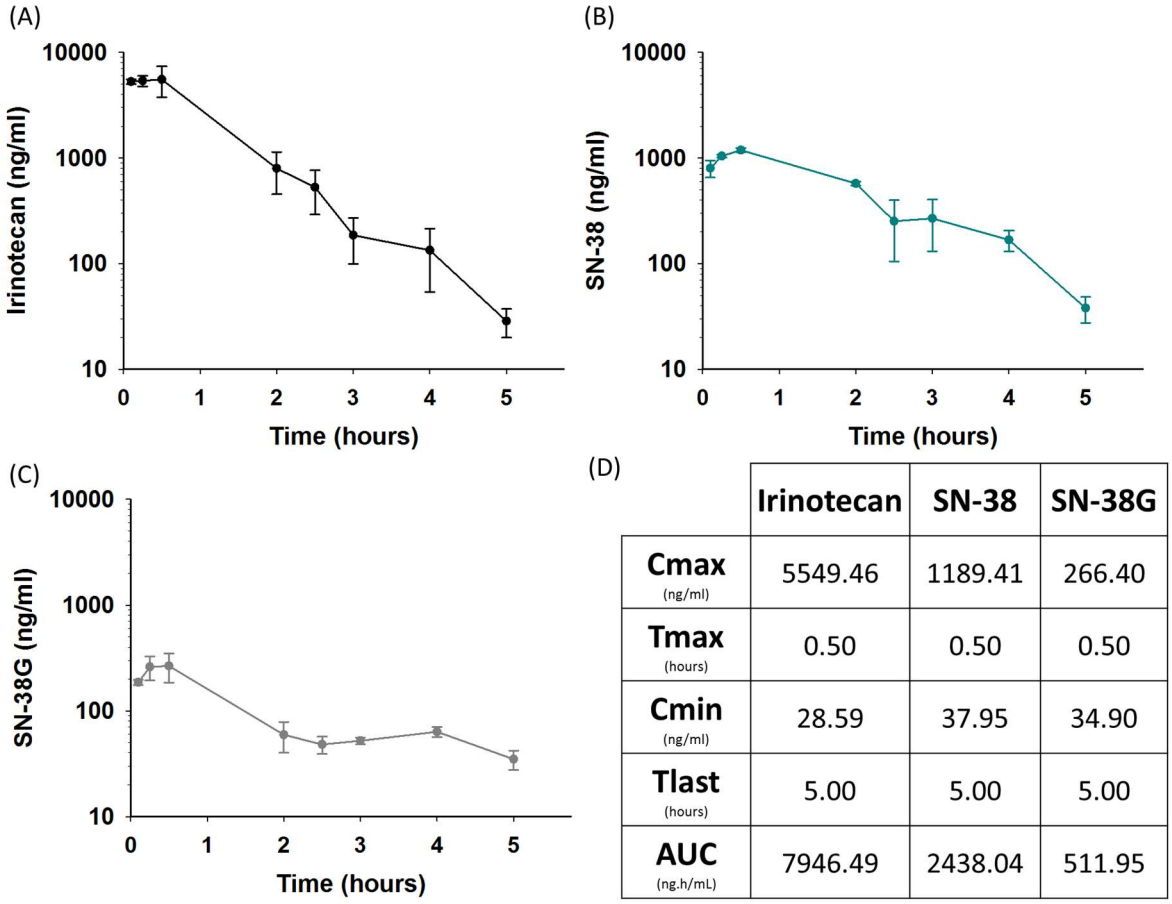

(D)

	Irinotecan	SN-38	SN-38G
Cmax (ng/ml)	5549.46	1189.41	266.40
Tmax (hours)	0.50	0.50	0.50
Cmin (ng/ml)	28.59	37.95	34.90
Tlast (hours)	5.00	5.00	5.00
AUC (ng.h/mL)	7946.49	2438.04	511.95

Figure 2.6 The plasma concentration-time curves of **(A)** irinotecan, **(B)** SN-38, and **(C)** SN-38G following administration of irinotecan to BALB/c mice. Pharmacokinetic parameters for each compound were derived and are shown in panel **(D)**. Data are shown as average ±SD (n=3).

2.5 Discussion

The described bioanalytical method, based on simple protein precipitation and LC-MS/MS determination, quantifies irinotecan and its main metabolites. The method, which has been successfully validated according to the FDA guidance on bioanalytical method validation is highly sensitive, precise and accurate. The required sample volume was 100µL and the sample preparation was straightforward and efficient, an advantage over some methods (D'Esposito, Tattam, Ramzan, & Murray, 2008; Khan, Ahmad, & Ahmad, 2003; L. P. Rivory et al., 1996). The sensitivity of the method (LLOQ - irinotecan 5ng/ml, SN-38 2ng/ml and SN-38G 2ng/ml) was better than what has already been reported in the literature (Atasilp et al., 2018; X. Chen et al., 2012; D'Esposito et al., 2008; Taneja, Gota, Gurjar, & Singh, 2019). Greater LLOQ values had been reported for irinotecan and its metabolites by Marangon *et al.,* however, this might be explained by differences (mouse vs. human) in the nature of the samples analysed (Marangon et al., 2015). Other advantages include a short analysis time (5.5 minutes) permitting high sample throughput and good selectivity i.e. negligible matrix effect. The analysis time was much quicker in comparison to those published in the literature 18 minutes (Atasilp et al., 2018; Marangon et al., 2015) or 12 minutes (Martinez-Chavez et al., 2020). Many of the published methods (see cited review) are only able to quantify irinotecan and SN-38 and some use an estimate to determine the levels of SN-38G (Ramesh et al., 2010). Here we additionally directly quantified the levels of SN-38G, which will give a clear understanding of the clearance and inactivation of SN-38. This has clear implications in trying to understand mechanisms for both toxicity and efficacy involved in irinotecan pharmacokinetics.

The LC-MS/MS method was fully validated and applicable to a number of matrices including DMEM growth media and PBS, demonstrating its versatility. Only one other publication has detailed the quantification of irinotecan and SN-38 in DMEM (Hu et al., 2007) and they were also unable to quantify SN-38G within their method. Our method was successfully applied to determine irinotecan and its metabolites in mouse plasma. The plasma-concentration time curves, together with the derived pharmacokinetic parameters as shown in Figure 2.6D, indicated a short half-life, rapid elimination and

low bioavailability of irinotecan within BALB/c mice, corroborating with similar *in vivo* studies (Basu et al., 2016; Prijovich et al., 2014; Taneja et al., 2019). The initial rise in the concentration of SN-38 could be explained by the biological conversion of irinotecan into its active metabolite SN-38. This method can be used in future PK/PD studies for irinotecan or its novel formulations. A more in-depth pharmacokinetic analysis of this data is presented in chapter 4 as part of a larger study. Further improvements to the method that could be made would be to include additional irinotecan metabolites such as APC and NPC and to take into consideration both the lactone (active) and carboxylate (inactive) forms of irinotecan and SN-38. This would provide a more in-depth understanding of the inter-conversion and plasma pharmacokinetics of both irinotecan and SN-38.

2.6 Conclusion

In this chapter, we developed and validated an LC-MS/MS method with acceptable accuracy, precision, and extraction recovery with good linearity according to the US FDA guidance on bioanalytical method validation. The method was successfully applied to a pharmacokinetic study of irinotecan and its metabolites. This method was subsequently used in experiments outlined in chapter 4.

Chapter 3: Monolayer (2D) and Spheroid (3D) Colorectal Cancer Models as a Tool for Assessing and Understanding Chemotherapeutic Effectiveness during Pre-Clinical Development

Abstract

Colorectal cancer, the second most common cause of cancer deaths worldwide, is associated with a poor prognosis due to the lack of effective therapies. Most promising pre-clinical drug candidates ultimately fail, largely caused by the poor predictive value of pre-clinical models. Over the past decade, the evaluation of anticancer drugs using two-dimensional cell cultures has delivered significantly useful pharmacological analyses. However, these cultures lack many of the characteristics and complexity seen *in vivo*. This has led to the development of three-dimensional culture systems, which have been shown to better mimic tumours and their microenvironment. Consequently, they are better placed for the assessment of pharmaceutical candidates. Accordingly, HCT116 and CT26 cells were cultured as spheroids and characterised in terms of their growth kinetics, morphology and histology.

The response of monolayer and spheroid colorectal cancer cell lines to the topoisomerase I inhibitor irinotecan and its active metabolite SN-38 treatment were compared. Cell viability, immunohistochemistry, immunofluorescence (IF) and subsequent protein expression with Western blotting was assessed. Uniform, compact spheroids formed after five days in culture. Results showed that cells cultured as spheroids differed significantly from monolayer, in terms of drug response to both irinotecan and SN-38. Cell lines in monolayer typically exhibited increased sensitivity (lower IC_{50} values at 72hrs) to drugs, as compared to spheroids. Spheroids also showed morphological changes such as increased cell size, nuclear changes and a decrease in spheroid diameter. Repeated exposures in spheroids, did lead to a reduction in cell viability i.e. spheroids became more sensitive (21-fold reduction for HCT116, and a 9- and 3-fold reduction for CT26 in IC_{50} for irinotecan and SN-38). Notable differences between cultures were also observed in protein expression and drug uptake, both of which were consistently decreased in spheroids. Taken together, the data indicated that the cellular environment in which cells are cultured can considerably influence a drug's efficacy and mechanism

of action. Spheroids are likely to be a better representation of *in vivo* solid tumours and can provide a physiologically relevant model for evaluating the effects of anticancer agents pre-clinically, however, the usefulness of monolayer cultures should not be completely overlooked.

3.1 Introduction

Despite significant improvements in CRC therapy, there is still a need for innovative drug screening methodologies. Patients with advanced CRC are often limited to traditional chemotherapies, as their primary therapeutic option. Additionally, patients relapsing after initial chemotherapy is a challenge in approximately 30-50% of cases (Broadbridge et al., 2013; Ryuk et al., 2014). Therefore, enabling more effective therapies to treat CRC, remains an urgent unmet medical need.

Three approaches are currently employed in the discovery and development of novel cancer drugs: high throughput drug screening (HTS), rational drug design and the development of analogues of existing drugs (Colotta, 2008; Schwartsmann et al., 2002). These approaches rely on *in vitro* assays based on clonogenicity, proliferation and cytotoxicity. However, a major problem is that promising pre-clinical activity (≤5%) often does not translate clinically into patient benefit (Chabner & Roberts, 2005). Lack of clinical efficacy and/or unacceptable toxicity profiles are the two main causes of drug failure during development. Several factors have contributed to this, specifically pre-clinical models failing to adequately recapitulate the complexity and heterogeneity of human cancers. To overcome this, many techniques have been developed that attempt to bridge the gap between pre-clinical and clinical studies.

Table 3.1 Summary of the differences in two-dimensional vs. three-dimensional cell culture models

Characteristic	**Type of culture**		**Ref.**
	2D	**3D**	
***In vivo*-likeness**	Do not mimic the natural structure of the tissue or tumour mass	Resemble organisation seen *in vivo*	(Kapalczynska et al., 2018)
Proliferation	Proliferate rapidly	Cells tend to proliferate slower	(X. Xu et al., 2012)
Polarity	Partial/forced polarisation	Polarisation is conserved	(Duval et al., 2017; Freytes, Wan, & Vunjak-Novakovic, 2009)
Cell morphology	Sheet-like, flat and elongated cells	Form aggregate/spheroid structures and contain multiple layers	(Antoni, Burckel, Josset, & Noel, 2015; J. B. Kim, 2005; Zanoni et al., 2016)
Gene/protein expression	Display differential gene/protein levels compared with *in vivo* models	Expression of genes and proteins similar to those seen *in vivo*.	(Chang & Hughes-Fulford, 2009; K. J. Price et al., 2012; Szot, Buchanan, Freeman, & Rylander, 2011)
Drug responses	Offer little resistance to drugs and tend to be more sensitive	Display more resistance to drug treatments and provide a more accurate representation	(Bruningk, Rivens, Box, Oelfke, & Ter Haar, 2020; Gurski, Petrelli, Jia, & Farach-Carson, 2010; Hongisto et al., 2013)
Culture formation	Within a few hours	Ranges from a few hours to a few days	(Chaicharoenaudomrung, Kunhorm, & Noisa, 2019)

Traditional monolayer cell culture (two dimensional - 2D) techniques have delivered significantly useful pharmacological analyses in various disease settings, such as Parkinson's, HIV, diabetes and cancer (Breslin & O'Driscoll, 2013). Other advantages involving low cost, ease of application, high throughput, and control over microenvironmental features, has meant that 2D cultures are a standard method for assessing cellular responses. Despite this, cells cultured in 2D show clear limitations. For instance, cells do not grow in a physiological environment that allows them to completely mimic the different properties and behaviours observed *in vivo.* Cells are also forced to polarise and increase their exchange area to culture media due to the attachment to rigid and flat substrates (Freytes et al., 2009). This leads to over-nutrition, increased oxygenation and non-reproducibility of *in vivo* molecular gradients. Additionally, the composition, configuration and production of the extracellular matrix (ECM) is considerably altered (Edmondson, Broglie, Adcock, & Yang, 2014). As a result, anticancer agents administered to 2D cell cultures reach cells without any physical barrier, whereas the same molecules delivered *in vivo* encounter a differently associated stroma and a range of cell-cell and cell-matrix interactions, which influence the concentration present throughout the tumour microenvironment (Edmondson et al., 2014; Sensi, D'Angelo, D'Aronco, Molinaro, & Agostini, 2018). It is, therefore, necessary to improve *in vitro* testing methods to provide a more informed prediction of drug candidate efficacy and safety. As such, there is increasing interest in applying three dimensional (3D) *in vitro* models to enhance the selection of lead candidates for *in vivo* evaluation.

3D culture models such as spheroids could serve as an intermediary between 2D cultures and the highly complex nature of *in vivo* tumours. Spheroids are tightly bound, sphere-shaped cellular aggregates that have been extensively studied since their development in the 1970s (Mueller-Klieser, 1987; Sutherland, McCredie, & Inch, 1971). Depending on the cell type and growth conditions they can range in size from 20µm up to 1mm in diameter. The increased cell-cell and cell-matrix contacts in spheroids not only alters gene expression patterns and resistance to anticancer agents but also limits the diffusion of drugs, nutrients, oxygen and waste products into and out of spheroids (as

depicted in Figure 3.1). Spheroids have a stratified cellular composition, with an outer layer of proliferating cells, a viable layer of quiescent cells in the middle and if large enough (usually larger than 500µm) necrotic cells are present in the core of the spheroid (Kunz-Schughart, Freyer, Hofstaedter, & Ebner, 2004; R. Z. Lin & Chang, 2008; Mehta, Hsiao, Ingram, Luker, & Takayama, 2012). Such cellular heterogeneity is also apparent in non-vascularised tumour regions (Mueller-Klieser, 2000).

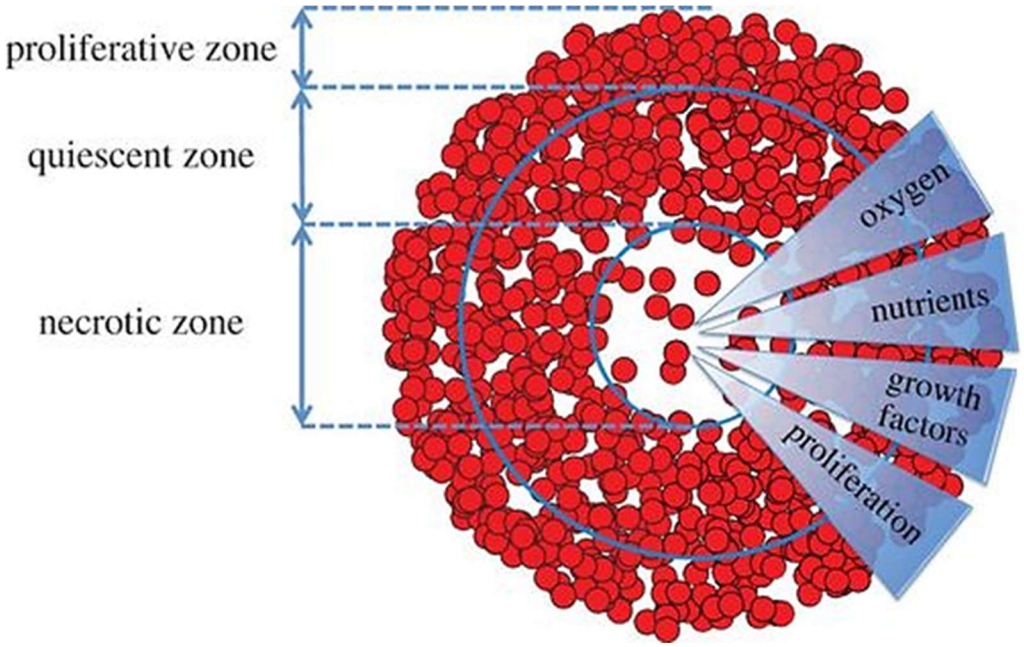

Figure 3.1 Schematic diagram of a spheroid. Spheroids are 3-D microscale tissues that exhibit an inherent gradient of nutrients, oxygen and metabolites within themselves. In the proliferative zone, cells receive enough oxygen and nutrients to proliferate. The quiescent zone is a region of viable and non-proliferative cells. In the necrotic zone, cell death occurs due to an accumulation of toxic waste products and a lack of oxygen and nutrient supply. Due to similarities between *in vivo* tissues and spheroids as well as mass transport limitations, spheroids can serve as high throughput screening platforms for drug and carrier effectiveness. Adapted from (Dini et al., 2016).

Spheroids are considered an appropriate *in vitro* model for drug screening in the field of oncology due to their ability to better recapitulate the complex architectural, biological and physiological nature of the tumour microenvironment *in vitro*. Spheroids are subjected to different adhesive, topographical and mechanical factors, then cells grown in 2D (Baker & Chen, 2012; Ekert et al., 2014; Friedrich, Seidel, Ebner, & Kunz-Schughart, 2009; C. Wang et al., 2014). Spheroids maintain many properties of their tumour counterparts which are lost in 2D i.e. a higher degree of the structural, morphological

and functional differentiation and *in vivo* like growth kinetics and resistance patterns to chemotherapeutics. Additionally, certain components (cell-cell and cell-ECM interactions) are expressed to a higher degree in spheroids, hence they can establish physiological drug delivery barriers, which are also seen *in vivo*. Spheroids, therefore, have the potential to serve as an improved assay format, relevant to the development of nanomedicines. Previous reports have compared anticancer activity in 2D and 3D cell culture models and differential drug sensitivity between cultures were observed (Ekert et al., 2014; Harma et al., 2010; Hongisto et al., 2013; Riedl et al., 2017; Zoetemelk, Rausch, Colin, Dormond, & Nowak-Sliwinska, 2019).

Nanomedicines have been largely investigated in 2D cultures, as this model is relatively simple and cheap. Tumour spheroids are one of the most popular models of 3D cell cultures used as a more advanced system for testing the anticancer effect of nanomedicines *in vitro* (Friedrich et al., 2009). Tumour spheroids are often used to assess NP penetration and toxicity, as this process mimics one of the most important barriers to NP entry into the tumour *in vivo*. Many factors, such as NP size, shape, charge and targeting ability can influence a NPs cellular internalisation and its diffusion inside the spheroid (Agarwal et al., 2015). Researchers have developed many different methods for evaluating the transport of nanomedicines in 3D cultures. Penetration of fluorescent-labelled nanomedicines or those containing fluorescent materials inside may be easily studied both in live or fixed spheroids by fluorescent or confocal microscopy (Agarwal et al., 2015; Hornung et al., 2015; Leite et al., 2019). In this case, images are usually analysed and the depth of NP penetration together with the amount of NPs are estimated. Additionally, Hoechst 33342 has been used to discriminate between cells in the core and periphery of spheroids (J. M. Lee et al., 2018; Ozcelikkale et al., 2017; E. Yang et al., 2015). Tchoryk *et al*. used staining with Hoechst 33342 to evaluate doxorubicin and its liposomal formulation transport into different layers of HCT116 spheroids (Tchoryk et al., 2019). In the case of doxorubicin or other fluorescent substances or NPs, it is possible to analyse its extent of penetration and also evaluate its accumulation by mean fluorescence intensity in cells (Hornung et al., 2015; Ma et al.,

2012). Another method of measuring NP penetration in spheroids involves directly measuring the drug released from NPs by utilising chromatographic techniques. Lu *et al.* evaluated the accumulation of albumin-polycaprolactone NPs encapsulating albendazole in pancreatic spheroids (H. Lu, Noorani, Jiang, Du, & Stenzel, 2017). Following treatment, they lysed the spheroids, then extracted albendazole with acetonitrile and evaluated its concentration by high-pressure liquid chromatography. Therefore, spheroids have the capacity of offering more appropriate pre-clinical models for evaluating therapeutic candidates, as well as being more efficient in predicting *in vivo* anticancer activity, compared with their monolayer counterparts. We hypothesised that characteristics of spheroids would enable them to mimic the *in vivo*/clinical environment better than monolayer cultures, with such properties influencing the therapeutic effect of drugs.

In this chapter, the generation, growth, and characterisation of CRC tumour spheroids are outlined. As it is well known that cells at different tumour stages are exhibiting different sensitivity to drugs, a panel of classical CRC cell lines were additionally examined: HCT116, CT26, DLD-1 and LoVo. This part of the thesis also systematically evaluated the response of irinotecan and its active metabolite SN-38 in both 2D and 3D cultures using various molecular biological techniques. Mechanisms relating to how cultures systems can influence and differentially modulate response to such treatments was thereafter assessed, with conclusions being drawn as to which system better captures the *in vivo* microenvironment.

3.2 Materials and Methods

3.2.1 Materials

All materials used in cell culture were obtained from Sigma-Aldrich (Dorset, UK) and all other reagents were purchased from Thermo Fisher Scientific (Loughborough, UK) unless otherwise stated. Patient tissue samples (patient-matched healthy colonic mucosa, primary CRC and CRC liver metastasis) were obtained through Liverpool Bio-Innovation Hub Biobank, with ethical approval granted by the Biobank governance board (LBIH project number: 19-07).

3.2.2 Cell Lines and Maintenance

The human CRC cell lines DLD-1 (ATCC®, CCL-221), HCT116 (ECACC®, 91091005) and LoVo (ATCC®, CCL-229) and mouse colon cancer cell line CT26 (ATCC®, CRL-2638) were obtained from American Type Culture Collection or the European Collection of Cell Cultures. All cells were routinely screened for mycoplasma contamination by polymerase chain reaction (PCR). Table 3.2 shows brief information on the histology and origin of the cell lines used.

Table 3.2 Details of Cell Lines

Cell Line	Histology	Origin
CT26	Murine colon carcinoma	Induced by the administration of the carcinogen N-nitroso-N-methylurethane to BALB/c mice
DLD-1	Colorectal adenocarcinoma	Adult, Male
HCT116	Dukes' type D, Primary colon carcinoma	48-year-old Male
LoVo	Dukes' type C, grade IV, colorectal adenocarcinoma	56-year-old Male

The complete growth medium used for the CT26 cells was Roswell Park Memorial Institute (RPMI) culture medium and that for the Human CRC cells was Dulbecco's Modified Eagle's Medium-high glucose (DMEM). Both mediums were supplemented with 10% heat-inactivated Foetal Bovine Serum (FBS), 100U/mL penicillin and 100µg/mL streptomycin. The cells were cultured in 75cm^2 Nunclon cell culture flasks (VWR, Lutterworth) and incubated in a humidified atmosphere at 37°C, 5% CO_2. They were grown to 70–80% confluence before being passaged (twice a week) using 0.25% Trypsin-EDTA (5 min, 37°C) (Invitrogen, Paisley). Cell density was determined using a haemocytometer. For this, cell

suspensions were mixed with an equal volume of 0.4% trypan blue solution. Viable cells at the central grid (5x5 squares) were counted using the x20 objective lens of a phase-contrast microscope (ECLIPSE TS100/100-F, Nikon). The volume required for the specific cell count was calculated and diluted in media for seeding as follows:

$$\text{Cells/ml} = \text{Number of counted cells} \times 2 \text{ (dilution factor)} \times 1 \times 10^4 \text{ (haemocytometer factor)}$$

3.2.3 Monolayer (2D) Culture

For the monolayer culture method (2D), 100µL/well of each cancer cell line was dispensed into flat bottomed 96 well plates. The optimised seeding densities were as follows: CT26 - $2x10^3$, DLD-1 - $3x10^3$, HCT116 - $5x10^3$, LoVo - $5x10^3$ cells/well. The cells were left to adhere overnight (24hrs), before conducting any further experiments.

3.2.4 Spheroid (3D) Culture

Single-cell suspensions of CT26 ($1x10^3$ cells/well) and HCT116 ($1.25x10^3$ cells/well) cells at optimised densities were grown (100µl total volume) in the ultra-low attachment (ULA) 96-well round-bottom plates (Corning, Flintshire). The plates are provided pre-coated with a hydrophilic polymer, that prevents attachment and triggers the formation of a single spheroid per well. The cells were spun at 700 x g for 7 minutes using a plate centrifuge to encourage the formation of a single spheroid and minimise cell death. The ULA plates were incubated at 37°C, 5% CO_2 for 5 days to allow for the development of stable spheroids, before conducting any further analysis. During the growth period, the medium was exchanged on day three day by removing 50µl of old media and replacing it with the same volume of fresh growth medium. Care was taken not to disturb the spheroids.

3.2.5 Analysis of Spheroid Growth

Images of spheroids at different seeding densities were taken up to 16 days after initiation for growth determination. A 50% medium replenishment was performed every 48-72 hours using a multichannel pipette, to maintain nutrient levels. To examine spheroid growth over time, images (10 spheroids/day

using an x4 objective) were captured using a digital camera head (DS-Vi1, Nikon) and a stand-alone controller and display unit (DS-L3, Nikon). Images were analysed using the ImageJ software (National Institutes of Health, USA) applying an image of known scale as calibration. A published macro (Ivanov et al., 2014) was utilised to measure the circularity, radius, diameter, and volume of the spheroids in an automated manner.

3.2.6 Histological Analysis

3.2.6.1 Spheroid Processing and Embedding

At predefined time points (days 5, 8 and 11), spheroids (minimum of 24) were transferred from ULA plates into round bottom collection tubes using a 200µl pipette tip with the end cut off. All excess media was aspirated, and spheroids were fixed with 4% paraformaldehyde (PFA) solution (Merck, Germany) for 1 hour at 4°C (using enough PFA to cover the spheroids). The 4% PFA was rinsed off with three changes of phosphate-buffered saline (PBS) taking care not to disturb the spheroids (to ensure all the spheroids pool to the bottom of the collection tube, they were centrifuged briefly). Following the last wash, as much PBS was removed as possible.

Thereafter molten histogel was covered over the spheroids using a Pasteur pipette (4-6 drops). The collection tubes were placed in a fridge (4°C, 5minutes) to allow for solidification. The solidified histogel was gently removed from the collection tubes, transferred into labelled processing cassettes and left overnight in a container of 70% ethanol. The cassettes were then placed on the histocore PEARL tissue processor (Leica Biosystems, Newcastle upon Tyne) and processed using the “biopsy” protocol (samples were dehydrated in a series of ethanol solutions with increasing concentrations, cleared in xylene and infiltrated with molten paraffin). Processed cassettes were then transferred to a Thermo Shandon paraffin-embedding station. With a pair of heated forceps, the sample was orientated outwards (spheroids facing towards the surface) and embedded in paraffin wax.

3.2.6.2 Spheroid Sectioning and Staining

Paraffin-embedded spheroids were sectioned into 5µm sections using a Leica RM2235 microtome (Leica Biosystems, Newcastle upon Tyne) and mounted onto superfrost plus glass slides. Sections were then deparaffinised in xylene and rehydrated with descending ethanol concentrations. Routine staining was then performed with Haematoxylin and Eosin (H&E) (Feldman & Wolfe, 2014) and Alcian blue pH 2.5 (Lai & Lü, 2012) according to standard protocols.

For immunohistochemistry (IHC), sections were deparaffinised, rehydrated through a series of graded alcohol dilutions and endogenous peroxidase neutralised with a 0.3% hydrogen peroxide blocking solution (Abcam, Cambridge) for 10 minutes. Heat-induced antigen retrieval (90°C, 2 minutes) was carried out in Coplin jars, using universal HIER antigen retrieval reagent (Abcam, Cambridge). After blocking with 10% goat serum for 15 minutes at room temperature (RT), sections were incubated overnight (1:200, 4°C) with primary antibodies, Ki-67 (Novus Biologicals, NB110-89717, Oxfordshire) and cleaved caspase-3 (Cell Signalling Technologies, 9661S, London). This was followed up by incubation with a goat HRP conjugated secondary antibody for 1 hour at RT. Thereafter each section was reacted with a 3,3'-diaminobenzidine (DAB) solution (Abcam, Cambridge) per the manufacturer's instructions and counterstained with haematoxylin. The slides were coverslipped with DPX mountant and air-dried overnight before being assessed (Ki-67 and cleaved-caspase 3 staining was conducted by the Veterinary pathology department, Leahurst Campus, University of Liverpool).

3.2.6.3 Monolayer Staining

Cells were cultured on poly-L-lysine coated coverslips and fixed with 4% PFA for 20 minutes at 4°C. H&E staining was then performed according to standard protocols.

3.2.6.4 Imaging

All stained slides were digitally scanned at ×200 magnification using an Aperio ScanScope CS2 digital slide scanner (Leica Biosystems, Newcastle upon Tyne). Images were subsequently taken with Aperio

ImageScope viewing software (Leica Biosystems Imaging). Further analysis of positive staining was conducted on the software using the Aperio positive pixel count v9 algorithm.

3.2.7 Drug Treatment

3.2.7.1 Drugs

Irinotecan and SN-38 were purchased from Hangzhou J&H chemical company (J&H Chemical, Shanghai, China). Stocks solutions for both drugs were prepared in hybri-max sterile filtered dimethyl sulfoxide (DMSO) and stored at -80°C. Subsequent dilutions were prepared in pre-warmed culture medium, immediately before use.

3.2.7.2 Monolayer Experiments

Cells were cultured in monolayer as described in section 3.2.3 After 24 hours, all media was aspirated and replaced with 100µL of each concentration of media containing drug (wells were 0.1% DMSO by volume). Drug concentrations for each cell line were previously determined in preliminary range-finding experiments. For irinotecan, the concentrations ranged from 0.01 to 100µM. Each plate contained vehicle control wells of 0.1% DMSO in growth media and untreated control cells. The plates were incubated with drugs for 72 hours at 37°C, 5% CO_2 before further assessment. Cells were treated with SN-38 in the same manner, however, the concentrations ranged from 0.5 to 200nM.

3.2.7.3 Spheroid Experiments

HCT116 and CT26 spheroids were grown as previously described in section 3.2.4. On Day 5, 50µl of growth media was removed without disturbing the spheroids. It was replaced with 50µL of each concentration of media containing drug (wells were 0.1% DMSO by volume). For irinotecan, the concentrations ranged from 0.01 to 100µM and for SN-38 the concentrations ranged from 0.5 to 200nM. Each plate contained vehicle control wells of 0.1% DMSO in growth media and untreated control spheroids. The plates were incubated with drugs for an initial 72 hours at 37°C, 5% CO_2 before further assessment. Repeat exposure studies were carried out for a further 72 hours by following the same procedure. This is shown in the schematic below (see Figure 3.2). After specific incubation times,

a minimum of 24 spheroids were harvested for further analysis. Supplementary repeat exposure experiments (drug treatment on day 5, 8, 11, 14 and 17) were also performed to explore the sensitivity of the spheroids. Cell viability was measured following drugs exposure for up to 360 hours.

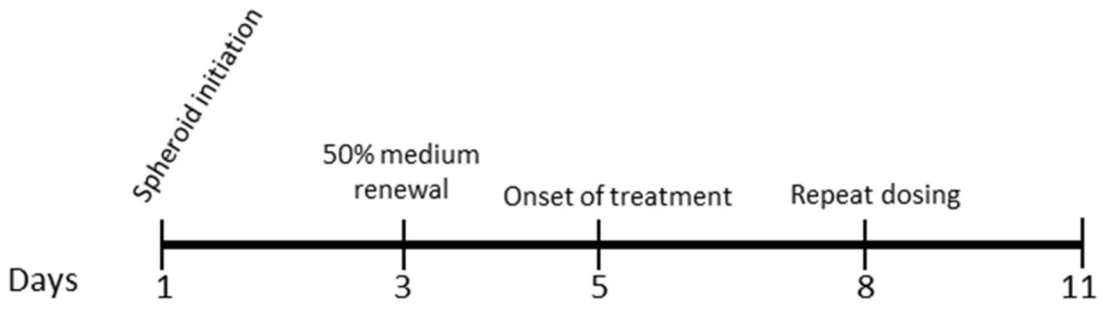

Figure 3.2 Time table for setting up and performing spheroid-based drug assays with established tumour cell lines

3.2.7.4 Determination of Cell Viability Following Treatment

Cell viability was measured using the CellTiter-Glo luminescent cell viability assay (Promega, Hampshire) according to the manufacturer's instructions. The ATP assay is based on the quantification of the amount of intracellular ATP which correlates with the number of metabolically active (viable) cells. Briefly, 100µL of CellTiter-Glo reagent was added to each well of the spheroid or monolayer cells plates. For cells in monolayer, the plate was agitated using an orbital shaker at 60rpm for 2 minutes to induce cell lysis. For spheroids, the plates were agitated at 60rpm for 5 minutes to induce cell lysis. Thereafter, the plates were left for 10 minutes to equilibrate at RT and 100 µL lysate was transferred to a white opaque walled 96-well flat-bottomed plate. The luminescence was measured at 570nm wavelength using a Varioskan flash plate reader. Media alone with CellTiter-Glo reagent was used as a blank control and subtracted from sample values. Cell viability was calculated as a percentage of untreated vehicle control samples (0.1% DMSO treated). Six replicates were used for each experiment (n=6) and at least two independent experiments were conducted. A concentration-response curve was plotted and IC_{50} values determined.

3.2.8 Western Blotting

3.2.8.1 Cell Lysis

Monolayer cells were seeded on 6 well plates and incubated for 24 hours until sub-confluent. For drug treatment, cells were incubated with previously determined IC_{50} concentrations for 72 hours. Following incubation, cell lysates were prepared on ice by washing cells twice with ice-cold 1x PBS and then by the addition of 300µL radioimmunoprecipitation assay (RIPA) buffer (150mM NaCl, 1.0% IGEPAL CA-630, 0.5% sodium deoxycholate, 0.1% sodium dodecyl sulphate (SDS), 50mM Tris, pH 8.0) supplemented with 1x Halt™ protease and phosphatase inhibitor (PPI) cocktail for 30 minutes. Cells were thereafter scraped and transferred into 1.5mL Eppendorf tubes. The lysate was clarified by centrifugation (14,000rpm, 20minutes, 4°C) and the supernatant was collected and stored at -40°C.

Spheroids (minimum of 24, either control or IC_{50} drug-treated) were collected in 1.5mL Eppendorf tubes using a 100µL pipette tip with the end cut off. Tubes were centrifuged gently, and the medium was removed. Ice-cold PBS (500µL) was added, and tubes were centrifuged gently again, before the removal of the PBS. RIPA buffer containing 1x PPI (150µL) was added and left on ice for 30 minutes. Lysates were homogenised via sonication (3 x 10-second cycles at pulse setting 2) using a Microson™ ultrasonic cell disruptor XL (Cole Palmer, UK). The lysate was clarified by centrifugation (14,000rpm, 20minutes, 4°C), and the supernatant was collected and stored at -40°C.

3.2.8.2 Tissue Lysis

Tissues of interest were thawed on ice and washed with PBS. A clean scalpel was used to dissect the tissue sample, which was then placed into a precooled 1.5ml round bottom Eppendorf tubes containing a metal bead. Ice cold RIPA buffer containing 1x PPI (300µL) was rapidly added to the tube. Samples were homogenised on a mixer mill MM 400 (Retsch, UK) set at an oscillation frequency of 30Hz for 2 minutes. All lysate was then placed into a fresh Eppendorf tube, before being clarified by centrifugation (14,000rpm, 20minutes, 4°C). The supernatant was collected and stored at -40°C.

3.2.8.3 Protein Determination

The protein content of all samples was determined using the Pierce bicinchoninic acid (BCA) assay according to the manufacturer's instructions. The assay is based on the colourimetric detection of the cuprous cation (Cu^{+}). The total amount of protein was quantified from a standard curve, generated from known concentrations (20–2000µg/mL) of bovine serum albumin (BSA) made up in RIPA buffer. Each standard and unknown samples were analysed at an absorbance of 562nm (Varioskan), with a sample to working reagent ratio of 1:8 (25µl:200µl). Volumes of sample and deionised water (dH_2O) required for western blotting were then calculated.

3.2.8.4 Immunoblotting

Protein samples (20µg) were mixed with 10x NuPAGE dithiothreitol (DTT) reducing agent and 4x NuPAGE lithium dodecyl sulphate (LDS) sample buffer, and the volume was adjusted to 15µL using dH_2O. Samples were boiled (90°C, 10minutes) and centrifuged briefly. Together with a molecular weight (MW) marker (precision plus protein kaleidoscope pre-stained protein standards) they were loaded onto a NuPAGE Novex precast 4-12% Bis-Tris gels and electrophoresed with MOPS SDS running buffer under reducing conditions (200V, 50minutes). Antioxidant was included in the running buffer to prevent re-oxidation of proteins during electrophoresis. A trans-blot turbo transfer system (Bio-Rad Laboratories, Hertfordshire) was used to transfer proteins on to 0.2µm nitrocellulose membranes (mixed MW protocol: 7minutes, 2.5A, 25V). The membranes were blocked for 2 hours at RT in 5% non-fat milk in TBS-T buffer (0.01M Tris-HCl, pH 8.5; 0.15M NaCl; 0.1% Tween20), before incubation overnight at 4°C with the different primary antibodies (see Table 3.3 for dilutions). All blots were washed TBS-T (3 times, 5minutes) before being incubated with the appropriate horseradish peroxidase (HRP)–coupled secondary antibody for 1 hour at RT (see Table 3.3 for dilutions). After a further 4 washes in TBS-T, the bands were visualised through chemiluminescence detection either in an automated manner using a chemidoc MP imaging system (Bio-Rad Laboratories, Hertfordshire), or manually by covering the membranes with western lighting plus ECL (Perkin Elmer, Buckinghamshire)

and visualising it in a darkroom with Amersham hyperfilm ECL (GE Healthcare, Buckinghamshire). Once visualised, densitometry analysis was performed using ImageJ software. To correct for protein loading, the quantified protein of interest was related to its corresponding loading control i.e. actin band. The untreated control sample within each experiment was assigned an arbitrary value of 1.0, to which bands from all other conditions were relatively expressed.

Table 3.3 Antibodies for western blotting

Antibody	1° Dilution	2° Dilution
Actin (ProteinTech, 66009-1-Ig)	1:20,000	1:5000 Mouse
Carboxylesterase 1 (Abcam, ab45957)	1:1000	1:5000 Rabbit
Carboxylesterase 2 (Abcam, ab137606)	1:1000	1:5000 Rabbit
MRP2 (Invtirogen, PA5-4997)	1:1000	1:5000 Rabbit
Topoisomerase 1 (Abcam, ab109374)	1:2500	1:5000 Rabbit
UGT (Cell Signalling Technologies, 4371S)	1:1000	1:5000 Rabbit
UGT1A1 (Abcam, ab194697)	1:1000	1:5000 Rabbit
γH2AX (Cell Signalling Technologies, 9718S)	1:1000	1:5000 Rabbit

Both primary and secondary antibodies were made up in 2% non-fat milk in TBS-T buffer

3.2.9 Immunofluorescence

3.2.9.1 Monolayer

Monolayer cells (HCT116 and CT26) were grown on poly-L-lysine coated coverslips as previously described in section 3.2.6.3. Cells were treated for either 0.5, 1, 3 and 24 hours with irinotecan or SN-38 IC_{50} concentrations and fixed for 15 minutes at 4°C in 4% PFA. A permeabilisation step was performed with 0.25% Triton X-100 in PBS for 15 minutes at 4°C. To render the DNA-protein crosslinks more accessible to antibody, the coverslips were incubated in 1% SDS at RT for 5 minutes. Coverslips were then washed three times with PBS and blocked in IF blocking buffer for 2 hours at RT (PBS with 1% glycerol, 0.1% gelatin from cold-water fish, 5% normal goat serum, 0.1% BSA and 0.4% sodium azide). Coverslips were incubated overnight at 4°C with primary antibodies (dilutions are shown in

Table 3.4) in IF blocking buffer. They were then extensively washed with PBS over 20 minutes and stained with fluorochrome-conjugated secondary antibody (Alexa Fluor 488 or 568) diluted 1:1000 in IF blocking buffer for 1 hour at RT. After further extensive washes with PBS, coverslips were counterstained (cell nuclei) with 1µg/ml Hoechst 33258 in PBS. Coverslips were mounted on superfrost glass slides using prolong gold antifade reagent and sealed using clear nail polish. Images were captured on a Zeiss inverse Axio observer confocal microscope (Zeiss LSM 710, Carl Zeiss) using an x20/x40/x63 objective with apotome. IF was also performed on cells in the absence of either primary or secondary antibodies as a control measure. Drug treatment with gemcitabine or 0.1% DMSO was also used as a negative control.

3.2.9.2 Spheroid Sections

Spheroids (HCT116 and CT26) were grown and treated for 24 hours with irinotecan or SN-38 predetermined IC_{50} concentrations. Subsequently, spheroids were processed and sectioned as described in section 3.2.6.1 and 3.2.6.2. Heated (50˚C, 10minutes) spheroid sections were dewaxed with xylene, before being rehydrated with a series of ethanol solutions of descending concentrations (100-25%) and then rinsed in dH_2O. A pap-pen (Abcam, Cambridge) was used to create a hydrophobic ring around the spheroids and slides were permeabilised, blocked and incubated as per section 3.2.9.1.

3.2.9.3 Whole-mount spheroids

Spheroids (HCT116 and CT26) were grown and treated for 24 hours with irinotecan or SN-38 at predetermined IC_{50} concentrations. Spheroids were transferred from ULA plates into round bottom collection tubes using a 200µl pipette tip with the end cut off and fixed in PFA for 1 hour at 4°C. Spheroids were then permeabilised, blocked and incubated with the same reagents as per section 3.2.9.1. However, following counterstaining with 1µg/ml Hoechst 33258, a fructose-glycerol clearing solution (100µl) was added for 20 minutes at RT (Dekkers et al., 2019). A pap pen was used to draw a circle onto superfrost glass slides. Spheroids were then picked up (using pre-coated (IF blocking buffer)

200ul tips with the end cut off) and placed within the circle. A coverslip was lowered on top of the spheroids and slight pressure was applied, prior to sealing with clear nail polish. Thereafter maximum intensity projection images of spheroids were taken using a Zeiss inverse Axio observer confocal microscope using an x20/x40 objective with apotome.

Table 3.4 Antibodies for immunofluorescence

Antibody	Dilution
Alexa Fluor 488 goat anti-mouse IgG (Invitrogen, A-11001)	1:1000
Alexa Fluor 568 goat anti-rabbit IgG (Invitrogen, A-11001)	1:1000
α-TopoIcc (Merck, MABE1084)	0.67:1000 (0.67µg/ml)
γH2AX (Cell Signalling Technologies, 9718S)	1:400

3.2.10 Statistical Analysis

Unless otherwise stated, all reported values are the average with their respective standard deviation (SD). The number of replicates is always indicated in the figure legends. Quantitative experiments were conducted at least in biological triplicates and datasets were analysed with SigmaPlot version 14.0 (Systat Software, Inc., San Jose California USA). A two-way analysis of variance (ANOVA) with Holm-Šídák multiple comparison post-hoc test was used to compare data sets. A p-value of <0.05 was considered significant.

3.3 Results

3.3.1 Analysis of Spheroid Growth Kinetics - Spheroid Formation and Cultivation

To optimise spheroid culture conditions, different seeding densities which may affect spheroid formation and growth were investigated over 16 days. HCT116 cells were seeded at 1250, 2500 and 5000 cells/well and CT26 cells at 500, 1000 and 2500 cells/well. The dependence of spheroid size on seeding density is illustrated in Figure 3.3a and Figure 3.4a where the spheroid diameter is plotted against time. All seeding densities resulted in the formation of spheroids varying in size, with cells aggregating to form a single spheroid within 3 days. Initially, all spheroid diameters increased exponentially, the rate of growth thereafter started to decrease i.e. spheroid growth plateau. As seen in Figure 3.3b and Figure 3.4b higher seeding densities resulted in irregularly-shaped (ellipsoidal) structures, the formation of large dark regions (quiescent/dead cells) and greater size variations, following five days in culture. A seeding density of 1250 or 1000 cells/well for HCT116 and CT26 spheroids respectively, formed spheroids that displayed a compact cellular assembly with a circular structure. This compaction led to the formation of distinct dark borders around spheroids. As a result, these seeding densities (1250 or 1000 cells/well for HCT116 and CT26 spheroids respectively) were chosen for all subsequent experiments.

With the optimal seeding density, the average diameter of HCT116 spheroids was 374 ± 16.6µm and CT26 spheroids 350 ± 26.1µm after five days of culture. Spheroid shape and diameter was further monitored over time and spheroids maintained their uniform shape over a 16-day culture period (see Figure 3.3c and Figure 3.4c). HCT116 spheroids increased in diameter over the 16-day culture period from 253 ± 20.6µm to 739 ± 7.18µm. Similarly, CT26 spheroids increased from 210 ± 34.7µm to 805 ± 2.70µm. No substantial morphological changes were observed i.e. cell detachment or budding of secondary spheroids. These spheroids were therefore deemed suitable for long term experiments, due to their homogeneity and uniformity in shape and size.

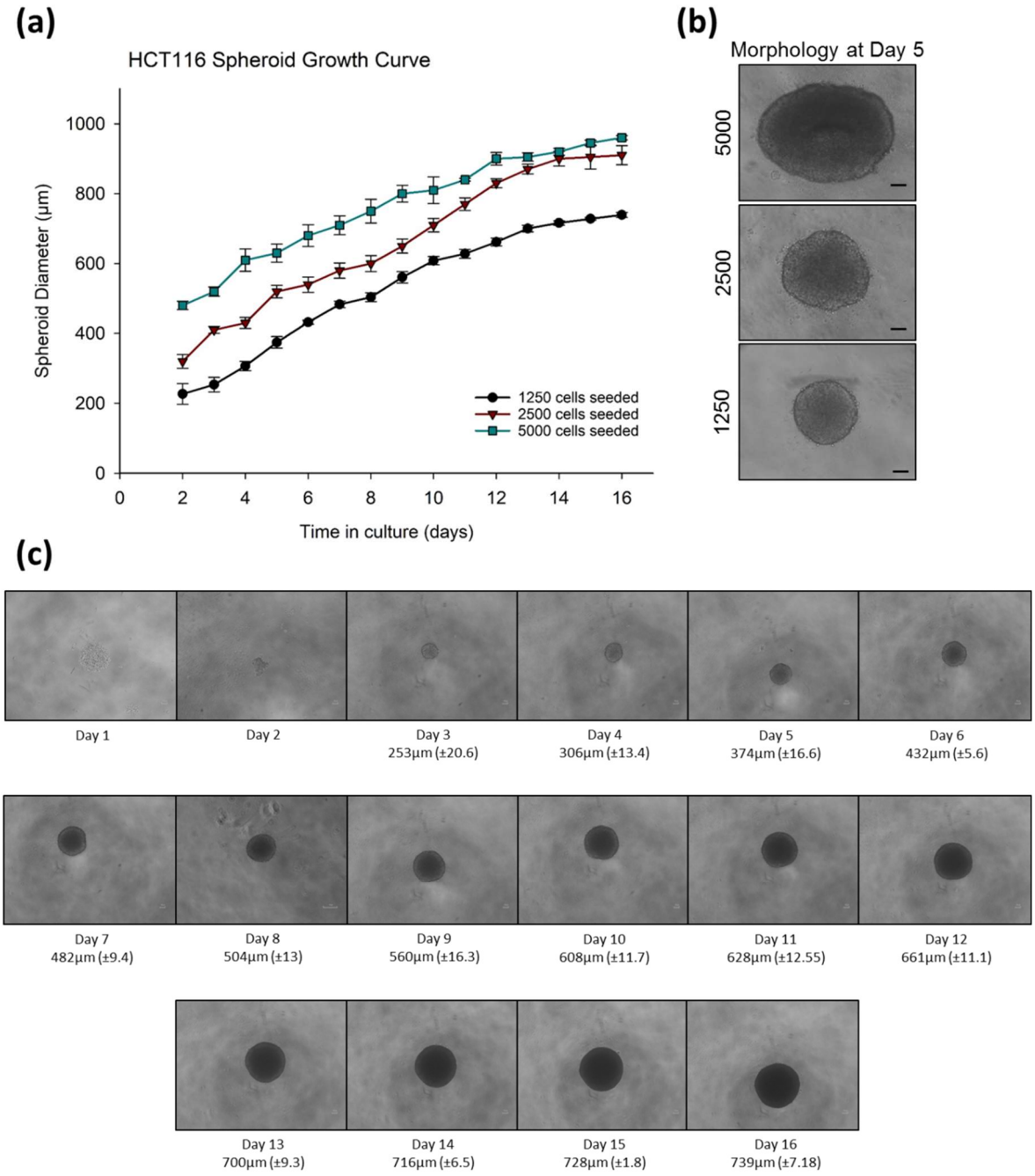

Figure 3.3 Effect of cell density on HCT116 spheroid formation **(a)** Spheroid diameter of HCT116 cells seeded at three densities (1250, 2500 and 5000 cells/well) cultured for 16 days. (n=10, data shown as average ± SD) **(b)** Representative phase-contrast images (x10 objective) of each density shown at day 5. Scale bar is 100µm **(c)** Representative phase-contrast images (x4 objective) of HCT116 cells seeded in ULA plates at an optimised density of 1250 cells/well. Scale bars represents 100µm (n=3 using 6 technical replicates, data shown as average ± SD).

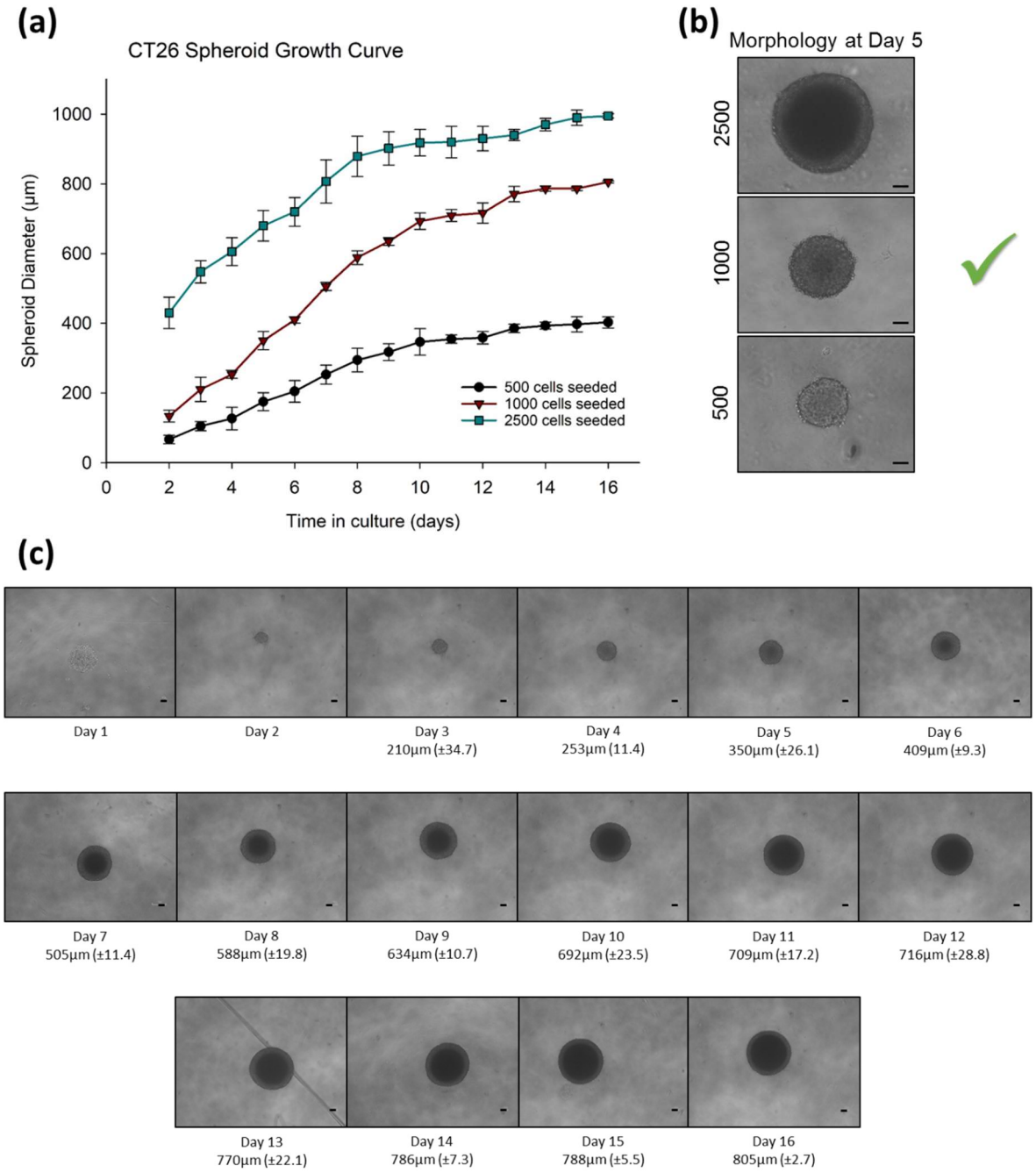

Figure 3.4 Effect of cell density on CT26 spheroid formation **(a)** Spheroid diameter of CT26 cells seeded at three densities (500, 1000 and 2500 cells/well) cultured for 16 days. (n=10, data shown as average ± SD) **(b)** Representative phase-contrast images (x10 objective) of each density shown at day 5. Scale bar is 100µm **(c)** Representative phase-contrast images (x4 objective) of CT26 cells seeded in ULA plates at an optimised density of 1000 cells/well. Scale bars represents 100µm (n=3 using 6 technical replicates, data shown as average ± SD).

3.3.2 Immunohistological Characterisation of Spheroids

To gauge the applicability of the spheroids, sectioning and immunohistochemistry were performed for further characterisation. From Figure 3.5a, H&E staining of HCT116 spheroids revealed a compact internal arrangement, densely packed with cells. As the spheroids grew in diameter the H&E staining became less intense. Clearly defined cell boundaries were seen over the culture period, with staining consistent with the formation of central areas of necrosis emerging at day 11. The proliferative cell marker, Ki-67, showed proliferating cells (Ki-67^{+}) throughout HCT116 spheroids on day 5 of culture (0.567), as seen by the homogenous brown staining (peroxidase). At later time points, the proliferating cells were more concentrated towards the outermost layer of the spheroid (Day 8 and 11). Similarly, the amount of Ki-67^{+} cells decreased to 0.357 on day 8 and 0.196 at day 11. The apoptosis marker, cleaved caspase-3, was not identified (negligible amount of brown staining) in any of the HCT116 spheroids. Alcian blue staining which indicates the presence of acidic sulphated muco-substances was only observed on day 11 of culture (see black arrows in Figure 3.5d).

CT26 spheroids were also characterised in the same manner (see Figure 3.6). As per the above, CT26 spheroids also exhibited a highly organised 3D tissue-like structure with tightly compacted cells. However, on day 11, necrosis seemed to be apparent in the centre of spheroids (as seen by the presence of lighter pink - stained only with eosin). The amount of Ki-67 expressing cells markedly decreased over time (0.074 to 0.015), in a similar manner to the HCT116 spheroids. When comparing both cells lines at day 5 in culture CT26 spheroids displayed a lower proliferative activity (lower concentration of DNA in the S phase). However, this could have been due to CT26 cells proliferating much quicker initially, which would have been visible at an earlier time point. Low levels of active caspase-3-mediated apoptosis were found to be induced in the core of the CT26 spheroids (day 11), whilst the CT26 spheroids were negative for Alcian blue staining.

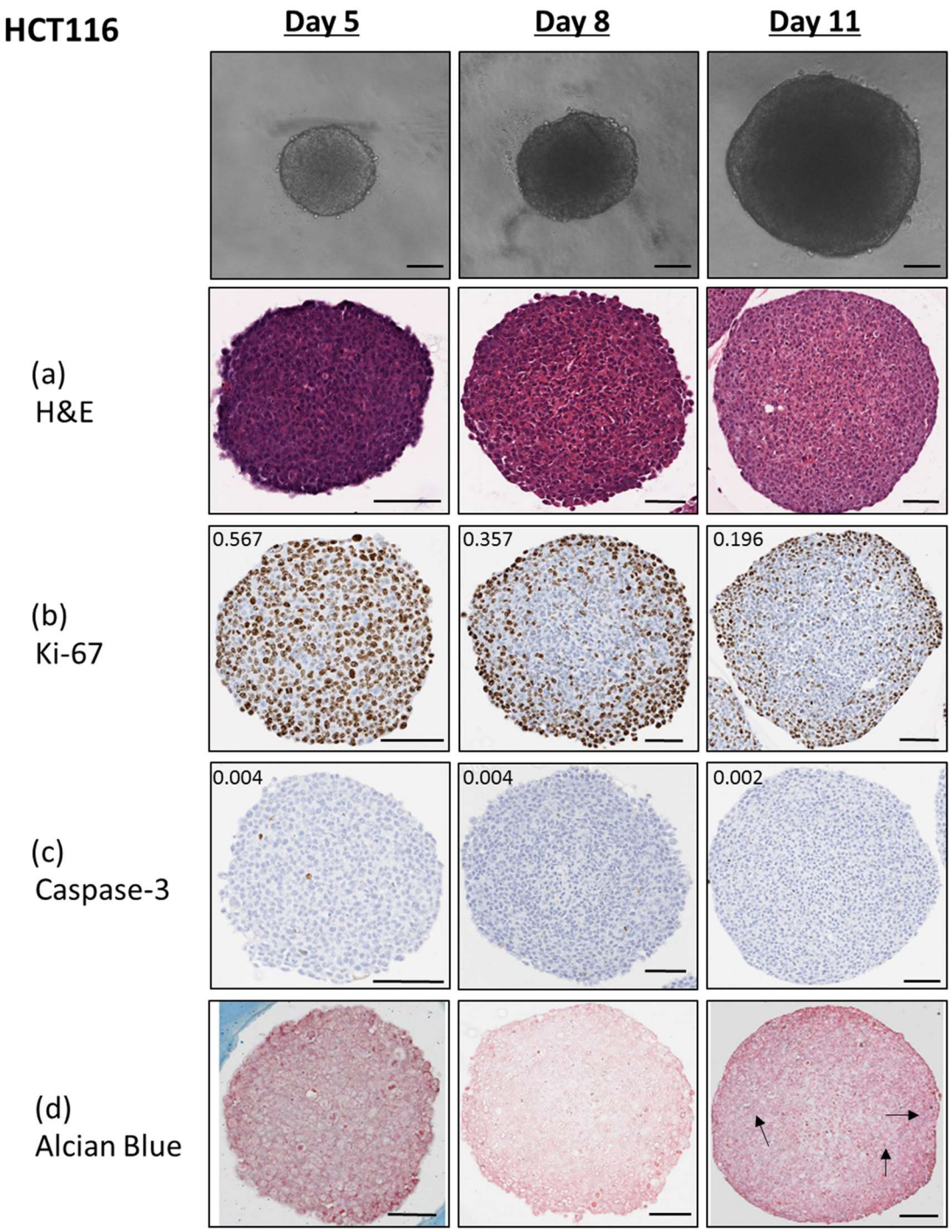

Figure 3.5 Immunohistological assessment of HCT116 spheroids. HCT116 spheroids at Day 5, 8 and 11 were processed, sectioned (5µm) and stained with **(A**) H&E: for morphology **(B)** Ki-67: a proliferation marker, **(C)** Caspase-3: a marker of apoptosis and **(D)** Alcian Blue: for acidic mucins. Images were analysed using the Aperio positive pixel count v9 algorithm. The values for positivity represent an average of three spheroids. Scale bars represent 100µm.

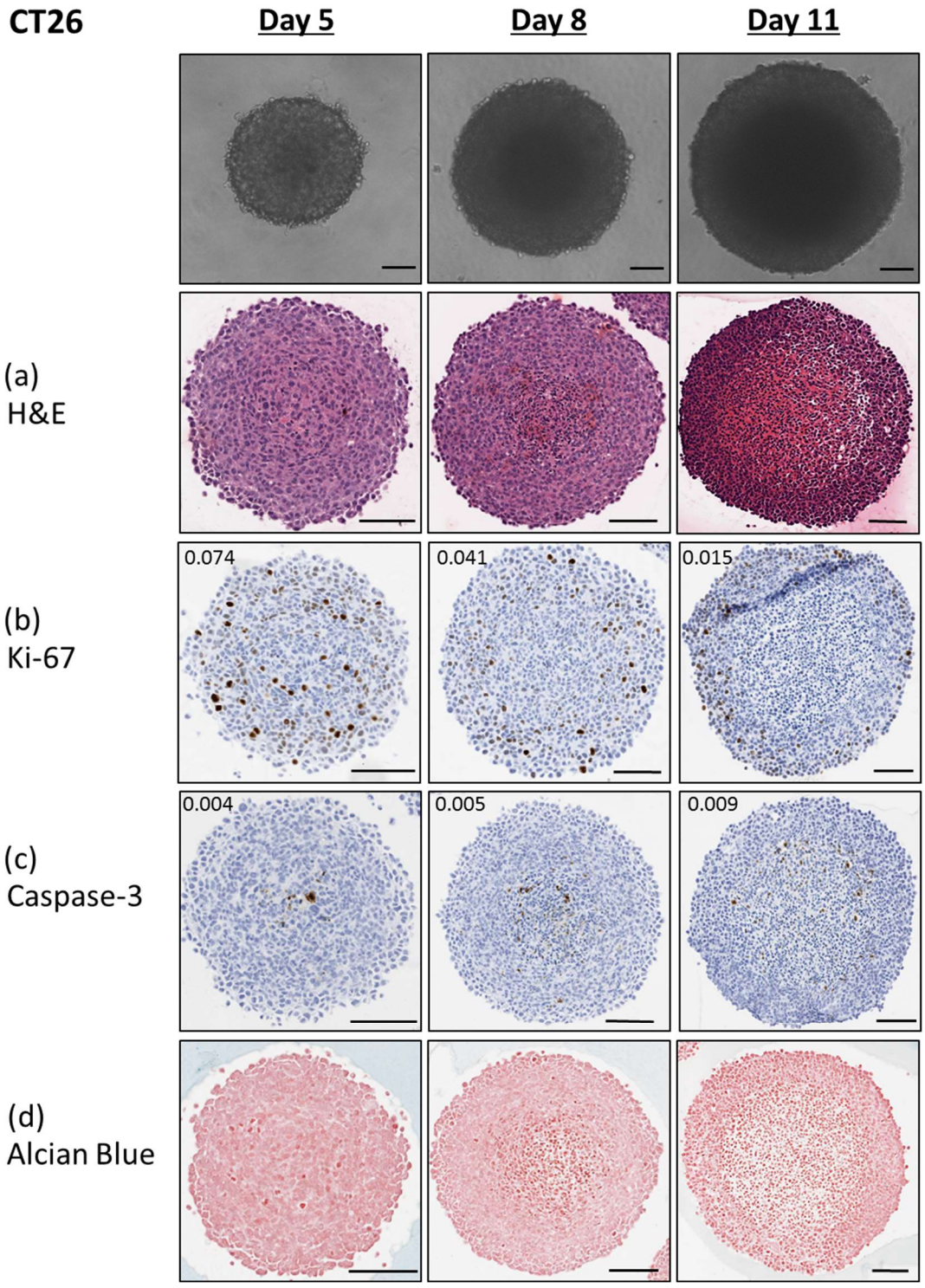

Figure 3.6 Immunohistological assessment of CT26 spheroids. CT26 spheroids at Day 5, 8 and 11 were processed, sectioned (5µm) and stained with **(A**) H&E: for morphology **(B)** Ki-67: a proliferation marker, **(C)** Caspase-3: a marker of apoptosis and **(D)** Alcian Blue: for acidic mucins. Images were analysed using the Aperio positive pixel count v9 algorithm. The values for positivity represent an average of three spheroids. Scale bars represent 100µm.

3.3.3 Chemosensitivity of Monolayer and Spheroids Following Drug Treatment

The viability of cells in the 2D culture systems exposed to various concentrations of irinotecan or SN-38 was determined by an ATP assay following 72 hours of treatment. The quantitative data was statistically analysed and the IC_{50} values were determined. A concentration-dependent reduction in ATP cell viability was observed in all monolayer cells, in response to both drugs as seen in Figure 3.7. DLD-1 cells were seen to be the most sensitive cell line to irinotecan and CT26 cells the least sensitive. With SN-38, the LoVo cell line was the most sensitive and CT26 cells again displayed the lowest sensitivity. From calculated IC_{50} values, SN-38 was seen to be between 50-500-fold more potent than its parent prodrug irinotecan (see Table 3.5).

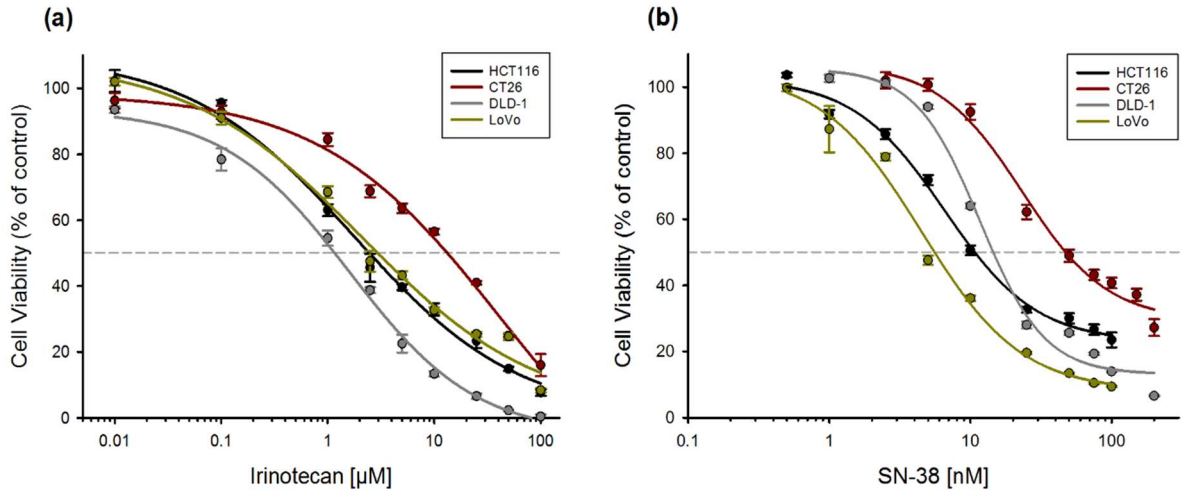

Figure 3.7 Concentration-response curves for cells grown in 2d. ATP levels were measured in monolayer (2D) cells treated with **(a)** irinotecan [µM] or **(b)** SN-38 [nM], for 72 hours (n=3 using 6 technical replicates, Average ± %SD). Cell viability was calculated as a percentage of untreated vehicle control samples (DMSO – 0.1%). The dashed horizontal line represents the half-maximal inhibitory concentration (IC_{50}).

The measurement of drug sensitivity was repeated for HCT116 and CT26 spheroids. Cell viability was measured in spheroids at time points of 72 hours or 144 hours. After 72 hours, HCT116 spheroids exhibited a concentration-dependent reduction in ATP cell viability, however, they also demonstrated a lower sensitivity to both drugs in comparison to 2D cells. Following 144hrs (i.e. two repeated drug treatments on day 5 and day 8), the spheroids showed greater sensitivity, as revealed by the concentration-response curve shifting to the left (Figure 3.8).

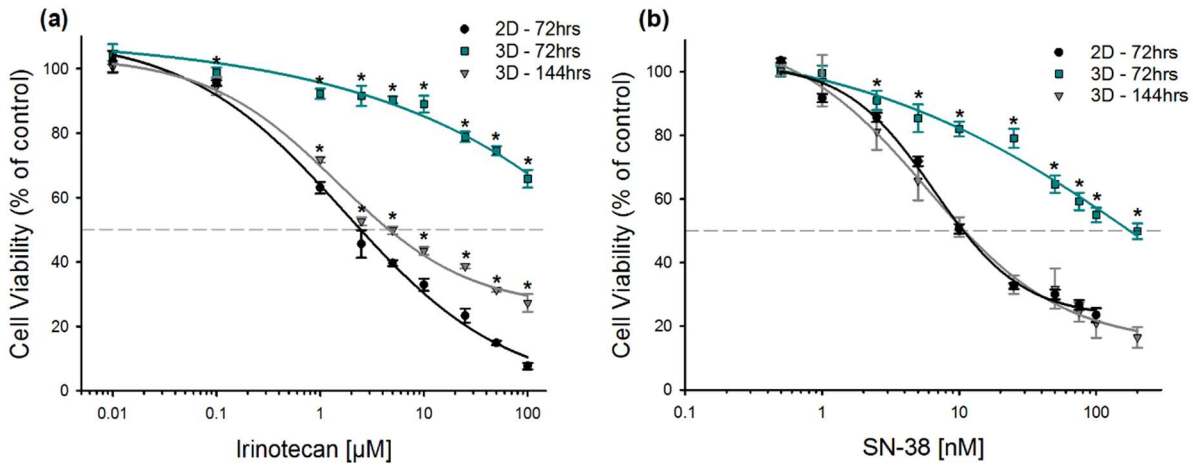

Figure 3.8 Concentration-response curves for HCT116 cells grown in 2D vs. 3D**.** ATP levels were measured in HCT116 cells treated with **(a)** irinotecan [µM] or **(b)** SN-38 [nM], for 72 hours in 2D and 72/144 hours in 3D (n=3 using 6 technical replicates, average ± %SD). Cell viability was calculated as a percentage of untreated vehicle control samples (DMSO – 0.1%). The dashed horizontal line represents the half-maximal inhibitory concentration (IC_{50}). Statistical analysis was performed using a two-way ANOVA followed by Holm-Šídák multiple comparison post-hoc test. A P-value of *P < 0.05 for each drug concentration between 2D and 3D cultures, was considered significant.

A similar pattern was present in CT26 spheroids, with spheroids displaying a lower sensitivity to both drugs, as compared to responses seen in monolayer (as depicted in Figure 3.9). CT26 cells overall in both 2D and 3D cultures were seen to be less sensitive than HCT116 cells.

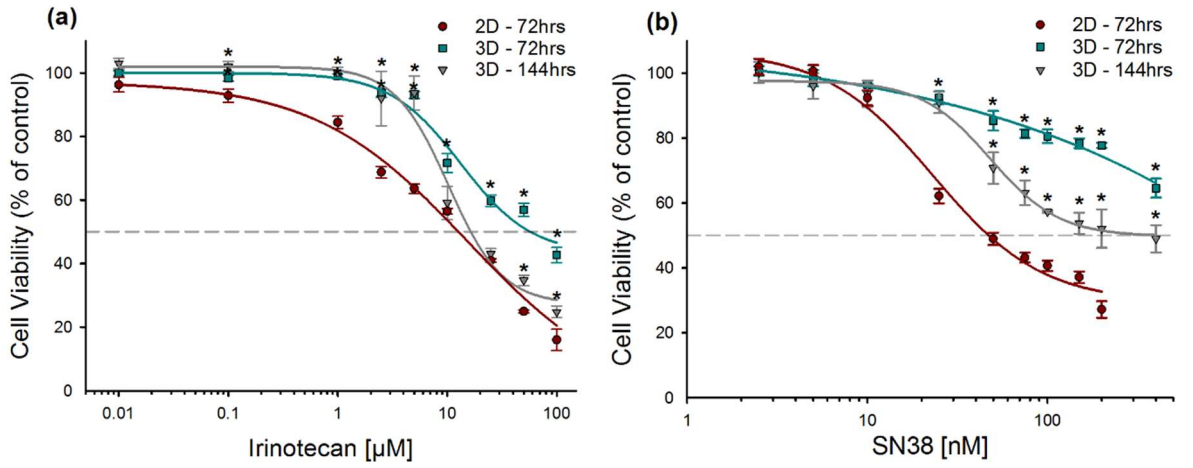

Figure 3.9 Concentration-response curves for CT26 cells grown in 2d vs. 3d. ATP levels were measured in CT26 cells treated with **(a)** irinotecan [µM] or **(b)** SN-38 [nM], for 72 hours in 2D and 72/144 hours in 3D (n=3 using 6 technical replicates, average ± %SD). Cell viability was calculated as a percentage of untreated vehicle control samples (DMSO – 0.1%). The dashed horizontal line represents the half-maximal inhibitory concentration (IC_{50}). Statistical analysis was performed using a two-way ANOVA followed by Holm-Šídák multiple comparison post-hoc test. A P-value of *P < 0.05 for each drug concentration between 2D and 3D cultures, was considered significant.

The above results (Figure 3.8 and Figure 3.9) showed that the efficacy of the irinotecan and SN-38 was lower in HCT116 and CT26 spheroids, than in monolayer culture (data for LoVo and DLD-1 spheroids is in the appendix Figure B.3). Consequently, the IC_{50} values determined in spheroids at 72 hours was significantly higher than those obtained in monolayer cultures, with enhanced sensitivity being observed in spheroids following repeated exposure (144 hours) (see Table 3.5).

Table 3.5 The comparative IC_{50} values calculated from cell lines treated with irinotecan and SN-38 in 2D and 3D cell culture

Cell line	Monolayer (2D)		Spheroid (3D)			
	Irinotecan 72hrs [nM]	SN-38 72hrs [nM]	Irinotecan 72hrs [nM]	Irinotecan 144hrs [nM]	SN-38 72hrs [nM]	SN-38 144hrs [nM]
HCT116	2430 (±310.91)	10.52 (±2.34)	**	4479.9 (±323.55)	170.38 (±38.94)	10.87 (±4.75)
CT26	12478.40 (±1235.62)	41.12 (±17.66)	55687.3 (±212.04)	16418.90 (±247.12)	**	374.42 (±39.81)
DLD-1	1156.45 (±36.88)	20.87 (±11.62)	-	-	**	87.07 (±24.32)
LoVo	2906.60 (±171.47)	6.35 (±1.48)	-	-	**	8.97 (±11.46)

Values shown are the average (±SD) n=3
**IC_{50} value was not determined
- Not tested

3.3.4 Monitoring the Effect of Repeated Chemotherapeutic Exposure in Spheroids

Predicting cytotoxicity after repeated exposure to drugs or chemicals is important for drug development and safety assessment, yet it remains impractical using conventional 2D *in vitro* systems due to the requirement of maintaining a relevant cellular phenotype for an extended duration. To further investigate the sensitivity of spheroids, HCT116 and CT26 spheroids were subjected to a three-week assay, involving five repeated treatments, with either irinotecan, SN-38 or 0.1% DMSO control. As seen in Figure 3.10 with each subsequent repeated exposure, HCT116 spheroids produced a significantly more potent response with an IC_{50} of 206.16µM and 7.75nM respectively for irinotecan and SN-38 at 360 hours (five repeated exposures). Under the same treatment conditions, the IC_{50} of CT26 spheroids was 6005.30µM and 117.90nM respectively for irinotecan and SN-38 (Figure 3.11). However, both spheroid cultures when repeatedly treated with SN-38 displayed a limit of sensitivity as subsequent exposures after 144 hours, did not significantly impact the IC_{50} values (see Table 3.6).

Morphological changes of the spheroids following drug treatment displayed spheroid shrinkage, as seen by the reduction in spheroid diameter. Also, the loss of spheroid integrity (spherical nature) and blebbing on the spheroid surface, was evident following repeated drug exposures. Cell death and induction of apoptosis at higher drug concentrations were evidenced by the shedding of dead cells and loss of cellular cohesion. In summary, the sensitivity of spheroid cultures was further elevated by extending drug exposure duration.

Table 3.6 The comparative IC_{50} values following repeated exposures with irinotecan and SN-38 in 3D cell culture

Repeated Exposure time (hours)	**HCT116 Spheroids**		**CT26 Spheroids**	
	Irinotecan	SN-38	Irinotecan	SN-38
72	**	170.38 (±38.94)	55687.30 (±212.04)	**
144	4479.9 (±323.55)	10.87 (±4.75)	16418.90 (±247.12)	374.42 (±39.81)
216	727.73 (±87.43)	8.72 (±1.98)	11962.65 (±512.79)	158.04 (±15.94)
288	669.13 (±54.19)	8.65 (±2.32)	11707.20 (±178.16)	141.77 (±12.46)
360	206.16 (±112.32)	7.75 (±2.64)	6005.30 (±790.43)	117.90 (±27.71)

Values shown are the average (±SD) n=3
**IC_{50} value was not determined

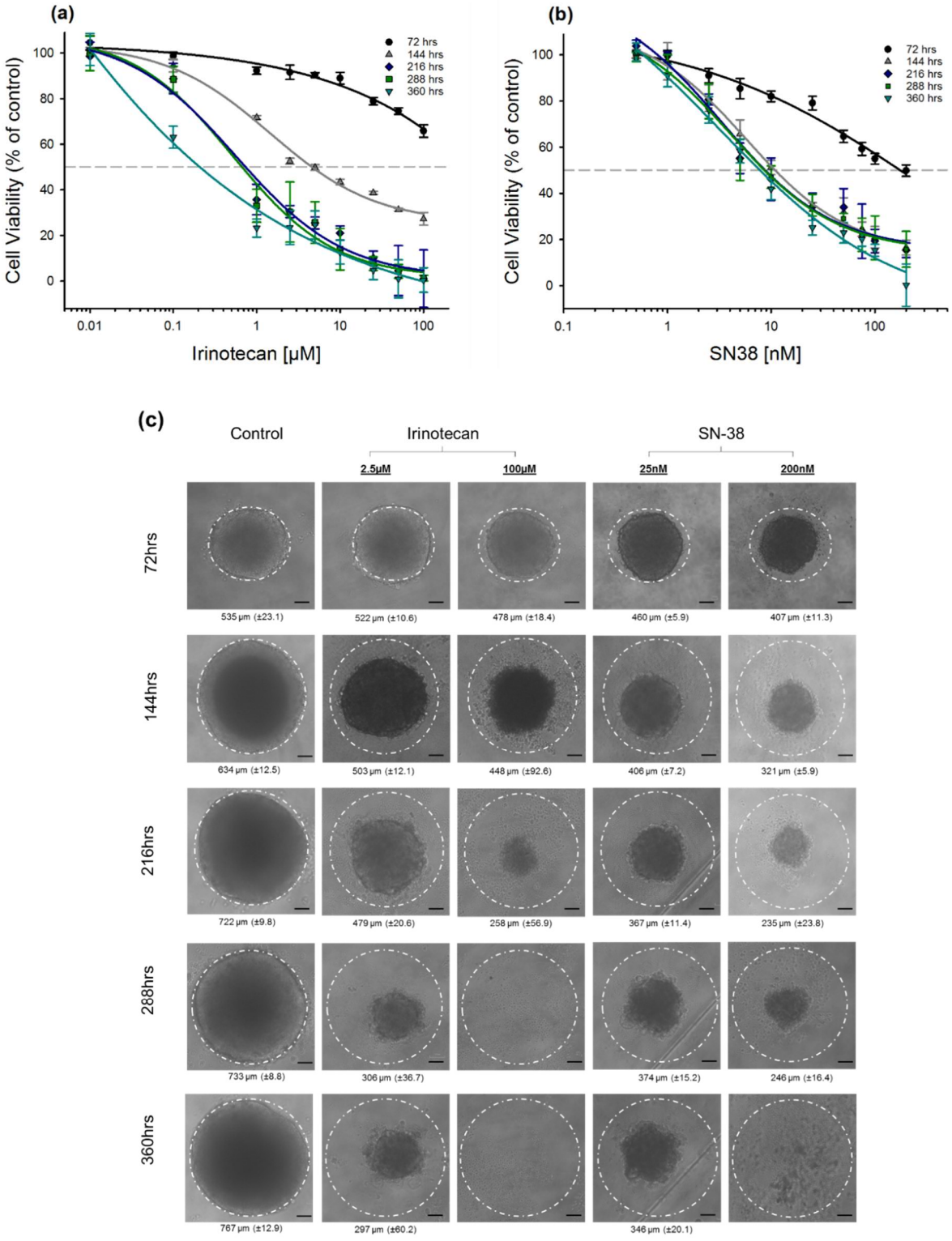

Figure 3.10 The effect of repeated drug treatment on HCT116 spheroids. ATP levels were measured in HCT116 spheroids repeatedly exposed to **(a)** irinotecan [µM] or **(b)** SN-38 [nM] (n=3 using 6 technical replicates, average ± %SD). Cell viability was calculated as a percentage of untreated vehicle control samples (DMSO – 0.1%) and concentration-response curves were plotted. The dashed horizontal line represents the half-maximal inhibitory concentration (IC_{50}). **(c)** Typical phase-contrast images (x10 objective) of HCT116 spheroids following repeated drug exposures with irinotecan or SN-38. The dashed circle represents the size of the control spheroid (0.1% DMSO) which is reported as a visual guide. Diameters are shown as an average ± SD (n = 3, using 6 technical replicates). The scale bars represent 100µm.

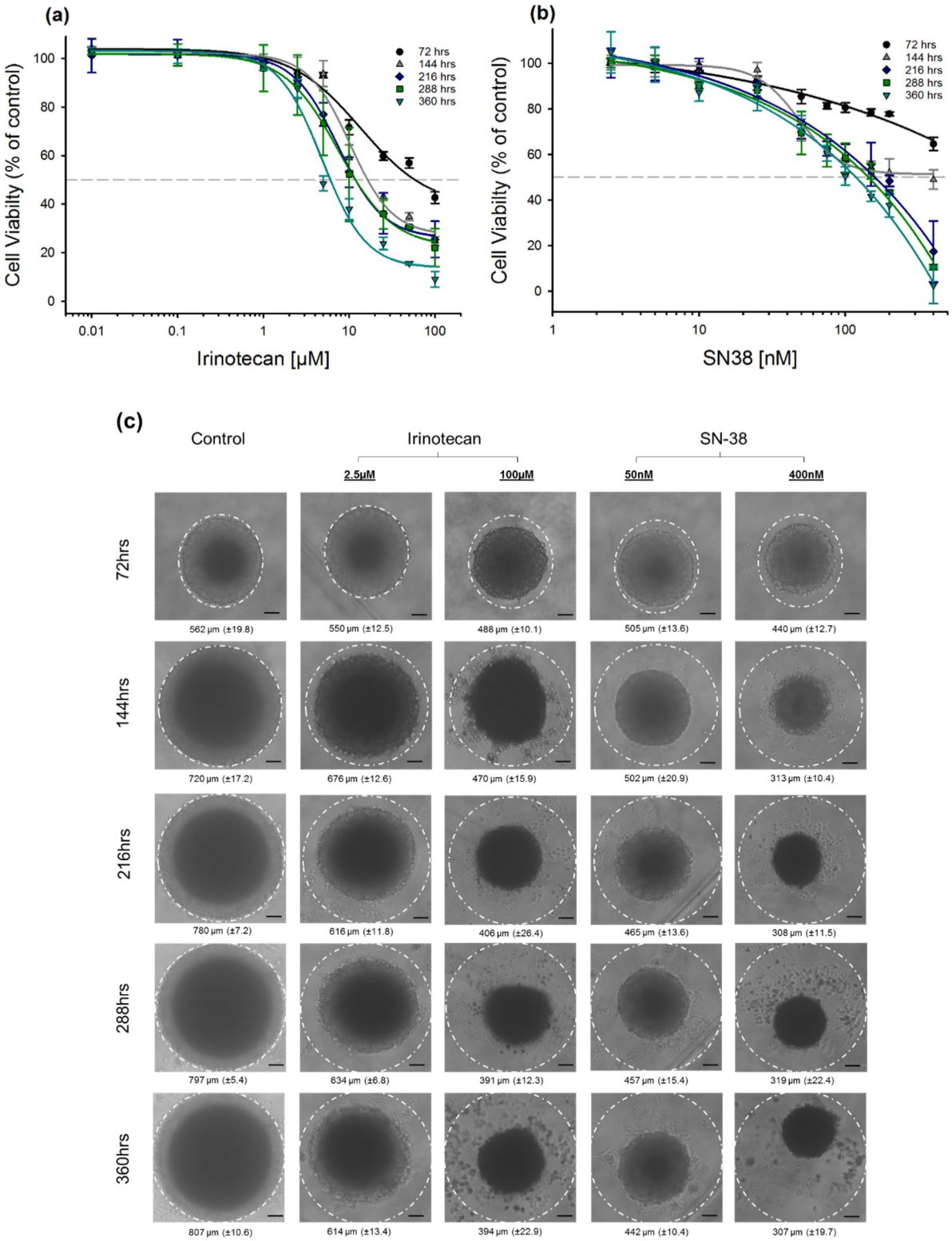

Figure 3.11 The effect of repeated drug treatment on CT26 spheroids. ATP levels were measured in CT26 spheroids repeatedly exposed to **(a)** irinotecan [µM] or **(b)** SN-38 [nM] (n=3 using 6 technical replicates, average ± %SD). Cell viability was calculated as a percentage of untreated vehicle control samples (DMSO – 0.1%) and concentration-response curves were plotted. The dashed horizontal line represents the half-maximal inhibitory concentration (IC_{50}). **(c)** Typical phase-contrast images (x10 objective) of CT26 spheroids following repeated drug exposures with irinotecan or SN-38. The dashed circle represents the size of the control spheroid (0.1% DMSO) which is reported as a visual guide. Diameters are shown as an average ± SD (n = 3, using 6 technical replicates). The scale bars represent 100µm.

3.3.5 Effect of Drug Treatment on Spheroid Histology

Spheroids were exposed to fixed concentrations of irinotecan (100μM) or SN-38 (200 or 400nM) for 72 hours. Previous results displayed that exposure of HCT116 and CT26 spheroids to irinotecan or SN-38 caused a dose-dependent reduction in cell viability in both types of spheroids. HCT116 spheroids were more sensitive to the cytotoxic effects of both drugs, compared to the CT26 spheroids (Table 3.6). To assess the effect of the drugs on spheroids, H&E staining was done to initially examine the morphology of the cells. To further assess the mechanism of cell death/reduction cleaved caspase 3^+ and Ki-67^+ staining was carried out.

Initial examination of morphological characteristics using H&E staining showed that specific differences between the treatment groups and controls could be easily identified. In particular, evidence of necrosis and vacuole formation in spheroids was noted. Cells within both irinotecan and SN-38 treated spheroids (Figure 3.12a and Figure 3.13a) were enlarged and swollen, with paler cytoplasms (indicated by arrows). Pyknosis of cells with nuclear condensation, together with nuclear fragmentation and a dilated cytoplasm was also evidenced (indicated by arrowheads). Cells in both HCT116 and CT26 spheroids appeared to be less organised with more acellular gaps present, as compared to controls. Additionally, cells grown in 2D that were also treated with SN-38 showed similar characteristics i.e. swollen, elongated cells with nuclear condensation present. These images have been included in the appendix (Figure B.2). Drug treatment caused a marked decrease in the number of Ki-67^+ cells in both HCT116 and CT26 spheroids (see positivity values). Interestingly, no significant increase in caspase-3 activation was present in HCT116 spheroids following drug treatment. In contrast, CT26 spheroids showed an increase in the number of cleaved caspase-3^+ cells following both irinotecan and SN-38 treatment. Results suggested that drug-induced apoptosis was predominantly limited to cells located on the surface of the spheroids.

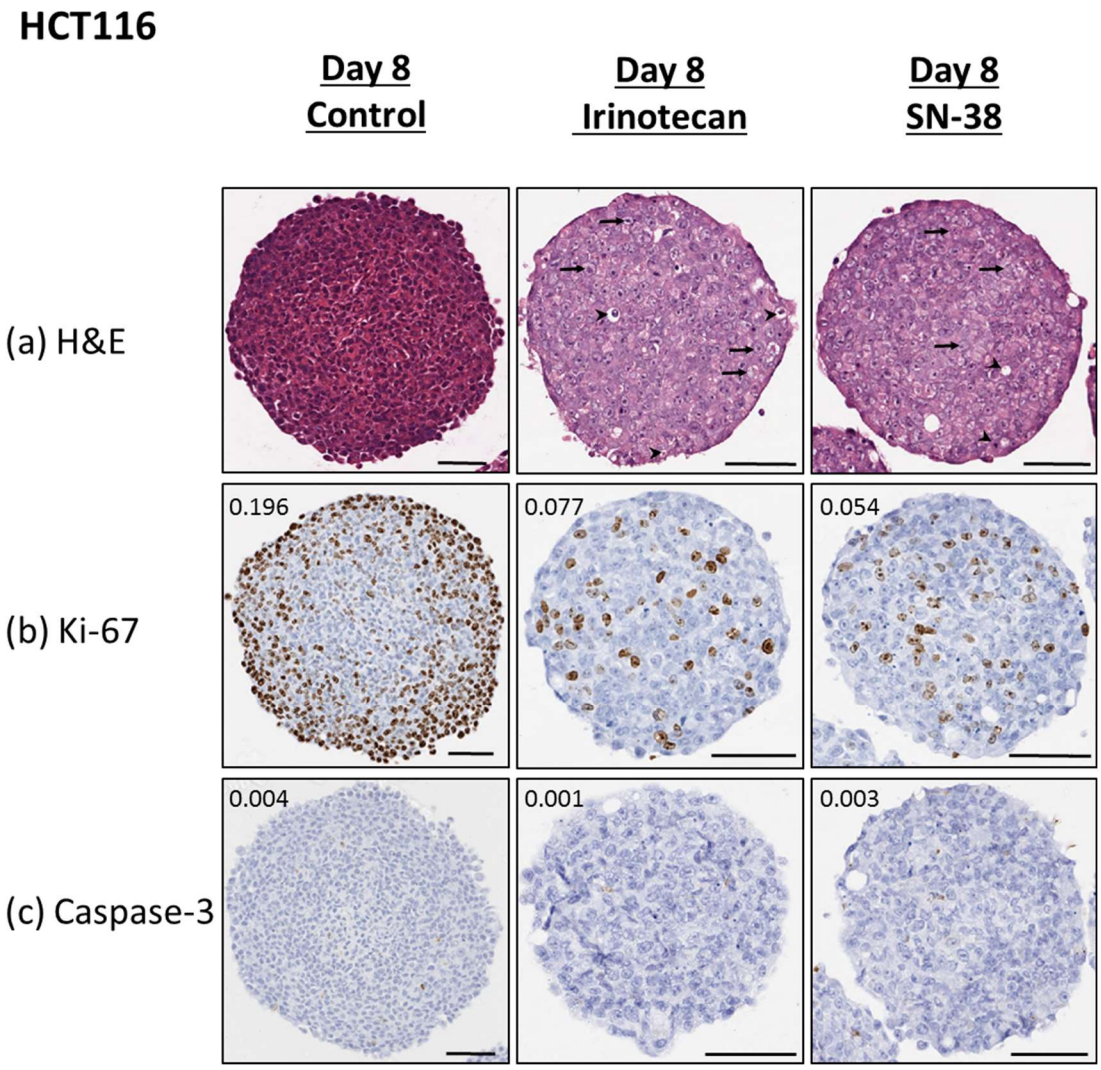

Figure 3.12 Histological assessment of HCT116 spheroids following drug treatment. HCT116 spheroids at Day 5 were treated with irinotecan [100µM], SN-38 [200nM] or 0.1% DMSO for 72hrs. Spheroids were sectioned (5µm) and stained with **(a)** H&E, for morphology (arrows indicating features of necrosis) **(b)** Ki-67, a proliferation marker and **(c)** Caspase-3, a marker of apoptosis. Slides were scanned using the Leica Aperio CS2 slide scanner. Images were then processed using the ImageScope software. Images were analysed using the Aperio positive pixel count v9 algorithm. The values for positivity represent an average of three spheroids. Scale bars represent 100µm.

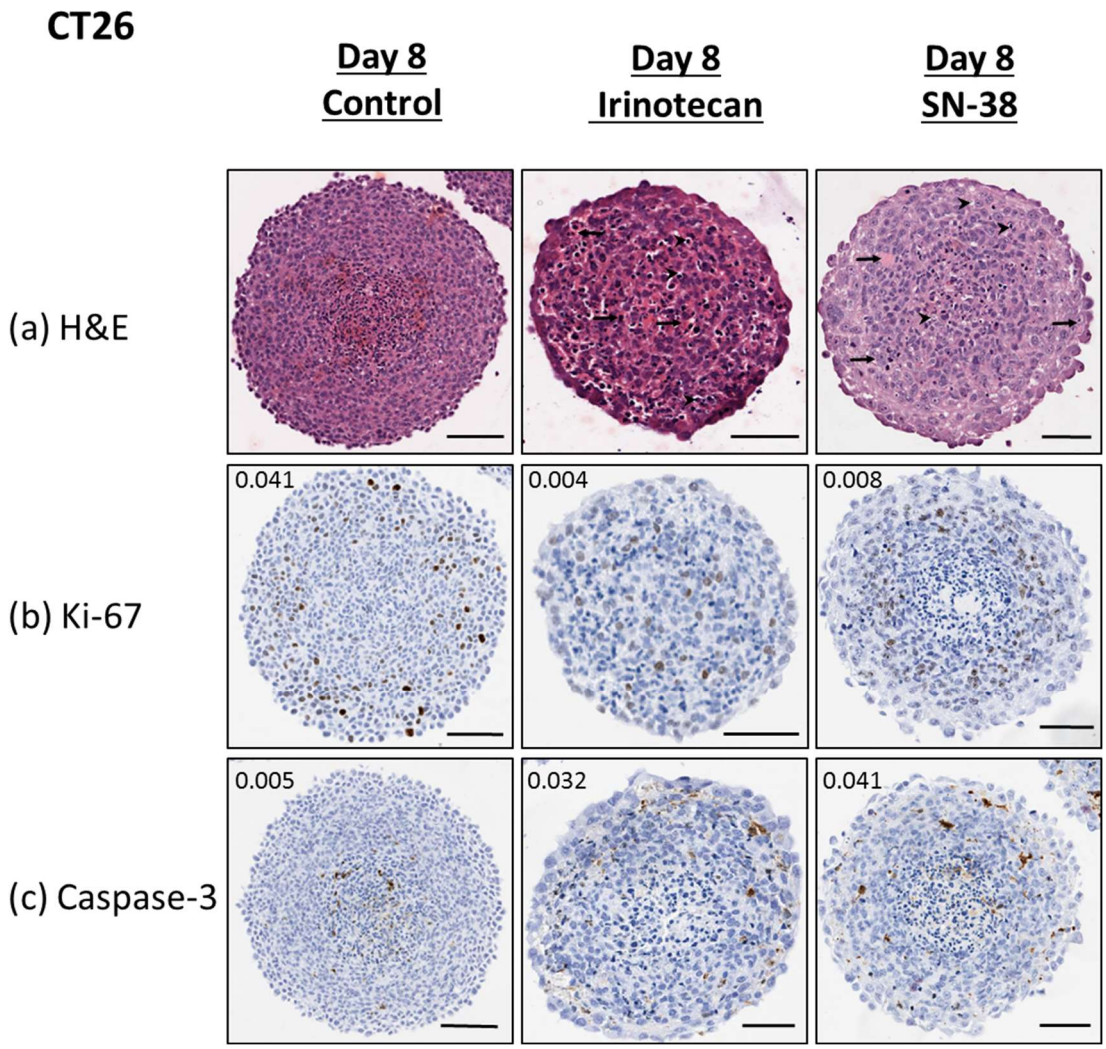

Figure 3.13 Histological assessment of CT26 spheroids following drug treatment**.** CT26 spheroids at Day 5 were treated with irinotecan [100µM], SN-38 [400nM] or 0.1% DMSO for 72hrs. Spheroids were sectioned (5µm) and stained with **(a)** H&E, for morphology (arrows indicating features of necrosis) **(b)** Ki-67, a proliferation marker and **(c)** Caspase-3, a marker of apoptosis. Slides were scanned using the Leica Aperio CS2 slide scanner. Images were then processed using the ImageScope software. Images were analysed using the Aperio positive pixel count v9 algorithm. The values for positivity represent an average of three spheroids. Scale bars represent 100µm.

3.3.6 Detection of Topoisomerase I-DNA Covalent Complexes

The mechanism of action of both irinotecan and SN-38 causes them to bind and stabilise the TOPI-DNA cleavage complex, thus leading to DNA damage when replication or transcription occurs. These agents induce their cytotoxicity by stabilising TOPI-DNA covalent complexes, which in turn interacts with advancing replication forks or transcription complexes to generate lethal lesions. Such complexes could act as surrogate markers for drug uptake/penetration. IF was therefore used to detect these complexes both in monolayer and spheroid culture (α-TopoIcc). Besides the presence of the DNA damage marker, γH2AX was also investigated as a marker of efficacy. In both 2D and 3D cultures, previously determined IC_{50} or maximal concentrations as indicated were used (see Table 3.5).

As seen from Figure 3.14 and Figure 3.15 HCT116 and CT26 cells grown in monolayer showed detectable TOPI-DNA covalent complexes following 24 hours of drug treatment with irinotecan or 1-hour drug treatment with SN-38. This was displayed by small areas of punctate staining (green foci) throughout the nucleus. The 0.1% DMSO treated and gemcitabine treated negative controls demonstrated the specificity of the staining for TOPI-DNA covalent complexes. The induction of γH2AX (red foci) was also observed following drug treatment. A further time course experiment was performed with SN-38 in both cell lines in monolayer (see appendix Figure B.4 and Figure B.5). HCT116 and CT26 cells were treated with SN-38 for 30 minutes, 1 hour, 3 hours and 24 hours and were then processed for IF. Staining for α-TopoIcc was detectable after 30 minutes and peaked at 1 hour, before then diminishing. Evidence of DNA damage via the marker γH2AX was also detectable at 30 minutes and for the remainder of the time points.

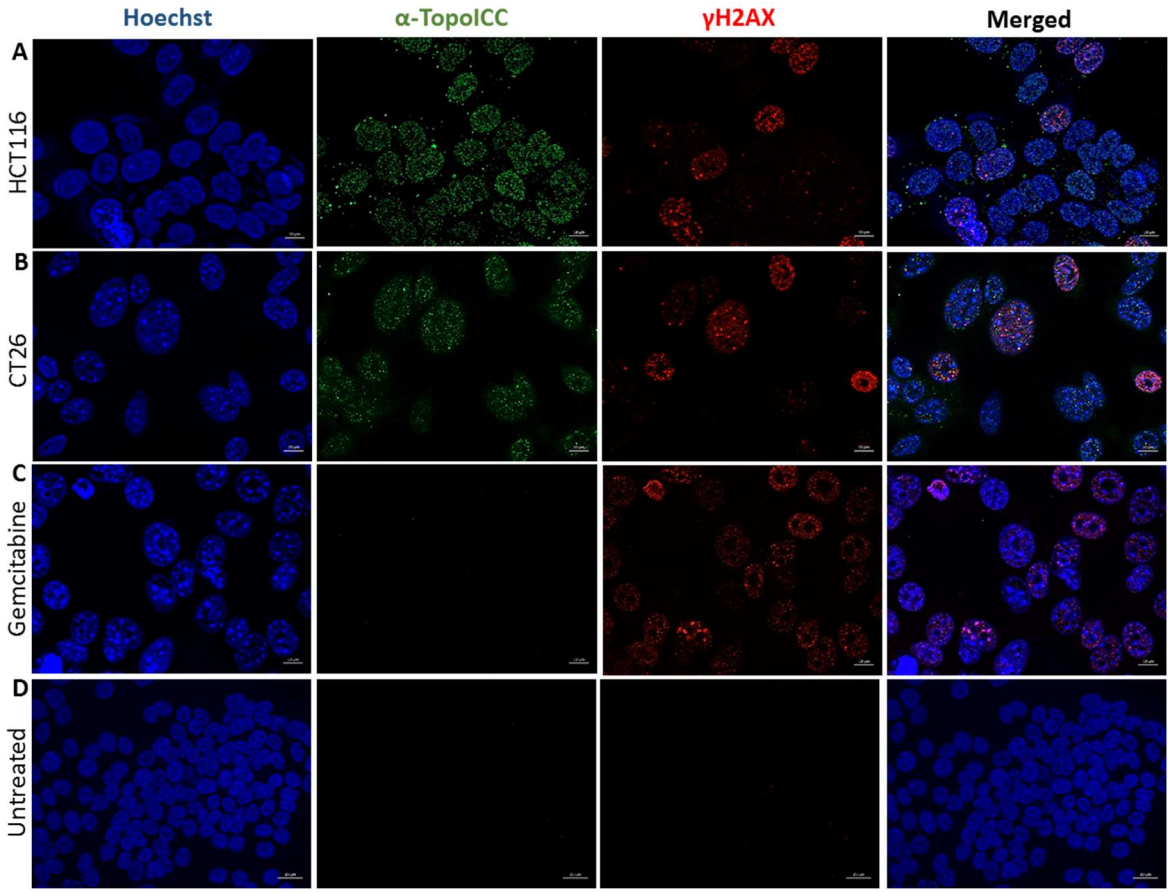

Figure 3.14 Detection of topoisomerase I-DNA covalent complexes by fluorescence microscopy following irinotecan treatment in 2D. After treatment for 24 hours with irinotecan at previously determined IC_{50} concentrations **(A)** HCT116 and **(B)** CT26 cells were fixed, permeabilised, incubated with SDS and stained with α-TopoIcc antibody (green), γH2AX (red) and Hoechst 33258 (blue). **(C)** CT26 cells treated with 100µM gemcitabine were used as a negative control. **(D)** HCT116 cells treated with 0.1% DMSO were used as an additional negative control. Images were taken on a Zeiss inverse Axio observer confocal microscope (Zeiss LSM 710, Carl Zeiss) using an x63 objective with apotome. Scale bars represent 10µm.

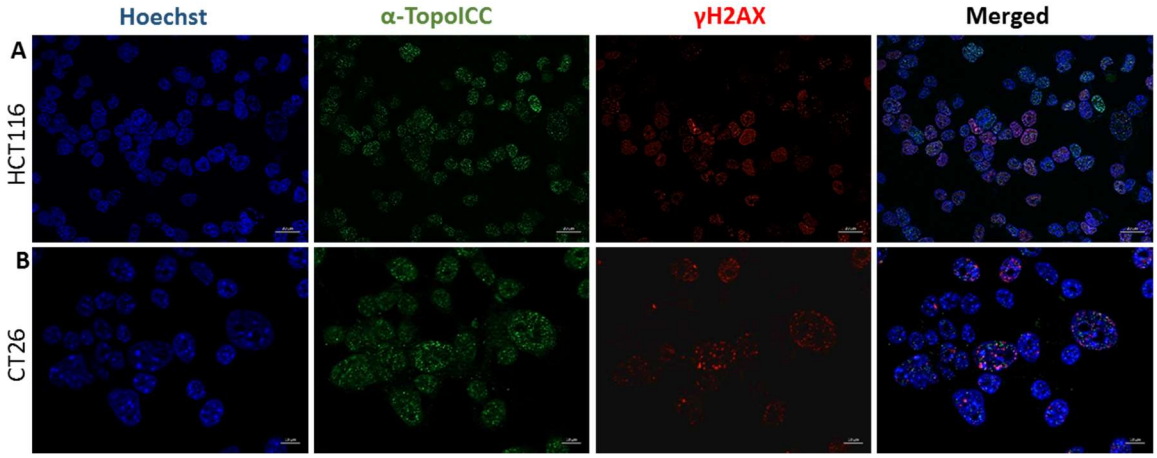

Figure 3.15 Detection of topoisomerase I-DNA covalent complexes by fluorescence microscopy following SN-38 treatment in 2D. After treatment for 1 hour with SN-38 at previously determined IC_{50} concentrations **(A)** HCT116 and **(B)** CT26 cells were fixed, permeabilised, incubated with SDS and stained with α-TopoIcc antibody (green), γH2AX (red) and Hoechst 33258 (blue). Images were taken on a Zeiss inverse Axio observer confocal microscope (Zeiss LSM 710, Carl Zeiss) using an x40 objective with apotome. Scale bars represent 20µm.

Further analysis on spheroid sections or whole mount cleared spheroids, showed TOPI-DNA covalent complexes and induction of DNA damage to be present within spheroids following SN-38 drug treatment and consistent with the histology previously, more prominent levels of γH2AX were present towards the outer surface. Additional IF images of spheroid sections are provided in the appendix (Figure B.6) and γH2AX's proximity to the outer surface was further demonstrated in irinotecan treated spheroids. Even though both TOPI-DNA covalent complexes and γH2AX appeared detectable, observations remained unclear due to the lack of clear punctate staining. In summary, the reduced apoptotic levels in 3D systems further support the hypothesis of poor *in vitro* tumour penetration and increased drug resistance.

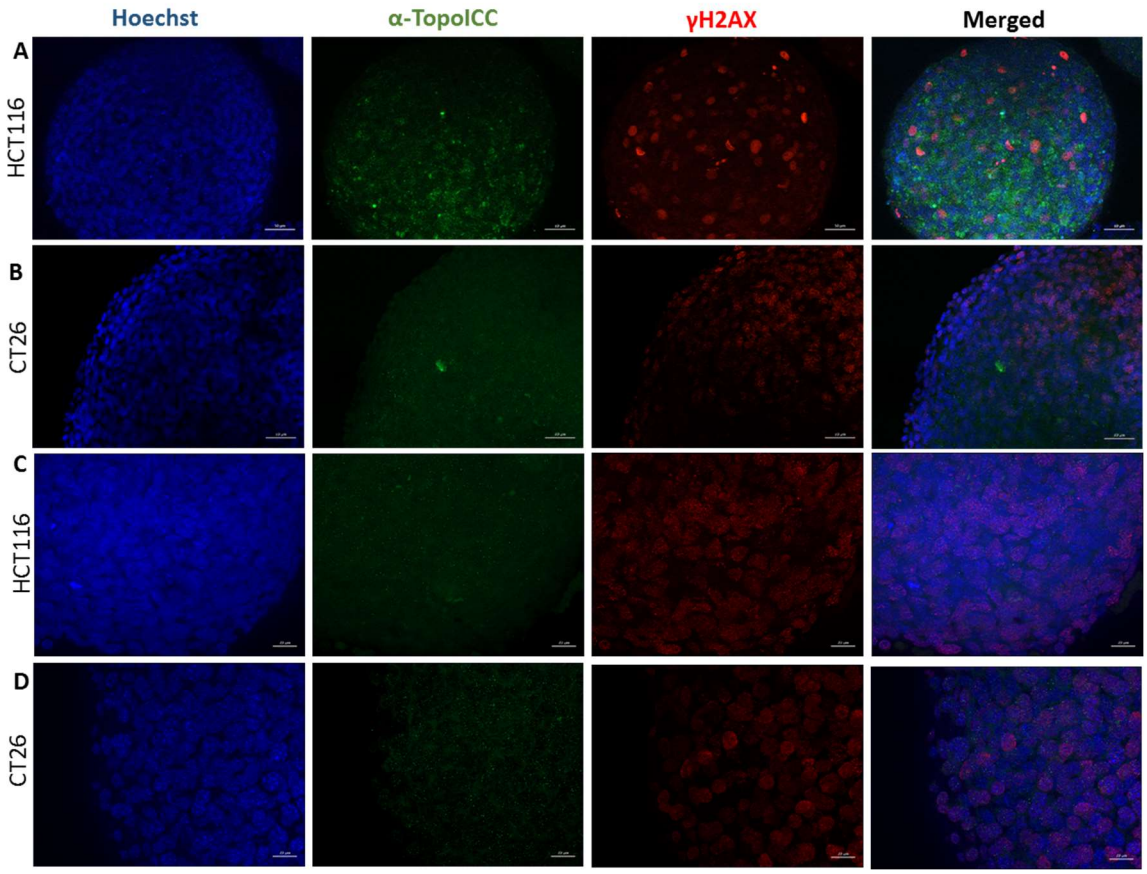

Figure 3.16 Detection of topoisomerase I-DNA covalent complexes by fluorescence microscopy following SN-38 treatment in 3D. After treatment for 24 hours with SN-38 at previously determined IC_{50} concentrations or a nominal concentration of 200nM. HCT116 and CT26 spheroids were fixed, permeabilised, incubated with SDS and stained with α-TopoIcc antibody (green), γH2AX (red) and Hoechst 33258 (blue). **(A)/(B)** are images of 5µm spheroid sections, whilst **(C)/(D)** are images of whole-mount spheroids. Images were taken on a Zeiss inverse Axio observer confocal microscope (Zeiss LSM 710, Carl Zeiss) using an x40/x20 objective with apotome. Scale bars represent 20µm.

3.3.7 Differential Expression of Proteins in Monolayer Cell Cultures

Four CRC cell lines were investigated to gain an understating of the expression of key proteins involved in the uptake, metabolism and clearance of irinotecan and SN-38. Cell lines were either treated with 0.1% DMSO (control) and to demonstrate the influence of irinotecan and SN-38 treatment on the proteins of interest, each of the four CRC cell lines were treated with previously determined IC_{50} concentrations for 72 hours (see Table 3.5). Western blot analysis (Figure 3.17) showed that all cell lines expressed MRP2 (ABCC2), a gene involved in the transport of irinotecan and SN-38, to a similar degree. TOP I expression was greatest in HCT116 cells, with the other three cell lines showing similar levels of expression. Following drug treatment, all cell lines showed a marked decrease in TOP I expression, relative to each respective control. The UGT1A1 protein, which plays a role in the inactivation of SN-38 was found to be absent in HCT116 cells. Its level of expression followed the following trend CT26>LoVo>DLD-1 and drug treatment did not impact UGT1A1 levels. Both CES1/2, which are involved in the hydrolysis of irinotecan, were present in all cell lines to varying levels, with greater heterogeneity present in CES2 expression. Moreover, the expression of γH2AX was enhanced following the administration of either irinotecan or SN-38, conforming to the IF results seen previously in Figure 3.14 and Figure 3.15. Overall 2D immunoblotting data demonstrated that the differential sensitivity of the CRC cell lines to either irinotecan or SN-38 could be attributed to the metabolism and clearance mechanisms i.e. UGT1A1 and CES levels.

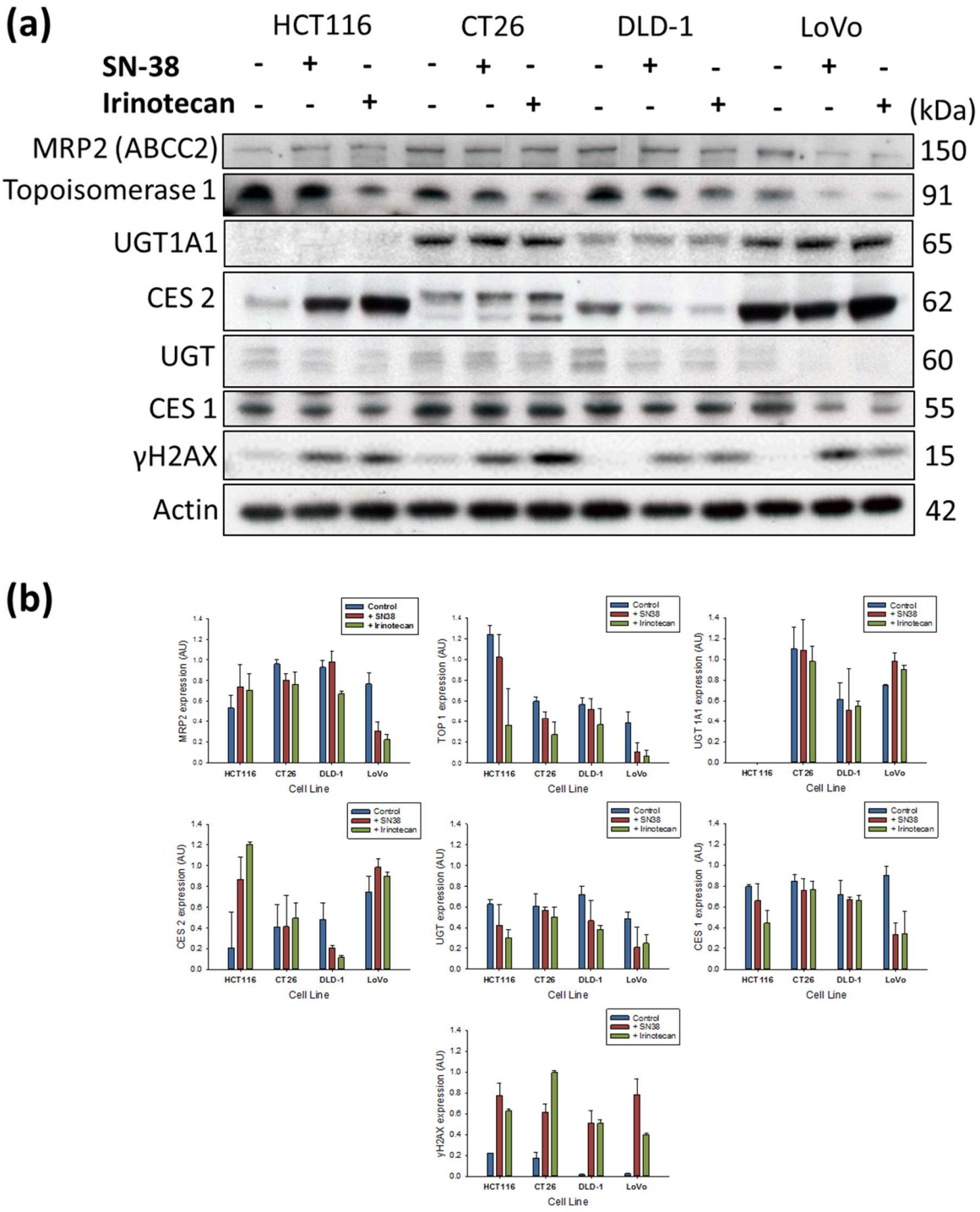

Figure 3.17 Western blotting of proteins in CRC cancer cell lines grown in monolayer (2D). CRC cells grown in 2D were treated with control (0.1% DMSO) or previously determined irinotecan and SN-38 IC_{50} concentrations for 72 hours. **(a)** Lysates were subjected to immunoblot analysis **(b)** The bands from three independent experiments were evaluated densitometrically and the average values ±SD were plotted after being normalised loading control (actin).

3.3.8 Investigating Protein Expression in Monolayer Cultures Compared to Spheroids

Thereafter, the molecular differences in CRC cells cultured in 2D or 3D were examined using Western blot analysis (Figure 3.18a). The amount of protein was quantified by densitometric evaluation (Figure 3.18b) of three biological replicates. MRP2 expression was similar in control 2D and 3D cells, however in both cultures increased expression of MRP2 was seen following drug treatment, with this being more evident in 3D cells. Similar to the data in Figure 3.17, UGT1A1 was not detected in the HCT116 cell line and lower expression was observed in 3D CT26 cells. Additionally, expression of TOP I, CES1/2 and γH2AX was seen to be considerably lower in 3D as compared to 2D cells. Following drug treatment, TOP I expression was suppressed to a greater degree in 2D cells compared to 3D. In summary, this data revealed a profound decrease in protein expression in cancer cells grown as spheroids, as compared to those cultured in the respective conventional 2D system.

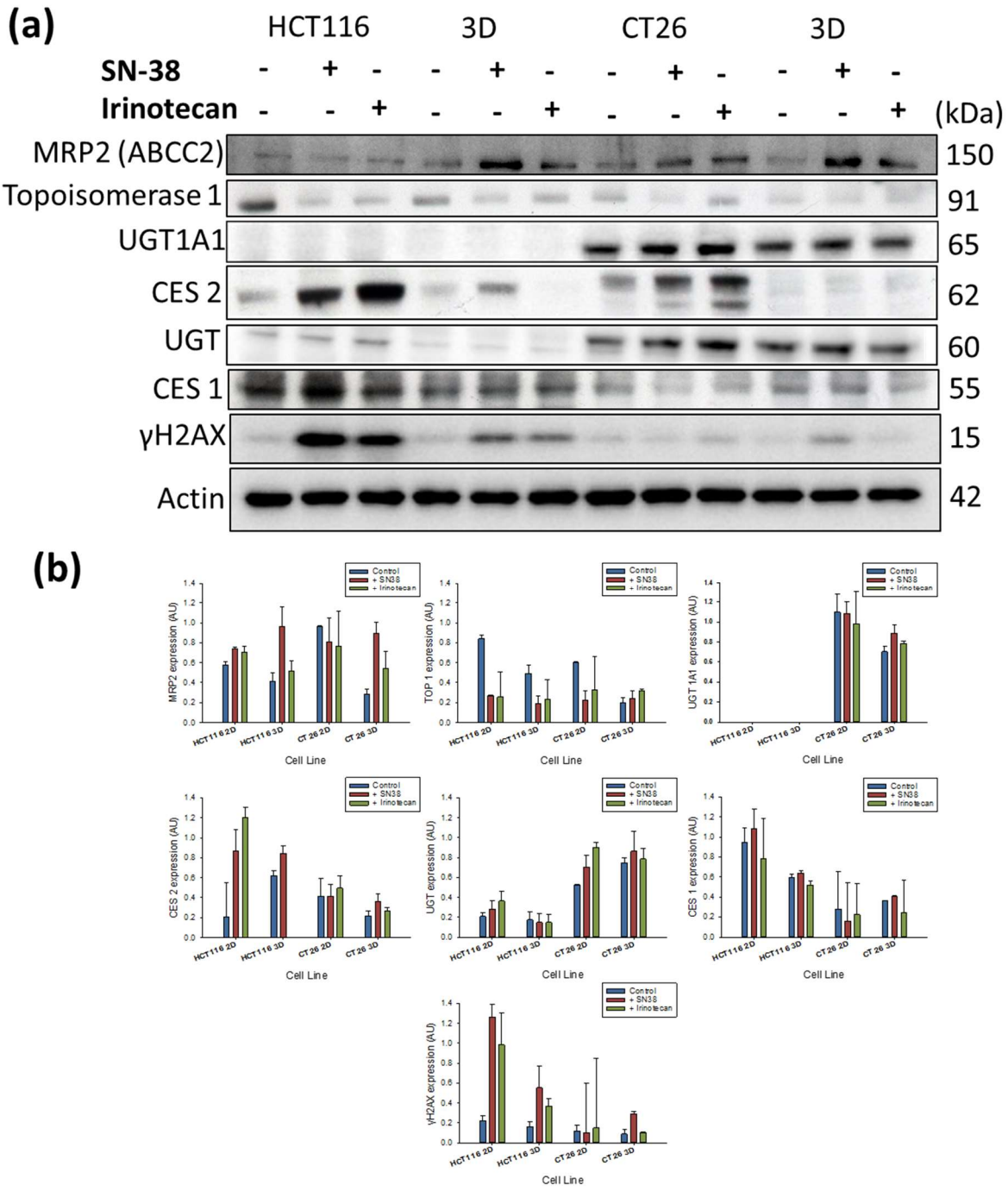

Figure 3.18 Comparison of CRC cells cultured in 2D vs. 3D. CRC cells grown in 2D and 3D were treated with control (0.1% DMSO) or previously determined irinotecan and SN-38 IC_{50} concentrations for 72 hours. Where IC_{50} was not determined a nominal concentration of 100µM for irinotecan or 200nM for SN-38 was used. **(a)** Lysates were subjected to immunoblot analysis **(b)** The bands from three independent experiments were evaluated densitometrically and the average values ±SD were plotted after being normalised loading control (actin).

3.3.9 Differential Protein Expression in Human Tissues and Cell Cultures

Cell lines traditionally have been used to study cancer biology and to build pre-clinical data guiding therapeutic strategies. Further analysis was performed to explore any similarities or differences in protein expression or expression patterns between human tissue and cells cultured in 2D and 3D. This would allow us to explore the relationship between tumour tissues and cancer cell lines and provide us with further knowledge as to how closely 2D or 3D cell cultures model the complex physiological behaviour (protein diversity and correlation) seen clinically in patient samples. Protein was extracted from patient-matched primary tumours, liver metastases and normal colonic mucosa. Histological staining (H&E) was performed, and this has been included in the appendix (Figure B.7). For proteins of interest concerning the uptake, activation and metabolism of irinotecan and SN-38, wide variation in protein expression between patients was observed. Proteins were generally highly expressed in tumour tissues, compared with non-tumour tissues. The data also showed that MRP2 and CES1 are expressed both in the tumour tissues and cancer cell lines. The CT26 cell line demonstrated similar levels of UGT1A1 expression, to that found within patient samples. However, TOP I levels were significantly higher in cells lines as compared to the tissue, wherein only two of the nine patient samples demonstrated any detectable levels of expression.

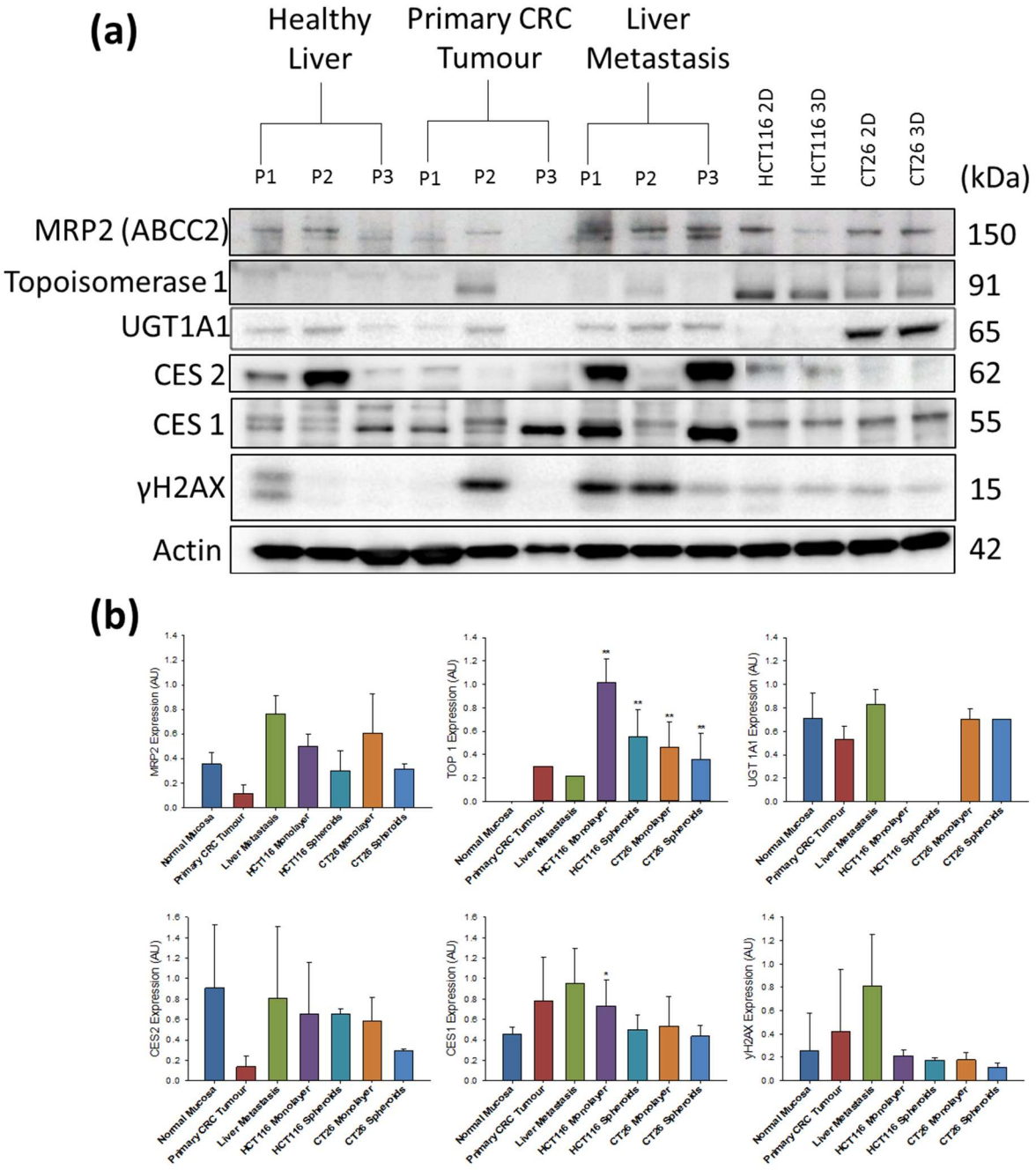

Figure 3.19 Comparison of human tissue vs. CRC cells cultured *in vitro* **(a)** Western blot analysis and quantification of proteins implicated in the uptake, metabolism and mechanism of irinotecan and SN-38. Patient tissue was provided by the LBIH biobank. Cells were cultured *in vitro* and processed without any treatment **(b)** The blots were quantified using densitometry and the average values of the independent experiments were plotted after normalization with actin. Data are shown as the average ± SD of three independent experiments. Statistical analysis was performed using a two-way ANOVA followed by Holm-Šídák multiple comparison post-hoc test (P-values are indicated as * $P < 0.05$ and ** $P < 0.01$ vs. normal mucosa).

3.4 Discussion

The overall survival rate of individuals with CRC undergoing systemic therapy has improved over the past 30 years. However, the five-year survival rate for metastatic CRC is still low at around 14% (Lichtenstern, Ngu, Shalapour, & Karin, 2020). Despite some success in targeted therapy, the attrition rates of anticancer drugs in clinical trials remains high. Evidently, there is an urgent need for more innovative pre-clinical *in vitro* models, to thoroughly test promising compounds before proceeding into clinical trials. Spheroid (3D) models could offer superior predictive power by more realistically recapitulating the response of tumours to anticancer compounds *in vitro*. This chapter focussed on the comparison of 2D monolayers with 3D spheroids. Spheroids were initially characterised and features such as morphology, protein expression and chemosensitivity were explored. In particular, the response of CRC cancer cell lines to irinotecan and SN-38 treatment was investigated.

Spheroid diameter was optimised for uniformity and to reduce variability in the subsequent assays. Spheroids demonstrated a phase of exponential growth followed by a decline in growth rate (Figure 3.3a and Figure 3.4a), which associated with the accumulation of non-proliferating (quiescent) and necrotic cells. A similar growth pattern is evident in tumours as, during the initial growth period, the volume of a tumour increases exponentially in the avascular growth phase, thereafter cellular growth is maintained in a dormant phase (Ward & King, 1997). The morphology of both the HCT116 and CT26 spheroids according to the stage of development was consistent with previous reports (Riedl et al., 2017; Valcarcel et al., 2008; Zoetemelk et al., 2019). Monolayer cell cultures displayed a flattened cellular morphology (see appendix Figure B.1) and cells here have a reduced cell-cell and cell-ECM interaction (Edmondson et al., 2014). These cultures are known to exhibit exponential cell proliferation, which is ultimately limited by surface availability.

Histological H&E staining showed that once spheroids grew to 350-400µm in diameter (day 5 in culture), they were comprised of a highly compact, dense cellular network. Furthermore, H&E staining showed intense haematoxylin staining at the spheroid edge, suggesting a larger volume of nucleic

acids which is indicative of an outer proliferating rim (Mehta et al., 2012; Sutherland, 1988; Zanoni et al., 2016). Alcian blue staining in HCT116 spheroids was seen to a lower degree to what has been reported in the literature (Tchoryk et al., 2019). This could have been due to differences in culture conditions. Nevertheless, the detection of glycosaminoglycans within HCT116 spheroids signifies the presence of an ECM and suggests that spheroids offer a penetration barrier, as seen *in vivo*. Negligible levels of cleaved-caspase-3, further displayed that spheroids do not undergo apoptosis. To investigate proliferation, staining of Ki-67 staining was performed (Figure 3.5b and Figure 3.6b). Ki-67 is a nuclear protein involved in cell proliferation, it is present throughout the cell cycle (G_1, S, G_2, and mitosis) but is absent during cellular quiescence (G_0) (Gerdes et al., 1984). With increasing spheroid size, quiescent cells accumulated in the centre, whilst proliferation was still ongoing at the outer rim, confirmed by the presence of Ki-67 positively stained cells (Figure 3.5b and Figure 3.6b). The higher rate of proliferation in the spheroid periphery is explained by their easier access to oxygen and nutrients (Tredan, Galmarini, Patel, & Tannock, 2007). This closely reflects the *in vivo* situation of actively proliferating tumour cells, which are in close proximity to the capillaries (Friedrich, Ebner, & Kunz-Schughart, 2007). In contrast, cells within spheroids remain in a senescent or necrotic state due to the lack of oxygen (hypoxia) and nutrients (Minchinton & Tannock, 2006; Tredan et al., 2007). This also resembles tumours *in vivo*, as quiescent cells persist in regions distant from blood vessels, where glucose and oxygen are limited (Kyle, Baker, & Minchinton, 2012). Based on these observations, HCT116 and CT26 cells formed valid spheroids that displayed various *in vivo* like properties and they were subsequently investigated as pre-clinical test objects.

Both irinotecan and SN-38 displayed enhanced efficacy in 2D cultures over their 3D counterpart's i.e. elevated chemoresistance as seen by the higher IC_{50} values (see Table 3.5). The calculated IC_{50} values were consistent with literature findings (Friedrich et al., 2009; Kinoshita et al., 2018; Zoetemelk et al., 2019). These results supported the notion that cytotoxic compounds, which target DNA replication and repair machinery, have limited activity in 3D models and that spheroid models are less sensitive to such therapy (Karlsson, Fryknas, Larsson, & Nygren, 2012; Nunes, Barros, Costa, Moreira, & Correia,

2019; Skardal, Devarasetty, Rodman, Atala, & Soker, 2015). It has been shown previously that relative sensitivities, correlates with the mechanism of action (Hartung, 2009; Kunz-Schughart et al., 2004; Vinci et al., 2012). For example, it has been reported that small-molecule kinase inhibitors are more sensitive in 3D cultures, while cell cycle inhibitors are more sensitive in 2D cultures. This is hypothesised to be a result of differences in the cultures, with respect to signalling pathways and genomic expression over time. Another suggestion for this differing sensitivity is that as 2D cells spend increased time in active cell cycle and DNA synthesis compared to 3D cultures (proliferate much slower), this provides a greater opportunity for such compounds to act (Gong et al., 2015; Luca et al., 2013). Also, the growth media in 2D cultures is consistently distributed throughout all cells present, whereas a gradient-like distribution is present for 3D cultures, possibly leading to the unequal distribution of chemotherapeutics and lower activity (Kapalczynska et al., 2018). Other factors contributing to the reduced drug sensitivity in our study, could be due to the increased proportion of quiescent cells (i.e. spheroids have a lower percentage of actively dividing cells as compared to monolayers), hypoxia, ECM (intercellular interactions with high interstitial fluid pressure provide a physical barrier to limit drug diffusion) or altered gene expression including overexpression of efflux pumps, all hallmarks of *in vivo* tumours.

IF studies from drug-treated spheroids confirmed that irinotecan and SN-38 rapidly stabilise TOPI-DNA covalent complexes (Figure 3.16). These TOPI-DNA covalent complexes act like other bulky DNA adducts, stalling replication forks, leading to replication fork collapse with accompanying DNA double-strand breaks. Histological and IF results indicated that drug-induced apoptosis was primarily concentrated in cells located on the outer surface area of the spheroids. The simplest explanation is that cells on the inside of the spheroid are protected from drug penetration by the cells on the outside of the spheroid (Perche & Torchilin, 2012). However, the spheroid organisation (cell layers) is likely responsible for the impaired therapeutic efficacy of anticancer drugs. For instance, within the inner layer of the spheroid, i.e. the hypoxic region, cells proliferate much slower and these regions were mainly constituted of senescent and necrotic cells. Hence drugs that are most effective in targeting

rapidly dividing cells, would be expected to have an inferior therapeutic effect within the interior regions of the spheroid. Both irinotecan and SN-38 have mechanisms of action (formation of cleavable complexes during S-phase) that preferentially targets these actively dividing cells (Strumberg et al., 2000; Ueno, Nonaka, Yamazaki, Deguchi, & Murai, 2002). Alternatively, as cells in hypoxia demonstrate resistance to apoptotic cell death, drugs that promote cell death through the formation of reactive oxygen species (e.g. doxorubicin and cisplatin) also have a lower therapeutic efficacy (Minchinton & Tannock, 2006; Tredan et al., 2007). These concepts could explain why HCT116 cells were much more sensitive than CT26 to both drugs i.e. they had a greater number of proliferating cells. Furthermore, the results also imply that cells in the central area may obtain a form of apoptotic resistance in 3D spheroids (see Figure 3.12 and Figure 3.13). It was only after repeated drug exposure studies, that spheroids displayed similar sensitivity to 2D cultures (see Table 3.6). However, after certain repeat exposures, spheroids displayed a limit of sensitivity. This is likely a result of dysregulation of apoptotic pathways, restricted drug transport and mechanisms of drug resistance associated with the spheroid microenvironment. Temporal processes such as drug metabolism and transport are known to be important factors implicated in resistance to chemotherapy and achieving optimal clinical therapy.

The differential responses to irinotecan and SN-38 may additionally be explained by several mechanisms. Differential protein expression was observed in monolayer cell lines (Figure 3.17). For instance, the expression of UGT1A1 was greatest in the CT26 cell line and completely absent in the HCT116 cell line, which has previously been reported (Belanger, Tojcic, Harvey, & Guillemette, 2010; Gagnon, Bernard, Villeneuve, Tetu, & Guillemette, 2006). UGT1A1 is well known to be responsible for the inactivation of SN-38 (Gagne et al., 2002). Differences in the levels of UGT1A1 has the potential to modify the glucuronidation capacity at the target cell level and, hence, the biological effect of the drug i.e. lower rates of SN-38 glucuronidation would retain higher levels of the compound. This would support that UGT1A1 is associated with drug resistance and higher levels of UGT activity and expression was identified as a characteristic associated with a resistance phenotype to SN-38 in CRC

cells (Cummings et al., 2004). Similarly, differences in the expression of TOP I (formation of cleavable complexes), CES1 and CES2 (conversion of the prodrug to the active drug) could have contributed to the differential sensitivities of the cell lines. In addition, drug treatment elevated CES2 expression in all cell lines, apart from DLD-1, to differing degrees. These results are consistent with reports of CES2 expression being regulated by the tumour suppressor gene *p53,* which is known to be activated by both drugs (Takeba et al., 2007; D. Xiao et al., 2013). Further work to investigate the role of CES1/CES2 in the differential sensitivity, could incorporate knockdown and knockout experiments. Correspondingly, the immunoblotting data highlights the importance of employing a range of CRC subtypes for interpreting drug responses with respect to general biology, association with prognosis, changes of expression patterns of specific genes and target-proteins (Ahmed et al., 2013) (detailed differences between cell lines employed are outlined in the appendix Table B.1). Such information is of great value to understand in detail the molecular mechanisms by which therapeutic candidates act. However, a number of these biological differences, that contribute to how the cells are exposed and thus react to therapeutic agents, are more accurately imitated in 3D culture systems. In the present analysis, 3D cultures displayed a higher chemoresistance to anticancer drugs in comparison to cells grown in 2D. As a whole, protein expression was found to be lower in 3D, in comparison to 2D cultures. However, increased expression of MRP2 was observed following drug treatment in the spheroids, thereby suggesting enhanced drug efflux led to a lower intracellular accumulation of drug (Candeil et al., 2004; Gaedtke, Thoenes, Culmsee, Mayer, & Wagner, 2007). This corresponded to the decreased levels of DNA damage present and the restricted drug uptake and penetration detailed earlier. This is consistent with spheroid permeability data obtained in previous studies (Galateanu et al., 2016; Sensi et al., 2018; X. Wang et al., 2013).

Besides, no clear relevance between the culture systems (2D and 3D) and patient tissue was seen. Large variation was present, which could have been caused by the heterogenic nature of the patient samples. Furthermore, a tumour can consist of different clones, which may have different protein composition and show varying degrees of central necrosis (Greaves & Maley, 2012). Some of the

differences observed between cancer tissues and cell lines may reflect cellular changes resulting from *in vitro* culture, inter-individual variation, or variation in treatment regimens (see γH2AX levels in Figure 3.19) the patients may have undertaken. Thus, conclusions from *in vitro* modelling systems cannot always be transferred to the clinical setting. Further investigations on differentially expressed proteins and their mechanisms, may be of scientific and clinical importance. Additional studies could be done to gather a deeper understanding of differences at the protein level between 2D and 3D cultures and could involve quantitative proteomic analysis. Analysis of spheroids once they have become more sensitive i.e. after repeated exposures would also help to clarify important distinctions between the cultures, in regards to understanding the response to anticancer drugs. To better simulate the microenvironment of tumours *in vitro* (closely resemble cellular heterogeneity in tumour tissues) and in turn make the spheroids more physiologically relevant, heterotypic spheroids or spheroid co-cultures (aggregates of cancer cells, endothelial cells and immune cells – macrophages/tissue-specific fibroblasts) could be employed (Costa, Gaspar, Coutinho, & Correia, 2014; Courau et al., 2019; S. A. Kim, Lee, & Kuh, 2015). Moreover, embedding 3D tumour models into a microfluidic device that enables controlled media flow and mimics drugs pharmacokinetics could further improve the predictability of the model to the *in vivo* situation. Such models would allow access to monitoring drug penetration and measure changes in pharmacodynamic biomarkers in real-time. Looking ahead, a combination of techniques for the generation of patient-derived tumour spheroids appears to be a promising solution to bridge the gap between the results from preclinical models and clinical trials (Arnadottir et al., 2018; Bregenzer et al., 2019; Kondo et al., 2019; Pyo, Hong, Lee, & Cho, 2020; Shuford et al., 2019; van der Waals et al., 2019). Organotypic multicellular spheroids are required for accurate reproduction of the tumour microenvironment. Tumour cells in these spheroids are surrounded by non-tumour cells and stromal components that are commonly found in the tumour microenvironment. There are several methods for obtaining organotypic tumour spheroids, including enzymatic dissociation of tissues to isolate spheroids with cellular heterogeneity, similar to the primary tumour (Kondo et al., 2011). In many cases, these cultures are generated using

mechanical dissociation of patient-derived tumour tissues. As a result, this model is capable of proliferation and can retain many of the histological features within the original tissues. Vlachogiannis *et al.* established a biobank of patient-derived organoids from metastatic colorectal and gastroesophageal cancer patients (Vlachogiannis et al., 2018). The authors demonstrated that phenotypic and molecular profiling of established organoids closely matched the original tumour. They compared *ex vivo* drug responses of the organoids with xenograft mouse models, as well as with clinical responses in patients and demonstrated that their methodology can predict clinical responses with 100% sensitivity and 93% specificity (Vlachogiannis et al., 2018). *In vitro* 2D and 3D cell culture models are most promising to be adopted for testing of patient-derived cells in clinics, due to their compatibility with high throughput, possibility to be performed within 2–3 days, and requirement of relatively low cell numbers. Performing such *in vitro* sensitivity tests as a routine in clinical practice will open a new era of precision medicine in oncology and will help to navigate the decision making toward successful therapy for each individual patient.

In summary, the data implies that the manner in which cells are cultured (i.e. 2D or 3D) can substantially impact the effect of a drug. Also, this research highlights that it is a combination of the specific drug and the cellular environment that influences the cellular response. Reliable and robust screening systems are highly desired for the development and selection of antitumour drugs and functional delivery systems. 3D culture presents an attractive solution to the limitations of 2D culture. However, they have their limitations and challenges. As a result of the requirement for a large number of spheroids within a test sample, molecular biological assays including RT-PCR and Western blotting are costly and difficult to perform. Other techniques such as histology require tedious handling and protocols are generally low throughput. This often makes spheroid-based assays difficult to scale up. However, as spheroids can establish authentic pathophysiological features of interest, they are ideal as a supplement to monolayer-based assays for advanced drug testing and improved estimation of *in vivo* antitumour efficacy. In particular, spheroids would be valuable for the evaluation of

nanomedicine, as they have the potential to establish the penetration barriers seen *in vivo*, thereby allowing a more accurate study of the uptake, penetration, distribution and subsequent effect of differing drug delivery systems.

3.5 Conclusion

The results in this chapter have demonstrated that spheroid models, of both HCT116 and CT26 cells, represent a suitable model to form part of an *in vitro* cytotoxicity screening system. The formation of highly reproducible, uniform spheroids was presented, with simple standardised protocols utilised for cell viability assessment. These spheroids had appropriate growth kinetics, histological features and biological characteristics. The spheroids more closely mimicked the arrangement of cancer cells and the environment to which they are exposed *in vivo*. These features subsequently affect the cellular protein expression and the penetration, binding and bioactivity of therapeutic drugs. Hence, due to their intrinsic characteristics, spheroids represent a promising approach for the pre-clinical evaluation of newly developed anticancer therapies, in particular nanotherapeutics. The following chapter will detail the incorporation of spheroids as part of a tiered *in vitro* screening approach.

Chapter 4: Nanomedicines for Colorectal Cancer Therapy: *In Vitro* and *In Vivo* Assessment of SN-38 Encapsulated Nanoparticles

Abstract

The therapeutic effect and clinical utility of irinotecan has been extremely restricted by several factors such as the low conversion rate to its active metabolite SN-38, high inter-patient variability, and dose-limiting toxicity. SN-38 displays 100-1000-fold more potent cytotoxicity *in vitro* compared to irinotecan, but the administration of SN-38 is unachievable due to its poor solubility and instability. The present chapter successfully synthesised polymer-based SN-38 encapsulated nanoparticles. 41 different water-soluble formulations were iteratively screened initially to assess drug release. Thereafter, 10 select candidates were assessed for cytotoxicity and macrophage uptake, with 2 formulations being chosen for pharmacokinetic analysis *in vivo*. Drug release was measured in PBS at pH 7.4 for 48 hours. No initial burst release was observed in the majority of the polymer nanomaterials. Moreover, CA formulations released SN-38 in a much slower and sustained manner in comparison to SB formulations. All nanoparticles displayed potent *in vitro* antitumour activity, similar to free SN-38, against colorectal cancer cell lines in both monolayer and spheroids. Macrophage uptake was also investigated, with only 8 of the 10 polymer nanomaterial's displaying a lower cellular accumulation ratio ($p \leq 0.05$ for 5 of these formulations). However, in a mouse model, the pharmacokinetic analysis revealed no benefit of the nanoparticles (SB1 or CA16) in terms of plasma exposure compared to irinotecan. Further preclinical testing of the material in regard to its biocompatibility, immunotoxicity, and a thorough analysis of its uptake by organs of the mononuclear phagocyte system is required. In summary, the data in this chapter demonstrated that the designed nanoparticles showed suitable characteristics *in vitro,* but these did not translate *in vivo* into the sustained and prolonged exposure of SN-38.

4.1 Introduction

Chemotherapy is an important treatment option for patients, however, chemotherapeutic drugs such as irinotecan have various drawbacks such as nonspecific uptake by healthy tissue, inadequate circulation times, poor exposure to/suboptimal accumulation within tumour sites and a narrow therapeutic window. The efficient delivery of chemotherapeutic drugs to tumours remains an obstacle in the treatment of cancer and the continual development of drug delivery technologies, is fundamental to future advances. Nanoparticles (NPs) offer a promising approach in countering such limitations, because of their more favourable bio-distribution, improved biocompatibility, enhanced targeting, proficiency in protecting drug/cargo from hydrolytic or enzymatic inactivation and inherent ability to overcome multiple biological barriers e.g. avoidance of the mononuclear phagocytic system (MPS) (Arshad et al., 2020). Due to their submicron size range (10–1000nm), NPs can evade renal clearance (<20nm) and uptake by the liver and spleen (>150nm). Also, NPs can preferentially accumulate within tumours, via the enhanced permeation and retention (EPR) effect (Kobayashi, Watanabe, & Choyke, 2013; Maeda et al., 2000). The EPR effect is a consequence of the disorganised nature of the tumour vasculature, which results in increased permeability of polymer therapeutics and drug retention at the tumour site. Hence, NP-mediated delivery has the potential for improving the efficacy and safety of different classes of anticancer agents.

Because of its potency, SN-38 represents an attractive molecule for anticancer drug development. Its hydrophobic nature prevents its administration clinically (poor water solubility 11–38μg/mL and high partition coefficient LogP: 2.65). Moreover, the instability of SN-38 in physiological circulation (pH 7.4) is an obstacle in its development, as the open carboxylate form of SN-38 has no therapeutic effect resulting in low anti-tumour activity. To overcome these limitations, various nanoscale pharmaceutical delivery systems are currently being developed and investigated. These include polymeric conjugates, dendrimers, liposomes, micelles, and polymer NPs (Carie et al., 2011; England et al., 2017; Koizumi et al., 2006; Roger, Lagarce, & Benoit, 2011; J. A. Zhang et al., 2004). Such delivery systems can improve solubility, efficacy, and circulation time, whilst reducing toxicity. Researchers have addressed the poor

solubility of SN-38 by covalently attaching SN-38 to a polymer or peptide i.e. a prodrug approach that is dependent upon enzymatic/chemical cleavage in order to release the active drug (Koizumi et al., 2006; Meyer-Losic et al., 2008; Sapra et al., 2008). A formulation such as NK012, as well as a pegylated SN-38 formulation (EZN-2208), are currently in clinical trials (Hamaguchi et al., 2010; Sapra et al., 2009). Similarly, a liposomal formulation encapsulating SN-38 was part of a Phase II trial for the treatment of metastatic CRC (NCT00311610). Various other carriers have been or are being investigated, as detailed in Table 4.1 below.

Table 4.1 SN-38 based nanoformulations currently in development

Product Name (Owner Company)	Phases	Country/Region	Route (Dosage form)	Admin Regime	Drug Delivery Category	NME/Generic/OTC
IT-141 (Intezyne, Inc.)	Phase 1	-	Infusion IV (Injection Lyophilized Powder For Solution)	Once for 2-weeks	NP, Micelle	NME Not Marketed
PEN-866 (Madrigal Pharmaceuticals, Inc.)	Phase 2 Phase 1 Preclinical Preclinical Discontinued	USA	Infusion IV (Injection Lyophilized Powder For Solution)	-	Conjugates, Small Molecule NP Polymer Receptor/Carrier	NME Not Marketed
SP1063C (Supratek Pharma Inc.)	Preclinical	-	Infusion IV	-	Cyclodextrins/Solubilizers	New Formulation
TRX-920 (TaiRx, Inc.)	Preclinical	USA	Oral	-	Other Oral Delivery	New Formulation
IMMU-130 (Immunomedics Inc.)	Phase 2 Preclinical	-	Injectable IV	2-16 mg/kg once for 2-weeks	Conjugates, Antibody-ADC Receptor/Carrier	NME Not Marketed
BEL-0222 (Belrose Pharma Inc.)	Phase 2 Phase 1 Phase 2 Discontinued Phase 1 Discontinued Preclinical Discontinued	China USA	Infusion IV (Injection Lyophilized Powder For Solution)	9-16.5 mg/m^2 once a week	Injectable Depot, Other Conjugates, PEG Polymer	NME Not Marketed
IMMU-132 (Immunomedics Inc.)	Registration Phase 3 Phase 2 Preclinical Discontinued	Europe USA	Infusion IV	8-18 mg/kg once a week	Conjugates, Antibody-ADC Receptor/Carrier	NME Not Marketed
DFP-13318 (ProLynx LLC)	Phase 1 Preclinical Phase 1 Discontinued	Asia USA	Infusion IV	Once for 2-4 weeks	Conjugates, PEG Polymer	NME Not Marketed
IMMU-132 + Imfinzi Co-Therapy (Immunomedics Inc.)	Phase 2	-	Injection	-	Injection, Other	NME Not Marketed
ATT-11T (Aposense Ltd.)	Preclinical	USA	Injectable IV (Injection Emulsion)	-	Conjugates, Small Molecule	NME Not Marketed
hPAM4/SN-38 Conjugate (Immunomedics Inc.)	Preclinical	-	Injection	-	Conjugates, Antibody-ADC Receptor/Carrier	NME Not Marketed

NK012 (Nippon Kayaku Co., Ltd.)	Phase 2 Phase 1 Preclinical Phase 1 Discontinued Preclinical Discontinued	USA	Infusion IV (Injection Lyophilized Powder For Solution)	9-28 mg/m^2 once for 21-28 days	Conjugates, PEG Polymer NP, Micelle	NME Not Marketed
Epratuzumab/SN-38/Veltuzumab Conjugate (Immunomedics Inc.)	Preclinical	-	Injection	-	Injection, Other	NME Not Marketed New Combination
ZAPS/SN-38 (Molecular Targeting Technologies, Inc.)	Preclinical Preclinical Discontinued	-	Injection	-	Injection, Other	NME Not Marketed

IV – intravenous, NME - new molecular entity, OTC - over-the-counter
(All data was exported from the PharmaCircle database)

A significant clinical advantage could be gained through the direct administration of the active metabolite, SN-38, using a drug delivery technology that is not reliant upon hepatic activation and metabolism. Also, the possibility to achieve greater site-specificity, whilst simultaneously protecting the drug within its active form would improve the therapeutic index. These features would allow for higher plasma and tissue levels of SN-38 with a consequential increase in anti-tumoral efficacy, whilst limiting toxicities and inter-patient variability. Sterically stabilised polymeric NPs can be generated via co-nanoprecipitation, which is a process that describes the precipitation of a polymer with a second polymer that can act as a stabilising species. This subsequently presents an opportunity for the potential encapsulation and delivery of therapeutic agents. Extensively branched, high molecular weight copolymers differing in composition were combined. A large library of polymeric materials was generated, in which the chemical compositions were varied through the incorporation of different monomer, copolymer and initiator chemistries. Based on this rationale, an encapsulated formulation of SN-38 was generated, using a hyperbranched polydendron NP system (Hatton, Chambon, McDonald, Owen, & Rannard, 2014). This resulted in the aqueous solubility of SN-38 without modification of the drug. These polymer NPs were iteratively screened *in vitro* to select the best candidates, before *in vivo* evaluation. For those materials termed CA formulations, the preparation involved the simultaneous nanoprecipitation of highly branched hydrophobic vinyl copolymers with amphiphilic PEG-based AB block copolymers and SN-38. Those materials termed SB formulations involved the preparation of polymers through the use of novel PEG-based caprolactone monomers. Factors taken into consideration included drug release, as it was crucial that the NPs still contain the drug once they reach the tumour to have any therapeutic effect. Thereafter, the cytotoxic activity of the NPs was measured to assess the ability of drug-containing NPs to kill cancer cells once they arrive at the tumour site. Macrophage uptake was assessed as they are a key clearance mechanism for NPs and evading uptake would increase the time NPs spend in systemic circulation. The plasma pharmacokinetic profile of the best candidates, compared to that of irinotecan and free SN-38, was examined *in vivo*, using BALB/c mice.

It was hypothesised that the encapsulation of SN-38 within these NPs would slow the release rate of the drug by augmenting drug retention. It was anticipated that this release behaviour would maintain SN-38's cytotoxic effects in tumour cells, whilst being minimally cleared via the MPS. It was further hypothesised that these characteristics of the NPs, would prolong plasma exposure of SN-38 *in vivo*.

4.2 Materials and Methods

4.2.1 Materials

Irinotecan and SN-38 were purchased from Hangzhou J&H chemical company (J&H Chemical, Shanghai, China). Drug-free mouse plasma was purchased from BioIVT (West Sussex, UK). All other reagents and consumables were purchased from Sigma Aldrich (Dorset, UK) or Thermo Fisher Scientific (Loughborough, UK) unless otherwise stated, and were of LC-MS grade or the highest analytical grade commercially available.

4.2.2 Animals

All animal experiments were performed in accordance with criteria outlined in a Home Office UK approved project licence (PPL 70/8563/OWEN) granted under the Animals (Scientific Procedures) Act 1986 and approved by the Animal Ethics Committee at the University of Liverpool. Male BALB/c mice weighing between 20-25g were purchased from Charles River Laboratories (Margate, UK) and housed in a licenced specified pathogen-free establishment. Mice were given free access to food and water and housed at a temperature between 19°C and 23°C under a 12-hour light-dark cycle.

4.2.3 SN-38 Nanoparticles Preparation and Characterisation

NPs were synthesised in the university's chemistry department (Liverpool, UK). Briefly, following co-nanoprecipitation of branched PEG polymers (NP formation and solvent evaporation), rapid formation of sterically stabilised SN-38 NPs in aqueous media was possible. All polymer co-nanoprecipitations were conducted from tetrahydrofuran (THF) into stirred water. SN-38 (1mg/ml in THF) was incorporated within the initial THF solution to target drug loadings as shown in Table 4.2 and Table 4.3. The mixtures were left to stir for 24 hours at ambient temperature to allow for the complete evaporation of THF. Several NP formulations were synthesised, that differed in terms of percentage SN-38 loading and physical polymer properties i.e. monomer composition and polymer backbones.

Dynamic light scattering (DLS) measurements (for a hydrodynamic diameter) and zeta potentials were performed using a Malvern Zetasizer Nano ZS instrument with a wavelength of 630nm. Measurements

were performed at 25°C at a NP concentration of 1 mg/ml. Dispersions were measured without additional filtration or centrifugation, in a polystyrene disposable fluorometric cuvette (size measurements) or a disposable capillary zeta flow cell (zeta measurements). Size measurements were obtained as an average of 3 individual measurements and were rounded to the nearest 5 nm. The DLS analyses revealed monomodal intensity-derived particle size distributions with an average hydrodynamic diameter of <200nm for all nanomaterials.

Table 4.2 Nanoparticle formulations differing in the monomer composition

Nanoparticle Formulation	Monomer Composition	SN-38 Loading (%)
SB1	PEG_{5K}-PCL_{40}-$BOD_{0.7}$	10
SB2	PEG_{5K}-PCL_{40}-$BOD_{0.7}$	50
SB3	PEG_{5K}-PCL_{40}-$BOD_{0.7}$	75
SB4	PEG_{5K}-$PMOP_{40}$-$BOD_{0.7}$ (12 week old)	10
SB5	PEG_{5K}-$PMOP_{40}$-$BOD_{0.7}$	10
SB6	PEG_{5K}-$PPOP_{40}$-$BOD_{0.7}$	10
SB7	PEG_{5K}-$PMOP_{40}$-$BOD_{0.7}$	10
SB8	PEG_{5K}-$PMOP_{40}$-$BOD_{0.7}$	50
SB9	PEG_{5K}-$PMOP_{40}$-$BOD_{0.7}$	75
SB10	PEG_{5K}-$PPOP_{40}$-$BOD_{0.7}$	10
SB11	PEG_{5K}-$PPOP_{40}$-$BOD_{0.7}$	50
SB12	PEG_{5K}-$PPOP_{40}$-$BOD_{0.7}$	75
SB13	PEG_{5K}-$PPHLOP_{40}$-$BOD_{0.7}$	10
SB14	PEG_{5K}-$PPHLOP_{40}$-$BOD_{0.7}$	50
SB15	PEG_{5K}-$PPHLOP_{40}$-$BOD_{0.7}$	75
SB16	PEG_{5K}-$PBOP_{40}$-$BOD_{0.7}$	10
SB17	PEG_{5K}-$PBOP_{40}$-$BOD_{0.7}$	50
SB18	PEG_{5K}-$PBOP_{40}$-$BOD_{0.7}$	75
SB19	PEG_{5K}-PCL_{80}-$BOD_{0.8}$	10
SB20	PEG_{5K}-PCL_{80}-$BOD_{0.8}$	50
SB21	PEG_{5K}-PCL_{80}-$BOD_{0.8}$	75

PEG, polyethylene glycol; PCL, polycaprolactone
MOP, POP, BOP and PHLOP are all bespoke monomers

Table 4.3 Nanoparticle formulations differing in the polymer composition

Nanoparticle Formulation	Polymer Composition	SN-38 Loading (%)
CA1	$BuMA_{100}$-co-$EGDMA_{0.95}$: PEG_{5k}-$HPMA_{100}$	2.5
CA2	$EHMA_{100}$-co-$EGDMA_{0.80}$: PEG_{5k}-$HPMA_{100}$	2.5
CA3	$EHMA_{100}$-co-$EGDMA_{0.80}$: PEG_{5k}-$HPMA_{100}$	5
CA4	$EHMA_{100}$-co-$EGDMA_{0.80}$: PEG_{5k}-$HPMA_{100}$	5
CA5	$EHMA_{100}$-co-Bisphenol : PEG_{5k}-$HPMA_{100}$	5
CA6	$EHMA_{20}$-co-Bisphenol : PEG_{5k}-$HPMA_{100}$	5
CA7	$EHMA_{20}$-co-EGDMA : PEG_{5k}-$HPMA_{100}$	5
CA8	$BuMA_{100}$-co-EGDMA : PEG_{5k}-$HPMA_{100}$	5
CA9	$EHMA_{100}$-co-$EGDMA_{o.95}$: PEG_{5k}-$HPMA_{100}$	50
CA10	$EHMA_{100}$-co-GDMA : PEG_{5k}-$HPMA_{100}$	5
CA11	$EHMA_{20}$-co- GDMA : PEG_{5k}-$HPMA_{100}$	5

CA12	$EHMA_{100}$-co-BpGDMA : PEG_{5k}-$HPMA_{100}$	5
CA13	$EHMA_{100}$-co-UDMA : PEG_{5k}-$HPMA_{100}$	5
CA14	$EHMA_{20}$-co-UDMA : PEG_{5k}-$HPMA_{100}$	5
CA15	$EHMA_{100}$-co-$DSDMA_{0.75}$: PEG_{5k}-$HPMA_{100}$	5
CA16	$EHMA_{20}$-co-$DSDMA_{0.75}$: PEG_{5k}-$HPMA_{100}$	5
CA17	$EHMA_{100}$-co-GDMA : PEG_{5k}-$HPMA_{100}$	10
CA18	$EHMA_{100}$-co-BPGDMA : PEG_{5k}:$HPMA_{100}$	10
CA19	$BuMA_{50}$-co-$HPMA_{50}$-co-EGMA : PEG_{5k}:$HPMA_{100}$	5
CA20	$EHMA_{20}$-co-BPGDMA : PEG_{5k}:$HPMA_{100}$	5
CA21	$BuMa_{20}$- Bisphenol : PEG_{5k}:$HPMA_{100}$	5

BPGDMA, bisphenol A glycerolate dimethacrylate; BUMA, butyl methacrylate; DSDMA, disulfide dimethacrylate; EHMA, ethyl α-hydroxymethylacrylate; GDMA, glycerol dimethacrylate; HPMA, hydroxypropyl methacrylate; PEG, polyethylene glycol; UDMA, urethane dimethacrylate.

4.2.4 Cell Culture

4.2.4.1 Monolayer (2D) Culture

DLD-1, HCT116, LoVo and CT26 cells were maintained and cultured in monolayer as described in section 3.2.3.

4.2.4.2 Spheroid (3D) Culture

HCT116 and CT26 spheroids, at 1000 and 1250 cells/well respectively, were cultured for 5 days as described in section 3.2.4.

4.2.5 *In vitro* Assessment of SN-38 Release

In vitro release studies were conducted using a previously published rapid equilibrium dialysis setup (Pierce RED Device), as shown in the schematic below (Bakshi et al., 2018). The inserts comprised of two compartments, separated by an O-ring-sealed dialysis membrane - 8kDa molecular-weight cut-off. SN-38 NPs were diluted to 250ng/ml in PBS (pH 7.4). Free SN-38 was dissolved in DMSO before dilution with PBS, such that DMSO comprised <1% of the final volume. To assess release, 0.5mL of samples to be investigated were added to the donor compartment and 1mL of pre-warmed PBS was added to the acceptor compartment. Plates containing the inserts were placed on an orbital shaker (Heidolph Rotomax 120; 100rpm, 48hours, 37°C ± 1°C). Each insert represented a single time-point and at specified time intervals both acceptor (1mL) and donor fluid (0.5mL) were removed. Aliquots of each timed sample were then used to determine levels of SN-38 in each compartment, applying the validated LC-MS/MS method outlined in Chapter 2:. All experiments were performed ensuring sink

conditions. Data were expressed as the percentage of SN-38 released i.e. the amount which diffused across the membrane.

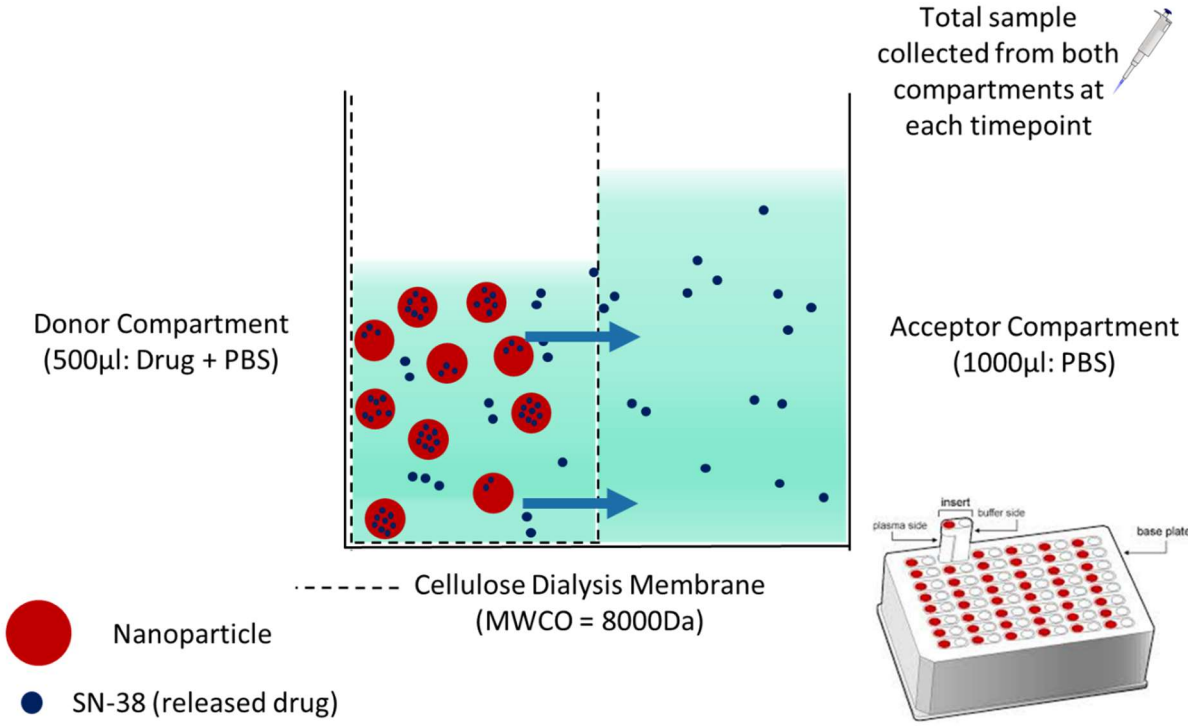

Figure 4.1 An overview of the equilibrium dialysis method which was used for the measurement SN-38 release. Theoretically, the drug molecules diffuse across the dialysis membrane until the concentration gradient is zero. Hence, 50% release (equilibrium) represents the maximum release in this setup.

4.2.6 *In Vitro* Cytotoxicity

4.2.6.1 Monolayer (2D) Experiments

After cells had adhered (24 hours), all media was aspirated and replaced with 100µL of each concentration of media containing SN-38 NPs (wells were 0.1% H_2O by volume). The concentrations used, varied between 0.5-200nM. Blank NP and solvent only controls (0.1% H_2O) were also included within the plate setup. Time points of 24, 48, 72 and 96 hours post-treatment, were used to assess the cytotoxicity of the NPs. The data were also compared to results obtained following exposure to irinotecan and free SN-38 solution in 0.1% DMSO, using the same time points.

4.2.6.2 Spheroid (3D) Experiments

Following 5 days in culture, 50µl of growth media was removed from HCT116 and CT26 spheroids. It was replaced with 50µL of each concentration of media containing SN-38 NPs (wells were 0.1% H2O

by volume). The concentrations used, ranged between 0.5-200nM for HCT116 spheroids and 2.5-400nM for CT26 spheroids. Blank NP and solvent only controls (0.1% H_2O) were also included within the plate setup. Time points of 72- and 144-hours post-treatment, were used to assess the cytotoxicity of the NPs. The data were also compared to results obtained following exposure to irinotecan and free SN-38 solution in 0.1% DMSO, using the same time points.

4.2.6.3 Determination of Cell Viability Following Treatment

Cell viability was measured using the CellTiter-Glo luminescent cell viability assay (Promega, Hampshire) as described in section 3.2.7.4. Cell viability was calculated as a percentage of untreated vehicle control (blank NP samples or 0.1% DMSO). A concentration-response curve was plotted and used to determine an IC_{50} value (average ± SD, n=3).

4.2.7 Macrophage Uptake

Monocytes were isolated by ficoll plaque separation of anonymised healthy volunteer buffy coats, purchased from the NHS Blood and Transfusion Service. Freshly isolated $CD14^+$ monocytes were differentiated into classically activated M1 macrophages using macrophage generation media DXF (PromoCell, Heidelberg, Germany). Macrophages were detached using macrophage detachment solution DXF (PromoCell, Heidelberg, Germany) and subsequently, $1x10^6$ macrophages were plated onto 24 well plates. They were left to adhere for 3 hours. Following this, they were treated at a fixed concentration of 50µM for 24 hours with selected nano-formulations. Both extracellular and intracellular (following lysis with H_2O) levels of SN-38 were quantified using the developed LC-MS/MS method, see Chapter 2:. Data were presented as a cellular accumulation ratio (CAR) (average ± SD, n=3).

Cellular **A**ccumulation **R**atio =
$$\frac{(intracellular\ concentration)}{(extracellular\ concentration)}$$

4.2.8 *In Vivo*: Pharmacokinetic Evaluation

To characterise the plasma pharmacokinetics, mice (n=3) were intravenously injected (tail vein) with freshly prepared SB1 at 2mg/kg, CA16 at 2mg/kg, free SN-38 at 2mg/kg or irinotecan at 40mg/kg. Free

SN-38 and irinotecan were made up in 10% and 2.5% DMSO containing saline, respectively. Where possible, blood was collected in heparinised tubes following cardiac puncture at 0.083-, 0.25-, 0.5-, 2-, 2.5-, 3-, 4- and 5-hours following dose administration. Samples were centrifuged at 10,000 rpm for 10 minutes to separate plasma and stored at −40°C until analysis. The previously developed LC-MS/MS method detailed in Chapter 2: was used for determining concentrations of irinotecan, SN-38 and SN-38G. Pharmacokinetic parameters were calculated using the PK Solver add-in (Y. Zhang, Huo, Zhou, & Xie, 2010).

4.2.9 Statistical Analysis

Unless otherwise stated, all reported values are the average with their respective standard deviation (SD). The number of replicates is always indicated in the figure legends. Experiments were conducted at least in biological triplicates and datasets were analysed with SigmaPlot version 14.0 (Systat Software, Inc., San Jose California USA). A two-way analysis of variance (ANOVA) with Holm-Šídák multiple comparison post-hoc test was used to compare data sets. A p-value of < 0.05 was considered significant.

4.3 Results

4.3.1 Characterisation and Selection of NPs

4.3.1.1 Drug Release

A total of 41 different NPs were screened in an iterative manner using the dialysis method. The *in vitro* release behaviour of the SN-38 loaded NPs is summarised, with the percentage release over 48 hours shown in Figure 4.2 and Figure 4.4 and percentage release over 8 hours shown in Figure 4.3 and Figure 4.5. Most of the free SN-38 quickly diffused across the dialysis membrane and the process was essentially complete (approaching equilibrium) following 8 hours (see black markers on all graphs for free SN-38). For several of the SB NPs, an initial burst release was present, similar to that seen with free SN-38. This was followed by a gradual sustained release up to 48 hours (Figure 4.2 and Figure 4.3). Only polycaprolactone (SB1 and SB2) and PBOP (SB17 and SB18) based NPs showed a slower release than free SN-38 over the first two hours.

However, this behaviour was not observed in CA NPs, which showed a clear reduction in drug release in comparison to the free drug (Figure 4.4 and Figure 4.5). No burst release was present and CA NPs displayed a typical slower sustained drug release profile. Release of SN-38 from CA NPs was consistently lower than free SN-38 up to 24 hours. In particular, a lower DPn value (number-average degree of polymerisation) of 20 monomer units (Figure 4.5a) in comparison to 100 monomer units (Figure 4.5b) lead to a reduction in SN-38 release (See CA6 vs. CA3 and CA20 vs. CA12). Changes to the DPn value within the other polymeric systems had little effect on SN-38 release. In both sets of NPs, increasing drug loading did not seem to impact the release rate. For select candidates, additional release studies were completed in PBS at a lower pH (5.5). These experiments displayed a faster release profile for the NPs in a more acidic environment (see appendix Figure B.8).

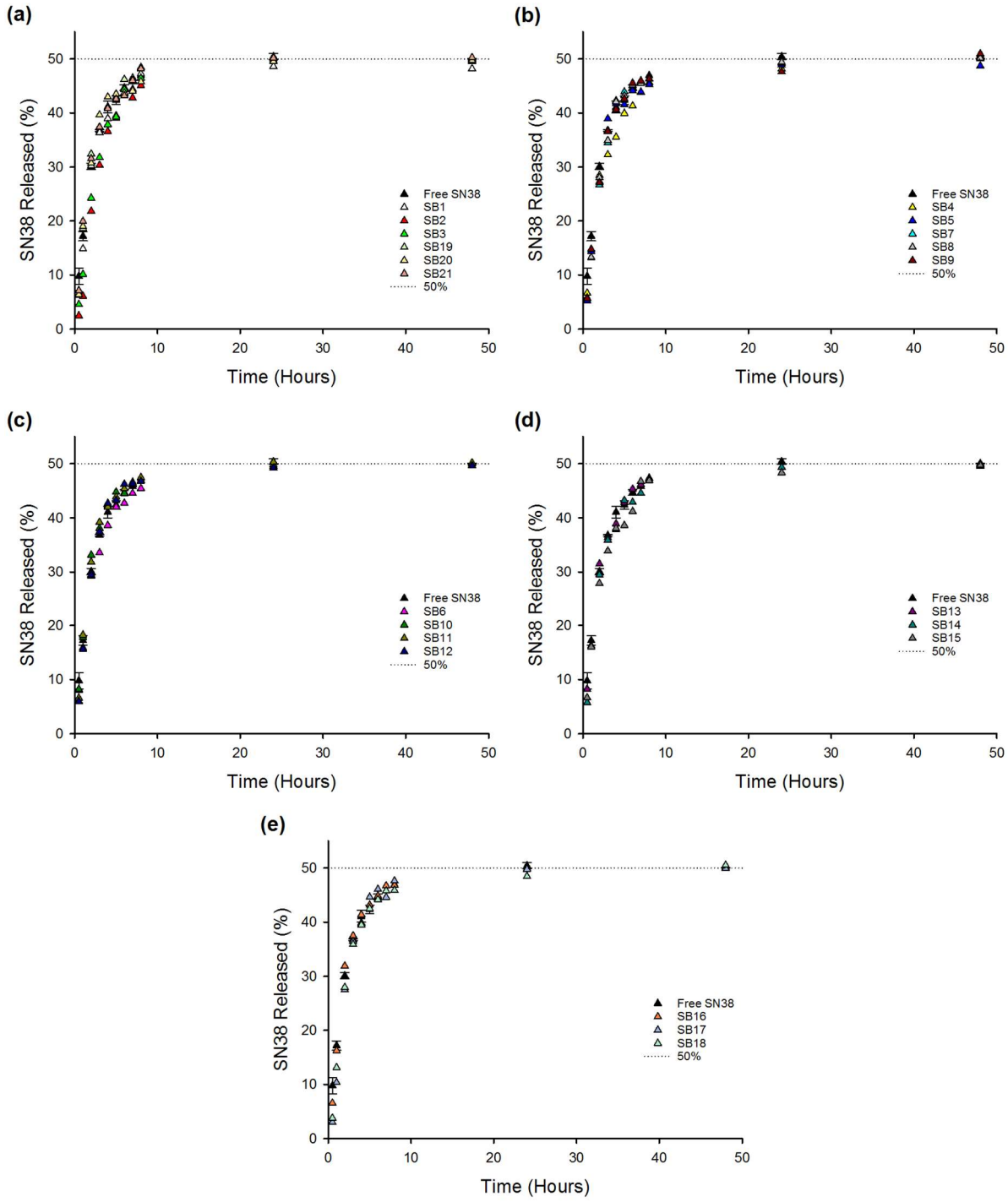

Figure 4.2 Drug release profiles of free SN-38 and SN-38 loaded SB polymer nanoparticles, in phosphate-buffered saline at pH 7.4, over 48 hours. Increasingly loaded nanoparticles with polycaprolactone monomer compositions are shown in (**a**), PMOP monomer compositions in **(b)**, PPOP monomer compositions in **(c)**, PPHLOP monomer compositions in **(d)** and PBOP monomer compositions in **(e)**. The dotted line at 50% represents the maximum release achievable in this setup. Where error bars are present, each point is shown as the average ± SD (n = 3).

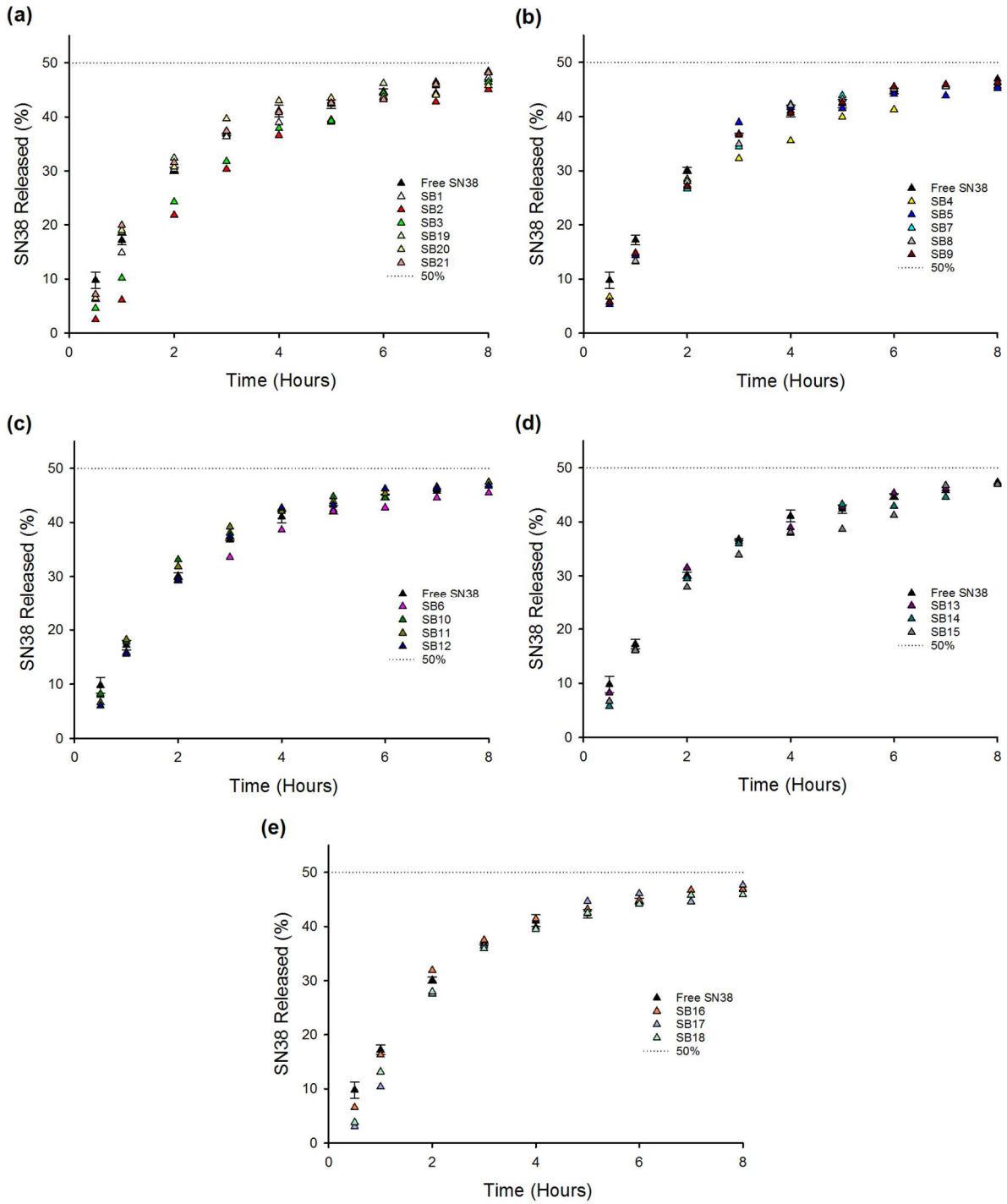

Figure 4.3 Drug release profiles of free SN-38 and SN-38 loaded SB polymer nanoparticles, in phosphate-buffered saline at pH 7.4, for the first 8 hours. Increasingly loaded nanoparticles with polycaprolactone monomer compositions are shown in (**a**), PMOP monomer compositions in **(b)**, PPOP monomer compositions in **(c)**, PPHLOP monomer compositions in **(d)** and PBOP monomer compositions in **(e)**. The dotted line at 50% represents the maximum release achievable in this setup. Where error bars are present, each point is shown as the average ± SD (n = 3).

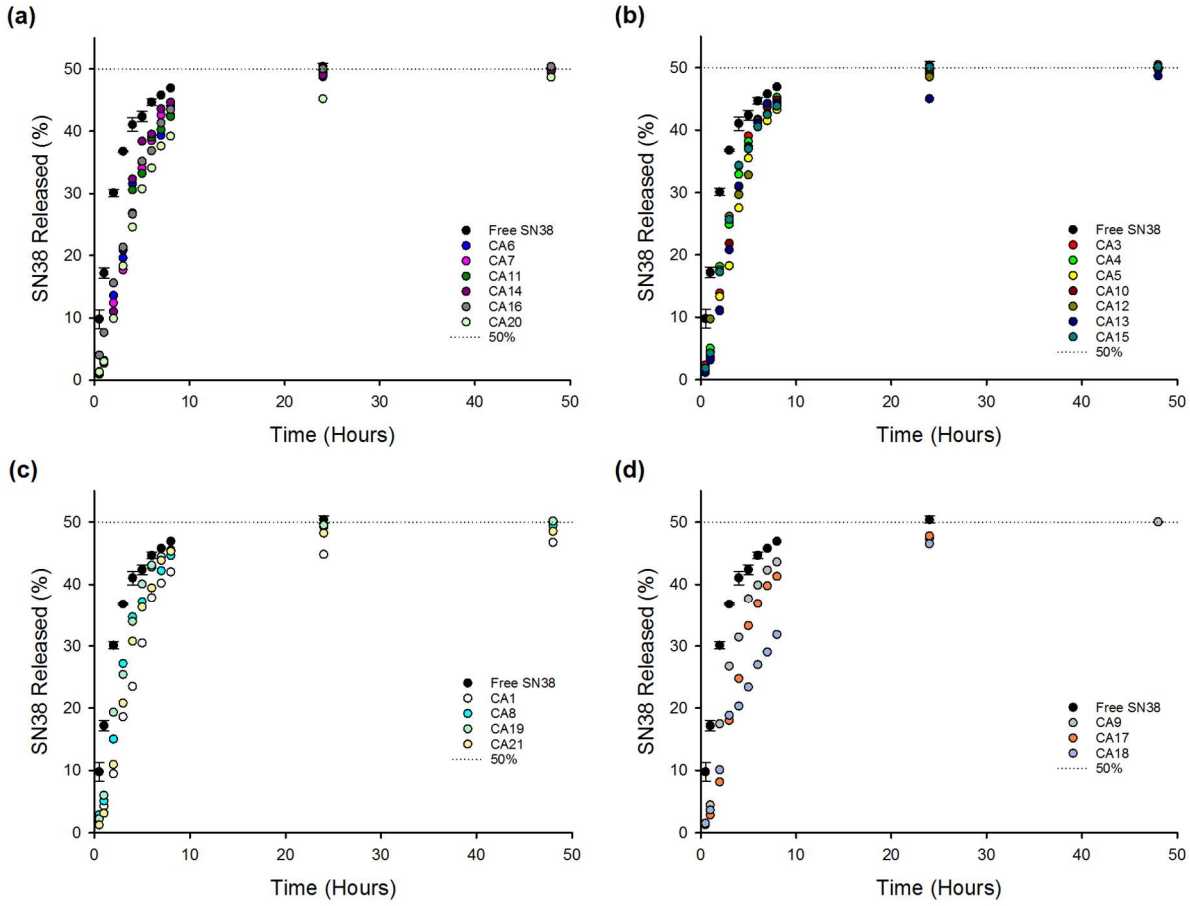

Figure 4.4 Drug release profiles of free SN-38 and SN-38 loaded CA polymer nanoparticles, in phosphate-buffered saline at pH 7.4, over 48 hours. Nanoparticles with an $EHMA_{20}$ monomer composition are shown in **(a)**, $EHMA_{100}$ monomer compositions in **(b)**, BUMA monomer compositions in **(c)** and differently loaded EHMA monomer compositions in **(d)**. The dotted line at 50% represents the maximum release achievable in this setup. Where error bars are present, each point is shown as the average ± SD (n = 3).

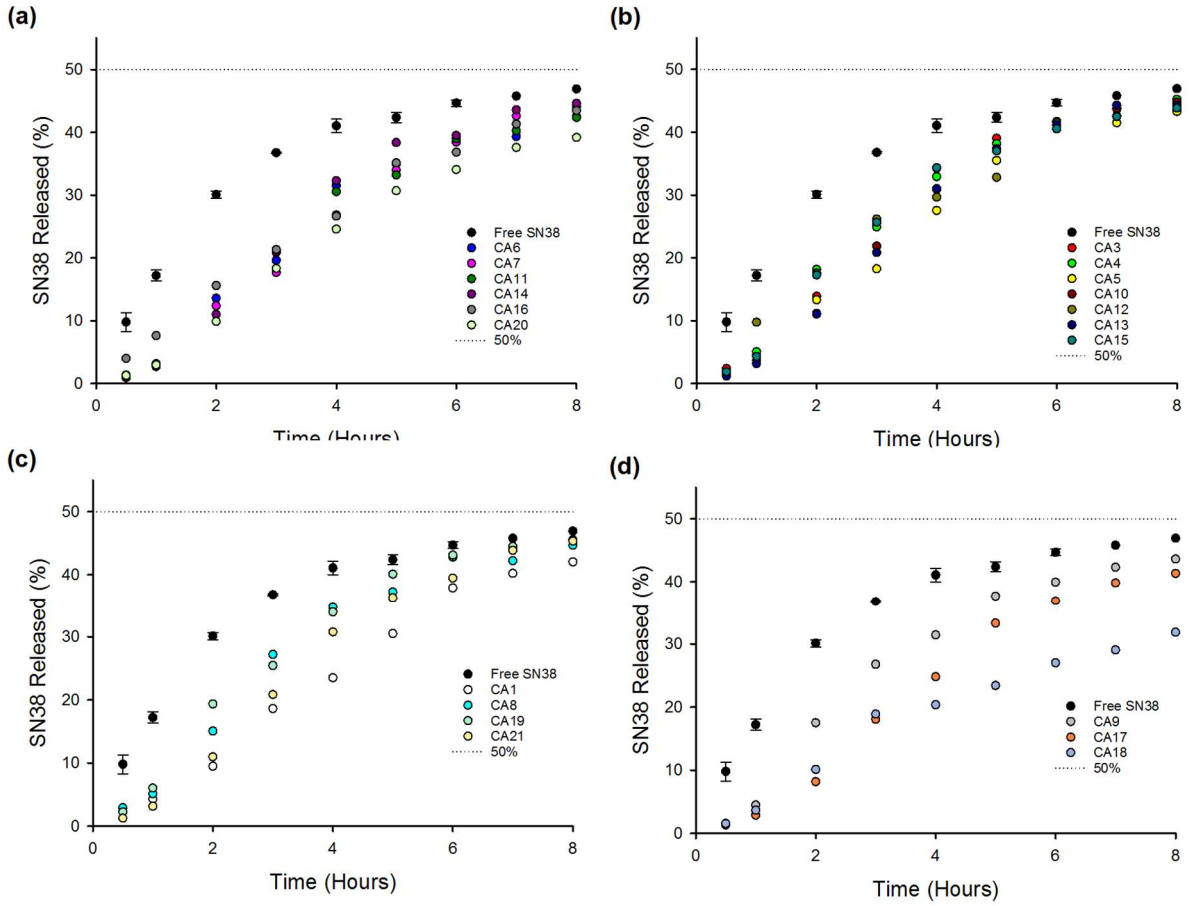

Figure 4.5 Drug release profiles of free SN-38 and SN-38 loaded CA polymer nanoparticles, in phosphate-buffered saline at pH 7.4, for the first 8 hours. Nanoparticles with an $EHMA_{20}$ monomer composition are shown in (**a)**, $EHMA_{100}$ monomer compositions in **(b)**, BUMA monomer compositions in **(c)** and differently loaded EHMA monomer compositions in **(d)**. The dotted line at 50% represents the maximum release achievable in this setup. Where error bars are present, each point is shown as the average ± SD (n = 3).

The SN-38 release profiles of the best candidates, from each set of NPs in PBS (pH 7.4), is shown in the figure below (Figure 4.6). Candidate formulations were selected based on their ability to release SN-38 in a slower, sustained manner over time. These included SB1, SB2, SB3, SB7, SB8, CA1, CA14, CA16, CA18 and CA19.

(a)

Time (Hours)	SN38	SB1	SB2	SB3	SB7	SB8	CA1	CA14	CA16	CA18	CA19
0.5	9.78	6.24	2.47	4.57	5.78	5.80	2.46	1.18	4.00	1.52	2.24
1	17.20	14.87	6.10	10.15	13.24	13.27	4.37	2.70	7.63	3.66	6.02
2	30.09	30.27	21.84	24.26	26.71	28.03	9.34	11.00	15.59	10.12	19.33
3	36.76	36.34	30.34	31.76	34.47	34.90	19.28	20.98	21.34	18.85	25.42
4	41.05	38.99	36.58	37.86	42.26	42.07	24.25	32.31	26.66	20.33	33.93
5	42.36	39.47	39.07	39.26	43.90	43.20	30.68	38.39	35.15	23.38	40.06
6	44.67	43.49	43.74	44.34	45.02	45.13	38.35	39.50	36.85	26.99	43.09
7	45.79	46.45	42.76	44.38	45.73	45.52	41.16	43.58	41.33	29.02	44.47
8	46.91	47.25	45.07	46.44	46.31	46.33	44.11	44.62	43.48	31.83	45.52
24	50.40	48.59	49.54	49.80	49.19	49.39	45.58	48.95	50.03	46.53	49.52
48	50.04	48.16	49.52	49.66	50.38	50.16	48.95	49.71	50.37		50.16

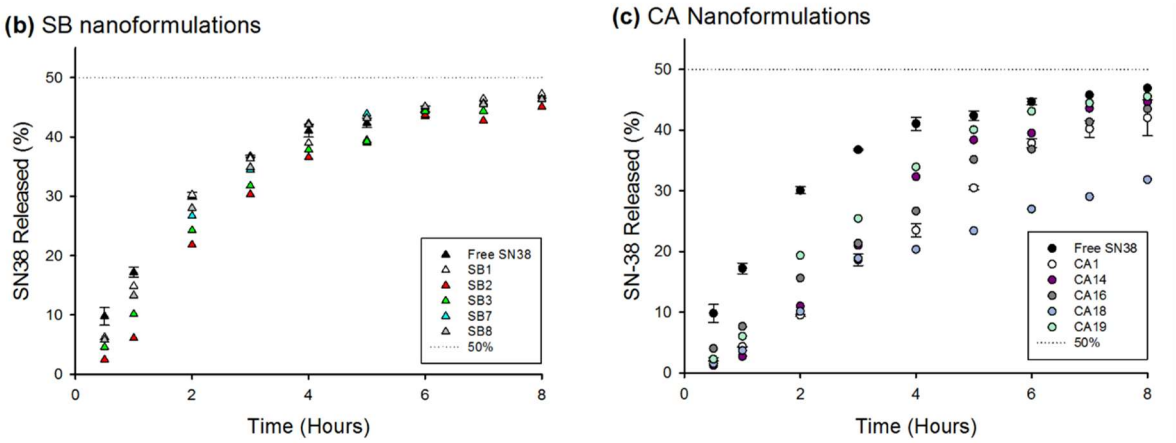

Figure 4.6 The ten best nanoparticles identified from the *in vitro* drug release screen. The release profiles for free SN-38 and selected candidates are listed in **(a)**. The data for the first 8 hours is depicted in a graphical format as shown in **(b)** and **(c).** The dotted line at 50% represents the maximum release achievable in this setup. Where error bars are present, each point is shown as the average ± SD (n=3).

4.3.1.2 Cytotoxicity Studies

The sensitivity of a panel of CRC cell lines to free SN-38, the 10 selected NPs and irinotecan was compared using an ATP assay. The cell viability was quantified at 24-, 48-, 72- and 96-hours post-incubation in monolayer culture, or 72- and 144-hours post-incubation in spheroid culture. As shown in Figure 4.7, both free SN-38 and all NPs were potent to differing degrees and the sensitivity of the cells to NPs after 96 hours, was similar to free SN-38 across the cell lines. Overall, a trend showing that slower releasing CA NPs were slightly less potent (higher IC_{50} values), than the faster releasing SB NPs was seen. However, irinotecan was several orders of magnitude less toxic than either free SN-38 or any of the NPs at all time points. Data for 24 hours cytotoxicity is not included here, as IC_{50} concentrations were not achieved. All individual graphs for monolayer studies have been included in the appendix, see Figure B.9.

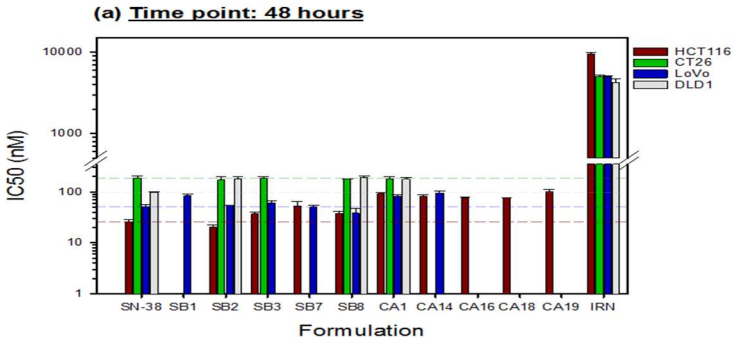

(d) 48 hour IC_{50} values (nM)

48hrs Cell line	SN38	SB1	SB2	SB3	SB7	SB8	CA1	CA14	CA16	CA18	CA19	Irinotecan
HCT116	25.79 (±2.269)	N.D	19.95 (±2.27)	36.82 (±3.21)	52.40 (±12.8)	37.98 (±3.31)	92.13 (±3.47)	81.61 (5.42)	76.33 (±2.04)	75.74 (1.11)	99.42 (±12.19)	9525.45 (±390.77)
CT26	186.43 (±21.65)	N.D	171.20 (±29.22)	185.75 (±14.47)	N.D	177.36 (±4.56)	178.00 (±23.32)	N.D	N.D	N.D	N.D	18381.3 (1081.88)
LoVo	51.11 (±5.568)	83.67 (±6.15)	53.81 (±1.42)	60.84 (±5.12)	50.25 (±3.78)	38.16 (±9.22)	80.72 (±6.54)	94.89 (±7.01)	N.D	N.D	N.D	17914.3 (636.81)
DLD-1	97.25 (±3.24)	N.D	180.62 (±16.87)	N.D	N.D	192.49 (±15.63)	177.78 (±14.52)	N.D	N.D	N.D	N.D	4259.35 (±529.59)

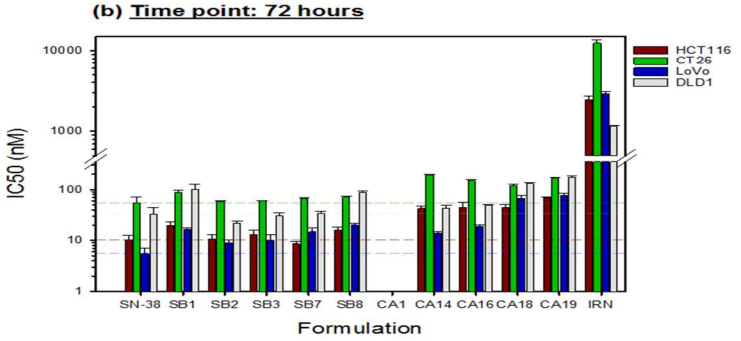

(e) 72 hour IC_{50} values (nM)

72hrs Cell line	SN38	SB1	SB2	SB3	SB7	SB8	CA1	CA14	CA16	CA18	CA19	Irinotecan
HCT116	10.32 (±2.34)	19.60 (±3.36)	10.56 (±2.32)	13.17 (±2.80)	8.58 (±1.04)	15.92 (±2.28)	no data	42.08 (±4.95)	44.30 (±11.23)	44.64 (±5.57)	68.99 (±2.64)	2430.00 (±310.91)
CT26	53.98 (±17.66)	87.31 (±10.03)	58.17 (±1.99)	60.67 (±0.14)	67.37 (±2.24)	70.21 (±4.50)	no data	191.72 (±4.35)	148.47 (±4.50)	118.81 (±9.42)	165.86 (±7.71)	12478.40 (±1235.62)
LoVo	5.53 (±1.4)	16.71 (±0.81)	9.07 (±1.30)	9.95 (±3.27)	14.74 (±2.85)	19.95 (±1.42)	no data	13.93 (±1.00)	19.01 (±1.38)	66.99 (±9.76)	76.21 (±8.28)	2906.60 (±171.47)
DLD-1	33.00 (±11.62)	101.42 (±25.74)	21.79 (±1.94)	30.49 (±4.04)	34.28 (±3.56)	88.71 (±3.49)	no data	43.19 (±5.64)	49.69 (±1.04)	129.86 (±7.65)	172.87 (±14.37)	1156.45 (±36.88)

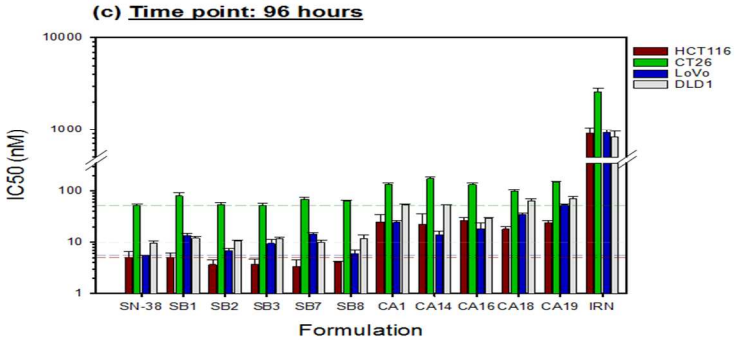

(f) 96 hour IC_{50} values (nM)

96hrs Cell line	SN38	SB1	SB2	SB3	SB7	SB8	CA1	CA14	CA16	CA18	CA19	Irinotecan
HCT116	5.03 (±1.44)	5.01 (±1.02)	3.63 (±0.88)	3.74 (±0.96)	3.37 (±1.19)	4.07 (±0.16)	24.81 (±10.09)	22.18 (±13.37)	26.32 (±4.19)	17.93 (±1.85)	23.64 (±2.38)	906.39 (±140.91)
CT26	51.90 (±4.17)	79.98 (±11.10)	54.11 (±5.90)	52.74 (±4.45)	68.69 (±6.62)	63.39 (±1.34)	133.00 (±9.71)	173.30 (±14.17)	131.90 (±9.59)	99.46 (±4.85)	148.47 (±3.82)	2596.40 (±235.62)
LoVo	5.50 (±0.10)	13.36 (±1.45)	6.85 (±0.65)	9.44 (±1.86)	14.44 (±0.78)	6.02 (±1.06)	24.42 (±2.38)	13.91 (±2.65)	17.89 (±5.90)	35.03 (±2.18)	52.98 (±2.20)	926.13 (±71.47)
DLD-1	9.65 (±1.01)	12.04 (±1.05)	10.5 (±0.29)	11.59 (±1.07)	9.90 (±1.15)	11.71 (±2.13)	53.26 (±1.37)	53.13 (±0.72)	29.55 (±0.62)	64.25 (±6.10)	70.92 (±6.43)	832.97 (±120.35)

Figure 4.7 Potency of SN-38 encapsulated nanoparticles compared to free SN-38 and irinotecan in monolayer colorectal cancer cell lines. IC_{50} values (nM) were determined at 48 hours (**a** and **d**), 72 hours (**b** and **e**) and 96 hours (**c** and **f**). Dashed lines are indicative of the IC_{50} for free SN-38 within each cell line. Data are presented as average ± SD. (N.D - IC_{50} not determined)

Like the data seen in monolayer cells, spheroids treated with NPs showed varying degrees of cytotoxicity (Figure 4.8), with the faster releasing SB NPs being more potent than the slower releasing CA NPs. Moreover, as seen in Figure 4.9 and Figure 4.10, following NP treatment a clear reduction in spheroid size was present, similar to that seen with free SN-38 or irinotecan treatment in the previous chapter. Also, blank NPs did not impact the viability of the spheroids. Individual graphs for all spheroid studies have been included in the appendix, see Figure B.10. As all formulations were still significantly more potent than the parent drug, irinotecan, the cytotoxicity data was therefore not able to exclude any further candidates.

(a) Time point: 144 hours

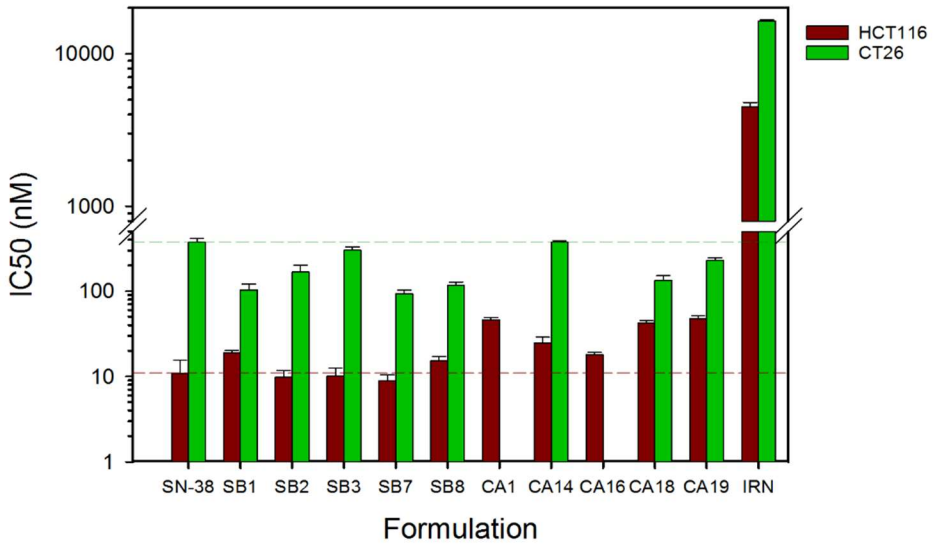

(b) 72 hour IC_{50} values (nM)

72hrs	SN38	SB1	SB2	SB3	SB7	SB8	CA1	CA14	CA16	CA18	CA19	Irinotecan
Cell line												
HCT116	170.38 (±38.94)	N.D	179.99 (±18.18)	89.70 (±13.20)	N.D	N.D	N.D	N.D	N.D	N.D	N.D	N.D
CT26	N.D	N.D	N.D	N.D	N.D	N.D	N.D	N.D	N.D	N.D	N.D	55687.30 (±212.04)

(c) 144 hour IC_{50} values (nM)

144hrs	SN38	SB1	SB2	SB3	SB7	SB8	CA1	CA14	CA16	CA18	CA19	Irinotecan
Cell line												
HCT116	10.87 (±4.75)	18.91 (±1.26)	9.78 (±1.98)	10.10 (±2.42)	8.93 (±1.51)	15.20 (±2.04)	46.26 (±2.95)	24.80 (±4.13)	17.95 (±1.17)	42.10 (±3.03)	47.64 (±4.07)	4479.90 (±323.55)
CT26	374.42 (±39.81)	103.13 (±17.61)	167.50 (±34.89)	303.24 (±28.20)	93.34 (±9.53)	117.76 (±10.48)	N.D	377.53 (±14.01)	N.D	132.93 (±18.83)	229.10 (±17.11)	16418.90 (±247.12)

Figure 4.8 Potency of SN-38 encapsulated nanoparticles compared to free SN-38 and irinotecan in spheroid colorectal cancer cell lines. IC_{50} values (nM) were determined at, 72 hours **(b)** and 144 hours **(a)** and **(c)**. Dashed lines are indicative of the IC_{50} for free SN-38 within each cell line. Data are presented as average ± SD. (N.D - IC_{50} not determined).

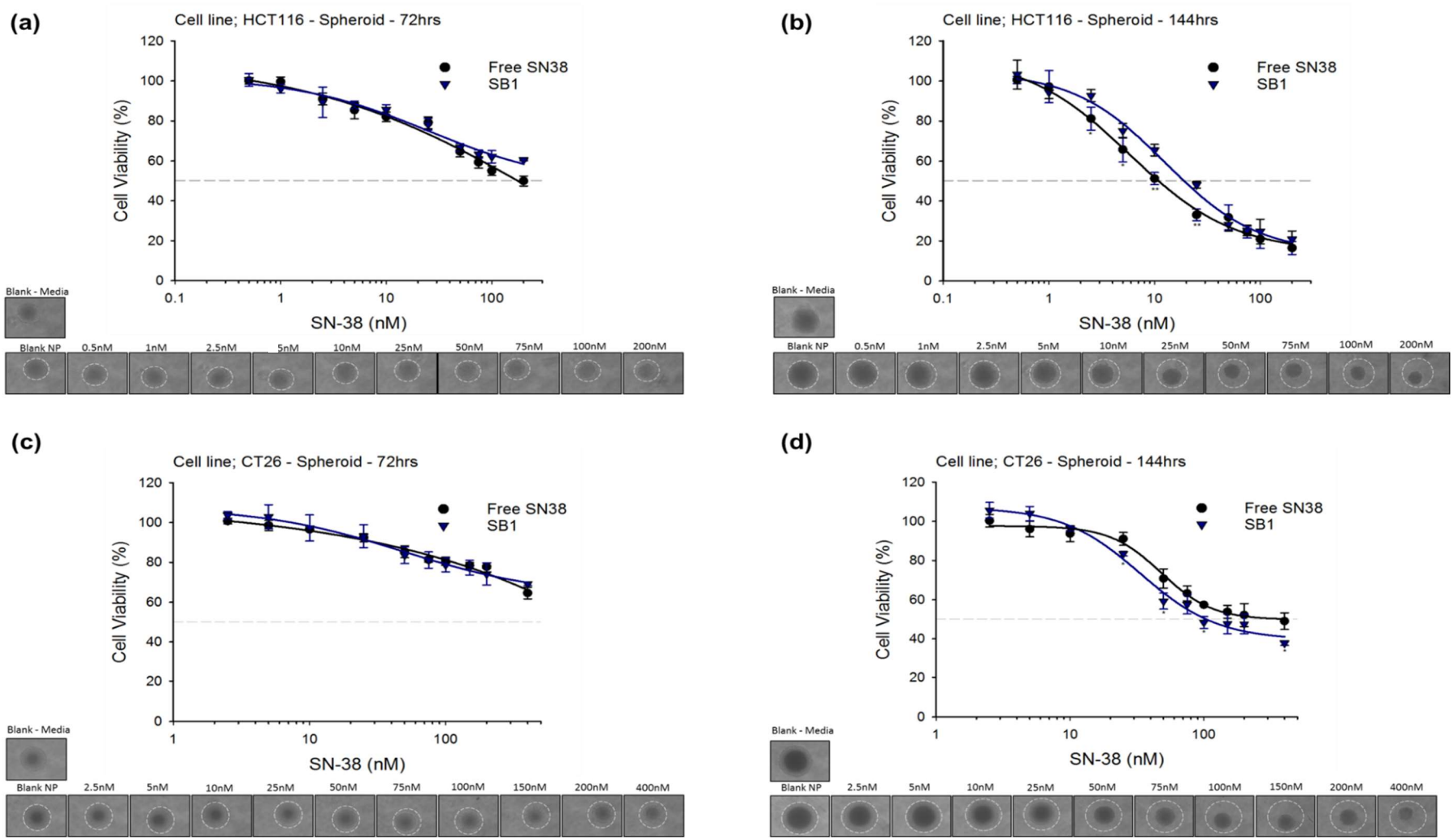

Figure 4.9 Cytotoxicity of SB1 NPs in spheroids. ATP levels were measured in HCT116 and CT26 spheroids treated with SN-38 or SB1 NPs, for 72 **(a)** and **(c)** or 144 hours **(b)** and **(d).** Cell viability was calculated as a percentage of untreated vehicle control (DMSO – 0.1% or blank NP samples). Representative phase-contrast images (10x objective) are documented to capture spheroid integrity following treatment with SB1. Data points are average ± SD, with n=6 individual spheroids per condition. Comparison between treatments with a two-way ANOVA and a Holm-Šídák post-hoc analysis showed statistically significant differences denoted with *$p < 0.05$ and **$p < 0.001$.

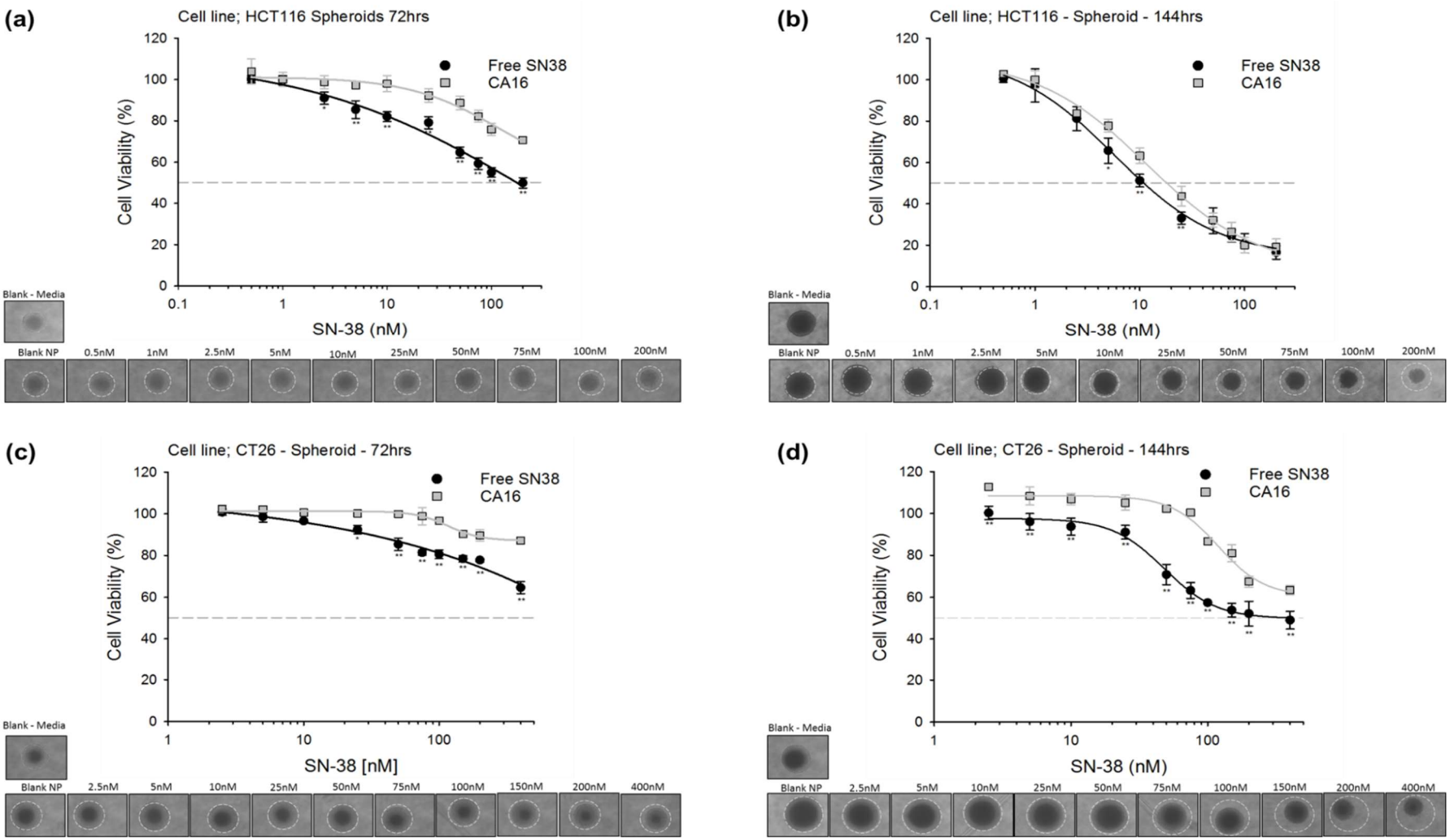

Figure 4.10 Cytotoxicity of CA16 NPs in spheroids. ATP levels were measured in HCT116 and CT26 spheroids treated with SN-38 or CA16 NPs, for 72 **(a)** and **(c)** or 144 hours **(b)** and **(d).** Cell viability was calculated as a percentage of untreated vehicle control (DMSO – 0.1% or blank NP samples). Representative phase-contrast images (10x objective) are documented to capture spheroid integrity following treatment with SB1. Data points are average ± SD, with n=6 individual spheroids per condition. Comparison between treatments with a two-way ANOVA and a Holm-Šídák post-hoc analysis showed statistically significant differences denoted with *$p < 0.05$ and **$p < 0.001$.

4.3.1.3 Macrophage Uptake

For the final phase of the *in vitro* screen and to gain an understanding of the fate of NPs *in vivo,* the 10 NP candidates were further investigated using an *in vitro* cellular uptake assay. NPs were incubated with M1 macrophages for 24 hours at 37°C. A CAR was calculated, with a higher CAR indicating higher NP uptake. Figure 4.11 shows a significantly decreased uptake (lower CAR) of SB NPs when compared to free SN-38 (SB1<SB7<SB8<SB2<SB3, ranking order concerning CAR). CA1, CA14 and CA16 also demonstrated a lower macrophage uptake, however, these differences did not reach levels of significance. CA18 and CA19 were the only NPs to exhibit a higher average uptake when compared to free SN-38. Furthermore, when comparing both types of formulations SB NPs accumulated less in the macrophages than CA NPs.

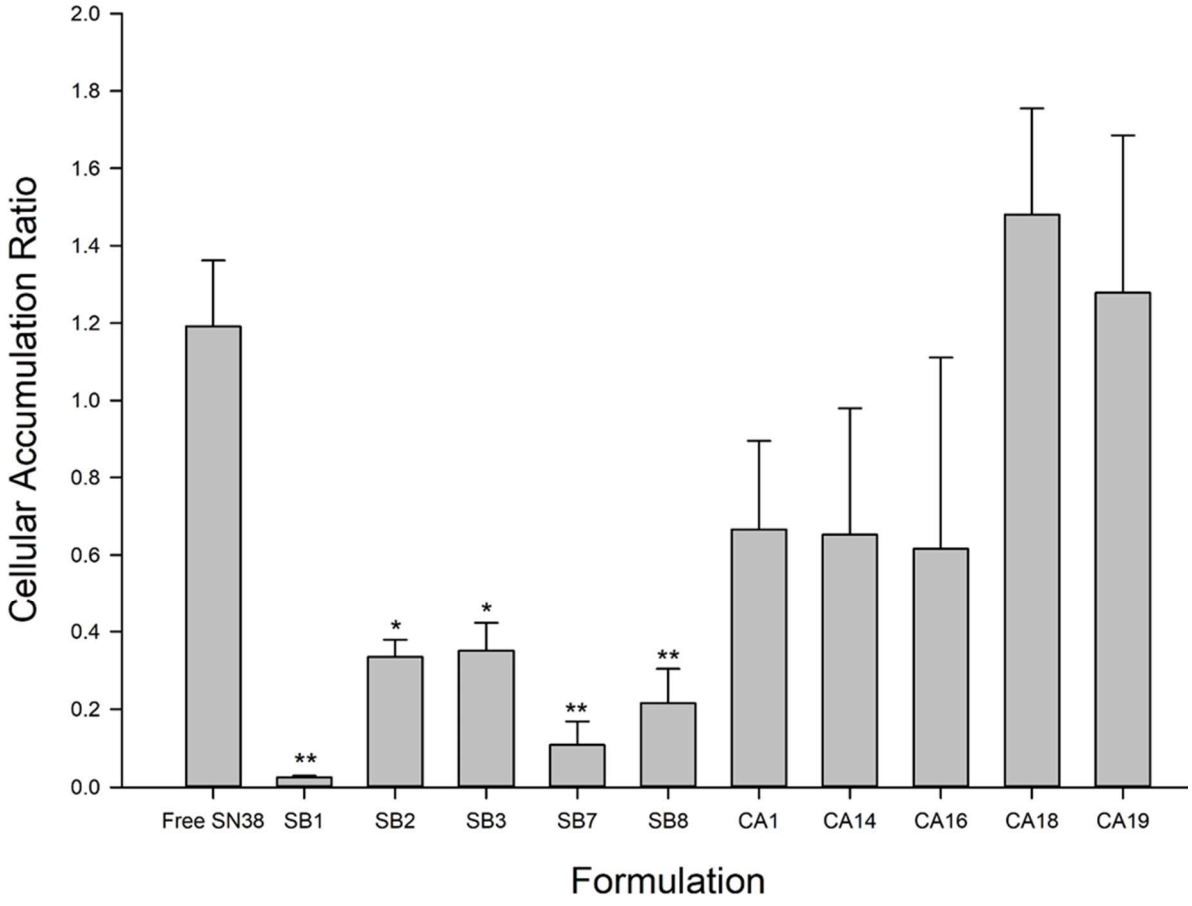

Figure 4.11 Uptake of nanoparticles by macrophages. M1 macrophages ($1x10^6$) were plated out and treated (50µM) for 24 hours with the above polymer nanomaterials or free SN-38. Both extracellular and intracellular levels of SN-38 were quantified and a cellular accumulation ratio was calculated. Data shown as average ± SD (n=3) was assessed using a one way ANOVA with Holm-Šídák post hoc analysis. Levels of significance are denoted as * for $p \leq 0.05$ and ** for $p \leq 0.01$.

4.3.2 Candidate Selection

In order to select the best candidates, for each formulation, to proceed for *in vivo* analysis, all three parameters, drug release, cytotoxicity and macrophage uptake were taken into consideration. For the SB formulations, SB7 and SB8 were excluded as their release profile was similar to that of free SN-38 (see Figure 4.3). SB1, SB2 and SB3 all had similar cytotoxic effects (Figure 4.7 and Figure 4.8) and as SB1 had the lowest macrophage uptake profile (Figure 4.11) it was therefore chosen. Similarly, all CA formulations showed slower sustained release profiles and demonstrated adequate cytotoxicity, in comparison to the parent drug. As CA16 had on average the lowest macrophage uptake, it was given preference. A summary is shown in Figure 4.12.

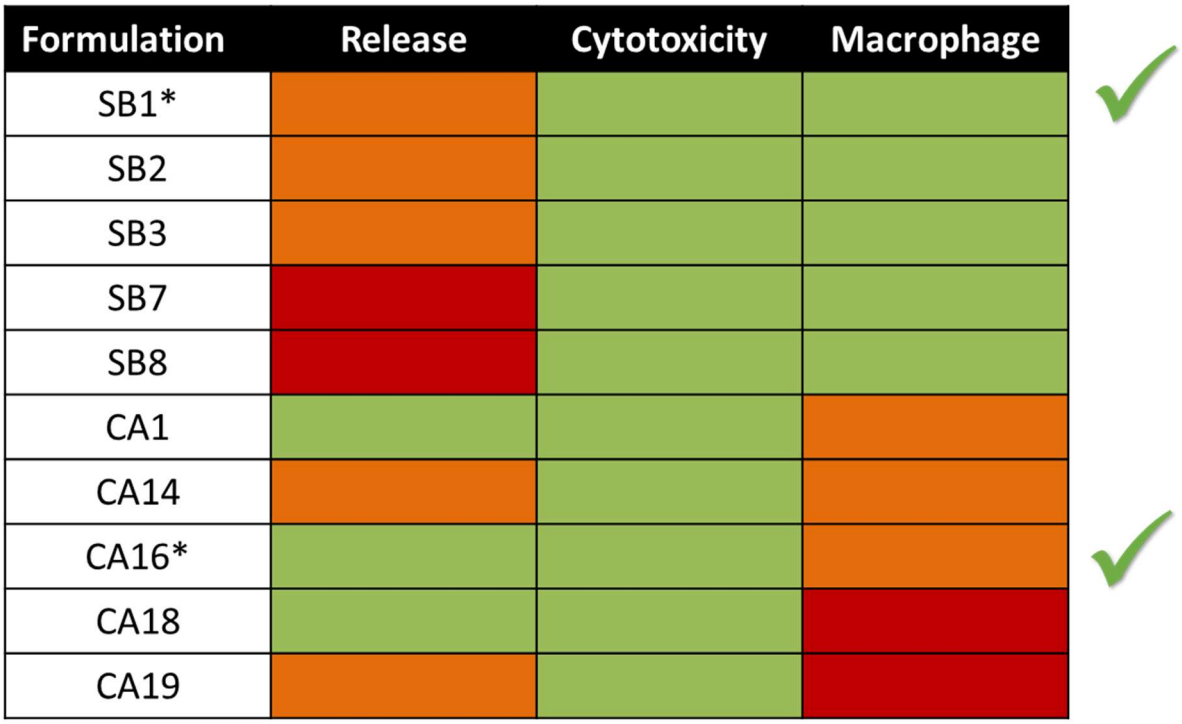

Figure 4.12 Summary of candidates from the *in vitro* tiered screen.
* highlights the candidates chosen for further *in vivo* evaluation.

4.3.3 *In Vivo* Plasma Pharmacokinetics

The pharmacokinetics of SB1 and CA16 NPs, following a single intravenous (tail vein) administration, was assessed by measuring SN-38 concentrations in blood using LC-MS/MS. These values were compared with concentrations measured in mice, following dosing with irinotecan and free SN-38. The plasma concentration-time profiles are presented in Figure 4.13 and the respective pharmacokinetic parameters are summarised in Table 4.4. A full overview of the pharmacokinetic parameters is detailed in the appendix (see Table B.2, Table B.3, Table B.4 and Table B.5).

After injection of irinotecan (40mg/kg), the concentrations of SN-38 in plasma declined rapidly with time, in a log-linear fashion. However, the clearance of SN-38 from both SB1 (2mg/kg) and CA16 (2mg/kg) was considerably faster and the maximum concentration of SN-38 observed was 3- and 23-fold lower when compared to irinotecan administration, for SB1 and CA16 respectively. Data points for both SB1 (all time-points apart from 0.083 hours) and CA16 (at all time-points) were significantly lower ($P \leq 0.001$) than the concentrations observed following irinotecan administration. Similarly, a lower AUC was observed following NP administration, compared with irinotecan. Following administration of free SN-38 (2mg/kg), SN-38 levels were significantly reduced at 5 minutes after dosing and similar levels were observed throughout all time points.

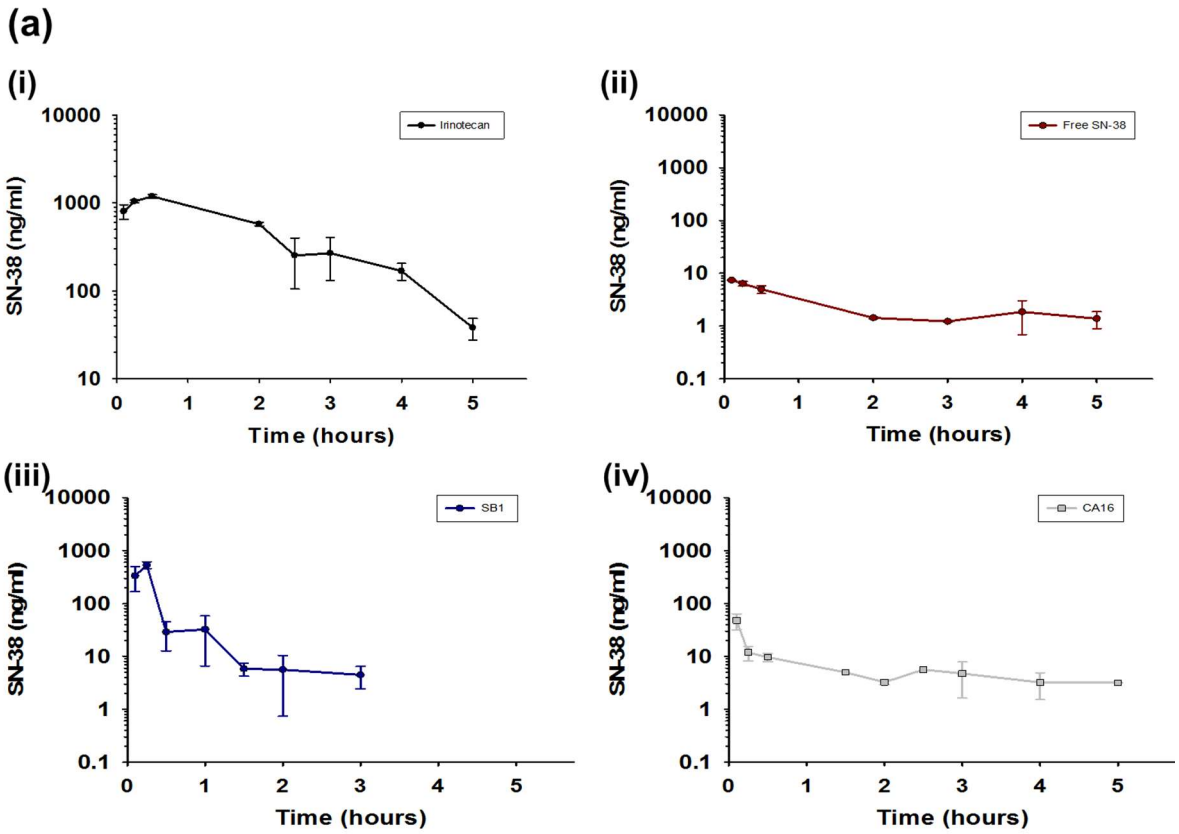

Figure 4.13 Plasma concentration-time profiles of SN-38 following intravenous administration of **(i)** irinotecan, **(ii)** free SN-38, **(iii)** SB1 and **(iv)** CA16 in BALB/c mice. Data are shown as average ±SD (n=3). Statistical analysis was performed using a two-way ANOVA followed by Holm-Šídák multiple comparison post-hoc test. A P-value of $P < 0.05$ was considered significant and where indicated * represent $P \leq 0.001$.

Table 4.4 Pharmacokinetic parameters of irinotecan, free SN-38, SB1 and CA16 after intravenous administration in BALB/c mice

Parameter	Irinotecan	Free SN-38	SB1	CA16
AUC_{0-t} (ng/ml hrs)	2478.13	12.51	170.62	37.00
$AUC_{0-\infty}$ (ng/ml hrs)	2530.88	16.49	194.72	50.72
C_{max} (ng/ml)	1189.41	7.41	388.69	47.98
T_{max} (hrs)	0.5	0.083	0.25	0.083
$T_{1/2}$ (hrs)	0.96	2.00	3.74	2.95

AUC, area under the curve; $t_{½}$, half-life; C_{max}, maximum concentration and T_{max}, time of maximum concentration observed
Data are shown as average ±SD (n=3)

The plasma concentrations of SN-38G were also determined (Figure 4.14). Maximum levels of SN-38G were found at 30 minutes after administration for irinotecan and CA16. For SB1, T_{max} was at 15

minutes. Both SB1 and CA16 had a greater glucuronidation ratio, in comparison to irinotecan (SN-38G AUC/SN-38 AUC; 0.21, 1.56 and 1.01 for irinotecan, SB1 and CA16 respectively). SN-38G levels, following SN-38 administration, could not be determined. A full list of pharmacokinetic parameters for SN-38G is outlined in the appendix (see Table B.6, Table B.7 and Table B.8)

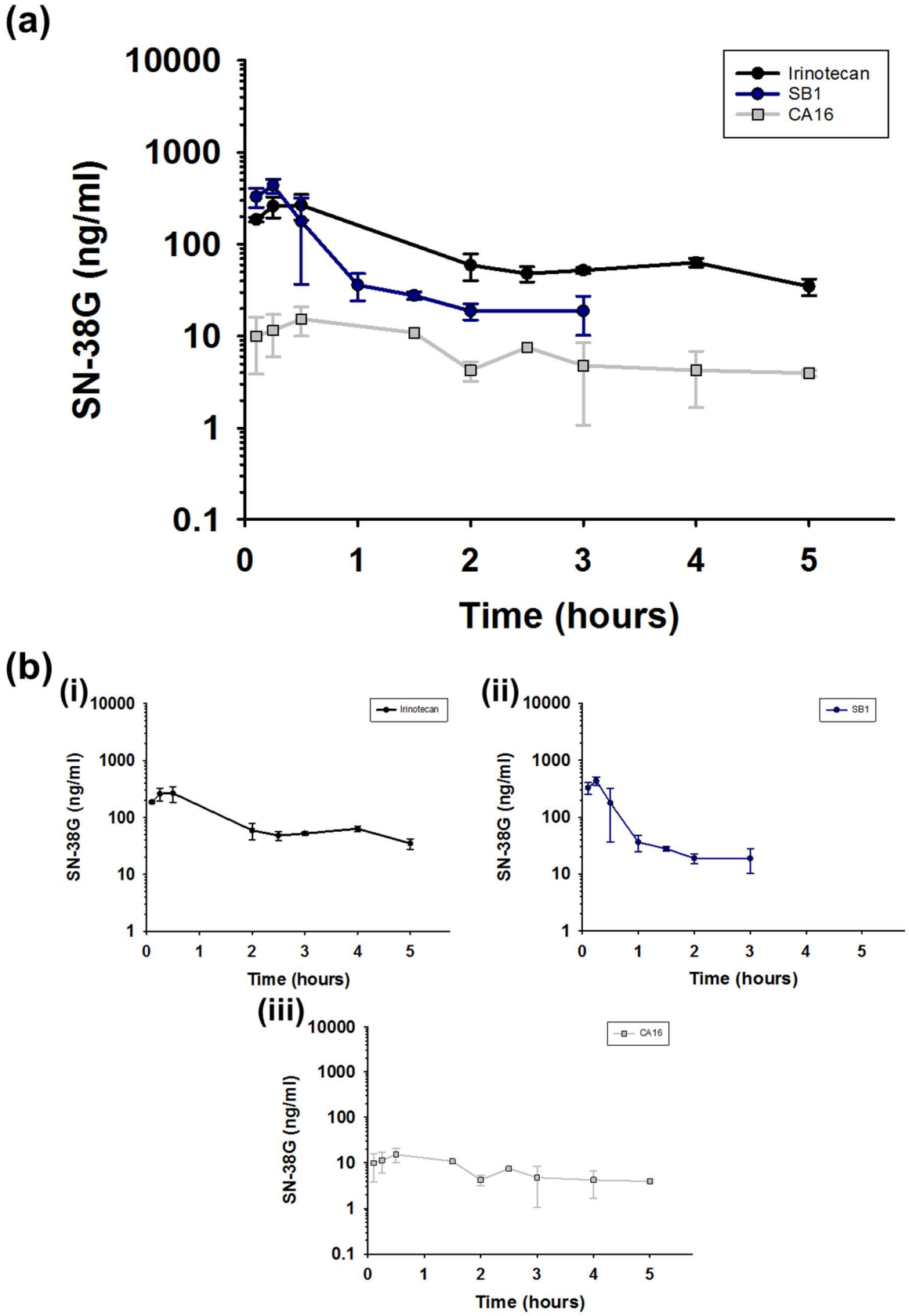

Figure 4.14 Plasma concentration-time profiles of SN-38 glucuronide following intravenous administration of irinotecan, SB1 and CA16 in BALB/c mice. An overview is provided in **(a)** with each plot indicated in **(b)**. Data are shown as average ±SD (n=3).

4.4 Discussion

SN-38, the active metabolite of irinotecan, is a 100–1000 times more potent at inhibiting TOP I (Kawato, Aonuma, Hirota, Kuga, & Sato, 1991; Rothenberg et al., 1993). Even though irinotecan is applied clinically as a prodrug its efficacy is related to maintaining inhibition of TOP I for prolonged periods and dependent upon CES enzymes for conversion to the active metabolite. Irinotecan treatment is frequently followed by late-stage diarrhoea (24% grade 4 incidence) and this limits the dose of irinotecan that can be administered safely in subsequent administrations, thereby reducing response rates in patients (Rothenberg, 2001; Saigi et al., 2004; Ychou et al., 2002). However, the clinical application of SN-38 itself has been hampered by its poor solubility, dose-limiting toxicities, and instability at physiological pH. In this chapter, polymeric NPs encapsulating SN-38 were formulated, providing better solubility by efficiently encapsulating the hydrophobic SN-38 drug molecules.

To demonstrate controlled and sustained SN-38 release, the drug release kinetics were initially assessed. The rate of drug release is a key parameter affecting the bioavailability and therefore efficacy and toxicity of a drug formulation. A burst release was avoided as it would lead to the drug being cleared rapidly, whilst also causing increased toxicity (Jeong, Bae, & Kim, 2000; Liechty, Kryscio, Slaughter, & Peppas, 2010). Similarly, NPs releasing SN-38 too slowly would lead to insufficient levels of the drug at the target site, producing no therapeutic benefit. A suitable release profile (steady-state concentration of SN-38) was subsequently required as it would give rise to sustained therapeutic drug concentrations at target cells, whilst also allowing for better internalisation. Moreover, previous reports have shown that with a suitable release profile, SN-38 glucuronidation is less efficient (Patnaik et al., 2009). Based on the release data, free SN-38 showed an initial rapid release. The early burst release phase of SN-38 could be due to the low interaction between SN-38 and the vehicle (polymer NP) itself. Moreover, passive diffusion determined by the concentration gradient was the major driving force (Fu & Kao, 2010). As seen in Figure 4.3 and Figure 4.5, certain SB formulations and to a greater extent CA formulations did not display an initial burst release, in comparison to free SN-38.

This slower release initially, was thought to be due to the entrapment of SN-38 drug molecules in the polymer matrix, which prevented its rapid release (Kamaly, Yameen, Wu, & Farokhzad, 2016). The slow-release rate was also expected due to the hydrophobic nature of SN-38. However, all SB formulations released SN-38 faster than CA formulations, with similar release profiles to free drug. A possible explanation for this could be the faster migration of the weakly adsorbed drug molecules, within or on the surface of the NP (Kamaly et al., 2016; Moreno Raja et al., 2019). On the other hand, CA NPs had a slower release profile. This could be due to the slower drug diffusion through the polymer matrix or existing pores present within the inner regions of these formulations (Fredenberg, Wahlgren, Reslow, & Axelsson, 2011). The release profiles were of a typical shape commonly obtained by other polymeric-based nano- or micro-particle delivery systems (M. Chen et al., 2017; England et al., 2017; Fang, Chuang, Wu, Lin, & Lu, 2018; H. C. Lin, Chuang, Cheng, Lin, & Fang, 2019). As a reduction in the release was seen in CA formulations by decreasing the DPn value and since the monomer and divinyl chemistry were consistent throughout, differences, therefore, were within the polymer primary chain length and the subsequent mass of the divinyl monomer. The reduction in SN-38 release in these formulations could be due to several factors influencing SN-38 interactions with the polymeric core of the NP. This could include the increased relative mass of monomer, the increase in chain-end concentration, or the variation in the glass transition temperature that would be present as the primary chain length decreases. Overall the *in vitro* release data highlighted the polymer nanomaterial's that were capable of sustaining SN-38 drug release and this was thought to be beneficial to prolong the time in circulation and reinforce the EPR effect *in vivo*.

Thereafter, to verify whether the released SN-38 was still pharmacologically active, *in vitro* cytotoxicity testing against a panel of CRC cell lines was performed. *In vitro*, the NPs were found to possess potent cytotoxic activity, which was similar to that of free SN-38, but several-fold more potent than irinotecan (Figure 4.7 and Figure 4.8). As an adjunct to monolayer, 3D spheroids were utilised to confirm the cytotoxicity mediated by the selected NPs. As previously shown in Chapter 3:, a similar trend in sensitivity (increased sensitivity) was observed with spheroids treated with SN-38 NPs. The

cytotoxicity data, therefore, indicated that both SB and CA polymer nanomaterial's could undergo efficient cellular uptake and subsequently release therapeutically active SN-38 into the intracellular environment. Before the *in vivo* animal study, an *in vitro* macrophage uptake assay was carried out to evaluate the phagocytosis of NPs by the M1 macrophages of MPS. The data revealed the 8 of the 10 NPs were less readily uptaken than free SN-38. Avoiding or minimising clearance via the MPS would allow for a prolonged time within the systemic circulation, improving the accumulation of the NPs at the tumour site through the EPR effect i.e. taking advantage of the leaky vasculature and poor lymphatic drainage could lead to the delivery of sufficient levels of drug payload. Additionally, all NPs demonstrated surface modification with PEG, which has also been reported to be an effective strategy against opsonisation and phagocytosis (Suk, Xu, Kim, Hanes, & Ensign, 2016). Based on the screening criteria, SB1 and CA16 were chosen for *in vivo* pharmacokinetic analysis.

Plasma SN-38 pharmacokinetic studies were performed in mice, to confirm whether there would be prolonged therapeutic levels of SN-38 in circulation (Figure 4.13). Compared to SN-38 derived from irinotecan, neither SB1 nor CA16 achieved the desired sustained exposure of SN-38 *in vivo* (both NPs produced significantly lower concentrations of SN-38, $P \leq 0.001$), similar to previous studies (M. Chen et al., 2017; Fang et al., 2018; H. C. Lin et al., 2019; Zhou et al., 2014). This was demonstrated as the plasma AUC from SN-38 exposure from irinotecan exposure was 14- and 66-fold higher than the SN-38 exposure from SB1 and CA16 respectively. Consistent with previous reports, SN-38 generated after administration of irinotecan was rapidly cleared into SN-38G (Adkins et al., 2015; Koizumi et al., 2006). Moreover, results were not obtained from free SN-38, most likely due to solubility issues. Interestingly both SB1 and CA16 displayed lower plasma levels of SN-38, as well as the inactive metabolite SN-38G (Figure 4.14). Hence, the data also suggested that the ability of the NPs to escape MPS was limited, meaning that the NPs were possibly accumulating within well-perfused organs (heart, liver, spleen, lung and kidney). This would corroborate with what was observed during the PK study as both SB1 and CA16 treated mice showed signs of slow and laboured breathing (SB1 time-points were shorter due to this reason). These findings are In agreement with the data in several recent publications, which

has shown SN-38 or irinotecan-based NPs to accumulate in organs such as the lungs, subsequently leading to acute respiratory distress syndrome or interstitial pulmonary disease (Fang et al., 2018; Maitani et al., 2013; Passero, Grapsa, Syrigos, & Saif, 2016; Sepehri et al., 2014; Sumitomo et al., 2008; Zhou et al., 2014). To summarise the pharmacokinetic behaviour of SN-38 loaded NPs demonstrated a decreased retention time and exposure of SN-38 in comparison to irinotecan.

However, there were some important limitations to our methodology, which could be improved to better interpret data on NP characteristics, biodistribution and pharmacokinetics. Given that equilibrium dialysis is predominantly a diffusion-controlled process, the appearance of free drug molecules in the acceptor chamber is dependent on the rate of diffusion of free drug molecules across the membrane (Wallace, Li, Nation, & Boyd, 2012). This may lead to an inaccurate representation of drug release, which has also been demonstrated in a study investigating the release of diazepam (Benita & Levy, 1993). Moreover, the methodology was not able to account for any unencapsulated drug present on the surface or within the NP solution and percentage encapsulation within most of the formulations was not confirmed. Hence any differences present could have been due to variations in drug loading. Improvements could have been implemented in our study by, making using of an ultracentrifugation method to separate the free drug from encapsulated fractions, further ensuring sink conditions through the addition of surfactants and measuring drug release in plasma to mimic the *in vivo* situation more closely, whilst also acquiring an understanding of the stability of the NPs within plasma. To further explore and understand the pharmacokinetic profiles of SB1 and CA16 and their bio-distribution, *in vitro* uptake studies using macrophages present in specific organs (liver, spleen, lung and kidney) could have been performed during the screening process. Similarly, specifically understanding the differences in M1 and M2 macrophage uptake would also have been valuable. Moreover, the formation of a protein corona on the NP surface and how this affects its interaction with cells (distribution and clearance) needed to be considered. Lastly, the biocompatibility was another important design feature that required investigation preclinically. This would have allowed

confirmation that in the absence of SN-38 loading, the polymer NPs were well tolerated and elicited no observable side effects (endotoxemia) or immune responses.

4.5 Conclusion

In conclusion, a panel of polymeric NPs encapsulating SN-38 were developed and characterised to enable the solubilisation and delivery of SN-38. Following an initial screen involving drug release, cytotoxicity and macrophage uptake, SB1 and CA16 were selected. Despite promising results *in vitro*, no benefit for the pharmacokinetic parameters was observed *in vivo*. Further research is required to fine-tune the NPs to achieve appropriate features in preclinical studies and to ultimately translate these NPs into the clinic.

Chapter 5: General discussion

5.1 Introduction

The neoadjuvant and adjuvant treatment of CRC with chemotherapy is currently reliant upon standardised regimens. Responses to standard therapy can vary considerably, with several patients experiencing toxic side effects and life-threatening complications. Bringing novel medications to patients remains a considerable challenge. Attrition rates within the pharmaceutical industry are high and many of the easily "druggable" targets have been already been addressed, leaving key targets that are considered "undruggable" by traditional small molecule medicinal chemistry or antibodies. One of the challenges to innovative medicines remains a lack of therapeutic index. Nanomedicines can enable new drug products by altering a candidate drug's distribution and enhancing drug concentrations at tumour sites relative to healthy tissue. This change in biodistribution together with careful selection of drug release rate from a NP has the potential to improve both efficacy and safety, therefore enabling promising treatments otherwise limited by a narrow therapeutic index. Commonly designed for intravenous injection, *in vivo* studies of NPs have been shown to deliver anticancer drugs more effectively to tumour cells (Carie et al., 2011; M. Chen et al., 2017; England et al., 2017). Of the numerous strategies being investigated, drug-loaded NPs show particular promise.

Irinotecan is a prodrug converted into the activate metabolite SN-38, which acts as a TOP I inhibitor, preventing cell division and replication. Its metabolism is complex, relying on the CES's, predominantly located within the liver and tumour site, for conversion to SN-38, UGT1A1 for glucuronidation to its inactive form SN-38G and the ABC transporters for excretion into bile. While irinotecan has clinical utility, its various limitations suggest further improvement may be possible. One key limitation is that only 2−10% of an injected dose of irinotecan is converted to SN-38 in humans (G. G. Chabot, 1997; Senter et al., 2001; J. G. Slatter et al., 2000). Also, the lactone E-ring of SN-38 can be readily converted to an open carboxylate form that is inactive against TOP I and excessively binds to human serum albumin (Mathijssen et al., 2001; J. G. Slatter et al., 2000; N. F. Smith, Figg, & Sparreboom, 2006).

Particularly, it was shown in humans that 24 hours after irinotecan infusion, approximately 25% and 55% of irinotecan and SN-38, respectively, were in the closed lactone form (G. G. Chabot, 1997). Preventing the conversion to the inactive open carboxylate form of the molecule may have therapeutic benefit. Finally, while SN-38 has 100- to 1000-fold more potent *in vitro* cytotoxic activity compared with irinotecan (G. G. Chabot, 1997), it has poor solubility in any pharmaceutically acceptable excipient and cannot be used for systemic applications.

The overriding aim of this thesis was to develop and characterise a panel of water-soluble SN-38 drug-loaded NPs. An *in vitro* tiered screening system was developed and the best candidates were selected for *in vivo* analysis. As we wanted to target CRC liver metastases, the approach involved developing NPs with long circulation times to enable better tumour uptake and to limit the release of SN-38 in systemic circulation, so to minimise non-target organ accumulation. To prolong systemic retention, the NPs needed to circumvent and minimise the liver, lung and spleen accumulation by possessing features to decrease scavenger cell uptake and subsequent off-target toxicity. This is typically controlled by the addition of polymers and depends on the size, surface charge, hydrophilicity, polymer type and protein binding. A schematic of what we were attempting to achieve is shown in Figure 5.1.

5.2 LC-MS/MS Method Development

Chapter 2: describes the development of an LC-MS/MS assay for the quantitative detection of irinotecan, SN-38 and SN-38G in a variety of biological matrices. The assay was fully validated to FDA standards. The assay was sensitive, specific, accurate, and reproducible, and was successfully used throughout various parts of the thesis. As demonstrated in Chapter 4:, the method was able to characterise the pharmacokinetic attributes and verify the appropriateness of the NP formulations to achieve the intended systemic exposure level. The assay could be additionally adapted to determine the concentrations of both the carboxylate and lactone forms of SN-38 (L. P. Rivory et al., 1994; X.

Yang et al., 2005). Given that only the lactone form is active, such measurements would provide greater insight into the pharmacokinetics and underlying mechanisms of SN-38 NPs.

5.3 The Establishment and Characterisation of Colorectal Cancer Spheroids

Traditional drug studies have been performed in 2D cultures, where cells are seeded to form a monolayer. This method has been extensively used by researchers and pharmaceutical companies because of its simplicity. However, the translation of the results obtained from cancer cell monolayers to a tumour is not promising, because 2D models are unable to replicate the cell-cell and cell-ECM signalling of complex 3D tissues (Pampaloni, Reynaud, & Stelzer, 2007). As a result, great effort has been made during the past few years to develop more reliable *in vitro* models, particularly by utilising 3D cell cultures (J. B. Kim, 2005). Therefore in Chapter 3: the applicability of an easy-to-use 3D cell culture platform based on CRC cell line spheroids was demonstrated. Using HCT116 and CT26 cells, methods were developed to (1) assess the histology and structure of spheroids, (2) analyse SN-38 and irinotecan cytotoxicity, (3) follow growth inhibitory effects over time (repeated exposures) similar to *in vivo* efficacy studies and (4) evaluate drug uptake. These methods were used to investigate the main hypothesis that 3D spheroids provide a more relevant *in vitro* model than monolayer cells for the testing of therapeutic agents. To investigate this, responses of cells to irinotecan and SN-38 in 2D and 3D were compared.

Spheroids grew according to sigmoidal growth patterns reflective of tumour growth *in vivo* (Figure 3.3 and Figure 3.4) and possessed histological features similar to those of the native tumour microenvironment including gradients in cell proliferation and regions of necrosis (Figure 3.5 and Figure 3.6). As shown in Figure 3.8 and Figure 3.9 spheroids demonstrated considerably greater resistance to treatment with irinotecan or SN-38, relative to cells grown in monolayer cultures. This may be a result of the limited exposure of cells within spheroids to treatment due to poor drug penetration, a reduction in cellular proliferation and/or resistance associated with 3-D cell adhesion. As a result, most of the cytotoxic effects of the drugs would, therefore, be observed in the outer layers

of the cells in the spheroids. Moreover, the quiescent zone in the tumour spheroid can alter the cytotoxic effect of drugs. As both irinotecan and SN-38 are DNA damaging agents, these drugs are effective in rapidly proliferating cancer cells. However, due to the non-proliferating nature of cells in the quiescent zone, which is located between the core and outer layer, cells in the dormant stage remain protected (Jo et al., 2018). For this reason, tumour spheroids may reduce in size, as observed in Figure 3.10C and Figure 3.11C but are not completely killed. Therefore, the tumour can resume proliferation once the cells in the outer layer are dead (Aljitawi et al., 2014; Chitcholtan, Asselin, Parent, Sykes, & Evans, 2013). However, following repeated exposures, spheroids became more sensitive with each subsequent treatment. However direct comparison to monolayers could not be made, as 2D cultures are not suited for long term culture. The cytotoxicity data was in agreement with the literature whereby many anticancer drugs with similar mechanisms of action (i.e. targeting actively proliferating cells) were more resistant than cells cultured in monolayer (Horning et al., 2008). Differential drug responses of cells grown in 3D versus 2D are not solely related to the differential zones of proliferation. Multiple studies report differences in gene and protein expression between 3D spheroids and 2D cultures that impact drug efficacy, metabolism, and cell communication (Aljitawi et al., 2014; Edmondson et al., 2014; O. Jeon, Marks, Wolfson, & Alsberg, 2016; Ravi, Paramesh, Kaviya, Anuradha, & Solomon, 2015; Sakai, Ito, & Kawakami, 2010; Sato et al., 2016). Our data revealed a profound decrease in protein expression in cancer cells grown as spheroids, as compared to those cultured in the respective conventional 2D system. However, MRP2 was induced to a greater degree in spheroids as compared to monolayer cells. Increased levels of this multidrug resistance protein have been previously associated with increased resistance to drug treatment (Hinoshita et al., 2000; Knuchel, Hofstadter, Jenkins, & Masters, 1989; Oloumi, MacPhail, Johnston, Banath, & Olive, 2000). This could have been another contributing factor to the reduced chemotherapeutic efficacy seen in our spheroids (Table 3.5). Further studies are required to investigate whether expression patterns observed in spheroids more closely resemble those found *in vivo*. In particular, understanding changes in protein expression in the repeated exposure studies, would further aid our understanding of the

mechanisms underlying the changes in sensitivity seen. Additionally, using proteomic approaches would be useful in determining the supposedly wide spectrum of changes between 2D and 3D cultured cells, both in terms of pathways involved and protein patterns. These could include studies on other cell lines, including primary tumour tissues, as well as other drugs and related proteins which would help further study the correlation and to understand the role of cell culture type in protein expression levels which may, in turn, impact the cellular responses to anti-cancer therapeutics. To better recapitulate the *in vivo* multicellular complexity and microenvironment of tumours, 3D co-cultures have been developed. Co-cultures usually combine tumour cells with stromal cell types such as endothelial cells, immune cells or cancer-associated fibroblasts. For example, co-culture of hepatic stellate cells (HSC) with tumour cells *in vitro* significantly increased the invasion and proliferation of tumour cells (Okabe et al., 2009). Implementing a vascular component in 3D cell culture models is important since blood vessels can create oxygen gradients that in turn can lead to endothelial sprouting and promote cell migration via chemotaxis (Mosadegh, Xiong, Dunham, & Min, 2015; Verbridge et al., 2013). Recently, microfabricated devices with capillary-like channels and spheroid-on-a-chip systems have become attractive platforms in mimicking the fluidic *in vivo* microenvironment. It is anticipated that such organotypic *in vitro* models will increase our understanding of human bodily functions, are of value for disease modelling and screening of novel therapeutic interventions.

Collectively, the results obtained in this chapter highlight the importance of incorporating complexity into *in vitro* tumour models used for studying cancer and for preclinical phases of the drug discovery process. Further enhancement of the spheroid model could help uncover the role of biochemical and mechanical cues of the tumour microenvironment on cancer cell behaviours.

5.4 Preclinical Assessment of SN-38 Loaded Nanoparticles

Despite improvements in chemotherapeutic drugs, the efficacy of conventional delivery systems for CRC is limited by non-specific toxic effects. Hence, there is a need to develop delivery systems capable of delivering high drug concentrations to the tumour site, while minimising damage to surrounding normal tissue. As discussed previously, NP mediated drug delivery is a promising technology that offers a degree of controlled release and the ability to limit the off-target effects in a way that the bulk material or the free drug is unable to. The overarching goal of Chapter 4: was to develop, characterise and evaluate a panel of SN-38 NP formulations, before systemic administration in mice *in vivo*, with an overall focus on delivery to CRC liver metastases. A tiered *in vitro* screen was used which consisted of assays involving drug release, cytotoxicity and macrophage uptake. It made use of the LC-MS/MS method and CRC spheroids which were developed and characterised in Chapter 2: and Chapter 3:, respectively. Candidates to take forward *in vivo* were selected on their capability of protecting SN-38 from premature burst release, maintaining the cytotoxicity of SN-38 in CRC cells and evading macrophage uptake. Ten NPs were selected on the basis that they did not show an initial burst release and had an overall slower sustained release profile in comparison to free SN-38 (Figure 4.6). Cytotoxicity was comparable to that obtained for free SN-38 and significantly increased in comparison to the parent drug, irinotecan (Figure 4.7 and Figure 4.8). An uptake assay was also used to differentiate between how NPs interact with M1 macrophages (Figure 4.11). As a result, SB1 and CA16 were taken forward for the proof-of-concept *in vivo* study. However, neither formulation showed any beneficial effects *in vivo* i.e. they did not prolong or enhance the levels of SN-38 in circulation (plasma half-life). As discussed in Chapter 4:, the non-specific uptake of NPs by the MPS in liver, spleen and lung may have contributed to the lower plasma levels of SN-38. This corroborated with the physical signs of toxicity in mice treated with either of the polymer nanomaterial's and also with previous studies utilising SN-38 NPs (Fang et al., 2018; H. Liu et al., 2015; Palakurthi, 2015).

It is important to consider the implications of these results for future studies, as certain limitations could be addressed. In comparison to SN-38 release data from the literature, not taking into account

the methodology used, the NPs developed within this thesis displayed faster release profiles (Al-Kasspooles et al., 2013; Carie et al., 2011; M. Chen et al., 2017; England et al., 2017; Fang et al., 2018; H. Zhang et al., 2013). This could indicate the need for developing NPs that release at an even slower rate than what has been presented in the thesis. Ideally, an *in vitro* release method should simulate *in vivo* conditions and release mechanisms. One disadvantage of the rapid equilibrium dialysis method employed is that it can occasionally restrict the diffusion and/or interact with drug molecules (D'Souza, 2014). Employing a beaker dialysis setup (larger volume) would ensure that sink conditions were maintained throughout and radiolabelling of the NPs would give important insights to address the above-mentioned issues. As demonstrated the macrophage uptake did not correlate to NP *in vivo* performance. More sophisticated testing of the polymer material and drug-loaded NPs involving the MPS within the different organ systems is required, to ensure that relevant correlative *in vivo* information is derived. This would help to elucidate how the NPs are cleared or elicit toxicity (leukocyte proliferation *in vitro*, release *in vitro* of TNF-α, IL-1β and IL-8), thereby providing guidelines for direct manipulation of the NPs physicochemical characteristics to minimise uptake and reduce potential inflammatory-mediated events. A further study that could be performed *in vivo* was to measure levels of the drug in the different organ compartments. Hence additional information regarding the biodistribution of the NPs would be generated, thereby allowing further fine-tuning of the NP physicochemical properties. In this regard, subsequent experiments with appropriately characterised and redeveloped NPs could be carried out using CRC liver metastases tumour models to investigate if NP administration leads to the improvement of *in vivo* therapeutic index and the performance of the therapeutic agent.

An alternative approach to reduce the non-specific uptake and enhance the selectivity of the NPs would be to introduce an active targeting component on the NP surface. Relevant tumour-specific targets could be identified through proteomic comparison of the liver metastases, primary tumour tissue and normal mucosa. Identified upregulated proteins that represent attractive targets could then be investigated for their suitability. Previous studies at the University of Liverpool (unpublished) have

uncovered the following tumour membrane proteins; Filamin-A, Neuroblast differentiation-associated protein AHNAK, Talin-1, Fibronectin, Complement C3, Ig gamma-1 chain C region, Alpha-enolase, Alpha-actinin-1, Clathrin heavy chain 1 and Vinculin. Another factor that needs consideration is drug loading (≥20% or greater is generally the accepted minimum level). Low drug loading may significantly limit the clinical application because repeated administration of a large number of inactive carriers into patients may induce systemic toxicity (Palakurthi, 2015). However, these NPs have the potential for patient stratification, as irinotecan treated mCRC patients were associated with lower response rates in individuals who displayed low expression of CES2 and high expression of TOP I (Shaojun, Li, Haixin, & Guisheng, 2018). This would suggest that irinotecan treatment is ineffective, due to the low generation of the active drug. Hence, directly delivering SN-38 via NPs would offer a potential solution to patients expressing such profiles (bypassing CES2 metabolism). In summary, the data presented in Chapter 4: showed the successful encapsulation of SN-38 in a water-soluble form. Further work is required to optimise the physicochemical properties of the NPs for proof-of-concept studies.

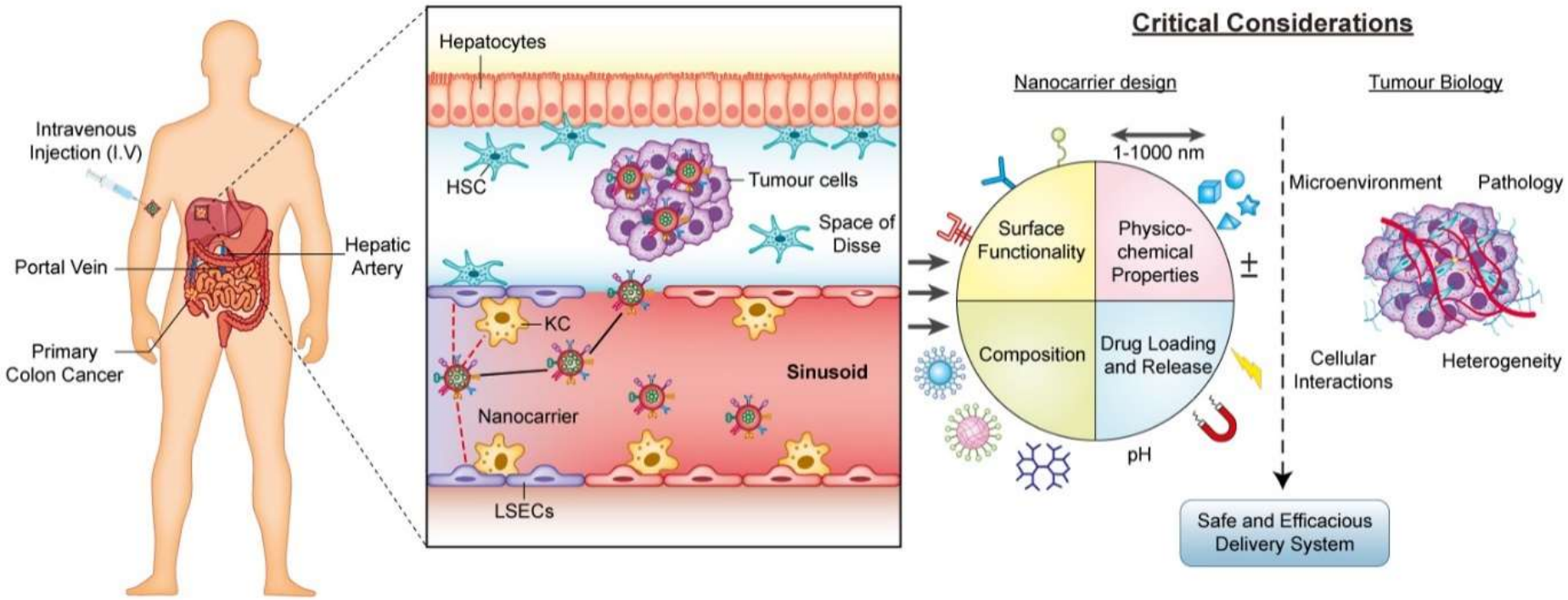

Figure 5.1 Following intravenous injection, nanoparticles are distributed systemically through the bloodstream. Nanoparticles can enter the liver via the portal vein after which, they have to evade tissue-resident macrophages (Kupffer cells and liver sinusoidal endothelial cells). If successful they can accumulate at the tumour site, by taking advantage of the enhanced permeation and retention effect. However, a fundamental understanding of tumour biology and its physiological features is necessary for the design and development of effective nanomedicines.

5.5 Future Considerations

Despite technological improvements in nanotechnology, the complexity of biological systems hinders the prospect of nanomedicines being applied in cancer therapy. When designing novel polymer-based drug-delivery systems for translation into the clinic, there are many considerations to take into account before and during development. Several biological barriers, aspects of the tumour biology, together with the physicochemical features of the nanocarrier need to be considered to develop effective nanotherapeutics for CRC patients with liver metastases. From a platform perspective, important features for polymer carriers include synthetic reproducibility, low toxicity/immunogenicity, a suitable clearance mechanism/biodegradability and capacity for high drug loading. Other considerations should include ease of manufacture, formulation, analytical characterisation and low cost of goods. Based on the data presented in this thesis, it is clear that incorporating an interdisciplinary approach when developing nanomedicines should assure the appropriate disease-driven design and that this will form a critical step in improving their clinical translation.

5.5.1 Improving Translation

The application of nanotechnology in drug delivery is increasing rapidly. However, despite significant advances in materials understanding, clinical translation is still limited. Research is now shifting away from traditional methods that prioritise the drug delivery system, to disease-based design approaches; a concept where the underlying biology and the material's physicochemical properties are given precedence (Hare et al., 2017). As in the case of CRC liver metastases, a better understanding of the disease pathophysiology and how this can influence accumulation, distribution, retention and efficacy requires further consideration. However, these tumours can be highly heterogeneous and throughout the progression of the disease, intra- and inter-patient variability is apparent (Moro, Bozoky, & Gerling, 2018; Sveen et al., 2016; Vermaat et al., 2012). Consequently, certain tumours may be more

amenable to NP drug delivery than others, as fewer barriers may impede the disease-specific localisation of NPs.

A major issue with the clinical translation of NPs is the gap between preclinical and clinical studies. Currently, preclinical models of CRC liver metastases do not completely recapitulate the different aspects of these tumours nor the heterogeneity. The majority of animal models are syngeneic or xenografts and use *ex vivo* manipulated tumours. Therefore, their ability to mimic CRC liver metastases is limited. Differences in features such as the size/pattern of the tumour, vascularity, levels of IFP and presence of hypoxia highlight some of the challenges of using such models for estimating clinical NP performance. To offset this, various sophisticated *in vitro* platforms that act as predictive human tissue models are being developed to profile NPs. Examples include 3D tumour models (spheroids and organoids) consisting of several cell types as well as components of the ECM, which display improved predictive power of *in vivo* pharmacological efficacy as compared to traditional monolayer cell culture (Durymanov et al., 2019; Fong, Toh, Yu, & Chow, 2017; Langhans, 2018). More recently it was demonstrated that organoids derived from human CRC liver metastases were able to recapitulate additional aspects of the disease (Buzzelli, Ouaret, Brown, Allen, & Muschel, 2018). When applied *in vivo*, metastatic CRC organoids were competent and colonised within the liver, displaying their potential for translation from *in vitro* to *in vivo* preclinical models (Cristobal et al., 2017; Fujii et al., 2016). As CRC metastasis is a multifaceted and heterogeneous disease, merging different organoid models offers the opportunity to study the effect of intratumoural heterogeneity on CRC phenotypes. Furthermore, patient-derived xenograft animal models which display metastasis are the 'go-to' models being used to characterise *in vivo* endpoints. They can mimic tumour cell interactions and generate a relevant tumour microenvironment (T. Jiang, Jin, Liu, & Pang, 2017). A shortcoming of patient-derived xenograft models is that the immune system is impaired, which impacts cancer progression (Jung et al., 2017). An alternative 'go to' approach for developing liver metastasis is the use of genetically engineered mouse models, which have intact immune systems. This method poses challenges in evaluating therapeutic responses, as the metastases have long latency (Young, Hong,

Lee, & Cho, 2017). At present, there is no ideal animal model for entirely recapitulating the mechanisms and processes found in human CRC liver metastasis. Consequently, multiple models are frequently needed to address specific clinically relevant experimental questions.

More advanced models termed 'organ-on-a-chip' systems may be key to accurately assessing the toxicity, pharmacokinetics and pharmacodynamics of NPs. These microfluidic devices can integrate vascular networks, reproduce the tumour microenvironment and have the potential for personalisation (Millard et al., 2017). However, the use of these devices for evaluating NPs has not been extensively implemented, meaning that there is not yet enough data to show their predictive power clinically. Nevertheless, the application of more relevant preclinical models in NP testing will likely translate to clinically beneficial outcomes in the medium- to long term.

Furthermore, features of the tumour as well as the various facets that compose the tumour vasculature and microenvironment may diminish the effects of NPs and need to be considered. These have been outlined below in Figure 5.2.

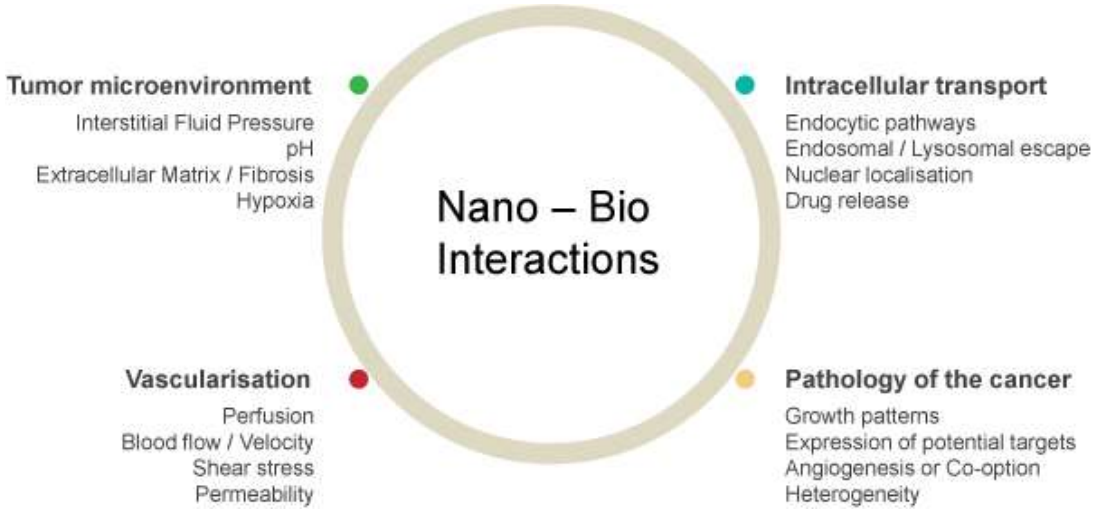

Figure 5.2 Overview of several key interactions involving NPs within the tumour

5.5.2 Vascularisation and Perfusion

As mentioned previously in 0, the tumour vasculature is tortuous and irregular leading to compromised blood flow. This may further influence the site-specific accumulation of NPs. Although the permeability of the tumour vasculature forms the basis of the EPR effect, it also allows excessive

extravasation of blood constituents such as fluid and plasma macromolecules. Elevated fluid viscosity inside the tumour mass is therefore apparent, hindering the movement of NPs. Vascular perfusion inside tumours is heterogeneous and certain intratumoural regions can be hypoperfused due to a decreased blood flow caused by plasma leakage, in conjunction with blood vessel compression (Stylianopoulos et al., 2018). Recent findings have revealed that the levels of type IV collagen are significantly higher inside liver metastases when compared to their primary tumours (Kai et al., 2019). In general, it is thought that liver metastases are poorly perfused in comparison to their primary tumour and their vascular permeability is limited (Tanei et al., 2016). Accordingly, NP delivery is limited as tumour cells are too distant from normal functioning vessels, ultimately restricting the distribution of therapeutic agents.

Previous research has shown that the hepatic artery supplies large metastatic tumours, whilst micrometastases (<2mm) have been reported to be predominantly supplied by the portal venous system (Casillas et al., 1997). More recent observations have shown that vascularisation also differs depending on the type of liver metastases. Due to vessel co-option, replacement liver metastases are often in continuum with the sinusoidal blood vessels, whereas in desmoplastic liver metastases the capillaries connect to blood vessels of the arteriole (Lazaris et al., 2018; Van den Eynden et al., 2012). Further evidence revealing that replacement liver metastases co-opt the pre-existing vasculature is indicated in reports, as co-opted vessels maintain expression of lymphatic vessel endothelial hyaluronan receptor (LYVE)-1 (Stessels et al., 2004). On the other hand, desmoplastic liver metastases contained very few LYVE-1-expressing vessels, indicative of angiogenesis. This angiogenesis seen in desmoplastic liver metastases is distinguished by regions of high vessel density termed vascular hotspots. These newly formed blood vessels appear leaky and functionally impaired due to the presence of fibrin deposits. In contrast, replacement liver metastases display a small amount of proliferating endothelial cells, with no apparent signs of fibrin deposition (Stessels et al., 2004). The appearance of vessel co-option could have important implications in the context of NP delivery. In this manner, liver metastases may incorporate ‘normal-looking’ vasculature i.e. less permeable and

unlikely to display the EPR effect. Hence, NPs whose actions solely rely on the abnormal vasculature may be impaired and any strategies to normalise the tumour vasculature through antiangiogenic therapies may be hindered by drug resistance, as seen from previous studies (Emblem & Jain, 2016; Frentzas et al., 2016; Qian, 2013). More recently, it was highlighted that approximately two-thirds of patients presented with mixed growth patterns (mixed phenotype of co-opted vessels and angiogenesis) (van Dam et al., 2017). Therapeutic approaches that can suppress both angiogenesis and vessel co-option may, therefore, be justified. In particular, specifically targeting the co-opted vasculature by capitalising on their altered protein expression via active targeting strategies, may be a possibility (Roodink et al., 2010).

Drug delivery strategies need to ensure sufficient drug penetration/distribution is achieved, such that both the peripheral and central regions of the tumour are accessed. Some researchers have sought to manipulate the tumour vasculature through utilising hyperthermia and growth factors, with the intent being to facilitate extravasation of NPs into the tumour microenvironment (Chatterjee, Diagaradjane, & Krishnan, 2011; W. Jiang, Huang, An, & Kim, 2015). This is exemplified by local hyperthermia (41°C) eliciting an increase in vascular permeability up to 10μm in a variety of tumour models, allowing greater penetration into the tumour microenvironment (L. Li et al., 2013). For instance, ThermoDox® (lyso-thermosensitive liposomal doxorubicin technology) was combined with image-guided radiofrequency ablation in a porcine model (Swenson et al., 2015). In the presence of heat, the amount of doxorubicin deposited increased and the treatment zone was enlarged. Despite this, no clinically meaningful benefit was found in patients with hepatocellular carcinoma in the phase III HEAT study (Lencioni & Cioni, 2016). Similarly, a phase 1 trial examined the combined treatment of thermosensitive liposomal doxorubicin and non-invasive focused ultrasound hyperthermia (39.5–43°C), with the latter being used to trigger drug release (Lyon et al., 2018). The study displayed enhanced intratumoural delivery in human liver tumours (patients investigated had solid primary or metastatic tumours), whilst also posing no additional safety concerns in comparison to standard chemotherapy alone. Hyperthermia itself is able to exert a cytotoxic effect and following combination

with certain cytotoxic agents, synergistic effects are present (Jacquet, Averbach, Stuart, Chang, & Sugarbaker, 1998; Kusamura, Dominique, Baratti, Younan, & Deraco, 2008). Other reports have also shown hyperthermia to modify membrane permeability, drug uptake and drug penetration (Di Miceli et al., 2012; Hompes et al., 2012). A recent meta-analysis displayed that patients with mCRC show a tendency towards increased median overall survival after cytoreductive surgery and hyperthermic intraperitoneal chemotherapy combined with resection of liver metastases, when compared to treatment with systemic chemotherapy (de Cuba et al., 2013). However, there are several challenges still facing the mentioned approaches, which include tumour heterogeneity and regional variation. The tumour vascular network remains a major obstacle in the vascular transportation of NPs.

5.5.3 The Tumour Microenvironment

The mCRC tumour microenvironment is a multifaceted dynamic system. Its regulation depends on the interactions between cellular (tumour cells and resident cells of the liver) and non-cellular components (hypoxia, pH, signalling molecules and ECM). Compared to normal tissue, the tumour microenvironment possesses numerous unique characteristics. It presents an acidic pH due to the Warburg effect and hypoxia is generated as cells residing deep in the tumour mass are deprived of oxygen because of inadequate vasculature, lack of nutrients and uncontrolled proliferation. In particular, hypoxia within CRC liver metastases has been observed at an average distance of 80µm from the vasculature and it is postulated that large oxygen consumption is the principal contributing factor (van Laarhoven et al., 2006). Taking into consideration such features of the tumour microenvironment when designing NPs, may aid their delivery into tumours. Various NPs have been designed to utilise the acidic pH microenvironment to selectively trigger release. For instance, polymeric micelles with a pH-sensitive component containing cell-penetrating peptides were designed for the treatment of CRC (Bao et al., 2016). Following intravenous administration, findings revealed the destabilisation of the polymer at lower pH (pH 6.8) allowed for enhanced action, both *in vitro* and *in vivo*, owing to improved targeting and cellular uptake. The hypoxia in tumours can also be employed to control drug release or activate prodrugs. Kulkarni *et al.* constructed lipid NPs containing a hypoxia-

sensitive component, which displayed a better penetration depth and cytotoxicity under hypoxic conditions (Kulkarni et al., 2016). Similarly, hypoxia-responsive doxorubicin NPs have been reported to selectively release drug under hypoxic conditions (Thambi et al., 2014). These NPs exhibited enhanced anti-tumour efficacy, higher toxicity to hypoxic cells and *in vivo* imaging showed them to successfully accumulate at the tumour site. The presence of improved penetration demonstrated the advantages offered by hypoxia-activated chemotherapeutic delivery. Even with recent advances in the development of hypoxia-responsive NPs, accessing hypoxic regions located deep inside the tumour remains an unmet challenge.

Another hurdle compromising the transport of NPs is the high interstitial fluid pressure (IFP). IFP is elevated as a result of the abnormal vasculature, intratumoural lymphatic vessels that do not effectively drain interstitial fluid and a dense ECM. Moreover, it has been demonstrated in the literature that patients with CRC liver metastases, had a mean IFP ten times above the IFP of normal liver tissues (Less et al., 1992). The IFP at regions close to the tumour margin is often normal, meaning that there is an outward pressure gradient (Jain, Tong, & Munn, 2007). Consequently, it can limit the ability of NPs to diffuse into the tumour interstitium, slow down their biodistribution, and hinder NP transport within the vasculature. In the worst-case scenario, the IFP can cause the intravasation of NPs back into the blood supply. To try and counteract this, researchers utilised gelatin-modified cationic lipid NPs intending to reduce tumour IFP and subsequently improve drug delivery. It was demonstrated that delivery of imatinib caused a significant reduction in tumour IFP when combined with docetaxel and quercetin in NPs (Gao et al., 2017). Likewise, the reduction of tumour IFP by eradicating fibroblasts promoted deeper chemotherapeutic penetration in HepG2 spheroids, thereby demonstrating that reducing tumour IFP could be beneficial for improving NP delivery (B. L. Chen et al., 2016). PEGPH20 is a therapeutic candidate currently being explored for improving local permeation, through the degradation of hyaluronan in the tumour microenvironment. This reduces tumour IFP, and PEGPH20 is thought to enable increased access to anti-cancer therapeutics and immune cells (Halozyme, 2019). Its use in advanced pancreatic adenocarcinoma and metastatic breast

cancer have shown encouraging results in terms of safety, overall survival and response rate, thereby prompting further studies (Gourd, 2018).

The ECM consists mainly of a cross-linked network of collagen, elastin fibres, proteoglycans and hyaluronic acid. ECM proteins can interact with growth factors promoting cell migration and metastatic progression. The ECM is often denser and highly cross-linked within tumours. Patients with CRC liver metastases have shown to display abnormal ECM protein synthesis and degradation, with collagen turnover related proteins being up-regulated (Van Huizen et al., 2019; Williamson, Sultanpuram, & Sendi, 2019). This may pose a significant barrier to the diffusion of NPs through the interstitium, causing drug release distant from the tumour cells. Within the tumour microenvironment transdifferentiated HSCs, tumour associated macrophages and the KCs create a reactive tumour stroma by producing a plethora of remodelling factors, including the proteolytic matrix metalloproteinase enzymes involved in ECM turnover (Kang, Gores, & Shah, 2011). This further impacts the composition, structure and elasticity of the ECM. These factors have to be accounted for, in order to obtain appropriate interstitial penetration and homogeneous drug distribution. In conjunction with this, combining locoregional therapy such as hepatic arterial infusion or transarterial chemoembolisation with nanotechnology and the use of intratumoural depots/implants for sustained release may overcome the limitations of tumour biology. In a rat model of CRC liver metastases, Kauffels *et al.* were able to show that delivery of drug-loaded into embolisation particles (Irinotecan with EmboCept® S) using hepatic arterial infusion led to significantly higher concentrations within the tumour when compared with systemic administration (Kauffels et al., 2019). The application and toxicity of such delivery strategies require further investigation.

It is still unknown to what extent the tumour microenvironment, influences the different metastatic growth patterns and directs whether blood vessels are pre-existing or newly formed. Such attributes of CRC liver metastases are not fully understood in humans, with research being primarily conducted in animal models. Experiments have suggested that the adopted growth pattern is strongly associated

with the route of dissemination into the liver (Bugyik et al., 2016; Paku, Kopper, & Nagy, 2005; Paku & Lapis, 1993). In a mouse model of liver metastases, once tumour cells were delivered into the liver via the arterial system they displayed signs of angiogenesis, as seen by the presence of numerous small vessels. Whereas, entry into the liver via the portal vein corresponded with co-option of sinusoidal vessels (Paku & Lapis, 1993). Mechanistic features of vascularisation at early stages of CRC liver metastases in humans have not been completely described. It is believed that many elements such as the tumour cells, angiogenic factors (VEGF, HIF-1α, E-selectin and endothelin) and the host microenvironment influence this process. Published reports have pointed out that activated HSCs play a central role in the development of the vasculature (Paku et al., 2005; B. Xu, Shen, Cao, & Jia, 2013). They are thought to create a proangiogenic microenvironment and to be responsible for the recruitment and survival of endothelial cells. Researchers investigated changes that occur in intratumoural microvessels and microcirculation during the establishment of liver metastases in mice. Findings showed that liver metastases smaller than 500μm were hypovascular, whilst those larger than 2000μm showed an exclusively arterial blood supply. Increased alpha-smooth muscle actin positive arterioles and levels of CD34 (a marker of tumour neovascularization) were also seen (Archer & Gray, 1989; Joo et al., 2011; Y. Liu & Matsui, 2007). Such features could have significant implications for the delivery of NPs, as accessing hypovascular tumours would be challenging and the differences in vascularisation will likely influence NP tumour accumulation.

5.5.4 Active Targeting

As mentioned in 0, the active targeting of NPs is also a promising approach to facilitate their internalisation. Active targeting approaches have been documented to provide clinical benefits in cancer therapy, in large part due to their ability to target molecular markers overexpressed on the membranes of cancerous cells in comparison with normal cells (Yu, Tai, Xue, Lee, & Lee, 2010). Many colon-targeted approaches employ targeting ligands such as folic acid, hyaluronic acid, lectin, mannose, EGFR and antibodies by surface functionalization of nano-drug delivery systems for the active targeting of a disease site (Byrne, Betancourt, & Brannon-Peppas, 2008). To meet the actual

need, these advanced medicines can be developed based on tumour genetic profiles allowing tailoring of targeting approaches and pre-selection of patients, so-called personalised nanomedicine (Fornaguera & Garcia-Celma, 2017; Lammers, Rizzo, Storm, & Kiessling, 2012; Patel, Pattni, Abouzeid, & Torchilin, 2013).

Additionally, the interactions between targeting ligands decorated on nano-drug delivery systems and particular receptors overexpressed at the diseased site or specific cells are expected to enhance the adhesion and internalisation of NPs. These effects will lead to selective drug accumulation at the target site that may increase therapeutic efficacy and reduce side effects. Endocytic pathways may result in trafficking, to either the acidic environment of lysosomes where the NP is subsequently degraded or a non-target organelle site. In light of this, recent research has focused on strategies to promote endosomal escape or avoid lysosomes. The incorporation of cationic polymers, such as polyethylenimine and poly-L-lysine, in NP design, represents a viable strategy for inducing release from endosomal compartments. The cationic charge of the NP interacts with the outer negatively charged surface of the endosomal membrane, leading to membrane flipping and subsequent destabilisation, also known as the flip-flop mechanism (Varkouhi, Scholte, Storm, & Haisma, 2011). Furthermore, pH-sensitive material can induce endosomal escape via the proton sponge effect. Buffering polymers absorb protons thereby preventing acidification of endosomal vesicles. This ultimately leads to osmotic swelling inside the endosome, membrane rupture and eventual leakage of NPs into the cytosol. Some drugs may take effect instantly, whilst those that act upon DNA must cross the nuclear membrane to exert their therapeutic effect.

5.6 Perspectives and Conclusion

Current therapeutic options to target CRC liver metastases are limited and the clinical need to deliver tolerable and effective therapeutics to such regions is clear. It is hoped that designing agents to efficiently access the liver and eradicate metastases, will provide a larger survival benefit in comparison to current chemotherapy, which is only of modest efficacy. In addition to CRC, the liver is a common site of metastasis for various types of solid tumours including sarcoma, breast, kidney, pancreatic, ovarian, prostate and lung cancers (Brodt, 2011; Fan & Gao, 2017; Hess et al., 2006). As a metastatic site, the liver poses significant challenges, which impairs drug distribution and subsequent efficacy. An anti-metastatic nanotechnology-based approach may therefore present a promising route for tackling such issues.

Evidently, successful drug delivery is hampered by the presence of several biological and physicochemical barriers mentioned above, which in turn impairs the ability to effectively treat cancers. Rather than designing nanomedicines that take a holistic approach i.e. addressing each and every stumbling block, the focus should remain on the development of a safe and efficacious drug delivery system. In relation to CRC liver metastases this involves selectively targeting the tumour cells, whilst simultaneously minimising non-specific interactions, be it binding with or uptake into other cell types located within the hepatic sinusoids (B cells, hepatocytes, KCs and LSECs). This may be central to additionally targeting micrometastases which often go undetected and are associated with poor prognosis. Efforts also need to be made to improve extravasation and intratumoural accumulation, both of which may benefit the efficacy of the treatment. Coincidentally, ensuring that the drug is either released so that it diffuses throughout the tumour region, or that the drug is delivered intact to its site of action, are critical factors in assuring efficacy. Although the physicochemical properties of nanomedicines may not be directly involved in the above processes, collectively with the tumour biology they play a key role in determining the interactions and pharmacokinetics of nanomedicines. In view of this, the physicochemical properties of the NP need to be optimised (size, charge, shape

and surface chemistry), making sure to integrate these biological factors into the design of nanomedicines so that they don't impede efficacy.

Other factors such as tumour heterogeneity concerning the EPR effect and enhanced circulation times are important features to consider, but they do not guarantee that nanomedicines will reach or access the tumour site. Simply relying on the EPR effect is not sufficient for delivery, especially into poorly perfused tumours e.g. replacement liver metastases. Added to this, some studies have indicated that extending circulation time beyond a certain point does not lead to improved efficacy (Nichols & Bae, 2013). Moreover, overexpression and specificity should not be conflated when considering targeting strategies. In particular, precautions should be taken for strategies that aim to reshape the tumour microenvironment. Such methods may promote tumour cell migration and increase drug resistance. For many a target, the intratumoural expression varies both spatially and temporally according to the microenvironmental conditions (Bae & Park, 2011). Hence, better characterisation of molecular targets that are specific to CRC liver metastases is essential, with serious consideration being given to whether a targeting strategy will convey an actual benefit.

During preclinical development, it is vital to understand the well-described interactions with components of the immunological and haematological systems (Halamoda-Kenzaoui et al., 2019; Rosslein et al., 2017; Urban, Liptrott, & Bremer, 2019) to de-risk translation (Halamoda-Kenzaoui et al., 2019). NPs carrying a cationic charge interact with biological membranes electrostatically, and trigger haemolysis, platelet activation and induction of leukocyte procoagulant activity (Dobrovolskaia, Shurin, & Shvedova, 2016). As well as surface charge, NPs with high aspect ratios have been shown to activate intracellular sensors such as the NLRP3 inflammasome (Baron et al., 2015). The use of surface coatings such as PEG may reduce interactions with immunological systems by preventing opsonisation by proteins such as immunoglobulins and components of the complement system. However, it has also been demonstrated that many people produce anti-PEG antibodies as a consequence of pre-exposure to PEG-containing products (B. M. Chen et al., 2016; Richter &

Akerblom, 1984). The presence of anti-PEG antibodies has been correlated with immediate-type hypersensitivity reactions to a PEGylated aptamer (Pegnivacogin) in a clinical trial (Povsic et al., 2016). Infusion reactions are immune-mediated toxicities that occur within the first minutes to hours of the systemic administration of various drug products, at their relevant therapeutic doses. Activation of complement and the resultant complement activation-related pseudoallergy is one mechanism underlying such infusion reactions to NPs (Neun, Barenholz, Szebeni, & Dobrovolskaia, 2018). A robust understanding of interactions with immunological and haematological systems is critically important to the translation of NPs for CRC.

Even though there has been a myriad of advances in nanomedicine and drug delivery, there are various concepts and mechanisms that are still not fully understood due to a lack of experimental data. Some questions that still need to be answered include; the dynamics underlying the EPR effect clinically within the different liver metastases growth patterns, the importance of biodegradability and clearance of the nanocarrier within the liver metastases from a toxicity perspective, the consequences of long term exposure to the NP, and the significance of modulating the different immune cells located in the sinusoids. It may be that patient or cancer-specific stratification is required to ultimately lead to an enhanced understanding and subsequent improved clinical success. It is apparent that greater insight into the opportunities and challenges presented by cancer nanomedicines is required. To support the successful development and clinical translation of nanomedicines, converging ideas from both nanotechnology and tumour biology is critical. If these challenges can be met, nanotechnology holds great promise for improving patient survival by transforming the paradigm of cancer treatment.

From a wider perspective, NPs hold great potential for antiviral repurposing, as they can be applied much more rapidly than new drug development. These advanced drug delivery technologies can be designed to act directly towards an infection, increase the effectiveness of conventional antiviral drugs/combinations, or even trigger the immune response of a patient. However, it is to be noted that

changes in formulation, dosing schedule, or route of administration for pre-existing drugs are not without significant challenges.

In conclusion, the work presented in this thesis demonstrated the development and characterisation of SN-38 NP formulations. They offer an alternative to solve issues surrounding the solubility of SN-38 and its delivery to tumour sites. Despite the promising *in vitro* data, the results of the pharmacokinetic studies did not reveal any benefit of the SN38-loaded NPs, compared to the prodrug irinotecan. NPs represent a potentially feasible and favourable choice for SN-38 in antitumour research and it is important to optimise the physicochemical parameters, as their use warrants further investigation.

References

Adkins, C. E., Nounou, M. I., Hye, T., Mohammad, A. S., Terrell-Hall, T., Mohan, N. K., . . . Lockman, P. R. (2015). NKTR-102 Efficacy versus irinotecan in a mouse model of brain metastases of breast cancer. *BMC Cancer, 15*, 685. doi:10.1186/s12885-015-1672-4

Adua, D., Di Fabio, F., Ercolani, G., Fiorentino, M., Gruppioni, E., Altimari, A., . . . Pinto, C. (2017). Heterogeneity in the colorectal primary tumor and the synchronous resected liver metastases prior to and after treatment with an anti-EGFR monoclonal antibody. *Mol Clin Oncol, 7*(1), 113-120. doi:10.3892/mco.2017.1270

Agarwal, R., Jurney, P., Raythatha, M., Singh, V., Sreenivasan, S. V., Shi, L., & Roy, K. (2015). Effect of shape, size, and aspect ratio on nanoparticle penetration and distribution inside solid tissues using 3D spheroid models. *Adv Healthc Mater, 4*(15), 2269-2280. doi:10.1002/adhm.201500441

Ahmed, D., Eide, P. W., Eilertsen, I. A., Danielsen, S. A., Eknaes, M., Hektoen, M., . . . Lothe, R. A. (2013). Epigenetic and genetic features of 24 colon cancer cell lines. *Oncogenesis, 2*, e71. doi:10.1038/oncsis.2013.35

Aird, W. C. (2007). Phenotypic heterogeneity of the endothelium: II. Representative vascular beds. *Circ Res, 100*(2), 174-190. doi:10.1161/01.RES.0000255690.03436.ae

Al-Kasspooles, M. F., Williamson, S. K., Henry, D., Howell, J., Niu, F., Decedue, C. J., & Roby, K. F. (2013). Preclinical antitumor activity of a nanoparticulate SN38. *Invest New Drugs, 31*(4), 871-880. doi:10.1007/s10637-012-9919-2

Alexis, F., Pridgen, E., Molnar, L. K., & Farokhzad, O. C. (2008). Factors affecting the clearance and biodistribution of polymeric nanoparticles. *Molecular Pharmaceutics, 5*(4), 505-515. doi:10.1021/mp800051m

Aljitawi, O. S., Li, D., Xiao, Y., Zhang, D., Ramachandran, K., Stehno-Bittel, L., . . . Garimella, R. (2014). A novel three-dimensional stromal-based model for in vitro chemotherapy sensitivity testing of leukemia cells. *Leuk Lymphoma, 55*(2), 378-391. doi:10.3109/10428194.2013.793323

Aloia, T. A., Vauthey, J. N., Loyer, E. M., Ribero, D., Pawlik, T. M., Wei, S. H., . . . Abdalla, E. K. (2006). Solitary colorectal liver metastasis: resection determines outcome. *Arch Surg, 141*(5), 460-466; discussion 466-467. doi:10.1001/archsurg.141.5.460

Amici, C., La Frazia, S., Brunelli, C., Balsamo, M., Angelini, M., & Santoro, M. G. (2015). Inhibition of viral protein translation by indomethacin in vesicular stomatitis virus infection: role of eIF2alpha kinase PKR. *Cell Microbiol, 17*(9), 1391-1404. doi:10.1111/cmi.12446

Anderson, V. R., & Curran, M. P. (2007). Nitazoxanide. *Drugs, 67*(13), 1947-1967. doi:10.2165/00003495-200767130-00015

Anselmo, A. C., & Mitragotri, S. (2016). Nanoparticles in the clinic. *Bioeng Transl Med, 1*(1), 10-29. doi:10.1002/btm2.10003

Antoni, D., Burckel, H., Josset, E., & Noel, G. (2015). Three-dimensional cell culture: a breakthrough in vivo. *Int J Mol Sci, 16*(3), 5517-5527. doi:10.3390/ijms16035517

Archer, S. G., & Gray, B. N. (1989). Vascularization of small liver metastases. *Br J Surg, 76*(6), 545-548. doi:10.1002/bjs.1800760607

Arnadottir, S. S., Jeppesen, M., Lamy, P., Bramsen, J. B., Nordentoft, I., Knudsen, M., . . . C, L. A. (2018). Characterization of genetic intratumor heterogeneity in colorectal cancer and matching patient-derived spheroid cultures. *Mol Oncol, 12*(1), 132-147. doi:10.1002/1878-0261.12156

Arshad, U., Sutton, P. A., Ashford, M. B., Treacher, K. E., Liptrott, N. J., Rannard, S. P., . . . Owen, A. (2020). Critical considerations for targeting colorectal liver metastases with nanotechnology. *Wiley Interdiscip Rev Nanomed Nanobiotechnol, 12*(2), e1588. doi:10.1002/wnan.1588

Ashton, S., Song, Y. H., Nolan, J., Cadogan, E., Murray, J., Odedra, R., . . . Barry, S. T. (2016). Aurora kinase inhibitor nanoparticles target tumors with favorable therapeutic index in vivo. *Sci Transl Med, 8*(325), 325ra317. doi:10.1126/scitranslmed.aad2355

AstraZeneca. (2019). AstraZeneca-Pipeline Retrieved from www.astrazeneca.com/our-science/pipeline

Atasilp, C., Chansriwong, P., Sirachainan, E., Reungwetwattana, T., Puangpetch, A., Prommas, S., . . . Sukasem, C. (2018). Determination of irinotecan, SN-38 and SN-38 glucuronide using HPLC/MS/MS: Application in a clinical pharmacokinetic and personalized medicine in colorectal cancer patients. *J Clin Lab Anal, 32*(1). doi:10.1002/jcla.22217

Awada, A., Garcia, A. A., Chan, S., Jerusalem, G. H., Coleman, R. E., Huizing, M. T., . . . Group, N.-S. (2013). Two schedules of etirinotecan pegol (NKTR-102) in patients with previously treated metastatic breast

cancer: a randomised phase 2 study. *Lancet Oncol, 14*(12), 1216-1225. doi:10.1016/S1470-2045(13)70429-7

Bae, Y. H., & Park, K. (2011). Targeted drug delivery to tumors: myths, reality and possibility. *J Control Release, 153*(3), 198-205. doi:10.1016/j.jconrel.2011.06.001

Baker, B. M., & Chen, C. S. (2012). Deconstructing the third dimension: how 3D culture microenvironments alter cellular cues. *J Cell Sci, 125*(Pt 13), 3015-3024. doi:10.1242/jcs.079509

Bakshi, R. P., Tatham, L. M., Savage, A. C., Tripathi, A. K., Mlambo, G., Ippolito, M. M., . . . Shapiro, T. A. (2018). Long-acting injectable atovaquone nanomedicines for malaria prophylaxis. *Nat Commun, 9*(1), 315. doi:10.1038/s41467-017-02603-z

Bao, Y., Guo, H. H., Lu, Y. L., Feng, W. M., Sun, X. R., Tang, C. W., . . . Shen, M. (2016). Blocking hepatic metastases of colon cancer cells using an shRNA against Rac1 delivered by activatable cell-penetrating peptide. *Oncotarget, 7*(47), 77183-77195. doi:10.18632/oncotarget.12854

Bardin, S., Guo, W., Johnson, J. L., Khan, S., Ahmad, A., Duggan, J. X., . . . Ahmad, I. (2005). Liquid chromatographic-tandem mass spectrometric assay for the simultaneous quantification of Camptosar and its metabolite SN-38 in mouse plasma and tissues. *J Chromatogr A, 1073*(1-2), 249-255. doi:10.1016/j.chroma.2004.08.060

Barenholz, Y. (2012). Doxil(R)--the first FDA-approved nano-drug: lessons learned. *J Control Release, 160*(2), 117-134. doi:10.1016/j.jconrel.2012.03.020

Baron, L., Gombault, A., Fanny, M., Villeret, B., Savigny, F., Guillou, N., . . . Couillin, I. (2015). The NLRP3 inflammasome is activated by nanoparticles through ATP, ADP and adenosine. *Cell Death &Amp; Disease, 6*, e1629. doi:10.1038/cddis.2014.576

Bast, R. C. (2016). *Holland-Frei cancer medicine*(9th edition. ed., pp. 1 online resource).

Basu, S., Zeng, M., Yin, T., Gao, S., & Hu, M. (2016). Development and validation of an UPLC-MS/MS method for the quantification of irinotecan, SN-38 and SN-38 glucuronide in plasma, urine, feces, liver and kidney: Application to a pharmacokinetic study of irinotecan in rats. *J Chromatogr B Analyt Technol Biomed Life Sci, 1015-1016*, 34-41. doi:10.1016/j.jchromb.2016.02.012

Batist, G., Gelmon, K. A., Chi, K. N., Miller, W. H., Jr., Chia, S. K., Mayer, L. D., . . . Louie, A. C. (2009). Safety, pharmacokinetics, and efficacy of CPX-1 liposome injection in patients with advanced solid tumors. *Clin Cancer Res, 15*(2), 692-700. doi:10.1158/1078-0432.CCR-08-0515

Batist, G., Sawyer, M., Gabrail, N., Christiansen, N., Marshall, J. L., Spigel, D. R., & Louie, A. (2008). A multicenter, phase II study of CPX-1 liposome injection in patients (pts) with advanced colorectal cancer (CRC). *Journal of Clinical Oncology, 26*(15). Retrieved from <Go to ISI>://WOS:000208457401124

Belanger, A. S., Tojcic, J., Harvey, M., & Guillemette, C. (2010). Regulation of UGT1A1 and HNF1 transcription factor gene expression by DNA methylation in colon cancer cells. *BMC Mol Biol, 11*, 9. doi:10.1186/1471-2199-11-9

Ben-Zvi, I., Kivity, S., Langevitz, P., & Shoenfeld, Y. (2012). Hydroxychloroquine: from malaria to autoimmunity. *Clin Rev Allergy Immunol, 42*(2), 145-153. doi:10.1007/s12016-010-8243-x

Bencharit, S., Morton, C. L., Howard-Williams, E. L., Danks, M. K., Potter, P. M., & Redinbo, M. R. J. N. s. b. (2002). Structural insights into CPT-11 activation by mammalian carboxylesterases. *9*(5), 337-342.

Benita, S., & Levy, M. Y. (1993). Submicron emulsions as colloidal drug carriers for intravenous administration: comprehensive physicochemical characterization. *J Pharm Sci, 82*(11), 1069-1079. doi:10.1002/jps.2600821102

Bland, J. M., & Altman, D. G. (1986). Statistical methods for assessing agreement between two methods of clinical measurement. *Lancet, 1*(8476), 307-310. Retrieved from https://www.ncbi.nlm.nih.gov/pubmed/2868172

Bojkova, D., McGreig, J. E., McLaughlin, K.-M., Masterson, S. G., Widera, M., Kraehling, V., . . . Cinatl, J. N. (2020). SARS-CoV-2 and SARS-CoV differ in their cell tropism and drug sensitivity profiles. doi: 10.1101/2020.1104.1103.024257 J bioRxiv. doi:10.1101/2020.04.03.024257 %J bioRxiv

Borba, M. G. S., Val, F. F. A., Sampaio, V. S., Alexandre, M. A. A., Melo, G. C., Brito, M., . . . CloroCovid, T. (2020). Effect of High vs Low Doses of Chloroquine Diphosphate as Adjunctive Therapy for Patients Hospitalized With Severe Acute Respiratory Syndrome Coronavirus 2 (SARS-CoV-2) Infection: A Randomized Clinical Trial. *JAMA Netw Open, 3*(4), e208857. doi:10.1001/jamanetworkopen.2020.8857

Bregenzer, M. E., Davis, C., Horst, E. N., Mehta, P., Novak, C. M., Raghavan, S., . . . Mehta, G. (2019). Physiologic Patient Derived 3D Spheroids for Anti-neoplastic Drug Screening to Target Cancer Stem Cells. *J Vis Exp*(149). doi:10.3791/59696

Breslin, S., & O'Driscoll, L. (2013). Three-dimensional cell culture: the missing link in drug discovery. *Drug Discov Today, 18*(5-6), 240-249. doi:10.1016/j.drudis.2012.10.003

Broadbridge, V. T., Karapetis, C. S., Beeke, C., Woodman, R. J., Padbury, R., Maddern, G., . . . Price, T. J. (2013). Do metastatic colorectal cancer patients who present with late relapse after curative surgery have a better survival? *Br J Cancer, 109*(5), 1338-1343. doi:10.1038/bjc.2013.388

Brodt, P. (2011). Liver Metastasis: Biology and Clinical Management Introduction. *Liver Metastasis: Biology and Clinical Management, 16*, 1-5. doi:10.1007/978-94-007-0292-9_1

Browning, D. J. (2014). Pharmacology of Chloroquine and Hydroxychloroquine. *Hydroxychloroquine and Chloroquine Retinopathy*, 35-63. doi:10.1007/978-1-4939-0597-3_2

Bruningk, S. C., Rivens, I., Box, C., Oelfke, U., & Ter Haar, G. (2020). 3D tumour spheroids for the prediction of the effects of radiation and hyperthermia treatments. *Sci Rep, 10*(1), 1653. doi:10.1038/s41598-020-58569-4

Bugyik, E., Renyi-Vamos, F., Szabo, V., Dezso, K., Ecker, N., Rokusz, A., . . . Paku, S. (2016). Mechanisms of vascularization in murine models of primary and metastatic tumor growth. *Chinese Journal of Cancer, 35*. doi:10.1186/s40880-016-0083-5

Bukreyeva, N., Mantlo, E. K., Sattler, R. A., Huang, C., Paessler, S., & Zeldis, J. (2020). The IMPDH inhibitor merimepodib suppresses SARS-CoV-2 replication in vitro. doi: 10.1101/2020.1104.1107.028589 J bioRxiv. Retrieved from https://www.biorxiv.org/content/biorxiv/early/2020/04/09/2020.04.07.028589.full.pdf

Burger, D. M., Agarwala, S., Child, M., Been-Tiktak, A., Wang, Y., & Bertz, R. (2006). Effect of Rifampin on Steady-State Pharmacokinetics of Atazanavir with Ritonavir in Healthy Volunteers. *50*(10), 3336-3342. doi:10.1128/AAC.00461-06 %J Antimicrobial Agents and Chemotherapy

Burke, T. G., & Mi, Z. (1994). The structural basis of camptothecin interactions with human serum albumin: impact on drug stability. *Journal of medicinal chemistry, 37*(1), 40-46.

Buzzelli, J. N., Ouaret, D., Brown, G., Allen, P. D., & Muschel, R. J. (2018). Colorectal cancer liver metastases organoids retain characteristics of original tumor and acquire chemotherapy resistance. *Stem Cell Res, 27*, 109-120. doi:10.1016/j.scr.2018.01.016

Byrne, J. D., Betancourt, T., & Brannon-Peppas, L. (2008). Active targeting schemes for nanoparticle systems in cancer therapeutics. *Adv Drug Deliv Rev, 60*(15), 1615-1626. doi:10.1016/j.addr.2008.08.005

Caly, L., Druce, J. D., Catton, M. G., Jans, D. A., & Wagstaff, K. M. (2020). The FDA-approved Drug Ivermectin inhibits the replication of SARS-CoV-2 in vitro. *Antiviral Research*, 104787. doi:https://doi.org/10.1016/j.antiviral.2020.104787

Candeil, L., Gourdier, I., Peyron, D., Vezzio, N., Copois, V., Bibeau, F., . . . Del Rio, M. (2004). ABCG2 overexpression in colon cancer cells resistant to SN38 and in irinotecan-treated metastases. *Int J Cancer, 109*(6), 848-854. doi:10.1002/ijc.20032

Cao, B., Wang, Y., Wen, D., Liu, W., Wang, J., Fan, G., . . . Wang, C. (2020). A Trial of Lopinavir-Ritonavir in Adults Hospitalized with Severe Covid-19. *N Engl J Med, 382*(19), 1787-1799. doi:10.1056/NEJMoa2001282

Carie, A., Rios-Doria, J., Costich, T., Burke, B., Slama, R., Skaff, H., & Sill, K. (2011). IT-141, a Polymer Micelle Encapsulating SN-38, Induces Tumor Regression in Multiple Colorectal Cancer Models. *J Drug Deliv, 2011*, 869027. doi:10.1155/2011/869027

Casillas, S., Dietz, D. W., Brand, M. I., Jones, S. C., Vladisavljevic, A., & Milsom, J. W. (1997). Perfusion to colorectal cancer liver metastases is not uniform and depends on tumor location and feeding vessel. *J Surg Res, 67*(2), 179-185. doi:10.1006/jsre.1996.4977

Chabner, B. A., & Roberts, T. G., Jr. (2005). Timeline: Chemotherapy and the war on cancer. *Nat Rev Cancer, 5*(1), 65-72. doi:10.1038/nrc1529

Chabot, G., Abigerges, D., Catimel, G., Culine, S., De Forni, M., Extra, J.-M., . . . Bugat, R. (1995). Population pharmacokinetics and pharmacodynamics of irinotecan (CPT-11) and active metabolite SN-38 during phase I trials. *Annals of oncology, 6*(2), 141-151.

Chabot, G. G. (1997). Clinical pharmacokinetics of irinotecan. *Clin Pharmacokinet, 33*(4), 245-259. doi:10.2165/00003088-199733040-00001

Chaicharoenaudomrung, N., Kunhorm, P., & Noisa, P. (2019). Three-dimensional cell culture systems as an in vitro platform for cancer and stem cell modeling. *World J Stem Cells, 11*(12), 1065-1083. doi:10.4252/wjsc.v11.i12.1065

Chan-Tack, K. M., Struble, K. A., & Birnkrant, D. B. (2008). Intracranial hemorrhage and liver-associated deaths associated with tipranavir/ritonavir: review of cases from the FDA's Adverse Event Reporting System. *AIDS Patient Care STDS, 22*(11), 843-850. doi:10.1089/apc.2008.0043

Chandrasekaran, A., Ahmad, S., Shen, L., DeMaio, W., Hultin, T., & Scatina, J. (2010). Disposition of bazedoxifene in rats. *Xenobiotica, 40*(8), 578-585. doi:10.3109/00498254.2010.492879

Chang, T. T., & Hughes-Fulford, M. (2009). Monolayer and spheroid culture of human liver hepatocellular carcinoma cell line cells demonstrate distinct global gene expression patterns and functional phenotypes. *Tissue Eng Part A, 15*(3), 559-567. doi:10.1089/ten.tea.2007.0434

Chatterjee, D. K., Diagaradjane, P., & Krishnan, S. (2011). Nanoparticle-mediated hyperthermia in cancer therapy. *Ther Deliv, 2*(8), 1001-1014. Retrieved from https://www.ncbi.nlm.nih.gov/pubmed/22506095

Chen, B. L., Dai, W. B., Mei, D., Liua, T. Z., Li, S. X., He, B., . . . Zhang, Q. (2016). Comprehensively priming the tumor microenvironment by cancer-associated fibroblast-targeted liposomes for combined therapy with cancer cell-targeted chemotherapeutic drug delivery system. *Journal of Controlled Release, 241*, 68-80. doi:10.1016/j.jconrel.2016.09.014

Chen, B. M., Su, Y. C., Chang, C. J., Burnouf, P. A., Chuang, K. H., Chen, C. H., . . . Roffler, S. R. (2016). Measurement of Pre-Existing IgG and IgM Antibodies against Polyethylene Glycol in Healthy Individuals. *Anal Chem, 88*(21), 10661-10666. doi:10.1021/acs.analchem.6b03109

Chen, C., Huang, J., Cheng, Z., Wu, J., Chen, S., Zhang, Y., . . . Wang, X. (2020). Favipiravir versus Arbidol for COVID-19: A Randomized Clinical Trial. doi: 10.1101/2020.1103.1117.20037432 J medRxiv. Retrieved from https://www.medrxiv.org/content/medrxiv/early/2020/03/27/2020.03.17.20037432.full.pdf

Chen, M., Li, W., Zhang, X., Dong, Y., Hua, Y., Zhang, H., . . . Zheng, A. (2017). In vitro and in vivo evaluation of SN-38 nanocrystals with different particle sizes. *Int J Nanomedicine, 12*, 5487-5500. doi:10.2147/IJN.S133816

Chen, W., Mook, R. A., Premont, R. T., & Wang, J. (2018). Niclosamide: Beyond an antihelminthic drug. *Cellular Signalling, 41*, 89-96. doi:https://doi.org/10.1016/j.cellsig.2017.04.001

Chen, X., Peer, C. J., Alfaro, R., Tian, T., Spencer, S. D., & Figg, W. D. (2012). Quantification of irinotecan, SN38, and SN38G in human and porcine plasma by ultra high-performance liquid chromatography-tandem mass spectrometry and its application to hepatic chemoembolization. *Journal of pharmaceutical and biomedical analysis, 62*, 140-148. doi:10.1016/j.jpba.2012.01.008

Chen, X., Zhao, B., Qu, Y., Chen, Y., Xiong, J., Feng, Y., . . . Li, F. (2020). Detectable serum SARS-CoV-2 viral load (RNAaemia) is closely associated with drastically elevated interleukin 6 (IL-6) level in critically ill COVID-19 patients. doi: 10.1101/2020.1102.1129.20029520 J medRxiv. Retrieved from https://www.medrxiv.org/content/medrxiv/early/2020/03/03/2020.02.29.20029520.full.pdf

Cheng, J., Teply, B. A., Sherifi, I., Sung, J., Luther, G., Gu, F. X., . . . Farokhzad, O. C. (2007). Formulation of functionalized PLGA-PEG nanoparticles for in vivo targeted drug delivery. *Biomaterials, 28*(5), 869-876. doi:10.1016/j.biomaterials.2006.09.047

Chiang, N. J., Chang, J. Y., Shan, Y. S., & Chen, L. T. (2016). Development of nanoliposomal irinotecan (nal-IRI, MM-398, PEP02) in the management of metastatic pancreatic cancer. *Expert Opin Pharmacother, 17*(10), 1413-1420. doi:10.1080/14656566.2016.1183646

Chitcholtan, K., Asselin, E., Parent, S., Sykes, P. H., & Evans, J. J. (2013). Differences in growth properties of endometrial cancer in three dimensional (3D) culture and 2D cell monolayer. *Exp Cell Res, 319*(1), 75-87. doi:10.1016/j.yexcr.2012.09.012

Choy, K.-T., Wong, A. Y.-L., Kaewpreedee, P., Sia, S. F., Chen, D., Hui, K. P. Y., . . . Yen, H.-L. (2020). Remdesivir, lopinavir, emetine, and homoharringtonine inhibit SARS-CoV-2 replication in vitro. *Antiviral Research, 178*, 104786. doi:https://doi.org/10.1016/j.antiviral.2020.104786

Ciotti, M., Basu, N., Brangi, M., & Owens, I. (1999). Glucuronidation of 7-ethyl-10-hydroxycamptothecin (SN-38) by the human UDP-glucuronosyltransferases encoded at the UGT1 locus. *260*(1), 199-202.

Cisterna, B. A., Kamaly, N., Choi, W. I., Tavakkoli, A., Farokhzad, O. C., & Vilos, C. (2016). Targeted nanoparticles for colorectal cancer. *Nanomedicine (Lond), 11*(18), 2443-2456. doi:10.2217/nnm-2016-0194

Clerici, M., Trabattoni, D., Pacei, M., Biasin, M., & Rossignol, J.-F. (2011). The anti-infective Nitazoxanide shows strong immumodulating effects (155.21). *186*(1 Supplement), 155.121-155.121.

Cohen, S., & Margel, S. (2012). Engineering of near IR fluorescent albumin nanoparticles for in vivo detection of colon cancer. *J Nanobiotechnology, 10*, 36. doi:10.1186/1477-3155-10-36

Cole, C., Fuller, R., Mallet, A., & Rowland, I. (1985). The influence of the host on expression of intestinal microbial enzyme activities involved in metabolism of foreign compounds. *Journal of applied bacteriology, 59*(6), 549-553.

Colotta, F. (2008). Anticancer drug discovery and development. *Adv Exp Med Biol, 610*, 19-42. doi:10.1007/978-0-387-73898-7_3

Combes, O., Barré, J., Duché, J.-C., Vernillet, L., Archimbaud, Y., Marietta, M. P., . . . Urien, S. (2000). In vitro binding and partitioning of irinotecan (CPT-11) and its metabolite, SN-38, in human blood. *Investigational new drugs, 18*(1), 1-5.

Corbett, A. H., Lim, M. L., & Kashuba, A. D. (2002). Kaletra (lopinavir/ritonavir). *Ann Pharmacother, 36*(7-8), 1193-1203. doi:10.1345/aph.1A363

Costa, E. C., Gaspar, V. M., Coutinho, P., & Correia, I. J. (2014). Optimization of liquid overlay technique to formulate heterogenic 3D co-cultures models. *Biotechnol Bioeng, 111*(8), 1672-1685. doi:10.1002/bit.25210

Courau, T., Bonnereau, J., Chicoteau, J., Bottois, H., Remark, R., Assante Miranda, L., . . . Le Bourhis, L. (2019). Cocultures of human colorectal tumor spheroids with immune cells reveal the therapeutic potential of MICA/B and NKG2A targeting for cancer treatment. *J Immunother Cancer, 7*(1), 74. doi:10.1186/s40425-019-0553-9

Cristobal, A., van den Toom, H. W. P., van de Wetering, M., Clevers, H., Heck, A. J. R., & Mohammed, S. (2017). Personalized Proteome Profiles of Healthy and Tumor Human Colon Organoids Reveal Both Individual Diversity and Basic Features of Colorectal Cancer. *Cell Reports, 18*(1), 263-274. doi:10.1016/j.celrep.2016.12.016

Cummings, J., Zelcer, N., Allen, J. D., Yao, D., Boyd, G., Maliepaard, M., . . . Jodrell, D. I. (2004). Glucuronidation as a mechanism of intrinsic drug resistance in colon cancer cells: contribution of drug transport proteins. *Biochem Pharmacol, 67*(1), 31-39. doi:10.1016/j.bcp.2003.07.019

Cunningham, D., Falk, S., & Jackson, D. (2002). Clinical and economic benefits of irinotecan in combination with 5-fluorouracil and folinic acid as first line treatment of metastatic colorectal cancer. *British Journal of Cancer, 86*(11), 1677-1683.

D'Esposito, F., Tattam, B. N., Ramzan, I., & Murray, M. (2008). A liquid chromatography/electrospray ionization mass spectrometry (LC–MS/MS) assay for the determination of irinotecan (CPT-11) and its two major metabolites in human liver microsomal incubations and human plasma samples. *Journal of Chromatography B, 875*(2), 522-530. doi:https://doi.org/10.1016/j.jchromb.2008.10.011

D'Souza, S. (2014). A Review of In Vitro Drug Release Test Methods for Nano-Sized Dosage Forms. *Advances in Pharmaceutics, 2014*, 304757. doi:10.1155/2014/304757

Damle, B., Stogniew, M., & Dowell, J. (2008). Pharmacokinetics and tissue distribution of anidulafungin in rats. *Antimicrob Agents Chemother, 52*(7), 2673-2676. doi:10.1128/AAC.01596-07

Davies, L. C., Jenkins, S. J., Allen, J. E., & Taylor, P. R. (2013). Tissue-resident macrophages. *Nature Immunology, 14*(10), 986-995. doi:10.1038/ni.2705

de Bruijn, P., Verweij, J., Loos, W. J., Nooter, K., Stoter, G., & Sparreboom, A. (1997). Determination of irinotecan (CPT-11) and its active metabolite SN-38 in human plasma by reversed-phase high-performance liquid chromatography with fluorescence detection. *J Chromatogr B Biomed Sci Appl, 698*(1-2), 277-285. doi:10.1016/s0378-4347(97)00290-9

de Cuba, E. M. V., Kwakman, R., Knol, D. L., Bonjer, H. J., Meijer, G. A., & te Velde, E. A. (2013). Cytoreductive surgery and HIPEC for peritoneal metastases combined with curative treatment of colorectal liver metastases Systematic review of all literature and meta-analysis of observational studies. *Cancer Treatment Reviews, 39*(4), 321-327. doi:10.1016/j.ctrv.2012.11.003

de Kock, M., Tarning, J., Workman, L., Nyunt, M. M., Adam, I., Barnes, K. I., & Denti, P. (2017). Pharmacokinetics of Sulfadoxine and Pyrimethamine for Intermittent Preventive Treatment of Malaria During Pregnancy and After Delivery. *CPT Pharmacometrics Syst Pharmacol, 6*(7), 430-438. doi:10.1002/psp4.12181

Dekkers, J. F., Alieva, M., Wellens, L. M., Ariese, H. C. R., Jamieson, P. R., Vonk, A. M., . . . Rios, A. C. (2019). High-resolution 3D imaging of fixed and cleared organoids. *Nat Protoc, 14*(6), 1756-1771. doi:10.1038/s41596-019-0160-8

Di Miceli, D., Alfieri, S., Caprino, P., Menghi, R., Quero, G., Cina, C., . . . Doglietto, G. B. (2012). Complications related to hyperthermia during hypertermic intraoperative intraperitoneal chemiotherapy (HIPEC) treatment. Do they exist? *European Review for Medical and Pharmacological Sciences, 16*(6), 737-742. Retrieved from <Go to ISI>://WOS:000305823100003

Diao, B., Wang, C., Wang, R., Feng, Z., Tan, Y., Wang, H., . . . Chen, Y. (2020). Human Kidney is a Target for Novel Severe Acute Respiratory Syndrome Coronavirus 2 (SARS-CoV-2) Infection. doi: 10.1101/2020.1103.1104.20031120 J medRxiv. Retrieved from https://www.medrxiv.org/content/medrxiv/early/2020/04/10/2020.03.04.20031120.full.pdf

Dini, S., Binder, B. J., Fischer, S. C., Mattheyer, C., Schmitz, A., Stelzer, E. H., . . . Green, J. E. (2016). Identifying the necrotic zone boundary in tumour spheroids with pair-correlation functions. *J R Soc Interface, 13*(123). doi:10.1098/rsif.2016.0649

Dobrovolskaia, M. A., Shurin, M., & Shvedova, A. A. (2016). Current understanding of interactions between nanoparticles and the immune system. *Toxicol Appl Pharmacol, 299*, 78-89. doi:10.1016/j.taap.2015.12.022

Dodds, H. M., Haaz, M.-C., Riou, J.-F., Robert, J., & Rivory, L. P. (1998). Identification of a new metabolite of CPT-11 (irinotecan): pharmacological properties and activation to SN-38. *Journal of Pharmacology Experimental Therapeutics, 286*(1), 578-583.

Donadon, M., Ribero, D., Morris-Stiff, G., Abdalla, E. K., & Vauthey, J. N. (2007). New paradigm in the management of liver-only metastases from colorectal cancer. *Gastrointest Cancer Res, 1*(1), 20-27. Retrieved from https://www.ncbi.nlm.nih.gov/pubmed/19262699

Douillard, J., Cunningham, D., Roth, A., Navarro, M., James, R., Karasek, P., . . . Alakl, M. (2000). Irinotecan combined with fluorouracil compared with fluorouracil alone as first-line treatment for metastatic colorectal cancer: a multicentre randomised trial. *The Lancet, 355*(9209), 1041-1047.

Drachman, N., Kadlecek, S., Pourfathi, M., Xin, Y., Profka, H., & Rizi, R. (2017). In vivo pH mapping of injured lungs using hyperpolarized [1-(13) C]pyruvate. *Magn Reson Med, 78*(3), 1121-1130. doi:10.1002/mrm.26473

Ducreux, M., Kohne, C. H., Schwartz, G. K., & Vanhoefer, U. (2003). Irinotecan in metastatic colorectal cancer: dose intensification and combination with new agents, including biological response modifiers. *Ann Oncol, 14 Suppl 2*, ii17-23. doi:10.1093/annonc/mdg724

Durymanov, M., Kroll, C., Permyakova, A., O'Neill, E., Sulaiman, R., Person, M., & Reineke, J. (2019). Subcutaneous Inoculation of 3D Pancreatic Cancer Spheroid Results in Development of Reproducible Stroma-Rich Tumors. *Translational Oncology, 12*(1), 180-189. doi:10.1016/j.tranon.2018.10.003

Duval, K., Grover, H., Han, L. H., Mou, Y., Pegoraro, A. F., Fredberg, J., & Chen, Z. (2017). Modeling Physiological Events in 2D vs. 3D Cell Culture. *Physiology (Bethesda), 32*(4), 266-277. doi:10.1152/physiol.00036.2016

Edmondson, R., Broglie, J. J., Adcock, A. F., & Yang, L. (2014). Three-dimensional cell culture systems and their applications in drug discovery and cell-based biosensors. *Assay Drug Dev Technol, 12*(4), 207-218. doi:10.1089/adt.2014.573

Ekert, J. E., Johnson, K., Strake, B., Pardinas, J., Jarantow, S., Perkinson, R., & Colter, D. C. (2014). Three-dimensional lung tumor microenvironment modulates therapeutic compound responsiveness in vitro--implication for drug development. *PLoS One, 9*(3), e92248. doi:10.1371/journal.pone.0092248

Emblem, K. E., & Jain, R. K. (2016). Improving treatment of liver metastases by targeting nonangiogenic mechanisms. *Nat Med, 22*(11), 1209-1210. doi:10.1038/nm.4228

England, R. M., Hare, J. I., Barnes, J., Wilson, J., Smith, A., Strittmatter, N., . . . Ashford, M. B. (2017). Tumour regression and improved gastrointestinal tolerability from controlled release of SN-38 from novel polyoxazoline-modified dendrimers. *J Control Release, 247*, 73-85. doi:10.1016/j.jconrel.2016.12.034

Ewing, J. (1928). *Neoplastic diseases; a treatise on tumors* (3d ed rev. and enl., with 546 illustrations. ed.). Philadelphia, London,: W.B. Saunders.

Fan, J., & Gao, Q. (2017). Metastatic Liver Cancer and Microenvironment. In X. Qin, J. Xu, & Y. Zhong (Eds.), *Multidisciplinary Management of Liver Metastases in Colorectal Cancer: Early Diagnosis and Treatment* (pp. 39-57). Dordrecht: Springer Netherlands.

Fang, Y. P., Chuang, C. H., Wu, Y. J., Lin, H. C., & Lu, Y. C. (2018). SN38-loaded <100 nm targeted liposomes for improving poor solubility and minimizing burst release and toxicity: in vitro and in vivo study. *Int J Nanomedicine, 13*, 2789-2802. doi:10.2147/IJN.S158426

FDA. (2016). Guidance for industry: bioanalytical method validation. 2001. *Rockville, MD, USA*.

FDA. (2020). Abbott L. Clinical Pharmacology and Biopharmaceutics review of Kaletra oral solution (NDA#021251). Retrieved from https://www.accessdata.fda.gov/drugsatfda_docs/nda/2000/21-226_Kaletra_biopharmr_P1.pdf

Feldman, A. T., & Wolfe, D. (2014). Tissue processing and hematoxylin and eosin staining. *Methods Mol Biol, 1180*, 31-43. doi:10.1007/978-1-4939-1050-2_3

Fernandez, F. G., Drebin, J. A., Linehan, D. C., Dehdashti, F., Siegel, B. A., & Strasberg, S. M. (2004). Five-year survival after resection of hepatic metastases from colorectal cancer in patients screened by positron emission tomography with F-18 fluorodeoxyglucose (FDG-PET). *Ann Surg, 240*(3), 438-447; discussion 447-450. doi:10.1097/01.sla.0000138076.72547.b1

Fintelman-Rodrigues, N., Sacramento, C. Q., Lima, C. R., da Silva, F. S., Ferreira, A. C., Mattos, M., . . . Souza, T. M. L. (2020). Atazanavir inhibits SARS-CoV-2 replication and pro-inflammatory cytokine production. doi: 10.1101/2020.1104.1104.020925 J bioRxiv. Retrieved from https://www.biorxiv.org/content/biorxiv/early/2020/04/05/2020.04.04.020925.full.pdf

Fitch, C. D., Chevli, R., & Gonzalez, Y. (1974). Chloroquine-resistant Plasmodium falciparum: effect of substrate on chloroquine and amodiaquin accumulation. *Antimicrob Agents Chemother, 6*(6), 757-762. doi:10.1128/aac.6.6.757

Flexner, C., Bate, G., & Kirkpatrick, P. (2005). Tipranavir. *Nature Reviews Drug Discovery, 4*(12), 955-956. doi:10.1038/nrd1907

Folprecht, G., Grothey, A., Alberts, S., Raab, H. R., & Kohne, C. H. (2005). Neoadjuvant treatment of unresectable colorectal liver metastases: correlation between tumour response and resection rates. *Ann Oncol, 16*(8), 1311-1319. doi:10.1093/annonc/mdi246

Fong, E. L. S., Toh, T. B., Yu, H., & Chow, E. K. H. (2017). 3D Culture as a Clinically Relevant Model for Personalized Medicine. *Slas Technology, 22*(3), 245-253. doi:10.1177/2472630317697251

Fornaguera, C., & Garcia-Celma, M. J. (2017). Personalized Nanomedicine: A Revolution at the Nanoscale. *J Pers Med, 7*(4). doi:10.3390/jpm7040012

Foundation, E. S. (2004). Nanomedicine–An ESF-European Medical Research Councils (EMRC) Forward Look Report.

Fox, L. M., & Saravolatz, L. D. (2005). Nitazoxanide: A New Thiazolide Antiparasitic Agent. *Clinical Infectious Diseases, 40*(8), 1173-1180. doi:10.1086/428839

Fredenberg, S., Wahlgren, M., Reslow, M., & Axelsson, A. (2011). The mechanisms of drug release in poly(lactic-co-glycolic acid)-based drug delivery systems--a review. *Int J Pharm, 415*(1-2), 34-52. doi:10.1016/j.ijpharm.2011.05.049

Frentzas, S., Simoneau, E., Bridgeman, V. L., Vermeulen, P. B., Foo, S., Kostaras, E., . . . Reynolds, A. R. (2016). Vessel co-option mediates resistance to anti-angiogenic therapy in liver metastases. *Nat Med, 22*(11), 1294-1302. doi:10.1038/nm.4197

Freytes, D. O., Wan, L. Q., & Vunjak-Novakovic, G. (2009). Geometry and force control of cell function. *J Cell Biochem, 108*(5), 1047-1058. doi:10.1002/jcb.22355

Friedrich, J., Ebner, R., & Kunz-Schughart, L. A. (2007). Experimental anti-tumor therapy in 3-D: spheroids--old hat or new challenge? *Int J Radiat Biol, 83*(11-12), 849-871. doi:10.1080/09553000701727531

Friedrich, J., Seidel, C., Ebner, R., & Kunz-Schughart, L. A. (2009). Spheroid-based drug screen: considerations and practical approach. *Nat Protoc, 4*(3), 309-324. doi:10.1038/nprot.2008.226

Fu, Y., & Kao, W. J. (2010). Drug release kinetics and transport mechanisms of non-degradable and degradable polymeric delivery systems. *Expert Opin Drug Deliv, 7*(4), 429-444. doi:10.1517/17425241003602259

Fujii, M., Shimokawa, M., Date, S., Takano, A., Matano, M., Nanki, K., . . . Sato, T. (2016). A Colorectal Tumor Organoid Library Demonstrates Progressive Loss of Niche Factor Requirements during Tumorigenesis. *Cell Stem Cell, 18*(6), 827-838. doi:10.1016/j.stem.2016.04.003

Fujisawa, T., & Mori, M. (1997). Influence of various bile salts on ββ-glucuronidase activity of intestinal bacteria. *Letters in applied microbiology, 25*(2), 95-97.

Gabizon, A., Shmeeda, H., & Barenholz, Y. (2003). Pharmacokinetics of pegylated liposomal doxorubicin - Review of animal and human studies. *Clinical pharmacokinetics, 42*(5), 419-436. doi:Doi 10.2165/00003088-200342050-00002

Gaedtke, L., Thoenes, L., Culmsee, C., Mayer, B., & Wagner, E. (2007). Proteomic analysis reveals differences in protein expression in spheroid versus monolayer cultures of low-passage colon carcinoma cells. *J Proteome Res, 6*(11), 4111-4118. doi:10.1021/pr0700596

Gagne, J. F., Montminy, V., Belanger, P., Journault, K., Gaucher, G., & Guillemette, C. (2002). Common human UGT1A polymorphisms and the altered metabolism of irinotecan active metabolite 7-ethyl-10-hydroxycamptothecin (SN-38). *Mol Pharmacol, 62*(3), 608-617. doi:10.1124/mol.62.3.608

Gagnon, J. F., Bernard, O., Villeneuve, L., Tetu, B., & Guillemette, C. (2006). Irinotecan inactivation is modulated by epigenetic silencing of UGT1A1 in colon cancer. *Clin Cancer Res, 12*(6), 1850-1858. doi:10.1158/1078-0432.CCR-05-2130

Galateanu, B., Hudita, A., Negrei, C., Ion, R. M., Costache, M., Stan, M., . . . Ginghina, O. (2016). Impact of multicellular tumor spheroids as an in vivolike tumor model on anticancer drug response. *Int J Oncol, 48*(6), 2295-2302. doi:10.3892/ijo.2016.3467

Gao, X., Zhang, J., Huang, Z., Zuo, T. T., Lu, Q., Wu, G. Y., & Shen, Q. (2017). Reducing Interstitial Fluid Pressure and Inhibiting Pulmonary Metastasis of Breast Cancer by Gelatin Modified Cationic Lipid Nanoparticles. *Acs Applied Materials & Interfaces, 9*(35), 29457-29468. doi:10.1021/acsami.7b05119

Garnock-Jones, K. P. (2011). Eltrombopag. *Drugs, 71*(10), 1333-1353. doi:10.2165/11207390-000000000-00000

Garrett, C. R., Bekaii-Saab, T. S., Ryan, T., Fisher, G. A., Clive, S., Kavan, P., . . . Goldberg, R. M. (2013). Randomized Phase 2 Study of Pegylated SN-38 (EZN-2208) or Irinotecan Plus Cetuximab in Patients With Advanced Colorectal Cancer. *Cancer, 119*(24), 4223-4230. doi:10.1002/cncr.28358

Gassen, N. C., Niemeyer, D., Muth, D., Corman, V. M., Martinelli, S., Gassen, A., . . . Rein, T. (2019). SKP2 attenuates autophagy through Beclin1-ubiquitination and its inhibition reduces MERS-Coronavirus infection. *Nat Commun, 10*(1), 5770. doi:10.1038/s41467-019-13659-4

Gassen, N. C., Papies, J., Bajaj, T., Dethloff, F., Emanuel, J., Weckmann, K., . . . Müller, M. A. (2020). Analysis of SARS-CoV-2-controlled autophagy reveals spermidine, MK-2206, and niclosamide as putative antiviral therapeutics. *bioRxiv*, 2020.2004.2015.997254. doi:10.1101/2020.04.15.997254

Ge, Y., Tian, T., Huang, S., Wan, F., Li, J., Li, S., . . . Zeng, J. (2020). A data-driven drug repositioning framework discovered a potential therapeutic agent targeting COVID-19. doi: 10.1101/2020.1103.1111.986836 J bioRxiv. Retrieved from https://www.biorxiv.org/content/biorxiv/early/2020/03/12/2020.03.11.986836.full.pdf

Geary, T. G., Divo, A. D., Jensen, J. B., Zangwill, M., & Ginsburg, H. (1990). Kinetic modelling of the response of Plasmodium falciparum to chloroquine and its experimental testing in vitro. Implications for mechanism of action of and resistance to the drug. *Biochem Pharmacol, 40*(4), 685-691. doi:10.1016/0006-2952(90)90302-2

Gekonge, B., Bardin, M. C., & Montaner, L. J. (2015). Short communication: Nitazoxanide inhibits HIV viral replication in monocyte-derived macrophages. *AIDS Res Hum Retroviruses, 31*(2), 237-241. doi:10.1089/aid.2014.0015

Gerdes, J., Lemke, H., Baisch, H., Wacker, H. H., Schwab, U., & Stein, H. (1984). Cell cycle analysis of a cell proliferation-associated human nuclear antigen defined by the monoclonal antibody Ki-67. *J Immunol, 133*(4), 1710-1715. Retrieved from https://www.ncbi.nlm.nih.gov/pubmed/6206131

Ghazaly, E., Perry, J., Kitromilidou, C., Powles, T., & Joel, S. (2014). Development and validation of an ultra-high performance LC-MS/MS assay for intracellular SN-38 in human solid tumour cell lines: comparison with a validated HPLC-fluorescence method. *J Chromatogr B Analyt Technol Biomed Life Sci, 969*, 213-218. doi:10.1016/j.jchromb.2014.08.024

Ginsburg, H., Nissani, E., & Krugliak, M. (1989). Alkalinization of the food vacuole of malaria parasites by quinoline drugs and alkylamines is not correlated with their antimalarial activity. *Biochem Pharmacol, 38*(16), 2645-2654. doi:10.1016/0006-2952(89)90550-9

Goel, P., & Gerriets, V. (2020). Chloroquine. In *StatPearls*. Treasure Island (FL).

Goel, S., Duda, D. G., Xu, L., Munn, L. L., Boucher, Y., Fukumura, D., & Jain, R. K. (2011). Normalization of the Vasculature for Treatment of Cancer and Other Diseases. *Physiological Reviews, 91*(3), 1071-1121. doi:10.1152/physrev.00038.2010

Golombek, S. K., May, J. N., Theek, B., Appold, L., Drude, N., Kiessling, F., & Lammers, T. (2018). Tumor targeting via EPR: Strategies to enhance patient responses. *Advanced Drug Delivery Reviews, 130*, 17-38. doi:10.1016/j.addr.2018.07.007

Gong, X., Lin, C., Cheng, J., Su, J., Zhao, H., Liu, T., . . . Zhao, P. (2015). Generation of Multicellular Tumor Spheroids with Microwell-Based Agarose Scaffolds for Drug Testing. *PLoS One, 10*(6), e0130348. doi:10.1371/journal.pone.0130348

Gonzalez, D., Schmidt, S., & Derendorf, H. (2013). Importance of relating efficacy measures to unbound drug concentrations for anti-infective agents. *Clin Microbiol Rev, 26*(2), 274-288. doi:10.1128/CMR.00092-12

Gorshkov, K., Chen, C. Z., Bostwick, R., Rasmussen, L., Xu, M., Pradhan, M., . . . Zheng, W. (2020). The SARS-CoV-2 cytopathic effect is blocked with autophagy modulators. *bioRxiv*. doi:10.1101/2020.05.16.091520

Gourd, E. (2018). PEGPH20 for metastatic pancreatic ductal adenocarcinoma. *Lancet Oncology, 19*(2), E81-E81. doi:10.1016/S1470-2045(17)30953-1

Greaves, M., & Maley, C. C. (2012). Clonal evolution in cancer. *Nature, 481*(7381), 306-313. doi:10.1038/nature10762

Grein, J., Ohmagari, N., Shin, D., Diaz, G., Asperges, E., Castagna, A., . . . Flanigan, T. (2020). Compassionate Use of Remdesivir for Patients with Severe Covid-19. *N Engl J Med*, 10.1056/NEJMoa2007016. Retrieved from https://www.ncbi.nlm.nih.gov/pubmed/32275812

Gritli, I., Garmey, E., Eliasof, S., Tellez, A., Davis, M. E., & Yun, Y. (2016). Polymeric Nanoparticles and Cancer: Lessons Learnt from CRLX101. *Nanomedicines: Design, Delivery and Detection, 51*, 199-232. doi:Book_Doi 10.1039/9781782622536

Gu, J., Han, B., & Wang, J. (2020). COVID-19: Gastrointestinal manifestations and potential fecal-oral transmission. *Gastroenterology*, doi: 10.1053/j.gastro.2020.1002.1054. Retrieved from https://www.ncbi.nlm.nih.gov/pubmed/32142785

Guo, Y. R., Cao, Q. D., Hong, Z. S., Tan, Y. Y., Chen, S. D., Jin, H. J., . . . Yan, Y. (2020). The origin, transmission and clinical therapies on coronavirus disease 2019 (COVID-19) outbreak - an update on the status. *Mil Med Res, 7*(1), 11. doi:10.1186/s40779-020-00240-0

Gupta, A., Tulsankar, S. L., Bhatta, R. S., & Misra, A. (2017). Pharmacokinetics, Metabolism, and Partial Biodistribution of "Pincer Therapeutic" Nitazoxanide in Mice following Pulmonary Delivery of Inhalable Particles. *Mol Pharm, 14*(4), 1204-1211. doi:10.1021/acs.molpharmaceut.6b01089

Gurski, L. A., Petrelli, N. J., Jia, X., & Farach-Carson, M. C. (2010). 3D Matrices for Anti-Cancer Drug Testing and Development. *Oncology Issues, 25*(1), 20-25. doi:10.1080/10463356.2010.11883480

Haaz, M.-C., Rivory, L. P., Riché, C., & Robert, J. (1997). The transformation of irinotecan (CPT-11) to its active metabolite SN-38 by human liver microsomes Differential hydrolysis for the lactone and carboxylate forms. *Naunyn-Schmiedeberg's archives of pharmacology, 356*(2), 257-262.

Haaz, M. C., Rivory, L., Jantet, S., Ratanasavanh, D., & Robert, J. (1997). Glucuronidation of SN-38, the active metabolite of irinotecan, by human hepatic microsomes. *Pharmacology and toxicology, 80*(2), 91-96.

Haffizulla, J., Hartman, A., Hoppers, M., Resnick, H., Samudrala, S., Ginocchio, C., . . . Group, U. S. N. I. C. S. (2014). Effect of nitazoxanide in adults and adolescents with acute uncomplicated influenza: a double-blind, randomised, placebo-controlled, phase 2b/3 trial. *Lancet Infect Dis, 14*(7), 609-618. doi:10.1016/S1473-3099(14)70717-0

Halamoda-Kenzaoui, B., Baconnier, S., Bastogne, T., Bazile, D., Boisseau, P., Borchard, G., . . . Bremer-Hoffmann, S. (2019). Bridging communities in the field of nanomedicine. *Regul Toxicol Pharmacol, 106*, 187-196. doi:10.1016/j.yrtph.2019.04.011

Halozyme. (2019). Halozyme Therapeutics - PEGPH20, A Therapeutic Candidate for the Treatment of HA-HIGH Cancer Retrieved from www.halozyme.com/technology/product-candidate/pegph20

Hamaguchi, T., Doi, T., Eguchi-Nakajima, T., Kato, K., Yamada, Y., Shimada, Y., . . . Matsumura, Y. (2010). Phase I study of NK012, a novel SN-38-incorporating micellar nanoparticle, in adult patients with solid tumors. *Clin Cancer Res, 16*(20), 5058-5066. doi:10.1158/1078-0432.CCR-10-0387

Hamaguchi, T., Tsuji, A., Yamaguchi, K., Takeda, K., Uetake, H., Esaki, T., . . . Tsukamoto, T. (2018). A phase II study of NK012, a polymeric micelle formulation of SN-38, in unresectable, metastatic or recurrent colorectal cancer patients. *Cancer Chemother Pharmacol, 82*(6), 1021-1029. doi:10.1007/s00280-018-3693-6

Hanahan, D., & Weinberg, R. A. (2011). Hallmarks of cancer: the next generation. *Cell, 144*(5), 646-674. doi:10.1016/j.cell.2011.02.013

Hanioka, N., Ozawa, S., Jinno, H., Ando, M., Saito, Y., & Sawada, J. (2001). Human liver UDP-glucuronosyltransferase isoforms involved in the glucuronidation of 7-ethyl-10-hydroxycamptothecin. *Xenobiotica, 31*(10), 687-699.

Hare, J. I., Lammers, T., Ashford, M. B., Puri, S., Storm, G., & Barry, S. T. (2017). Challenges and strategies in anti-cancer nanomedicine development: An industry perspective. *Adv Drug Deliv Rev, 108*, 25-38. doi:10.1016/j.addr.2016.04.025

Harma, V., Virtanen, J., Makela, R., Happonen, A., Mpindi, J. P., Knuuttila, M., . . . Nees, M. (2010). A comprehensive panel of three-dimensional models for studies of prostate cancer growth, invasion and drug responses. *PLoS One, 5*(5), e10431. doi:10.1371/journal.pone.0010431

Harrison, T. S., & Scott, L. J. (2005). Atazanavir. *Drugs, 65*(16), 2309-2336. doi:10.2165/00003495-200565160-00010

Hartung, T. (2009). Toxicology for the twenty-first century. *Nature, 460*(7252), 208-212. doi:10.1038/460208a

Hatton, F., Chambon, P., McDonald, T. O., Owen, A., & Rannard, S. P. (2014). Hyperbranched polydendrons: a new controlled macromolecular architecture with self-assembly in water and organic solvents. *Chemical Science, 5*(5), 1844-1853. doi:10.1039/C4SC00360H

Hatton, F., Tatham, L. M., Tidbury, L. R., Chambon, P., He, T., Owen, A., & Rannard, S. P. (2015). Hyperbranched polydendrons: a new nanomaterials platform with tuneable permeation through model gut epithelium. *Chem Sci, 6*(1), 326-334. doi:10.1039/c4sc02889a

Hess, K. R., Varadhachary, G. R., Taylor, S. H., Wei, W., Raber, M. N., Lenzi, R., & Abbruzzese, J. L. (2006). Metastatic patterns in adenocarcinoma. *Cancer, 106*(7), 1624-1633. doi:10.1002/cncr.21778

Hickson, S. E., Margineantu, D., Hockenbery, D. M., Simon, J. A., & Geballe, A. P. (2018). Inhibition of vaccinia virus replication by nitazoxanide. *Virology, 518*, 398-405. doi:10.1016/j.virol.2018.03.023

Hinoshita, E., Uchiumi, T., Taguchi, K., Kinukawa, N., Tsuneyoshi, M., Maehara, Y., . . . Kuwano, M. (2000). Increased expression of an ATP-binding cassette superfamily transporter, multidrug resistance protein 2, in human colorectal carcinomas. *Clin Cancer Res, 6*(6), 2401-2407. Retrieved from https://www.ncbi.nlm.nih.gov/pubmed/10873092

Hirani, V. N., Raucy, J. L., & Lasker, J. M. (2004). Conversion of the HIV protease inhibitor nelfinavir to a bioactive metabolite by human liver CYP2C19. *Drug Metab Dispos, 32*(12), 1462-1467. doi:10.1124/dmd.104.001743

Hoch, U., Staschen, C. M., Johnson, R. K., & Eldon, M. A. (2014). Nonclinical pharmacokinetics and activity of etirinotecan pegol (NKTR-102), a long-acting topoisomerase 1 inhibitor, in multiple cancer models. *Cancer Chemother Pharmacol, 74*(6), 1125-1137. doi:10.1007/s00280-014-2577-7

Hoffmann, M., Kleine-Weber, H., Schroeder, S., Kruger, N., Herrler, T., Erichsen, S., . . . Pohlmann, S. (2020). SARS-CoV-2 Cell Entry Depends on ACE2 and TMPRSS2 and Is Blocked by a Clinically Proven Protease Inhibitor. *Cell*, doi: 10.1016/j.cell.2020.1002.1052. Retrieved from https://www.ncbi.nlm.nih.gov/pubmed/32142651

Hompes, D., D'Hoore, A., Van Cutsem, E., Fieuws, S., Ceelen, W., Peeters, M., . . . Kerger, J. (2012). The Treatment of Peritoneal Carcinomatosis of Colorectal Cancer with Complete Cytoreductive Surgery and Hyperthermic Intraperitoneal Peroperative Chemotherapy (HIPEC) with Oxaliplatin: A Belgian Multicentre Prospective Phase II Clinical Study. *Annals of Surgical Oncology, 19*(7), 2186-2194. doi:10.1245/s10434-012-2264-z

Hongisto, V., Jernstrom, S., Fey, V., Mpindi, J. P., Kleivi Sahlberg, K., Kallioniemi, O., & Perala, M. (2013). High-throughput 3D screening reveals differences in drug sensitivities between culture models of JIMT1 breast cancer cells. *PLoS One, 8*(10), e77232. doi:10.1371/journal.pone.0077232

Horning, J. L., Sahoo, S. K., Vijayaraghavalu, S., Dimitrijevic, S., Vasir, J. K., Jain, T. K., . . . Labhasetwar, V. (2008). 3-D tumor model for in vitro evaluation of anticancer drugs. *Mol Pharm, 5*(5), 849-862. doi:10.1021/mp800047v

Hornung, A., Poettler, M., Friedrich, R. P., Zaloga, J., Unterweger, H., Lyer, S., . . . Janko, C. (2015). Treatment Efficiency of Free and Nanoparticle-Loaded Mitoxantrone for Magnetic Drug Targeting in Multicellular Tumor Spheroids. *Molecules, 20*(10), 18016-18030. doi:10.3390/molecules201018016

Hoskins, J. M., Goldberg, R. M., Qu, P., Ibrahim, J. G., & McLeod, H. L. (2007). UGT1A1*28 genotype and irinotecan-induced neutropenia: dose matters. *J Natl Cancer Inst, 99*(17), 1290-1295. doi:10.1093/jnci/djm115

Hsiang, Y. H., Liu, L. F., Wall, M. E., Wani, M. C., Nicholas, A. W., Manikumar, G., . . . Potmesil, M. (1989). DNA topoisomerase I-mediated DNA cleavage and cytotoxicity of camptothecin analogues. *Cancer Res, 49*(16), 4385-4389. Retrieved from https://www.ncbi.nlm.nih.gov/pubmed/2545341

Hu, Z. P., Yang, X. X., Chen, X., Chan, E., Duan, W., & Zhou, S. F. (2007). Simultaneous determination of irinotecan (CPT-11) and SN-38 in tissue culture media and cancer cells by high performance liquid chromatography: application to cellular metabolism and accumulation studies. *J Chromatogr B Analyt Technol Biomed Life Sci, 850*(1-2), 575-580. doi:10.1016/j.jchromb.2006.12.056

Humeniuk, R., Mathias, A., Cao, H., Osinusi, A., Shen, G., Chng, E., . . . German, P. (2020). Safety, Tolerability, and Pharmacokinetics of Remdesivir, an Antiviral for Treatment of COVID-19, in Healthy Subjects. *Clin Transl Sci*. doi:10.1111/cts.12840

Humerickhouse, R., Lohrbach, K., Li, L., Bosron, W. F., & Dolan, M. E. (2000). Characterization of CPT-11 hydrolysis by human liver carboxylesterase isoforms hCE-1 and hCE-2. *Cancer Res, 60*(5), 1189-1192. Retrieved from https://www.ncbi.nlm.nih.gov/pubmed/10728672

Innocenti, F., Kroetz, D. L., Schuetz, E., Dolan, M. E., Ramirez, J., Relling, M., . . . Ratain, M. J. (2009). Comprehensive pharmacogenetic analysis of irinotecan neutropenia and pharmacokinetics. *Journal of Clinical Oncology, 27*(16), 2604-2614. doi:10.1200/JCO.2008.20.6300

Ipsen Pharma. (2019). ONIVYDE® (Irinotecan liposome injection) | Health Care Professional Info. Retrieved from www.onivyde.com

Ivanov, D. P., Parker, T. L., Walker, D. A., Alexander, C., Ashford, M. B., Gellert, P. R., & Garnett, M. C. (2014). Multiplexing spheroid volume, resazurin and acid phosphatase viability assays for high-throughput screening of tumour spheroids and stem cell neurospheres. *PLoS One, 9*(8), e103817. doi:10.1371/journal.pone.0103817

Iyer, L., Hall, D., Das, S., Mortell, M. A., Ramírez, J., Kim, S., . . . Ratain, M. (1999). Phenotype-genotype correlation of in vitro SN-38 (active metabolite of irinotecan) and bilirubin glucuronidation in human liver tissue with UGT1A1 promoter polymorphism. *J Clinical Pharmacology, 65*(5), 576-582.

Iyer, L., King, C. D., Whitington, P. F., Green, M. D., Roy, S. K., Tephly, T. R., . . . Ratain, M. J. (1998). Genetic predisposition to the metabolism of irinotecan (CPT-11). Role of uridine diphosphate glucuronosyltransferase isoform 1A1 in the glucuronidation of its active metabolite (SN-38) in human liver microsomes. *J Clin Invest, 101*(4), 847-854. doi:10.1172/JCI915

Jacquet, P., Averbach, A., Stuart, O. A., Chang, D., & Sugarbaker, P. H. (1998). Hyperthermic intraperitoneal doxorubicin: pharmacokinetics, metabolism, and tissue distribution in a rat model. *Cancer Chemother Pharmacol, 41*(2), 147-154. Retrieved from https://www.ncbi.nlm.nih.gov/pubmed/9443628

Jain, R. K., & Stylianopoulos, T. (2010). Delivering nanomedicine to solid tumors. *Nat Rev Clin Oncol, 7*(11), 653-664. doi:10.1038/nrclinonc.2010.139

Jain, R. K., Tong, R. T., & Munn, L. L. (2007). Effect of vascular normalization by antiangiogenic therapy on interstitial hypertension, peritumor edema, and lymphatic metastasis: insights from a mathematical model. *Cancer Res, 67*(6), 2729-2735. doi:10.1158/0008-5472.CAN-06-4102

James, J. S. (1997). Nelfinavir (Viracept) approved: fourth protease inhibitor available. *AIDS Treat News*(No 267), 1-2. Retrieved from https://www.ncbi.nlm.nih.gov/pubmed/11364249

Jameson, G. S., Hamm, J. T., Weiss, G. J., Alemany, C., Anthony, S., Basche, M., . . . Von Hoff, D. D. (2013). A multicenter, phase I, dose-escalation study to assess the safety, tolerability, and pharmacokinetics of etirinotecan pegol in patients with refractory solid tumors. *Clin Cancer Res, 19*(1), 268-278. doi:10.1158/1078-0432.CCR-12-1201

Jazz Pharmaceuticals. (2019). Acute Myeloid Leukemia (AML) Treatment | VYXEOS® (daunorubicin and cytarabine). Retrieved from https://vyxeos.com/

Jeon, O., Marks, R., Wolfson, D., & Alsberg, E. (2016). Dual-crosslinked hydrogel microwell system for formation and culture of multicellular human adipose tissue-derived stem cell spheroids. *J Mater Chem B, 4*(20), 3526-3533. doi:10.1039/c6tb00064a

Jeon, S., Ko, M., Lee, J., Choi, I., Byun, S. Y., Park, S., . . . Kim, S. (2020). Identification of antiviral drug candidates against SARS-CoV-2 from FDA-approved drugs. doi: 10.1101/2020.1103.1120.999730 J bioRxiv. Retrieved from https://www.biorxiv.org/content/biorxiv/early/2020/03/28/2020.03.20.999730.full.pdf

Jeong, B., Bae, Y. H., & Kim, S. W. (2000). Drug release from biodegradable injectable thermosensitive hydrogel of PEG-PLGA-PEG triblock copolymers. *J Control Release, 63*(1-2), 155-163. doi:10.1016/s0168-3659(99)00194-7

Jiang, T., Jin, K., Liu, X. P., & Pang, Z. Q. (2017). Nanoparticles for tumor targeting. *Biopolymer-Based Composites: Drug Delivery and Biomedical Applications*, 221-267. doi:10.1016/B978-0-08-101914-6.00008-9

Jiang, W., Huang, Y. H., An, Y., & Kim, B. Y. S. (2015). Remodeling Tumor Vasculature to Enhance Delivery of Intermediate-Sized Nanoparticles. *ACS Nano, 9*(9), 8689-8696. doi:10.1021/acsnano.5b02028

Jiang, W., von Roemeling, C. A., Chen, Y. X., Qie, Y. Q., Liu, X. J., Chen, J. Z., & Kim, B. Y. S. (2017). Designing nanomedicine for immuno-oncology. *Nature Biomedical Engineering, 1*(2). doi:10.1038/s41551-017-0029

Jin, Z., Du, X., Xu, Y., Deng, Y., Liu, M., Zhao, Y., . . . Yang, H. (2020). Structure of Mpro from COVID-19 virus and discovery of its inhibitors. *Nature*, doi: 10.1038/s41586-41020-42223-y. Retrieved from https://doi.org/10.1038/s41586-020-2223-y

Jo, Y., Choi, N., Kim, K., Koo, H. J., Choi, J., & Kim, H. N. (2018). Chemoresistance of Cancer Cells: Requirements of Tumor Microenvironment-mimicking In Vitro Models in Anti-Cancer Drug Development. *Theranostics, 8*(19), 5259-5275. doi:10.7150/thno.29098

Jones, R. P., Jackson, R., Dunne, D. F., Malik, H. Z., Fenwick, S. W., Poston, G. J., & Ghaneh, P. (2012). Systematic review and meta-analysis of follow-up after hepatectomy for colorectal liver metastases. *Br J Surg, 99*(4), 477-486. doi:10.1002/bjs.8667

Joo, I., Lee, J. M., Kim, K. W., Klotz, E., Han, J. K., & Choi, B. I. (2011). Liver metastases on quantitative color mapping of the arterial enhancement fraction from multiphasic CT scans: evaluation of the hemodynamic features and correlation with the chemotherapy response. *Eur J Radiol, 80*(3), e278-283. doi:10.1016/j.ejrad.2010.12.002

Jung, J., Kim, J., Lim, H. K., Kim, K. M., Lee, Y. S., Park, J. S., & Yoon, D. S. (2017). Establishing a colorectal cancer liver metastasis patient-derived tumor xenograft model for the evaluation of personalized chemotherapy. *Annals of Surgical Treatment and Research, 93*(4), 173-180. doi:10.4174/astr.2017.93.4.173

Jurgeit, A., McDowell, R., Moese, S., Meldrum, E., Schwendener, R., & Greber, U. F. (2012). Niclosamide is a proton carrier and targets acidic endosomes with broad antiviral effects. *PLoS Pathog, 8*(10), e1002976. doi:10.1371/journal.ppat.1002976

Justice, A. C., Zingmond, D. S., Gordon, K. S., Fultz, S. L., Goulet, J. L., King, J. T., Jr., . . . the Veterans Aging Cohort Study Project, T. (2008). Drug Toxicity, HIV Progression, or Comorbidity of Aging: Does Tipranavir Use Increase the Risk of Intracranial Hemorrhage? *Clinical Infectious Diseases, 47*(9), 1226-1230. doi:10.1086/592302

Justice, A. C., Zingmond, D. S., Gordon, K. S., Fultz, S. L., Goulet, J. L., King, J. T., Jr., . . . Veterans Aging Cohort Study Project, T. (2008). Drug toxicity, HIV progression, or comorbidity of aging: does tipranavir use increase the risk of intracranial hemorrhage? *Clin Infect Dis, 47*(9), 1226-1230. doi:10.1086/592302

Kai, M., Ziemys, A., Liu, Y. T., Kojic, M., Ferrari, M., & Yokoi, K. (2019). Tumor Site-Dependent Transport Properties Determine Nanotherapeutics Delivery and Its Efficacy. *Transl Oncol, 12*(9), 1196-1205. doi:10.1016/j.tranon.2019.05.011

Kamaly, N., Yameen, B., Wu, J., & Farokhzad, O. C. (2016). Degradable Controlled-Release Polymers and Polymeric Nanoparticles: Mechanisms of Controlling Drug Release. *Chem Rev, 116*(4), 2602-2663. doi:10.1021/acs.chemrev.5b00346

Kaneda, N., Nagata, H., Furuta, T., & Yokokura, T. (1990). Metabolism and pharmacokinetics of the camptothecin analogue CPT-11 in the mouse. *Cancer Res, 50*(6), 1715-1720. Retrieved from https://www.ncbi.nlm.nih.gov/pubmed/2306725

Kang, N., Gores, G. J., & Shah, V. H. (2011). Hepatic stellate cells: partners in crime for liver metastases? *Hepatology, 54*(2), 707-713. doi:10.1002/hep.24384

Kapalczynska, M., Kolenda, T., Przybyla, W., Zajaczkowska, M., Teresiak, A., Filas, V., . . . Lamperska, K. (2018). 2D and 3D cell cultures - a comparison of different types of cancer cell cultures. *Arch Med Sci, 14*(4), 910-919. doi:10.5114/aoms.2016.63743

Karlsson, H., Fryknas, M., Larsson, R., & Nygren, P. (2012). Loss of cancer drug activity in colon cancer HCT-116 cells during spheroid formation in a new 3-D spheroid cell culture system. *Exp Cell Res, 318*(13), 1577-1585. doi:10.1016/j.yexcr.2012.03.026

Kauffels, A., Kitzmuller, M., Gruber, A., Nowack, H., Bohnenberger, H., Spitzner, M., . . . Sperling, J. (2019). Hepatic arterial infusion of irinotecan and EmboCept((R)) S results in high tumor concentration of SN-38 in a rat model of colorectal liver metastases. *Clin Exp Metastasis, 36*(1), 57-66. doi:10.1007/s10585-019-09954-5

Kawai, R., Mathew, D., Tanaka, C., & Rowland, M. (1998). Physiologically based pharmacokinetics of cyclosporine A: extension to tissue distribution kinetics in rats and scale-up to human. *J Pharmacol Exp Ther, 287*(2), 457-468. Retrieved from https://www.ncbi.nlm.nih.gov/pubmed/9808668

Kawato, Y., Aonuma, M., Hirota, Y., Kuga, H., & Sato, K. (1991). Intracellular roles of SN-38, a metabolite of the camptothecin derivative CPT-11, in the antitumor effect of CPT-11. *Cancer Res, 51*(16), 4187-4191. Retrieved from https://www.ncbi.nlm.nih.gov/pubmed/1651156

Kayaku, N. (2019). Status of New Drug Development. Retrieved from https://www.nipponkayaku.co.jp/english/ir/business/files/pharmaceuticals.pdf

Kelly, B. D., McLeod, V., Walker, R., Schreuders, J., Jackson, S., Giannis, M., . . . Owen, D. J. (2020). Abstract 1715: Anti-cancer activity of a SN-38 nanoparticle, DEP® irinotecan, in human colon cancer xenograft models. *Cancer Research, 80*(16 Supplement), 1715-1715. doi:10.1158/1538-7445.Am2020-1715

Khageh Hosseini, S., Kolterer, S., Steiner, M., von Manstein, V., Gerlach, K., Trojan, J., . . . Zornig, M. (2017). Camptothecin and its analog SN-38, the active metabolite of irinotecan, inhibit binding of the transcriptional regulator and oncoprotein FUBP1 to its DNA target sequence FUSE. *Biochem Pharmacol, 146*, 53-62. doi:10.1016/j.bcp.2017.10.003

Khan, S., Ahmad, A., & Ahmad, I. (2003). A sensitive and rapid liquid chromatography tandem mass spectrometry method for quantitative determination of 7-ethyl-10-hydroxycamptothecin (SN-38) in human plasma containing liposome-based SN-38 (LE-SN38). *Biomed Chromatogr, 17*(8), 493-499. doi:10.1002/bmc.257

Khawar, I. A., Kim, J. H., & Kuh, H. J. (2015). Improving drug delivery to solid tumors: priming the tumor microenvironment. *J Control Release, 201*, 78-89. doi:10.1016/j.jconrel.2014.12.018

Kim, J. B. (2005). Three-dimensional tissue culture models in cancer biology. *Semin Cancer Biol, 15*(5), 365-377. doi:10.1016/j.semcancer.2005.05.002

Kim, S. A., Lee, E. K., & Kuh, H. J. (2015). Co-culture of 3D tumor spheroids with fibroblasts as a model for epithelial-mesenchymal transition in vitro. *Exp Cell Res, 335*(2), 187-196. doi:10.1016/j.yexcr.2015.05.016

King, J. R., & Acosta, E. P. (2006). Tipranavir. *Clinical Pharmacokinetics, 45*(7), 665-682. doi:10.2165/00003088-200645070-00003

Kinoshita, T., Higuchi, H., Sakai, G., Hamamoto, Y., Takaishi, H., & Kanai, T. (2018). Analysis of sensitivity and cell death pathways mediated by anti-cancer drugs using three-dimensional culture system. *International Journal of Cancer Research, 14*(1), 1-12.

Knop, K., Hoogenboom, R., Fischer, D., & Schubert, U. S. (2010). Poly(ethylene glycol) in Drug Delivery: Pros and Cons as Well as Potential Alternatives. *Angewandte Chemie-International Edition, 49*(36), 6288-6308. doi:10.1002/anie.200902672

Knuchel, R., Hofstadter, F., Jenkins, W. E., & Masters, J. R. (1989). Sensitivities of monolayers and spheroids of the human bladder cancer cell line MGH-U1 to the drugs used for intravesical chemotherapy. *Cancer Res, 49*(6), 1397-1401. Retrieved from https://www.ncbi.nlm.nih.gov/pubmed/2493980

Ko, M., Jeon, S., Ryu, W.-S., & Kim, S. (2020). Comparative analysis of antiviral efficacy of FDA-approved drugs against SARS-CoV-2 in human lung cells: Nafamostat is the most potent antiviral drug candidate. *bioRxiv*, 2020.2005.2012.090035. doi:10.1101/2020.05.12.090035

Kobayashi, H., Watanabe, R., & Choyke, P. L. (2013). Improving conventional enhanced permeability and retention (EPR) effects; what is the appropriate target? *Theranostics, 4*(1), 81-89. doi:10.7150/thno.7193

Kobayashi, H., Watanabe, R., & Choyke, P. L. (2014). Improving Conventional Enhanced Permeability and Retention (EPR) Effects; What Is the Appropriate Target? *Theranostics, 4*(1), 81-89. doi:10.7150/thno.7193

Koizumi, F., Kitagawa, M., Negishi, T., Onda, T., Matsumoto, S., Hamaguchi, T., & Matsumura, Y. (2006). Novel SN-38-incorporating polymeric micelles, NK012, eradicate vascular endothelial growth factor-secreting bulky tumors. *Cancer Res, 66*(20), 10048-10056. doi:10.1158/0008-5472.CAN-06-1605

Kondo, J., Ekawa, T., Endo, H., Yamazaki, K., Tanaka, N., Kukita, Y., . . . Inoue, M. (2019). High-throughput screening in colorectal cancer tissue-originated spheroids. *Cancer Sci, 110*(1), 345-355. doi:10.1111/cas.13843

Kondo, J., Endo, H., Okuyama, H., Ishikawa, O., Iishi, H., Tsujii, M., . . . Inoue, M. (2011). Retaining cell-cell contact enables preparation and culture of spheroids composed of pure primary cancer cells from colorectal cancer. *Proc Natl Acad Sci U S A, 108*(15), 6235-6240. doi:10.1073/pnas.1015938108

Koo, H., Huh, M. S., Sun, I. C., Yuk, S. H., Choi, K., Kim, K., & Kwon, I. C. (2011). In Vivo Targeted Delivery of Nanoparticles for Theranosis. *Accounts of Chemical Research, 44*(10), 1018-1028. doi:10.1021/ar2000138

Krudsood, S., Looareesuwan, S., Tangpukdee, N., Wilairatana, P., Phumratanaprapin, W., Leowattana, W., . . . Taylor, W. R. J. (2010). New Fixed-Dose Artesunate-Mefloquine Formulation against Multidrug-Resistant Plasmodium falciparum in Adults: a Comparative Phase IIb Safety and Pharmacokinetic Study with Standard-Dose Nonfixed Artesunate plus Mefloquine. *54*(9), 3730-3737. doi:10.1128/AAC.01187-09 %J Antimicrobial Agents and Chemotherapy

Kruse, G., Esser, S., Stocker, H., Breske, A., Koerber, A., Kopperman, M., . . . Kurowski, M. (2005). The steady-state pharmacokinetics of nelfinavir in combination with tenofovir in HIV-infected patients. *Antivir Ther, 10*(2), 349-355. Retrieved from https://www.ncbi.nlm.nih.gov/pubmed/15865230

Kulkarni, P., Haldar, M. K., Katti, P., Dawes, C., You, S., Choi, Y., & Mallik, S. (2016). Hypoxia Responsive, Tumor Penetrating Lipid Nanoparticles for Delivery of Chemotherapeutics to Pancreatic Cancer Cell Spheroids. *Bioconjug Chem, 27*(8), 1830-1838. doi:10.1021/acs.bioconjchem.6b00241

Kunz-Schughart, L. A., Freyer, J. P., Hofstaedter, F., & Ebner, R. (2004). The use of 3-D cultures for high-throughput screening: the multicellular spheroid model. *J Biomol Screen, 9*(4), 273-285. doi:10.1177/1087057104265040

Kurita, A., & Kaneda, N. (1999). High-performance liquid chromatographic method for the simultaneous determination of the camptothecin derivative irinotecan hydrochloride, CPT-11, and its metabolites SN-38 and SN-38 glucuronide in rat plasma with a fully automated on-line solid-phase extraction system, PROSPEKT. *J Chromatogr B Biomed Sci Appl, 724*(2), 335-344. doi:10.1016/s0378-4347(98)00554-4

Kusamura, S., Dominique, E., Baratti, D., Younan, R., & Deraco, M. (2008). Drugs, carrier solutions and temperature in hyperthermic intraperitoneal chemotherapy. *J Surg Oncol, 98*(4), 247-252. doi:10.1002/jso.21051

Kyle, A. H., Baker, J. H., & Minchinton, A. I. (2012). Targeting quiescent tumor cells via oxygen and IGF-I supplementation. *Cancer Res, 72*(3), 801-809. doi:10.1158/0008-5472.CAN-11-3059

la Porte, C. J., Sabo, J. P., Beique, L., & Cameron, D. W. (2009). Lack of effect of efavirenz on the pharmacokinetics of tipranavir-ritonavir in healthy volunteers. *Antimicrob Agents Chemother, 53*(11), 4840-4844. doi:10.1128/AAC.00462-09

Lai, M., & Lü, B. (2012). 3.04 - Tissue Preparation for Microscopy and Histology. In J. Pawliszyn (Ed.), *Comprehensive Sampling and Sample Preparation* (pp. 53-93). Oxford: Academic Press.

Lammers, T., Rizzo, L. Y., Storm, G., & Kiessling, F. (2012). Personalized nanomedicine. *Clin Cancer Res, 18*(18), 4889-4894. doi:10.1158/1078-0432.CCR-12-1414

Langhans, S. A. (2018). Three-Dimensional in Vitro Cell Culture Models in Drug Discovery and Drug Repositioning. *Front Pharmacol, 9*, 6. doi:10.3389/fphar.2018.00006

Lazaris, A., Amri, A., Petrillo, S. K., Zoroquiain, P., Ibrahim, N., Salman, A., . . . Metrakos, P. (2018). Vascularization of colorectal carcinoma liver metastasis: insight into stratification of patients for anti-angiogenic therapies. *J Pathol Clin Res, 4*(3), 184-192. doi:10.1002/cjp2.100

Lee, B., Min, J. A., Nashed, A., Lee, S. O., Yoo, J. C., Chi, S. W., & Yi, G. S. (2019). A novel mechanism of irinotecan targeting MDM2 and Bcl-xL. *Biochem Biophys Res Commun, 514*(2), 518-523. doi:10.1016/j.bbrc.2019.04.009

Lee, J. M., Park, D. Y., Yang, L., Kim, E. J., Ahrberg, C. D., Lee, K. B., & Chung, B. G. (2018). Generation of uniform-sized multicellular tumor spheroids using hydrogel microwells for advanced drug screening. *Sci Rep, 8*(1), 17145. doi:10.1038/s41598-018-35216-7

Lee, K. S., Chung, H. C., Im, S. A., Park, Y. H., Kim, C. S., Kim, S. B., . . . Ro, J. (2008). Multicenter phase II trial of Genexol-PM, a Cremophor-free, polymeric micelle formulation of paclitaxel, in patients with metastatic breast cancer. *Breast Cancer Res Treat, 108*(2), 241-250. doi:10.1007/s10549-007-9591-y

Leite, P. E. C., Pereira, M. R., Harris, G., Pamies, D., Dos Santos, L. M. G., Granjeiro, J. M., . . . Smirnova, L. (2019). Suitability of 3D human brain spheroid models to distinguish toxic effects of gold and poly-lactic acid nanoparticles to assess biocompatibility for brain drug delivery. *Part Fibre Toxicol, 16*(1), 22. doi:10.1186/s12989-019-0307-3

Lencioni, R., & Cioni, D. (2016). RFA plus lyso-thermosensitive liposomal doxorubicin: in search of the optimal approach to cure intermediate-size hepatocellular carcinoma. *Hepat Oncol, 3*(3), 193-200. doi:10.2217/hep-2016-0005

Less, J. R., Posner, M. C., Boucher, Y., Borochovitz, D., Wolmark, N., & Jain, R. K. (1992). Interstitial Hypertension in Human Tumors .4. Interstitial Hypertension in Human Breast and Colorectal Tumors. *Cancer Research, 52*(22), 6371-6374. Retrieved from <Go to ISI>://WOS:A1992JX75400038

Li, L., ten Hagen, T. L., Bolkestein, M., Gasselhuber, A., Yatvin, J., van Rhoon, G. C., . . . Koning, G. A. (2013). Improved intratumoral nanoparticle extravasation and penetration by mild hyperthermia. *J Control Release, 167*(2), 130-137. doi:10.1016/j.jconrel.2013.01.026

Li, R., You, S., Hu, Z., Chen, Z. G., Sica, G. L., Khuri, F. R., . . . Deng, X. (2013). Inhibition of STAT3 by niclosamide synergizes with erlotinib against head and neck cancer. *PLoS One, 8*(9), e74670. doi:10.1371/journal.pone.0074670

Li, W., Moore, M. J., Vasilieva, N., Sui, J., Wong, S. K., Berne, M. A., . . . Farzan, M. (2003). Angiotensin-converting enzyme 2 is a functional receptor for the SARS coronavirus. *Nature, 426*(6965), 450-454. doi:10.1038/nature02145

Li, Y., Zhang, T., Liu, Q., & He, J. (2019). PEG-Derivatized Dual-Functional Nanomicelles for Improved Cancer Therapy. *Front Pharmacol, 10*, 808. doi:10.3389/fphar.2019.00808

Li, Z., Tan, S., Li, S., Shen, Q., & Wang, K. (2017). Cancer drug delivery in the nano era: An overview and perspectives (Review). *Oncol Rep, 38*(2), 611-624. doi:10.3892/or.2017.5718

Lichtenstern, C. R., Ngu, R. K., Shalapour, S., & Karin, M. (2020). Immunotherapy, Inflammation and Colorectal Cancer. *Cells, 9*(3). doi:10.3390/cells9030618

Liechty, W. B., Kryscio, D. R., Slaughter, B. V., & Peppas, N. A. (2010). Polymers for drug delivery systems. *Annu Rev Chem Biomol Eng, 1*, 149-173. doi:10.1146/annurev-chembioeng-073009-100847

Lien, E. A., Solheim, E., & Ueland, P. M. (1991). Distribution of tamoxifen and its metabolites in rat and human tissues during steady-state treatment. *Cancer Res, 51*(18), 4837-4844. Retrieved from https://www.ncbi.nlm.nih.gov/pubmed/1893376

Lin, C. K., Bai, M. Y., Hu, T. M., Wang, Y. C., Chao, T. K., Weng, S. J., . . . Lai, H. C. (2016). Preclinical evaluation of a nanoformulated antihelminthic, niclosamide, in ovarian cancer. *Oncotarget, 7*(8), 8993-9006. doi:10.18632/oncotarget.7113

Lin, H. C., Chuang, C. H., Cheng, M. H., Lin, Y. C., & Fang, Y. P. (2019). High Potency of SN-38-Loaded Bovine Serum Albumin Nanoparticles Against Triple-Negative Breast Cancer. *Pharmaceutics, 11*(11). doi:10.3390/pharmaceutics11110569

Lin, R. Z., & Chang, H. Y. (2008). Recent advances in three-dimensional multicellular spheroid culture for biomedical research. *Biotechnol J, 3*(9-10), 1172-1184. doi:10.1002/biot.200700228

LipoMedix. (2019). LipoMedix -®Product-Promitil. Retrieved from http://lipomedix.com/Products/%C2%AEProduct-Promitil

Liu, C., Zhao, G., Liu, J., Ma, N., Chivukula, P., Perelman, L., . . . Yu, L. (2009). Novel biodegradable lipid nano complex for siRNA delivery significantly improving the chemosensitivity of human colon cancer stem cells to paclitaxel. *J Control Release, 140*(3), 277-283. doi:10.1016/j.jconrel.2009.08.013

Liu, H., Lu, H., Liao, L., Zhang, X., Gong, T., & Zhang, Z. (2015). Lipid nanoparticles loaded with 7-ethyl-10-hydroxycamptothecin-phospholipid complex: in vitro and in vivo studies. *Drug Deliv, 22*(6), 701-709. doi:10.3109/10717544.2014.895069

Liu, P., Ruhnke, M., Meersseman, W., Paiva, J. A., Kantecki, M., & Damle, B. (2013). Pharmacokinetics of anidulafungin in critically ill patients with candidemia/invasive candidiasis. *Antimicrob Agents Chemother, 57*(4), 1672-1676. doi:10.1128/AAC.02139-12

Liu, X., Tang, I., Wainberg, Z. A., & Meng, H. (2020). Safety Considerations of Cancer Nanomedicine-A Key Step toward Translation. *Small, 16*(36), e2000673. doi:10.1002/smll.202000673

Liu, Y., & Matsui, O. (2007). Changes of intratumoral microvessels and blood perfusion during establishment of hepatic metastases in mice. *Radiology, 243*(2), 386-395. doi:10.1148/radiol.2432060341

Liu, Y., Yan, L. M., Wan, L., Xiang, T. X., Le, A., Liu, J. M., . . . Zhang, W. (2020). Viral dynamics in mild and severe cases of COVID-19. *Lancet Infect Dis*, doi: 10.1016/S1473-3099(1020)30232-30232. Retrieved from https://www.ncbi.nlm.nih.gov/pubmed/32199493

Lo, H. S., Hui, K. P. Y., Lai, H.-M., Khan, K. S., Kaur, S., Li, Z., . . . Ng, W.-L. (2020). Simeprevir suppresses SARS-CoV-2 replication and synergizes with remdesivir. *bioRxiv*, 2020.2005.2026.116020. doi:10.1101/2020.05.26.116020

Lovegrove, F. E., & Kain, K. C. (2008). Chapter 6 - Malaria Prevention. In E. C. Jong & C. Sanford (Eds.), *The Travel and Tropical Medicine Manual (Fourth Edition)* (pp. 76-99). Edinburgh: W.B. Saunders.

Lu, C. W., Liu, X. F., & Jia, Z. F. (2020). 2019-nCoV transmission through the ocular surface must not be ignored. *Lancet, 395*(10224), e39. doi:10.1016/S0140-6736(20)30313-5

Lu, H., Noorani, L., Jiang, Y., Du, A. W., & Stenzel, M. H. (2017). Penetration and drug delivery of albumin nanoparticles into pancreatic multicellular tumor spheroids. *J Mater Chem B, 5*(48), 9591-9599. doi:10.1039/c7tb02902k

Luca, A. C., Mersch, S., Deenen, R., Schmidt, S., Messner, I., Schafer, K. L., . . . Stoecklein, N. H. (2013). Impact of the 3D microenvironment on phenotype, gene expression, and EGFR inhibition of colorectal cancer cell lines. *PLoS One, 8*(3), e59689. doi:10.1371/journal.pone.0059689

Luo, H. Y., Yang, Z., Wei, W., Li, Y. Q., Pu, H. Y., Chen, Y., . . . Xu, R. H. (2018). Enzymatically synthesized poly(amino-co-ester) polyplexes for systemic delivery of pcDNA-miRNA-214 to suppress colorectal cancer liver metastasis. *Journal of Materials Chemistry B, 6*(40). doi:10.1039/c8tb01932k

Lv, Z., Chu, Y., & Wang, Y. (2015). HIV protease inhibitors: a review of molecular selectivity and toxicity. *HIV AIDS (Auckl), 7*, 95-104. doi:10.2147/HIV.S79956

Lyon, P. C., Gray, M. D., Mannaris, C., Folkes, L. K., Stratford, M., Campo, L., . . . Coussios, C. C. (2018). Safety and feasibility of ultrasound-triggered targeted drug delivery of doxorubicin from thermosensitive liposomes in liver tumours (TARDOX): a single-centre, open-label, phase 1 trial. *Lancet Oncology, 19*(8), 1027-1039. doi:10.1016/S1470-2045(18)30332-2

Ma, H. L., Jiang, Q., Han, S., Wu, Y., Cui Tomshine, J., Wang, D., . . . Liang, X. J. (2012). Multicellular tumor spheroids as an in vivo-like tumor model for three-dimensional imaging of chemotherapeutic and nano material cellular penetration. *Mol Imaging, 11*(6), 487-498. Retrieved from https://www.ncbi.nlm.nih.gov/pubmed/23084249

Mabb, A. M., Simon, J. M., King, I. F., Lee, H.-M., An, L.-K., Philpot, B. D., & Zylka, M. J. (2016). Topoisomerase 1 Regulates Gene Expression in Neurons through Cleavage Complex-Dependent and -Independent Mechanisms. *PLoS One, 11*(5), e0156439. doi:10.1371/journal.pone.0156439

Maeda, H., Wu, J., Sawa, T., Matsumura, Y., & Hori, K. (2000). Tumor vascular permeability and the EPR effect in macromolecular therapeutics: a review. *J Control Release, 65*(1-2), 271-284. doi:10.1016/s0168-3659(99)00248-5

Mahli, A., Saugspier, M., Koch, A., Sommer, J., Dietrich, P., Lee, S., . . . Hellerbrand, C. (2018). ERK activation and autophagy impairment are central mediators of irinotecan-induced steatohepatitis. *Gut, 67*(4), 746-756. doi:10.1136/gutjnl-2016-312485

Maitani, Y., Nakamura, Y., Kon, M., Sanada, E., Sumiyoshi, K., Fujine, N., . . . Shimizu, T. (2013). Higher lung accumulation of intravenously injected organic nanotubes. *Int J Nanomedicine, 8*, 315-323. doi:10.2147/IJN.S38462

Marangon, E., Posocco, B., Mazzega, E., & Toffoli, G. (2015). Development and validation of a high-performance liquid chromatography-tandem mass spectrometry method for the simultaneous determination of irinotecan and its main metabolites in human plasma and its application in a clinical pharmacokinetic study. *PLoS One, 10*(2), e0118194. doi:10.1371/journal.pone.0118194

Markowitz, M., Slater, L. N., Schwartz, R., Kazanjian, P. H., Hathaway, B., Wheeler, D., . . . McCallister, S. (2007). Long-term efficacy and safety of tipranavir boosted with ritonavir in HIV-1-infected patients failing

multiple protease inhibitor regimens: 80-week data from a phase 2 study. *J Acquir Immune Defic Syndr, 45*(4), 401-410. doi:10.1097/QAI.0b013e318074eff5

Maroun, J. A., Anthony, L. B., Blais, N., Burkes, R., Dowden, S. D., Dranitsaris, G., . . . Wong, R. (2007). Prevention and management of chemotherapy-induced diarrhea in patients with colorectal cancer: a consensus statement by the Canadian Working Group on Chemotherapy-Induced Diarrhea. *Curr Oncol, 14*(1), 13-20. doi:10.3747/co.2007.96

Martinez-Chavez, A., Rosing, H., Gan, C., Wang, Y., Schinkel, A. H., & Beijnen, J. H. (2020). Bioanalytical method for the simultaneous quantification of irinotecan and its active metabolite SN-38 in mouse plasma and tissue homogenates using HPLC-fluorescence. *J Chromatogr B Analyt Technol Biomed Life Sci, 1149*, 122177. doi:10.1016/j.jchromb.2020.122177

Mathijssen, R. H., van Alphen, R. J., Verweij, J., Loos, W. J., Nooter, K., Stoter, G., & Sparreboom, A. (2001). Clinical pharmacokinetics and metabolism of irinotecan (CPT-11). *Clin Cancer Res, 7*(8), 2182-2194. Retrieved from https://www.ncbi.nlm.nih.gov/pubmed/11489791

Matsumura, Y., & Maeda, H. (1986). A new concept for macromolecular therapeutics in cancer chemotherapy: mechanism of tumoritropic accumulation of proteins and the antitumor agent smancs. *Cancer Res, 46*(12 Pt 1), 6387-6392. Retrieved from https://www.ncbi.nlm.nih.gov/pubmed/2946403

McChesney, E. W., Banks, W. F., Jr., & Fabian, R. J. (1967). Tissue distribution of chloroquine, hydroxychloroquine, and desethylchloroquine in the rat. *Toxicol Appl Pharmacol, 10*(3), 501-513. doi:10.1016/0041-008x(67)90089-0

McHutchison, J. G., Shiffman, M. L., Cheung, R. C., Gordon, S. C., Wright, T. L., Pottage, J. C., Jr., . . . Alam, J. (2005). A randomized, double-blind, placebo-controlled dose-escalation trial of merimepodib (VX-497) and interferon-alpha in previously untreated patients with chronic hepatitis C. *Antivir Ther, 10*(5), 635-643. Retrieved from https://www.ncbi.nlm.nih.gov/pubmed/16152757

Mehta, G., Hsiao, A. Y., Ingram, M., Luker, G. D., & Takayama, S. (2012). Opportunities and challenges for use of tumor spheroids as models to test drug delivery and efficacy. *J Control Release, 164*(2), 192-204. doi:10.1016/j.jconrel.2012.04.045

Meyer-Losic, F., Nicolazzi, C., Quinonero, J., Ribes, F., Michel, M., Dubois, V., . . . Kearsey, J. (2008). DTS-108, a novel peptidic prodrug of SN38: in vivo efficacy and toxicokinetic studies. *Clin Cancer Res, 14*(7), 2145-2153. doi:10.1158/1078-0432.CCR-07-4580

Millard, M., Yakavets, I., Zorin, V., Kulmukhamedova, A., Marchal, S., & Bezdetnaya, L. (2017). Drug delivery to solid tumors: the predictive value of the multicellular tumor spheroid model for nanomedicine screening. *Int J Nanomedicine, 12*, 7993-8007. doi:10.2147/IJN.S146927

Miller, D. S., Kok, T., & Li, P. (2013). The virus inoculum volume influences outcome of influenza A infection in mice. *Lab Anim, 47*(1), 74-77. doi:10.1258/la.2012.011157

Miller, K. D., Lobel, H. O., Satriale, R. F., Kuritsky, J. N., Stern, R., & Campbell, C. C. (1986). Severe cutaneous reactions among American travelers using pyrimethamine-sulfadoxine (Fansidar) for malaria prophylaxis. *Am J Trop Med Hyg, 35*(3), 451-458. doi:10.4269/ajtmh.1986.35.451

MiNA Therapeutics. (2019). PIPELINE – MiNA Therapeutics | RNA Activation. Retrieved from www.minatx.com/pipeline/#section_two

Minchinton, A. I., & Tannock, I. F. (2006). Drug penetration in solid tumours. *Nat Rev Cancer, 6*(8), 583-592. doi:10.1038/nrc1893

Miner, K., Labitzke, K., Liu, B., Wang, P., Henckels, K., Gaida, K., . . . Sullivan, J. K. (2019). Drug Repurposing: The Anthelmintics Niclosamide and Nitazoxanide Are Potent TMEM16A Antagonists That Fully Bronchodilate Airways. *Front Pharmacol, 10*, 51. doi:10.3389/fphar.2019.00051

Mody, N., Tekade, R. K., Mehra, N. K., Chopdey, P., & Jain, N. K. (2014). Dendrimer, liposomes, carbon nanotubes and PLGA nanoparticles: one platform assessment of drug delivery potential. *AAPS PharmSciTech, 15*(2), 388-399. doi:10.1208/s12249-014-0073-3

Moertel, C. G., Schutt, A. J., Reitemeier, R., & Hahn, R. (1972). Phase II Study of Camptothecin (NSC-100880) in the Treatment of Advanced Gastrointestinal Cancer1 2 3. *Cancer chemotherapy reports, 56*(1), 95-101.

Moreno Raja, M., Lim, P. Q., Wong, Y. S., Xiong, G. M., Zhang, Y., Venkatraman, S., & Huang, Y. (2019). Chapter 18 - Polymeric Nanomaterials: Methods of Preparation and Characterization. In S. S. Mohapatra, S. Ranjan, N. Dasgupta, R. K. Mishra, & S. Thomas (Eds.), *Nanocarriers for Drug Delivery* (pp. 557-653): Elsevier.

Moro, C. F., Bozoky, B., & Gerling, M. (2018). Growth patterns of colorectal cancer liver metastases and their impact on prognosis: a systematic review. *Bmj Open Gastroenterology, 5*(1). doi:10.1136/bmjgast-2018-000217

Morris-Stiff, G., Tan, Y. M., & Vauthey, J. N. (2008). Hepatic complications following preoperative chemotherapy with oxaliplatin or irinotecan for hepatic colorectal metastases. *Eur J Surg Oncol, 34*(6), 609-614. doi:10.1016/j.ejso.2007.07.007

Mosadegh, B., Xiong, G., Dunham, S., & Min, J. K. (2015). Current progress in 3D printing for cardiovascular tissue engineering. *Biomed Mater, 10*(3), 034002. doi:10.1088/1748-6041/10/3/034002

Moss, L., Wagner, D., Kanaoka, E., Olson, K., Yueh, Y. L., & Bowers, G. D. (2015). The comparative disposition and metabolism of dolutegravir, a potent HIV-1 integrase inhibitor, in mice, rats, and monkeys. *Xenobiotica, 45*(1), 60-70. doi:10.3109/00498254.2014.942409

Motoya, T., Thevanayagam, L. N., Blaschke, T. F., Au, S., Stone, J. A., Jayewardene, A. L., . . . Aweeka, F. T. (2006). Characterization of nelfinavir binding to plasma proteins and the lack of drug displacement interactions. *HIV Med, 7*(2), 122-128. doi:10.1111/j.1468-1293.2006.00356.x

Mueller-Klieser, W. (1987). Multicellular spheroids. A review on cellular aggregates in cancer research. *J Cancer Res Clin Oncol, 113*(2), 101-122. doi:10.1007/BF00391431

Mueller-Klieser, W. (2000). Tumor biology and experimental therapeutics. *Crit Rev Oncol Hematol, 36*(2-3), 123-139. doi:10.1016/s1040-8428(00)00082-2

Murdoch, D., & Plosker, G. L. (2004). Anidulafungin. *Drugs, 64*(19), 2249-2258. doi:10.2165/00003495-200464190-00011

Na-Bangchang, K., Limpaibul, L., Thanavibul, A., Tan-Ariya, P., & Karbwang, J. (1994). The pharmacokinetics of chloroquine in healthy Thai subjects and patients with Plasmodium vivax malaria. *Br J Clin Pharmacol, 38*(3), 278-281. doi:10.1111/j.1365-2125.1994.tb04354.x

Nakajima, T. E., Yanagihara, K., Takigahira, M., Yasunaga, M., Kato, K., Hamaguchi, T., . . . Matsumura, Y. (2008). Antitumor effect of SN-38-releasing polymeric micelles, NK012, on spontaneous peritoneal metastases from orthotopic gastric cancer in mice compared with irinotecan. *Cancer Res, 68*(22), 9318-9322. doi:10.1158/0008-5472.CAN-08-2822

Nakajima, T. E., Yasunaga, M., Kano, Y., Koizumi, F., Kato, K., Hamaguchi, T., . . . Matsumura, Y. (2008). Synergistic antitumor activity of the novel SN-38-incorporating polymeric micelles, NK012, combined with 5-fluorouracil in a mouse model of colorectal cancer, as compared with that of irinotecan plus 5-fluorouracil. *International Journal of Cancer, 122*(9), 2148-2153. doi:10.1002/ijc.23381

Nalamachu, S., & Wortmann, R. (2014). Role of indomethacin in acute pain and inflammation management: a review of the literature. *Postgrad Med, 126*(4), 92-97. doi:10.3810/pgm.2014.07.2787

Nektar. (2019). Nektar | R&D Pipeline | Onzeald™ (etirinotecan pegol). Retrieved from www.nektar.com/pipeline/rd-pipeline/onzeald

Neun, B. W., Barenholz, Y., Szebeni, J., & Dobrovolskaia, M. A. (2018). Understanding the Role of Anti-PEG Antibodies in the Complement Activation by Doxil in Vitro. *Molecules, 23*(7), 1700. Retrieved from https://www.mdpi.com/1420-3049/23/7/1700

Nguyen, V. H., & Lee, B. J. (2017). Protein corona: a new approach for nanomedicine design. *International Journal of Nanomedicine, 12*, 3137-3151. doi:10.2147/Ijn.S129300

Nichols, J. W., & Bae, Y. H. (2013). Nanotechnology for Cancer Treatment: Possibilities and Limitations. In Y. H. Bae, R. J. Mrsny, & K. Park (Eds.), *Cancer Targeted Drug Delivery: An Elusive Dream* (pp. 37-56). New York, NY: Springer New York.

Nordlinger, B., Van Cutsem, E., Gruenberger, T., Glimelius, B., Poston, G., Rougier, P., . . . Ychou, M. (2009). Combination of surgery and chemotherapy and the role of targeted agents in the treatment of patients with colorectal liver metastases: recommendations from an expert panel. *Ann Oncol, 20*(6), 985-992. doi:10.1093/annonc/mdn735

Nunes, A. S., Barros, A. S., Costa, E. C., Moreira, A. F., & Correia, I. J. (2019). 3D tumor spheroids as in vitro models to mimic in vivo human solid tumors resistance to therapeutic drugs. *Biotechnol Bioeng, 116*(1), 206-226. doi:10.1002/bit.26845

Oberdorster, G. (2010). Safety assessment for nanotechnology and nanomedicine: concepts of nanotoxicology. *J Intern Med, 267*(1), 89-105. doi:10.1111/j.1365-2796.2009.02187.x

Ohashi, H., Watashi, K., Saso, W., Shionoya, K., Iwanami, S., Hirokawa, T., . . . Wakita, T. (2020). Multidrug treatment with nelfinavir and cepharanthine against COVID-19. *bioRxiv*, 2020.2004.2014.039925. doi:10.1101/2020.04.14.039925

Okabe, H., Beppu, T., Hayashi, H., Horino, K., Masuda, T., Komori, H., . . . Baba, H. (2009). Hepatic stellate cells may relate to progression of intrahepatic cholangiocarcinoma. *Annals of Surgical Oncology, 16*(9), 2555-2564. doi:10.1245/s10434-009-0568-4

Oloumi, A., MacPhail, S. H., Johnston, P. J., Banath, J. P., & Olive, P. L. (2000). Changes in subcellular distribution of topoisomerase IIalpha correlate with etoposide resistance in multicell spheroids and xenograft

tumors. *Cancer Res, 60*(20), 5747-5753. Retrieved from https://www.ncbi.nlm.nih.gov/pubmed/11059769

Orman, J. S., & Perry, C. M. (2008). Tipranavir: a review of its use in the management of HIV infection. *Drugs, 68*(10), 1435-1463. doi:10.2165/00003495-200868100-00006

Owens, T. S., Dodds, H., Fricke, K., Hanna, S. K., & Crews, K. R. (2003). High-performance liquid chromatographic assay with fluorescence detection for the simultaneous measurement of carboxylate and lactone forms of irinotecan and three metabolites in human plasma. *J Chromatogr B Analyt Technol Biomed Life Sci, 788*(1), 65-74. doi:10.1016/s1570-0232(02)01016-4

Ozcelikkale, A., Shin, K., Noe-Kim, V., Elzey, B. D., Dong, Z., Zhang, J. T., . . . Han, B. (2017). Differential response to doxorubicin in breast cancer subtypes simulated by a microfluidic tumor model. *J Control Release, 266*, 129-139. doi:10.1016/j.jconrel.2017.09.024

Paget, S. (1989). The distribution of secondary growths in cancer of the breast. 1889. *Cancer Metastasis Rev, 8*(2), 98-101. Retrieved from https://www.ncbi.nlm.nih.gov/pubmed/2673568

Paku, S., Kopper, L., & Nagy, P. (2005). Development of the vasculature in "pushing-type" liver metastases of an experimental colorectal cancer. *Int J Cancer, 115*(6), 893-902. doi:10.1002/ijc.20886

Paku, S., & Lapis, K. (1993). Morphological aspects of angiogenesis in experimental liver metastases. *Am J Pathol, 143*(3), 926-936. Retrieved from https://www.ncbi.nlm.nih.gov/pubmed/7689793

Palakurthi, S. (2015). Challenges in SN38 drug delivery: current success and future directions. *Expert Opin Drug Deliv, 12*(12), 1911-1921. doi:10.1517/17425247.2015.1070142

Pampaloni, F., Reynaud, E. G., & Stelzer, E. H. (2007). The third dimension bridges the gap between cell culture and live tissue. *Nat Rev Mol Cell Biol, 8*(10), 839-845. doi:10.1038/nrm2236

Parveen, S., & Sahoo, S. K. (2008). Polymeric nanoparticles for cancer therapy. *Journal of Drug Targeting, 16*(2), 108-123. doi:10.1080/10611860701794353

Passero, F. C., Jr., Grapsa, D., Syrigos, K. N., & Saif, M. W. (2016). The safety and efficacy of Onivyde (irinotecan liposome injection) for the treatment of metastatic pancreatic cancer following gemcitabine-based therapy. *Expert Rev Anticancer Ther, 16*(7), 697-703. doi:10.1080/14737140.2016.1192471

Patel, N. R., Pattni, B. S., Abouzeid, A. H., & Torchilin, V. P. (2013). Nanopreparations to overcome multidrug resistance in cancer. *Adv Drug Deliv Rev, 65*(13-14), 1748-1762. doi:10.1016/j.addr.2013.08.004

Patnaik, A., Papadopoulos, K. P., Beeram, M., Kee, D., Tolcher, A. W., Schaaf, L. J., . . . Buchbinder, A. (2009). Abstract C221: EZN-2208, a novel anticancer agent, in patients (pts) with advanced malignancies: A phase 1 dose-escalation study. *Molecular Cancer Therapeutics, 8*(12 Supplement), C221-C221. doi:10.1158/1535-7163.Targ-09-c221

Perche, F., & Torchilin, V. P. (2012). Cancer cell spheroids as a model to evaluate chemotherapy protocols. *Cancer Biol Ther, 13*(12), 1205-1213. doi:10.4161/cbt.21353

Perez, E. A., Awada, A., O'Shaughnessy, J., Rugo, H. S., Twelves, C., Im, S. A., . . . Cortes, J. (2015). Etirinotecan pegol (NKTR-102) versus treatment of physician's choice in women with advanced breast cancer previously treated with an anthracycline, a taxane, and capecitabine (BEACON): a randomised, open-label, multicentre, phase 3 trial. *Lancet Oncol, 16*(15), 1556-1568. doi:10.1016/S1470-2045(15)00332-0

Pienta, K. J., Robertson, B. A., Coffey, D. S., & Taichman, R. S. (2013). The cancer diaspora: Metastasis beyond the seed and soil hypothesis. *Clin Cancer Res, 19*(21), 5849-5855. doi:10.1158/1078-0432.CCR-13-2158

PMDA. (2014). Report on the Deliberation Results Retrieved from https://www.pmda.go.jp/files/000210319.pdf

PMDA. (2018). Report on the Deliberation Results - Xospata Tablets 40 mg. Retrieved from https://www.pmda.go.jp/drugs/2014/P201400148/800155000_22600AMX01325_I100_1.pdf

Pober, J. S., & Sessa, W. C. (2007). Evolving functions of endothelial cells in inflammation. *Nat Rev Immunol, 7*(10), 803-815. doi:10.1038/nri2171

Pohlen, U., Buhr, H. J., & Berger, G. (2011). Improvement of Biodistribution with PEGylated Liposomes Containing Docetaxel with Degradable Starch Microspheres for Hepatic Arterial Infusion in the Treatment of Liver Metastases: A Study in CC-531 Liver Tumor-bearing WAG RIJ Rats. *Anticancer Research, 31*(1), 153-159. Retrieved from <Go to ISI>://WOS:000286798000020

Pommier, Y., Pourquier, P., Fan, Y., & Strumberg, D. (1998). Mechanism of action of eukaryotic DNA topoisomerase I and drugs targeted to the enzyme. *Biochimica et Biophysica Acta -Gene Structure Expression, 1400*(1-3), 83-106.

Porche, D. J. (1997). Ritonavir (Norvir). *J Assoc Nurses AIDS Care, 8*(6), 81-83. doi:10.1016/S1055-3290(97)80061-1

Poujol, S., Pinguet, F., Malosse, F., Astre, C., Ychou, M., Culine, S., & Bressolle, F. (2003). Sensitive HPLC-fluorescence method for irinotecan and four major metabolites in human plasma and saliva: application to pharmacokinetic studies. *Clin Chem, 49*(11), 1900-1908. doi:10.1373/clinchem.2003.023481

Povsic, T. J., Lawrence, M. G., Lincoff, A. M., Mehran, R., Rusconi, C. P., Zelenkofske, S. L., . . . Levinson, A. I. (2016). Pre-existing anti-PEG antibodies are associated with severe immediate allergic reactions to pegnivacogin, a PEGylated aptamer. *J Allergy Clin Immunol, 138*(6), 1712-1715. doi:10.1016/j.jaci.2016.04.058

Price, K. J., Tsykin, A., Giles, K. M., Sladic, R. T., Epis, M. R., Ganss, R., . . . Leedman, P. J. (2012). Matrigel basement membrane matrix influences expression of microRNAs in cancer cell lines. *Biochem Biophys Res Commun, 427*(2), 343-348. doi:10.1016/j.bbrc.2012.09.059

Price, R. N., Nosten, F., Luxemburger, C., van Vugt, M., Phaipun, L., Chongsuphajaisiddhi, T., & White, N. J. (1997). Artesunate/mefloquine treatment of multi-drug resistant falciparum malaria. *Trans R Soc Trop Med Hyg, 91*(5), 574-577. doi:10.1016/s0035-9203(97)90032-8

Prijovich, Z. M., Burnouf, P. A., & Roffler, S. R. (2014). Versatile online SPE-HPLC method for the analysis of Irinotecan and its clinically relevant metabolites in biomaterials. *J Sep Sci, 37*(4), 360-367. doi:10.1002/jssc.201301191

Psaila, B., & Lyden, D. (2009). The metastatic niche: adapting the foreign soil. *Nat Rev Cancer, 9*(4), 285-293. doi:10.1038/nrc2621

Pugin, J., Dunn-Siegrist, I., Dufour, J., Tissieres, P., Charles, P. E., & Comte, R. (2008). Cyclic stretch of human lung cells induces an acidification and promotes bacterial growth. *Am J Respir Cell Mol Biol, 38*(3), 362-370. doi:10.1165/rcmb.2007-0114OC

Pyo, D. H., Hong, H. K., Lee, W. Y., & Cho, Y. B. (2020). Patient-derived cancer modeling for precision medicine in colorectal cancer: beyond the cancer cell line. *Cancer Biol Ther, 21*(6), 495-502. doi:10.1080/15384047.2020.1738907

Qian, C. N. (2013). Hijacking the vasculature in ccRCC--co-option, remodelling and angiogenesis. *Nat Rev Urol, 10*(5), 300-304. doi:10.1038/nrurol.2013.26

Qin, C., Zhou, L., Hu, Z., Zhang, S., Yang, S., Tao, Y., . . . Tian, D. S. (2020). Dysregulation of immune response in patients with COVID-19 in Wuhan, China. *Clin Infect Dis*, doi: 10.1093/cid/ciaa1248. Retrieved from https://www.ncbi.nlm.nih.gov/pubmed/32161940

Rainsford, K. D., James, C., Hunt, R. H., Stetsko, P. I., Rischke, J. A., Karim, A., . . . Hantsbarger, G. (1992). Effects of misoprostol on the pharmacokinetics of indomethacin in human volunteers. *Clin Pharmacol Ther, 51*(4), 415-421. doi:10.1038/clpt.1992.41

Raja, A., Lebbos, J., & Kirkpatrick, P. (2003). Atazanavir sulphate. *Nature Reviews Drug Discovery, 2*(11), 857-858. doi:10.1038/nrd1232

Ramesh, M., Ahlawat, P., & Srinivas, N. R. (2010). Irinotecan and its active metabolite, SN-38: review of bioanalytical methods and recent update from clinical pharmacology perspectives. *Biomed Chromatogr, 24*(1), 104-123. doi:10.1002/bmc.1345

Ravi, M., Paramesh, V., Kaviya, S. R., Anuradha, E., & Solomon, F. D. (2015). 3D cell culture systems: advantages and applications. *J Cell Physiol, 230*(1), 16-26. doi:10.1002/jcp.24683

Richardson, G., & Dobish, R. (2007). Chemotherapy induced diarrhea. *J Oncol Pharm Pract, 13*(4), 181-198. doi:10.1177/1078155207077335

Richter, A. W., & Akerblom, E. (1984). Polyethylene glycol reactive antibodies in man: titer distribution in allergic patients treated with monomethoxy polyethylene glycol modified allergens or placebo, and in healthy blood donors. *Int Arch Allergy Appl Immunol, 74*(1), 36-39.

Riedl, A., Schlederer, M., Pudelko, K., Stadler, M., Walter, S., Unterleuthner, D., . . . Dolznig, H. (2017). Comparison of cancer cells in 2D vs 3D culture reveals differences in AKT-mTOR-S6K signaling and drug responses. *J Cell Sci, 130*(1), 203-218. doi:10.1242/jcs.188102

Ritchie, E. C., Block, J., & Nevin, R. L. (2013). Psychiatric side effects of mefloquine: applications to forensic psychiatry. *J Am Acad Psychiatry Law, 41*(2), 224-235. Retrieved from https://www.ncbi.nlm.nih.gov/pubmed/23771936

Rivory, L. P., Bowles, M. R., Robert, J., & Pond, S. M. (1996). Conversion of irinotecan (CPT-11) to its active metabolite, 7-ethyl-10-hydroxycamptothecin (SN-38), by human liver carboxylesterase. *Biochemical pharmacology, 52*(7), 1103-1111.

Rivory, L. P., Chatelut, E., Canal, P., Mathieu-Boue, A., & Robert, J. (1994). Kinetics of the in vivo interconversion of the carboxylate and lactone forms of irinotecan (CPT-11) and of its metabolite SN-38 in patients. *Cancer Res, 54*(24), 6330-6333. Retrieved from https://www.ncbi.nlm.nih.gov/pubmed/7987823

Rivory, L. P., Riou, J. F., Haaz, M. C., Sable, S., Vuilhorgne, M., Commerçon, A., . . . Robert, J. (1996). Identification and properties of a major plasma metabolite of irinotecan (CPT-11) isolated from the plasma of patients. *Cancer Research, 56*(16), 3689-3694. Retrieved from https://www.scopus.com/inward/record.uri?eid=2-s2.0-0029760995&partnerID=40&md5=1bcc42f0e3c5f4991f28aa934cce1c25

Rivulgo, V., Sparo, M., Ceci, M., Fumuso, E., Confalonieri, A., Delpech, G., & Sánchez Bruni, S. F. (2013). Comparative Plasma Exposure and Lung Distribution of Two Human Use Commercial Azithromycin Formulations Assessed in Murine Model: A Preclinical Study. *BioMed Research International, 2013*, 392010. doi:10.1155/2013/392010

Rodgers, T., Leahy, D., & Rowland, M. (2005). Physiologically based pharmacokinetic modeling 1: predicting the tissue distribution of moderate-to-strong bases. *J Pharm Sci, 94*(6), 1259-1276. doi:10.1002/jps.20322

Rodgers, T., & Rowland, M. (2006). Physiologically based pharmacokinetic modelling 2: predicting the tissue distribution of acids, very weak bases, neutrals and zwitterions. *J Pharm Sci, 95*(6), 1238-1257. doi:10.1002/jps.20502

Rodgers, T., & Rowland, M. (2007). Mechanistic approaches to volume of distribution predictions: understanding the processes. *Pharm Res, 24*(5), 918-933. doi:10.1007/s11095-006-9210-3

Roger, E., Lagarce, F., & Benoit, J. P. (2011). Development and characterization of a novel lipid nanocapsule formulation of Sn38 for oral administration. *Eur J Pharm Biopharm, 79*(1), 181-188. doi:10.1016/j.ejpb.2011.01.021

Roodink, I., Franssen, M., Zuidscherwoude, M., Verrijp, K., van der Donk, T., Raats, J., & Leenders, W. P. (2010). Isolation of targeting nanobodies against co-opted tumor vasculature. *Lab Invest, 90*(1), 61-67. doi:10.1038/labinvest.2009.107

Rosenblum, D., Joshi, N., Tao, W., Karp, J. M., & Peer, D. (2018). Progress and challenges towards targeted delivery of cancer therapeutics. *Nature Communications, 9*. doi:10.1038/s41467-018-03705-y

Rossignol, J. F. (2014). Nitazoxanide: a first-in-class broad-spectrum antiviral agent. *Antiviral Res, 110*, 94-103. doi:10.1016/j.antiviral.2014.07.014

Rossignol, J. F. (2016). Nitazoxanide, a new drug candidate for the treatment of Middle East respiratory syndrome coronavirus. *J Infect Public Health, 9*(3), 227-230. doi:10.1016/j.jiph.2016.04.001

Rossignol, J. F., La Frazia, S., Chiappa, L., Ciucci, A., & Santoro, M. G. (2009). Thiazolides, a new class of anti-influenza molecules targeting viral hemagglutinin at the post-translational level. *J Biol Chem, 284*(43), 29798-29808. doi:10.1074/jbc.M109.029470

Rosslein, M., Liptrott, N. J., Owen, A., Boisseau, P., Wick, P., & Herrmann, I. K. (2017). Sound understanding of environmental, health and safety, clinical, and market aspects is imperative to clinical translation of nanomedicines. *Nanotoxicology, 11*(2), 147-149. doi:10.1080/17435390.2017.1279361

Rothenberg, M. L. (2001). Irinotecan (CPT-11): recent developments and future directions--colorectal cancer and beyond. *Oncologist, 6*(1), 66-80. doi:10.1634/theoncologist.6-1-66

Rothenberg, M. L., Kuhn, J. G., Burris, H. A., 3rd, Nelson, J., Eckardt, J. R., Tristan-Morales, M., . . . Rodriguez, G. I. (1993). Phase I and pharmacokinetic trial of weekly CPT-11. *Journal of Clinical Oncology, 11*(11), 2194-2204. doi:10.1200/JCO.1993.11.11.2194

Rothenberg, M. L., Meropol, N. J., Poplin, E. A., Van Cutsem, E., & Wadler, S. (2001). Mortality associated with irinotecan plus bolus fluorouracil/leucovorin: summary findings of an independent panel. *Journal of Clinical Oncology, 19*(18), 3801-3807. doi:10.1200/JCO.2001.19.18.3801

Rougier, P., Lepille, D., Bennouna, J., Marre, A., Ducreux, M., Mignot, L., . . . Mery-Mignard, D. (2002). Antitumour activity of three second-line treatment combinations in patients with metastatic colorectal cancer after optimal 5-FU regimen failure: a randomised, multicentre phase II study. *Annals of oncology, 13*(10), 1558-1567.

Roy, A. C., Park, S. R., Cunningham, D., Kang, Y. K., Chao, Y., Chen, L. T., . . . de Gramont, A. (2013). A randomized phase II study of PEP02 (MM-398), irinotecan or docetaxel as a second-line therapy in patients with locally advanced or metastatic gastric or gastro-oesophageal junction adenocarcinoma. *Ann Oncol, 24*(6), 1567-1573. doi:10.1093/annonc/mdt002

Rudakova, E., Boltneva, N., & Makhaeva, G. (2011). Comparative analysis of esterase activities of human, mouse, and rat blood. *Bulletin of experimental biology, 152*(1), 73-75.

Rychahou, P., Shu, Y., Simonelli, F., Zaytseva, Y., Elliott, V. A., Lee, E., . . . Evers, B. M. (2013). Targeting Colorectal Cancer Liver Metastases With Folate-Conjugated Ultrastable RNA Nanoparticles. *Gastroenterology, 144*(5), S873-S873. Retrieved from <Go to ISI>://WOS:000322997205097

Ryuk, J. P., Choi, G. S., Park, J. S., Kim, H. J., Park, S. Y., Yoon, G. S., . . . Kwon, Y. C. (2014). Predictive factors and the prognosis of recurrence of colorectal cancer within 2 years after curative resection. *Ann Surg Treat Res, 86*(3), 143-151. doi:10.4174/astr.2014.86.3.143

Sai, K., Kaniwa, N., Ozawa, S., & Sawada, J. (2002). An analytical method for irinotecan (CPT-11) and its metabolites using a high-performance liquid chromatography: parallel detection with fluorescence and mass spectrometry. *Biomed Chromatogr, 16*(3), 209-218. doi:10.1002/bmc.137

Saigi, E., Salut, A., Campos, J. M., Losa, F., Manzano, H., Batiste-Alentorn, E., . . . Anton, I. (2004). Phase II study of irinotecan (CPT-11) administered every 2 weeks as treatment for patients with colorectal cancer resistant to previous treatment with 5-fluorouracil-based therapies: comparison of two different dose schedules (250 and 200 mg/m2) according to toxicity prognostic factors. *Anticancer Drugs, 15*(9), 835-841. doi:10.1097/00001813-200410000-00003

Sakai, S., Ito, S., & Kawakami, K. (2010). Calcium alginate microcapsules with spherical liquid cores templated by gelatin microparticles for mass production of multicellular spheroids. *Acta Biomater, 6*(8), 3132-3137. doi:10.1016/j.actbio.2010.02.003

Samyang Biopharm. (2019). Genexol PM. Retrieved from https://samyangbiopharm.com/eng/ProductIntroduce/injection01

Sanders, J. M., Monogue, M. L., Jodlowski, T. Z., & Cutrell, J. B. (2020). Pharmacologic Treatments for Coronavirus Disease 2019 (COVID-19): A Review. *JAMA*, doi: 10.1001/jama.2020.6019. Retrieved from https://doi.org/10.1001/jama.2020.6019

Santos, A., Zanetta, S., Cresteil, T., Deroussent, A., Pein, F., Raymond, E., . . . Gouyette, A. (2000). Metabolism of irinotecan (CPT-11) by CYP3A4 and CYP3A5 in humans. *Clinical cancer research, 6*(5), 2012-2020.

Sapra, P., Kraft, P., Mehlig, M., Malaby, J., Zhao, H., Greenberger, L. M., & Horak, I. D. (2009). Marked therapeutic efficacy of a novel polyethylene glycol-SN38 conjugate, EZN-2208, in xenograft models of B-cell non-Hodgkin's lymphoma. *Haematologica, 94*(10), 1456-1459. doi:10.3324/haematol.2009.008276

Sapra, P., Zhao, H., Mehlig, M., Malaby, J., Kraft, P., Longley, C., . . . Horak, I. D. (2008). Novel delivery of SN38 markedly inhibits tumor growth in xenografts, including a camptothecin-11-refractory model. *Clin Cancer Res, 14*(6), 1888-1896. doi:10.1158/1078-0432.CCR-07-4456

Sasaki, Y., Yoshida, Y., Sudoh, K., Hakusui, H., Fujii, H., Ohtsu, T., . . . Itoh, K. (1995). Pharmacological correlation between total drug concentration and lactones of CPT-11 and SN-38 in patients treated with CPT-11. *Japanese journal of cancer research, 86*(1), 111-116.

Sato, M., Kawana, K., Adachi, K., Fujimoto, A., Yoshida, M., Nakamura, H., . . . Fujii, T. (2016). Spheroid cancer stem cells display reprogrammed metabolism and obtain energy by actively running the tricarboxylic acid (TCA) cycle. *Oncotarget, 7*(22), 33297-33305. doi:10.18632/oncotarget.8947

Schmid, D., Fay, F., Small, D. M., Jaworski, J., Riley, J. S., Tegazzini, D., . . . Scott, C. J. (2014). Efficient Drug Delivery and induction of Apoptosis in Colorectal Tumors Using a Death Receptor 5-Targeted Nanomedicine. *Molecular Therapy, 22*(12), 2083-2092. doi:10.1038/mt.2014.137

Schwartsmann, G., Ratain, M. J., Cragg, G. M., Wong, J. E., Saijo, N., Parkinson, D. R., . . . Di Leone, L. (2002). Anticancer drug discovery and development throughout the world. *Journal of Clinical Oncology, 20*(18 Suppl), 47S-59S. Retrieved from https://www.ncbi.nlm.nih.gov/pubmed/12235225

Senapati, S., Mahanta, A. K., Kumar, S., & Maiti, P. (2018). Controlled drug delivery vehicles for cancer treatment and their performance. *Signal Transduction and Targeted Therapy, 3*. doi:10.1038/s41392-017-0004-3

Sensi, F., D'Angelo, E., D'Aronco, S., Molinaro, R., & Agostini, M. (2018). Preclinical three-dimensional colorectal cancer model: The next generation of in vitro drug efficacy evaluation. *J Cell Physiol, 234*(1), 181-191. doi:10.1002/jcp.26812

Senter, P. D., Beam, K. S., Mixan, B., & Wahl, A. F. (2001). Identification and activities of human carboxylesterases for the activation of CPT-11, a clinically approved anticancer drug. *Bioconjug Chem, 12*(6), 1074-1080. doi:10.1021/bc0155420

Sepehri, N., Rouhani, H., Ghanbarpour, A. R., Gharghabi, M., Tavassolian, F., Amini, M., . . . Dinarvand, R. (2014). Human serum albumin conjugates of 7-ethyl-10-hydroxycamptothecin (SN38) for cancer treatment. *Biomed Res Int, 2014*, 963507. doi:10.1155/2014/963507

Shaojun, C., Li, H., Haixin, H., & Guisheng, L. (2018). Expression of Topoisomerase 1 and carboxylesterase 2 correlates with irinotecan treatment response in metastatic colorectal cancer. *Cancer Biol Ther, 19*(3), 153-159. doi:10.1080/15384047.2017.1414754

Shi, J. J., Kantoff, P. W., Wooster, R., & Farokhzad, O. C. (2017). Cancer nanomedicine: progress, challenges and opportunities. *Nature Reviews Cancer, 17*(1), 20-37. doi:10.1038/nrc.2016.108

Shida, Y., Takahashi, N., Nohda, S., & Hirama, T. (2011). Pharmacokinetics and Pharmacodynamics of Eltrombopag in Healthy Japanese Males. *Rinsho yakuri/Japanese Journal of Clinical Pharmacology and Therapeutics, 42*(1), 11-20. doi:10.3999/jscpt.42.11

Shuford, S., Wilhelm, C., Rayner, M., Elrod, A., Millard, M., Mattingly, C., . . . DesRochers, T. M. (2019). Prospective Validation of an Ex Vivo, Patient-Derived 3D Spheroid Model for Response Predictions in Newly Diagnosed Ovarian Cancer. *Sci Rep, 9*(1), 11153. doi:10.1038/s41598-019-47578-7

Skardal, A., Devarasetty, M., Rodman, C., Atala, A., & Soker, S. (2015). Liver-Tumor Hybrid Organoids for Modeling Tumor Growth and Drug Response In Vitro. *Ann Biomed Eng, 43*(10), 2361-2373. doi:10.1007/s10439-015-1298-3

Slatter, J. G., Schaaf, L. J., Sams, J. P., Feenstra, K. L., Johnson, M. G., Bombardt, P. A., . . . Lord, R. S. (2000). Pharmacokinetics, metabolism, and excretion of irinotecan (CPT-11) following I.V. infusion of [(14)C]CPT-11 in cancer patients. *Drug Metab Dispos, 28*(4), 423-433. Retrieved from https://www.ncbi.nlm.nih.gov/pubmed/10725311

Slatter, J. G., Su, P., Sams, J. P., Schaaf, L. J., & Wienkers, L. C. (1997). Bioactivation of the anticancer agent CPT-11 to SN-38 by human hepatic microsomal carboxylesterases and the in vitroassessment of potential drug interactions. *Drug Metabolism Disposition, 25*(10), 1157-1164.

Smith, C. A., Kulkarni, U., Chen, J., & Goldstein, D. R. (2019). Influenza virus inoculum volume is critical to elucidate age-dependent mortality in mice. *Aging Cell, 18*(2), e12893. doi:10.1111/acel.12893

Smith, N. F., Figg, W. D., & Sparreboom, A. (2006). Pharmacogenetics of irinotecan metabolism and transport: an update. *Toxicol In Vitro, 20*(2), 163-175. doi:10.1016/j.tiv.2005.06.045

Sparreboom, A., de Bruijn, P., de Jonge, M. J., Loos, W. J., Stoter, G., Verweij, J., & Nooter, K. (1998). Liquid chromatographic determination of irinotecan and three major metabolites in human plasma, urine and feces. *J Chromatogr B Biomed Sci Appl, 712*(1-2), 225-235. doi:10.1016/s0378-4347(98)00147-9

Sperker, B., Backman, J. T., & Kroemer, H. K. (1997). The role of β-glucuronidase in drug disposition and drug targeting in humans. *Clinical pharmacokinetics, 33*(1), 18-31.

Starpharma. (2019). DEP® irinotecan synergistic with Lynparza® in refractory human colon cancer model. Retrieved from https://starpharma.com/news/story/dep-irinotecan-synergistic-with-lynparza-in-refractory-human-colon-cancer-model

Stessels, F., Van den Eynden, G., Van der Auwera, I., Salgado, R., Van den Heuvel, E., Harris, A. L., . . . Vermeulen, P. B. (2004). Breast adenocarcinoma liver metastases, in contrast to colorectal cancer liver metastases, display a non-angiogenic growth pattern that preserves the stroma and lacks hypoxia. *British Journal of Cancer, 90*(7), 1429-1436. doi:10.1038/sj.bjc.6601727

Strassburg, C. P., Oldhafer, K., Manns, M. P., & Tukey, R. H. (1997). Differential Expression of the UGT1A Locus in Human Liver, Biliary, and Gastric Tissue: Identification ofUGT1A7 and UGT1A10 Transcripts in Extrahepatic Tissue. *Molecular pharmacology, 52*(2), 212-220.

Streeck, H., & Rockstroh, J. K. (2007). Review of tipranavir in the treatment of drug-resistant HIV. *Ther Clin Risk Manag, 3*(4), 641-651. Retrieved from https://www.ncbi.nlm.nih.gov/pubmed/18472987

Strumberg, D., Pilon, A. A., Smith, M., Hickey, R., Malkas, L., & Pommier, Y. (2000). Conversion of topoisomerase I cleavage complexes on the leading strand of ribosomal DNA into 5'-phosphorylated DNA double-strand breaks by replication runoff. *Mol Cell Biol, 20*(11), 3977-3987. doi:10.1128/mcb.20.11.3977-3987.2000

Stylianopoulos, T., Munn, L. L., & Jain, R. K. (2018). Reengineering the Physical Microenvironment of Tumors to Improve Drug Delivery and Efficacy: From Mathematical Modeling to Bench to Bedside. *Trends in Cancer, 4*(4), 292-319. doi:10.1016/j.trecan.2018.02.005

Suk, J. S., Xu, Q., Kim, N., Hanes, J., & Ensign, L. M. (2016). PEGylation as a strategy for improving nanoparticle-based drug and gene delivery. *Adv Drug Deliv Rev, 99*(Pt A), 28-51. doi:10.1016/j.addr.2015.09.012

Sumitomo, M., Koizumi, F., Asano, T., Horiguchi, A., Ito, K., Asano, T., . . . Matsumura, Y. (2008). Novel SN-38-incorporated polymeric micelle, NK012, strongly suppresses renal cancer progression. *Cancer Res, 68*(6), 1631-1635. doi:10.1158/0008-5472.CAN-07-6532

Sun, C.-b., Wang, Y.-y., Liu, G.-h., & Liu, Z. (2020). Role of the Eye in Transmitting Human Coronavirus: What We Know and What We Do Not Know. doi: 10.20944/preprints202003.200271.v202002.

Sutherland, R. M. (1988). Cell and environment interactions in tumor microregions: the multicell spheroid model. *Science, 240*(4849), 177-184. doi:10.1126/science.2451290

Sutherland, R. M., McCredie, J. A., & Inch, W. R. (1971). Growth of multicell spheroids in tissue culture as a model of nodular carcinomas. *J Natl Cancer Inst, 46*(1), 113-120. Retrieved from https://www.ncbi.nlm.nih.gov/pubmed/5101993

Sveen, A., Loes, I. M., Alagaratnam, S., Nilsen, G., Holand, M., Lingjaerde, O. C., . . . Lothe, R. A. (2016). Intra-patient Inter-metastatic Genetic Heterogeneity in Colorectal Cancer as a Key Determinant of Survival after Curative Liver Resection. *Plos Genetics, 12*(7). doi:10.1371/journal.pgen.1006225

Svenson, S., Wolfgang, M., Hwang, J., Ryan, J., & Eliasof, S. (2011). Preclinical to clinical development of the novel camptothecin nanopharmaceutical CRLX101. *Journal of Controlled Release, 153*(1), 49-55. doi:10.1016/j.jconrel.2011.03.007

Swenson, C. E., Haemmerich, D., Maul, D. H., Knox, B., Ehrhart, N., & Reed, R. A. (2015). Increased Duration of Heating Boosts Local Drug Deposition during Radiofrequency Ablation in Combination with Thermally Sensitive Liposomes (ThermoDox) in a Porcine Model. *PLoS One, 10*(10). doi:10.1371/journal.pone.0139752

Szot, C. S., Buchanan, C. F., Freeman, J. W., & Rylander, M. N. (2011). 3D in vitro bioengineered tumors based on collagen I hydrogels. *Biomaterials, 32*(31), 7905-7912. doi:10.1016/j.biomaterials.2011.07.001

Tahover, E., Bar-Shalom, R., Sapir, E., Pfeffer, R., Nemirovsky, I., Turner, Y., . . . Gabizon, A. A. (2018). Chemo-Radiotherapy of Oligometastases of Colorectal Cancer With Pegylated Liposomal Mitomycin-C Prodrug (Promitil): Mechanistic Basis and Preliminary Clinical Experience. *Frontiers in Oncology, 8*. doi:10.3389/fonc.2018.00544

Takahashi, A., Ohkohchi, N., Yasunaga, M., Kuroda, J., Koga, Y., Kenmotsu, H., . . . Matsumura, Y. (2010). Detailed Distribution of NK012, an SN-38-Incorporating Micelle, in the Liver and Its Potent Antitumor Effects in Mice Bearing Liver Metastases. *Clinical cancer research, 16*(19), 4822-4831. doi:10.1158/1078-0432.Ccr-10-1467

Takeba, Y., Kumai, T., Matsumoto, N., Nakaya, S., Tsuzuki, Y., Yanagida, Y., & Kobayashi, S. (2007). Irinotecan activates p53 with its active metabolite, resulting in human hepatocellular carcinoma apoptosis. *J Pharmacol Sci, 104*(3), 232-242. doi:10.1254/jphs.fp0070442

Tallman, M. N., Ritter, J. K., & Smith, P. C. (2005). Differential rates of glucuronidation for 7-ethyl-10-hydroxy-camptothecin (SN-38) lactone and carboxylate in human and rat microsomes and recombinant UDP-glucuronosyltransferase isoforms. *Drug Metabolism Disposition, 33*(7), 977-983.

Talmadge, J. E., & Fidler, I. J. (2010). AACR centennial series: the biology of cancer metastasis: historical perspective. *Cancer Res, 70*(14), 5649-5669. doi:10.1158/0008-5472.CAN-10-1040

Tanei, T., Leonard, F., Liu, X., Alexander, J. F., Saito, Y., Ferrari, M., . . . Yokoi, K. (2016). Redirecting Transport of Nanoparticle Albumin-Bound Paclitaxel to Macrophages Enhances Therapeutic Efficacy against Liver Metastases. *Cancer Res, 76*(2), 429-439. doi:10.1158/0008-5472.CAN-15-1576

Taneja, N., Gota, V., Gurjar, M., & Singh, K. K. (2019). Development and validation of high-performance liquid chromatographic method for quantification of Irinotecan and its active metabolite SN-38 in colon tumor bearing NOD/SCID mice plasma samples: application to pharmacokinetic study. *31*(3), 166. doi:10.1556/1326.2018.00370

Tang, W., Cao, Z., Han, M., Wang, Z., Chen, J., Sun, W., . . . Xie, Q. (2020). Hydroxychloroquine in patients with mainly mild to moderate coronavirus disease 2019: open label, randomised controlled trial. *BMJ, 369*, m1849. doi:10.1136/bmj.m1849

Tchoryk, A., Taresco, V., Argent, R. H., Ashford, M., Gellert, P. R., Stolnik, S., . . . Garnett, M. C. (2019). Penetration and Uptake of Nanoparticles in 3D Tumor Spheroids. *Bioconjug Chem, 30*(5), 1371-1384. doi:10.1021/acs.bioconjchem.9b00136

Tett, S. E., Cutler, D. J., Beck, C., & Day, R. O. (2000). Concentration-effect relationship of hydroxychloroquine in patients with rheumatoid arthritis--a prospective, dose ranging study. *J Rheumatol, 27*(7), 1656-1660. Retrieved from https://www.ncbi.nlm.nih.gov/pubmed/10914847

Teva UK. (2019). Myocet® (Doxorubicin hydrochloride) | Teva UK Limited - Teva UK. Retrieved from www.tevauk.com/hcp/myocet

Thambi, T., Deepagan, V. G., Yoon, H. Y., Han, H. S., Kim, S. H., Son, S., . . . Park, J. H. (2014). Hypoxia-responsive polymeric nanoparticles for tumor-targeted drug delivery. *Biomaterials, 35*(5), 1735-1743. doi:10.1016/j.biomaterials.2013.11.022

Tilmanis, D., van Baalen, C., Oh, D. Y., Rossignol, J.-F., & Hurt, A. C. (2017). The susceptibility of circulating human influenza viruses to tizoxanide, the active metabolite of nitazoxanide. *Antiviral Research, 147*, 142-148. doi:https://doi.org/10.1016/j.antiviral.2017.10.002

Tilmanis, D., van Baalen, C., Oh, D. Y., Rossignol, J. F., & Hurt, A. C. (2017). The susceptibility of circulating human influenza viruses to tizoxanide, the active metabolite of nitazoxanide. *Antiviral Res, 147*, 142-148. doi:10.1016/j.antiviral.2017.10.002

Touret, F., Gilles, M., Barral, K., Nougairede, A., Decroly, E., de Lamballerie, X., & Coutard, B. (2020). In vitro screening of a FDA approved chemical library reveals potential inhibitors of SARS-CoV-2 replication. doi:

10.1101/2020.1104.1103.023846 J bioRxiv. Retrieved from https://www.biorxiv.org/content/biorxiv/early/2020/04/05/2020.04.03.023846.full.pdf
Trabattoni, D., Gnudi, F., Ibba, S. V., Saulle, I., Agostini, S., Masetti, M., . . . Clerici, M. (2016). Thiazolides Elicit Anti-Viral Innate Immunity and Reduce HIV Replication. *Scientific Reports, 6*(1), 27148. doi:10.1038/srep27148
Tran, S., DeGiovanni, P. J., Piel, B., & Rai, P. (2017). Cancer nanomedicine: a review of recent success in drug delivery. *Clin Transl Med, 6*(1), 44. doi:10.1186/s40169-017-0175-0
Tredan, O., Galmarini, C. M., Patel, K., & Tannock, I. F. (2007). Drug resistance and the solid tumor microenvironment. *J Natl Cancer Inst, 99*(19), 1441-1454. doi:10.1093/jnci/djm135
Tripathy, D., Tolaney, S. M., Seidman, A. D., Anders, C. K., Ibrahim, N., Rugo, H. S., . . . Cortes, J. (2019). ATTAIN: Phase III study of etirinotecan pegol versus treatment of physician's choice in patients with metastatic breast cancer and brain metastases. *Future Oncol, 15*(19), 2211-2225. doi:10.2217/fon-2019-0180
Ueno, M., Nonaka, S., Yamazaki, R., Deguchi, N., & Murai, M. (2002). SN-38 induces cell cycle arrest and apoptosis in human testicular cancer. *Eur Urol, 42*(4), 390-397. doi:10.1016/s0302-2838(02)00321-4
Unis, G., Baker, T. P., Rajaprabhakaran, G., Sure, V. N., Jain, N. P., Abraham, V. M., . . . Katakam, P. V. (2016). Mitochondrial Mechanisms of Nelfinavir Toxicity in Human Brain Microvascular Endothelial cells. *30*(1_supplement), 953.954-953.954. doi:10.1096/fasebj.30.1_supplement.953.4
Urban, P., Liptrott, N. J., & Bremer, S. (2019). Overview of the blood compatibility of nanomedicines: A trend analysis of in vitro and in vivo studies. *Wiley Interdiscip Rev Nanomed Nanobiotechnol, 11*(3), e1546. doi:10.1002/wnan.1546
Valcarcel, M., Arteta, B., Jaureguibeitia, A., Lopategi, A., Martinez, I., Mendoza, L., . . . Vidal-Vanaclocha, F. (2008). Three-dimensional growth as multicellular spheroid activates the proangiogenic phenotype of colorectal carcinoma cells via LFA-1-dependent VEGF: implications on hepatic micrometastasis. *J Transl Med, 6*, 57. doi:10.1186/1479-5876-6-57
van Dam, P. J., van der Stok, E. P., Teuwen, L. A., Van den Eynden, G. G., Illemann, M., Frentzas, S., . . . Vermeulen, P. B. (2017). International consensus guidelines for scoring the histopathological growth patterns of liver metastasis. *Br J Cancer, 117*(10), 1427-1441. doi:10.1038/bjc.2017.334
Van den Eynden, G. G., Bird, N. C., Majeed, A. W., Van Laere, S., Dirix, L. Y., & Vermeulen, P. B. (2012). The histological growth pattern of colorectal cancer liver metastases has prognostic value. *Clinical & Experimental Metastasis, 29*(6), 541-549. doi:10.1007/s10585-012-9469-1
van der Waals, L. M., Laoukili, J., Jongen, J. M. J., Raats, D. A., Borel Rinkes, I. H. M., & Kranenburg, O. (2019). Differential anti-tumour effects of MTH1 inhibitors in patient-derived 3D colorectal cancer cultures. *Sci Rep, 9*(1), 819. doi:10.1038/s41598-018-37316-w
Van Huizen, N. A., Coebergh van den Braak, R. R. J., Doukas, M., Dekker, L. J. M., JNM, I. J., & Luider, T. M. (2019). Up-regulation of collagen proteins in colorectal liver metastasis compared with normal liver tissue. *J Biol Chem, 294*(1), 281-289. doi:10.1074/jbc.RA118.005087
van Laarhoven, H. W., Kaanders, J. H., Lok, J., Peeters, W. J., Rijken, P. F., Wiering, B., . . . van der Kogel, A. J. (2006). Hypoxia in relation to vasculature and proliferation in liver metastases in patients with colorectal cancer. *Int J Radiat Oncol Biol Phys, 64*(2), 473-482. doi:10.1016/j.ijrobp.2005.07.982
Vanderkooi, G., Prapunwattana, P., & Yuthavong, Y. (1988). Evidence for electrogenic accumulation of mefloquine by malarial parasites. *Biochem Pharmacol, 37*(19), 3623-3631. doi:10.1016/0006-2952(88)90394-2
Vanhoefer, U., Harstrick, A., Achterrath, W., Cao, S., Seeber, S., & Rustum, Y. M. (2001). Irinotecan in the treatment of colorectal cancer: clinical overview. *Journal of Clinical Oncology, 19*(5), 1501-1518.
Varkouhi, A. K., Scholte, M., Storm, G., & Haisma, H. J. (2011). Endosomal escape pathways for delivery of biologicals. *J Control Release, 151*(3), 220-228. doi:10.1016/j.jconrel.2010.11.004
Verbridge, S. S., Chakrabarti, A., DelNero, P., Kwee, B., Varner, J. D., Stroock, A. D., & Fischbach, C. (2013). Physicochemical regulation of endothelial sprouting in a 3D microfluidic angiogenesis model. *J Biomed Mater Res A, 101*(10), 2948-2956. doi:10.1002/jbm.a.34587
Vermaat, J. S., Nijman, I. J., Koudijs, M. J., Gerritse, F. L., Scherer, S. J., Mokry, M., . . . Voest, E. E. (2012). Primary Colorectal Cancers and Their Subsequent Hepatic Metastases Are Genetically Different: Implications for Selection of Patients for Targeted Treatment. *Clinical cancer research, 18*(3), 688-699. doi:10.1158/1078-0432.Ccr-11-1965
Vinci, M., Gowan, S., Boxall, F., Patterson, L., Zimmermann, M., Court, W., . . . Eccles, S. A. (2012). Advances in establishment and analysis of three-dimensional tumor spheroid-based functional assays for target validation and drug evaluation. *BMC Biol, 10*, 29. doi:10.1186/1741-7007-10-29

Vlachogiannis, G., Hedayat, S., Vatsiou, A., Jamin, Y., Fernandez-Mateos, J., Khan, K., . . . Valeri, N. (2018). Patient-derived organoids model treatment response of metastatic gastrointestinal cancers. *Science, 359*(6378), 920-926. doi:10.1126/science.aao2774

Walkey, C. D., Olsen, J. B., Guo, H., Emili, A., & Chan, W. C. (2012). Nanoparticle size and surface chemistry determine serum protein adsorption and macrophage uptake. *J Am Chem Soc, 134*(4), 2139-2147. doi:10.1021/ja2084338

Wall, M. E., & Wani, M. C. (1995). Camptothecin and taxol: discovery to clinic--thirteenth Bruce F. Cain Memorial Award Lecture. *Cancer Res, 55*(4), 753-760. Retrieved from https://www.ncbi.nlm.nih.gov/pubmed/7850785

Wall, M. E., & Wani, M. C. (1996). Camptothecin and taxol: from discovery to clinic. *J Ethnopharmacol, 51*(1-3), 239-253; discussion 253-234. doi:10.1016/0378-8741(95)01367-9

Wallace, S. J., Li, J., Nation, R. L., & Boyd, B. J. (2012). Drug release from nanomedicines: Selection of appropriate encapsulation and release methodology. *Drug Deliv Transl Res, 2*(4), 284-292. doi:10.1007/s13346-012-0064-4

Wang, C., Tang, Z., Zhao, Y., Yao, R., Li, L., & Sun, W. (2014). Three-dimensional in vitro cancer models: a short review. *Biofabrication, 6*(2), 022001. doi:10.1088/1758-5082/6/2/022001

Wang, M., Cao, R., Zhang, L., Yang, X., Liu, J., Xu, M., . . . Xiao, G. (2020). Remdesivir and chloroquine effectively inhibit the recently emerged novel coronavirus (2019-nCoV) in vitro. *Cell Res, 30*(3), 269-271. doi:10.1038/s41422-020-0282-0

Wang, X., Zhen, X., Wang, J., Zhang, J., Wu, W., & Jiang, X. (2013). Doxorubicin delivery to 3D multicellular spheroids and tumors based on boronic acid-rich chitosan nanoparticles. *Biomaterials, 34*(19), 4667-4679. doi:10.1016/j.biomaterials.2013.03.008

Wang, Y., Shen, L., Xu, N., Wang, J.-W., Jiao, S.-C., Liu, Z.-Y., & Xu, J.-M. (2012). UGT1A1 predicts outcome in colorectal cancer treated with irinotecan and fluorouracil. *World journal of gastroenterology: WJG, 18*(45), 6635.

Wang, Y., Zhang, D., Du, G., Du, R., Zhao, J., Jin, Y., . . . Wang, C. (2020). Remdesivir in adults with severe COVID-19: a randomised, double-blind, placebo-controlled, multicentre trial. *Lancet, 395*(10236), 1569-1578. doi:10.1016/S0140-6736(20)31022-9

Wang, Y. M., Lu, J. W., Lin, C. C., Chin, Y. F., Wu, T. Y., Lin, L. I., . . . Ho, Y. J. (2016). Antiviral activities of niclosamide and nitazoxanide against chikungunya virus entry and transmission. *Antiviral Res, 135*, 81-90. doi:10.1016/j.antiviral.2016.10.003

Ward, J. P., & King, J. R. (1997). Mathematical modelling of avascular-tumour growth. *IMA J Math Appl Med Biol, 14*(1), 39-69. Retrieved from https://www.ncbi.nlm.nih.gov/pubmed/9080687

Wasserman, E., Myara, A., Lokiec, F., Goldwasser, F., Trivin, F., Mahjoubi, M., . . . Cvitkovic, E. (1997). Severe CPT-11 toxicity in patients with Gilbert's syndrome: two case reports. *Annals of oncology, 8*(10), 1049-1051.

Weston, S., Haupt, R., Logue, J., Matthews, K., & Frieman, M. B. (2020). FDA approved drugs with broad anti-coronaviral activity inhibit SARS-CoV-2 in vitro. doi: 10.1101/2020.1103.1125.008482 J bioRxiv. Retrieved from https://www.biorxiv.org/content/biorxiv/early/2020/03/27/2020.03.25.008482.full.pdf

Wilhelm, S., Tavares, A. J., Dai, Q., Ohta, S., Audet, J., Dvorak, H. F., & Chan, W. C. W. (2016). Analysis of nanoparticle delivery to tumours. *Nature Reviews Materials, 1*(5). doi:10.1038/natrevmats.2016.14

Williams, J., Lansdown, R., Sweitzer, R., Romanowski, M., LaBell, R., Ramaswami, R., & Unger, E. (2003). Nanoparticle drug delivery system for intravenous delivery of topoisomerase inhibitors. *J Control Release, 91*(1-2), 167-172. doi:10.1016/s0168-3659(03)00241-4

Williamson, T., Sultanpuram, N., & Sendi, H. (2019). The role of liver microenvironment in hepatic metastasis. *Clin Transl Med, 8*(1), 21. doi:10.1186/s40169-019-0237-6

Wiseman, L. R., & Markham, A. (1996). Irinotecan. A review of its pharmacological properties and clinical efficacy in the management of advanced colorectal cancer. *Drugs, 52*(4), 606-623. doi:10.2165/00003495-199652040-00013

Wolfram, J., Zhu, M., Yang, Y., Shen, J., Gentile, E., Paolino, D., . . . Zhao, Y. (2015). Safety of Nanoparticles in Medicine. *Curr Drug Targets, 16*(14), 1671-1681. doi:10.2174/1389450115666140804124808

Wong, R. K. S., Tandan, V., De Silva, S., & Figueredo, A. (2007). Pre-operative radiotherapy and curative surgery for the management of localized rectal carcinoma. *Cochrane Database of Systematic Reviews*(2). doi:10.1002/14651858.CD002102.pub2

Wong, S. H., Lui, R. N., & Sung, J. J. (2020). Covid-19 and the Digestive System. *J Gastroenterol Hepatol*, doi: 10.1111/jgh.15047. Retrieved from https://www.ncbi.nlm.nih.gov/pubmed/32215956

World Health Organisation. (2020). COVID-19 Trials - International Clinical Trials Registry Platform (ICTRP). Retrieved from https://www.who.int/ictrp/search/en/

World Health Organization. (2020). WHO report on cancer: setting priorities, investing wisely and providing care for all.

Wu, Y., Guo, C., Tang, L., Hong, Z., Zhou, J., Dong, X., . . . Huang, X. (2020). Prolonged presence of SARS-CoV-2 viral RNA in faecal samples. *Lancet Gastroenterol Hepatol*, doi: 10.1016/S2468-1253(1020)30083-30082. Retrieved from https://www.ncbi.nlm.nih.gov/pubmed/32199469

Xiao, B., Han, M. K., Viennois, E., Wang, L. X., Zhang, M. Z., Si, X. Y., & Merlin, D. (2015). Hyaluronic acid-functionalized polymeric nanoparticles for colon cancer-targeted combination chemotherapy. *Nanoscale, 7*(42), 17745-17755. doi:10.1039/c5nr04831a

Xiao, D., Yang, D., Guo, L., Lu, W., Charpentier, M., & Yan, B. (2013). Regulation of carboxylesterase-2 expression by p53 family proteins and enhanced anti-cancer activities among 5-fluorouracil, irinotecan and doxazolidine prodrug. *Br J Pharmacol, 168*(8), 1989-1999. doi:10.1111/bph.12125

Xiao, K., Li, Y. P., Luo, J. T., Lee, J. S., Xiao, W. W., Gonik, A. M., . . . Lam, K. S. (2011). The effect of surface charge on in vivo biodistribution of PEG-oligocholic acid based micellar nanoparticles. *Biomaterials, 32*(13), 3435-3446. doi:10.1016/j.biomaterials.2011.01.021

Xie, R., Mathijssen, R. H., Sparreboom, A., Verweij, J., & Karlsson, M. O. (2002). Clinical pharmacokinetics of irinotecan and its metabolites: a population analysis. *Journal of Clinical Oncology, 20*(15), 3293-3301.

Xu, B., Shen, F., Cao, J., & Jia, L. (2013). Angiogenesis in liver metastasis of colo-rectal carcinoma. *Front Biosci (Landmark Ed), 18*, 1435-1443. Retrieved from https://www.ncbi.nlm.nih.gov/pubmed/23747894

Xu, T., Gao, X., Wu, Z., Selinger, D. W., & Zhou, Z. (2020). Indomethacin has a potent antiviral activity against SARS CoV-2 in vitro and canine coronavirus in vivo. doi: 10.1101/2020.1104.1101.017624 J bioRxiv. Retrieved from https://www.biorxiv.org/content/biorxiv/early/2020/04/05/2020.04.01.017624.full.pdf

Xu, X., Gurski, L. A., Zhang, C., Harrington, D. A., Farach-Carson, M. C., & Jia, X. (2012). Recreating the tumor microenvironment in a bilayer, hyaluronic acid hydrogel construct for the growth of prostate cancer spheroids. *Biomaterials, 33*(35), 9049-9060. doi:10.1016/j.biomaterials.2012.08.061

Yamamoto, N., Matsuyama, S., Hoshino, T., & Yamamoto, N. (2020). Nelfinavir inhibits replication of severe acute respiratory syndrome coronavirus 2 in vitro. doi: 10.1101/2020.1104.1106.026476 J bioRxiv. Retrieved from https://www.biorxiv.org/content/biorxiv/early/2020/04/08/2020.04.06.026476.full.pdf

Yang, E., Qian, W., Cao, Z., Wang, L., Bozeman, E. N., Ward, C., . . . Yang, L. (2015). Theranostic nanoparticles carrying doxorubicin attenuate targeting ligand specific antibody responses following systemic delivery. *Theranostics, 5*(1), 43-61. doi:10.7150/thno.10350

Yang, P., Tekwani, S., & Martin, G. S. (2020). In COVID-19, adding lopinavir-ritonavir to usual care did not shorten time to clinical improvement. *Ann Intern Med, 172*(12), JC63. doi:10.7326/ACPJ202006160-063

Yang, X., Hu, Z., Chan, S. Y., Goh, B. C., Duan, W., Chan, E., & Zhou, S. (2005). Simultaneous determination of the lactone and carboxylate forms of irinotecan (CPT-11) and its active metabolite SN-38 by high-performance liquid chromatography: application to plasma pharmacokinetic studies in the rat. *J Chromatogr B Analyt Technol Biomed Life Sci, 821*(2), 221-228. doi:10.1016/j.jchromb.2005.05.010

Yao, X., Ye, F., Zhang, M., Cui, C., Huang, B., Niu, P., . . . Liu, D. (2020). In Vitro Antiviral Activity and Projection of Optimized Dosing Design of Hydroxychloroquine for the Treatment of Severe Acute Respiratory Syndrome Coronavirus 2 (SARS-CoV-2). *Clin Infect Dis*, doi: 10.1093/cid/ciaa1237. Retrieved from https://www.ncbi.nlm.nih.gov/pubmed/32150618

Ychou, M., Raoul, J. L., Desseigne, F., Borel, C., Caroli-Bosc, F. X., Jacob, J. H., . . . Merrouche, Y. (2002). High-dose, single-agent irinotecan as first-line therapy in the treatment of metastatic colorectal cancer. *Cancer Chemother Pharmacol, 50*(5), 383-391. doi:10.1007/s00280-002-0506-7

Yeh, K. C. (1985). Pharmacokinetic overview of indomethacin and sustained-release indomethacin. *Am J Med, 79*(4C), 3-12. doi:10.1016/0002-9343(85)90510-8

Yih, T. C., & Al-Fandi, M. (2006). Engineered nanoparticles as precise drug delivery systems. *J Cell Biochem, 97*(6), 1184-1190. doi:10.1002/jcb.20796

Young, B., Hong, H. K., Lee, W. Y., & Cho, Y. B. (2017). Animal models of colorectal cancer with liver metastasis. *Cancer Letters, 387*, 114-120. doi:10.1016/j.canlet.2016.01.048

Younis, I. R., Malone, S., Friedman, H. S., Schaaf, L. J., & Petros, W. P. (2009). Enterohepatic recirculation model of irinotecan (CPT-11) and metabolite pharmacokinetics in patients with glioma. *Cancer chemotherapy, pharmacology and toxicology, 63*(3), 517-524.

Yu, B., Tai, H. C., Xue, W., Lee, L. J., & Lee, R. J. (2010). Receptor-targeted nanocarriers for therapeutic delivery to cancer. *Mol Membr Biol, 27*(7), 286-298. doi:10.3109/09687688.2010.521200

Zanoni, M., Piccinini, F., Arienti, C., Zamagni, A., Santi, S., Polico, R., . . . Tesei, A. (2016). 3D tumor spheroid models for in vitro therapeutic screening: a systematic approach to enhance the biological relevance of data obtained. *Sci Rep, 6*, 19103. doi:10.1038/srep19103

Zhang, C., Shi, L., & Wang, F. S. (2020). Liver injury in COVID-19: management and challenges. *Lancet Gastroenterol Hepatol*, doi: 10.1016/S2468-1253(1020)30057-30051. Retrieved from https://www.ncbi.nlm.nih.gov/pubmed/32145190

Zhang, H. (2016). Onivyde for the therapy of multiple solid tumors. *Onco Targets Ther, 9*, 3001-3007. doi:10.2147/OTT.S105587

Zhang, H., Hu, H. X., Zhang, H. R., Dai, W. B., Wang, X. L., Wang, X. Q., & Zhang, Q. (2015). Effects of PEGylated paclitaxel nanocrystals on breast cancer and its lung metastasis. *Nanoscale, 7*(24), 10790-10800. doi:10.1039/c4nr07450e

Zhang, H., Kang, Z., Gong, H., Xu, D., Wang, J., Li, Z., . . . Xu, H. (2020). The digestive system is a potential route of 2019-nCov infection: a bioinformatics analysis based on single-cell transcriptomes. doi: 10.1101/2020.1101.1130.927806 %J bioRxiv. Retrieved from https://www.biorxiv.org/content/biorxiv/early/2020/01/31/2020.01.30.927806.full.pdf

Zhang, H., Wang, J., Mao, W., Huang, J., Wu, X., Shen, Y., & Sui, M. (2013). Novel SN38 conjugate-forming nanoparticles as anticancer prodrug: in vitro and in vivo studies. *J Control Release, 166*(2), 147-158. doi:10.1016/j.jconrel.2012.12.019

Zhang, J. A., Xuan, T., Parmar, M., Ma, L., Ugwu, S., Ali, S., & Ahmad, I. (2004). Development and characterization of a novel liposome-based formulation of SN-38. *Int J Pharm, 270*(1-2), 93-107. doi:10.1016/j.ijpharm.2003.10.015

Zhang, K. E., Wu, E., Patick, A. K., Kerr, B., Zorbas, M., Lankford, A., . . . Webber, S. (2001). Circulating metabolites of the human immunodeficiency virus protease inhibitor nelfinavir in humans: structural identification, levels in plasma, and antiviral activities. *Antimicrob Agents Chemother, 45*(4), 1086-1093. doi:10.1128/AAC.45.4.1086-1093.2001

Zhang, R., Dong, Y., Sun, M., Wang, Y., Cai, C., Zeng, Y., . . . Zhao, Q. (2019). Tumor-associated inflammatory microenvironment in non-small cell lung cancer: correlation with FGFR1 and TLR4 expression via PI3K/Akt pathway. *J Cancer, 10*(4), 1004-1012. doi:10.7150/jca.26277

Zhang, W., Du, R. H., Li, B., Zheng, X. S., Yang, X. L., Hu, B., . . . Zhou, P. (2020). Molecular and serological investigation of 2019-nCoV infected patients: implication of multiple shedding routes. *Emerg Microbes Infect, 9*(1), 386-389. doi:10.1080/22221751.2020.1729071

Zhang, X. W., & Yap, Y. L. (2004). Old drugs as lead compounds for a new disease? Binding analysis of SARS coronavirus main proteinase with HIV, psychotic and parasite drugs. *Bioorg Med Chem, 12*(10), 2517-2521. doi:10.1016/j.bmc.2004.03.035

Zhang, Y., Huo, M., Zhou, J., & Xie, S. (2010). PKSolver: An add-in program for pharmacokinetic and pharmacodynamic data analysis in Microsoft Excel. *Comput Methods Programs Biomed, 99*(3), 306-314. doi:10.1016/j.cmpb.2010.01.007

Zhang, Y., Zhao, W., Mao, Y., Wang, S., Zhong, Y., Su, T., . . . Yang, H. (2020). Site-specific N-glycosylation Characterization of Recombinant SARS-CoV-2 Spike Proteins using High-Resolution Mass Spectrometry. doi: 10.1101/2020.1103.1128.013276 J bioRxiv. Retrieved from https://www.biorxiv.org/content/biorxiv/early/2020/03/29/2020.03.28.013276.full.pdf

Zhang, Y. N., Poon, W., Tavares, A. J., McGilvray, I. D., & Chan, W. C. W. (2016). Nanoparticle-liver interactions: Cellular uptake and hepatobiliary elimination. *J Control Release, 240*, 332-348. doi:10.1016/j.jconrel.2016.01.020

Zhao, Y., Zhao, Z., Wang, Y., Zhou, Y., Ma, Y., & Zuo, W. (2020). Single-cell RNA expression profiling of ACE2, the receptor of SARS-CoV-2. doi: 10.1101/2020.1101.1126.919985 J bioRxiv. Retrieved from https://www.biorxiv.org/content/biorxiv/early/2020/04/09/2020.01.26.919985.full.pdf

Zhijian, X., Hangping, Y., Jingshan, S., Nanping, W., Yechun, X., Xiangyun, L., . . . Lan-Juan, L. (2020). *Nelfinavir Is Active Against SARS-CoV-2 in Vero E6 Cells*.

Zhou, S., Li, N., Wang, X., Li, C., Tian, F., Ren, S., . . . Chen, X. (2014). In vitro cytotoxicity, pharmacokinetics and tissue distribution in rats of MXN-004, a novel conjugate of polyethylene glycol and SN38. *Xenobiotica, 44*(6), 562-569. doi:10.3109/00498254.2013.868061

Zoetemelk, M., Rausch, M., Colin, D. J., Dormond, O., & Nowak-Sliwinska, P. (2019). Short-term 3D culture systems of various complexity for treatment optimization of colorectal carcinoma. *Sci Rep, 9*(1), 7103. doi:10.1038/s41598-019-42836-0

Appendix A Prioritisation of Anti-SARS-Cov-2 Drug Repurposing Opportunities Based on Plasma and Target Site Concentrations Derived from their Established Human Pharmacokinetics

Abstract

As the first lockdown was announced and COVID-19 became a bigger issue in the UK, it led to the shutdown of universities and other research institutions. This prompted a change in research direction and we decided to pivot our focus onto COVID-19 research, with a specific focus on identifying potential therapeutic interventions. There is a rapidly expanding literature on the *in vitro* antiviral activity of drugs that may be repurposed for therapy or chemoprophylaxis against SARS-CoV-2. However, this has not been accompanied by a comprehensive evaluation of the target plasma and lung concentrations of these drugs following approved dosing in humans. Accordingly, EC_{90} values recalculated from *in vitro* anti-SARS-CoV-2 activity data were expressed as a ratio to the achievable maximum plasma concentrations (C_{max}) at an approved dose in humans (C_{max}/EC_{90} ratio). Only 19 of the 66 analysed drugs achieved a C_{max}/EC_{90} ratio above 1. A more in-depth assessment demonstrated that only nitazoxanide, nelfinavir, tipranavir (ritonavir-boosted) and sulfadoxine achieved plasma concentrations above their reported anti-SARS-CoV-2 activity across their entire approved dosing interval. An unbound lung to plasma tissue partition coefficient (K_pU_{lung}) was also simulated to derive a lung C_{max}/EC_{50} as a better indicator of potential human efficacy. Hydroxychloroquine, chloroquine, mefloquine, atazanavir (ritonavir-boosted), tipranavir (ritonavir-boosted), ivermectin, azithromycin and lopinavir (ritonavir-boosted) were all predicted to achieve lung concentrations over 10-fold higher than their reported EC_{50}. Nitazoxanide and sulfadoxine also exceeded their reported EC_{50} by 7.8- and 1.5-fold in the lung, respectively. This analysis may be used to select potential candidates for further clinical testing, while deprioritising compounds unlikely to attain target concentrations for antiviral activity. Future studies should focus on EC_{90} values and discuss findings in the context of achievable exposures in humans, especially within target compartments such as the lung, to maximise the potential for success of proposed human clinical trials.

A.1 Introduction

Coronavirus 2019 (COVID-19) is a respiratory disease caused by severe acute respiratory syndrome coronavirus 2 (SARS-CoV-2) infection. Fever, a persistent cough and respiratory symptoms are common, with some patients reporting vomiting, nausea, abdominal pains and diarrhoea (Gu, Han, & Wang, 2020). To date, no specific treatment is available, and this has resulted in significant morbidity and mortality globally. According to the International Clinical Trials Registry Platform search portal, 927 clinical trials for COVID-19 have been registered (World Health Organisation, 2020). This rapidly expanding pandemic warrants the urgent development of strategies, particularly to protect people at high risk of infection. Repurposing clinically evaluated drugs that have been utilised clinically with a known safety profile, is the quickest way to address this serious unmet clinical need. Antiviral drugs are urgently required for the treatment of patients with mild/moderate disease to prevent the worsening of symptoms and reduce the burden upon healthcare systems. However, a different approach is likely to be needed for patients that are already in a critical state, due to the immune dysregulation which is so apparent in severe cases (Qin et al., 2020).

Previous investigations have shown that the entry by SARS-CoV-2 occurs via the angiotensin-converting enzyme 2 (ACE2) receptor (W. Li et al., 2003). A study on normal lung tissue showed that 83% of ACE2-expressing cells were alveolar epithelial type II cells (Zhao et al., 2020), highlighting the lungs as the primary target organ that facilitate viral invasion and replication. Furthermore, the ACE2 receptor is also highly expressed in gastrointestinal epithelial cells, with SARS-CoV-2 RNA observed to be present in stool specimens of patients during infection (Gu et al., 2020; Wu et al., 2020). A recent retrospective analysis of 85 patients with laboratory-confirmed COVID-19 also indicated that SARS-CoV-2 infects human kidney tubules and induces acute tubular damage in some patients (Diao et al., 2020). Furthermore, 2–11% of patients with COVID-19 exhibit liver comorbidities (C. Zhang, Shi, & Wang, 2020). Of note is an observation of SARS and the Middle East respiratory syndrome (MERS) having a tropism to the gastrointestinal tract (Guo et al., 2020) and causing liver impairment in addition to respiratory disease. The genomic similarity between SARS-CoV-2 and SARS-CoV (79.6%

sequence identity) would imply that the current virus would act similarly and be present within the body systemically (Hoffmann et al., 2020; S. H. Wong, Lui, & Sung, 2020; H. Zhang et al., 2020). Therefore, treatment options that provide therapeutic concentrations of drug(s) within the systemic circulation and other affected organs are likely to be required.

In the absence of a vaccine, antiviral drugs could also be deployed as chemoprophylaxis to protect against infection and would present an essential tool for protecting healthcare staff and other key workers, as well as household contacts of those already infected. Chemoprevention drugs will need to penetrate the multiple sites where SARS-CoV-2 infection occurs and do so in sufficient concentrations to inhibit viral replication (W. Zhang et al., 2020). This may include the mucous membranes present in the nasal cavity and throat, the ocular surface, tears and the upper respiratory tract/lungs (C. W. Lu, Liu, & Jia, 2020; Sun, Wang, Liu, & Liu, 2020). However, therapeutic concentrations may not be needed in the systemic circulation for chemoprophylaxis, but this is yet to be determined. Although difficult and scarcely studied, work in animals has shown that the size of the inoculum of other respiratory viruses such as influenza is associated with the severity of the resultant disease (D. S. Miller, Kok, & Li, 2013; C. A. Smith, Kulkarni, Chen, & Goldstein, 2019). Reports with SARS-CoV-2 indicate that higher viral loads are indicative of poorer prognosis and correlate with the severity of symptoms, with viral load in severe cases reported to be 60 times higher than that of mild cases (X. Chen et al., 2020; Y. Liu et al., 2020). In light of this, even if a chemoprophylactic drug reduced inoculum size without completely blocking transmission, major benefits for morbidity and mortality may still be achievable.

Many ongoing global research efforts are focussed on screening the activity of existing compounds *in vitro* to identify candidates to repurpose for SARS-CoV-2. However, current data have not yet been systematically analysed in the context of the plasma and target site exposures that are achievable after administration of the approved doses to humans. The purpose of this work was to evaluate the existing *in vitro* anti-SARS-CoV-2 data to determine and prioritise drugs capable of reaching antiviral

concentrations within the blood plasma. Accepted physiologically based pharmacokinetic (PBPK) equation were also used to predict the expected concentration in the lung (Rodgers, Leahy, & Rowland, 2005; Rodgers & Rowland, 2006, 2007), to assess the potential of these drugs for therapy in this key disease site and the potential for chemoprevention.

A.2 Methods

A.2.1 Candidate Analysis

To identify compounds and their relevant potency and pharmacokinetic data, a literature search was performed on PubMed, Google Scholar, BioRxiv, MedRxiv, and ChemRxiv. The following search terms were used for *in vitro* activity data – (COVID-19 OR SARS-CoV-2) AND (EC50 OR IC50 OR antiviral). For pharmacokinetic data (Cmax OR pharmacokinetics) was used along with the drug name for drugs with reported anti-SARS-CoV-2 activity. Further clinical pharmacokinetic data were obtained from the Food and Drug Administration (FDA), the European Medicines Agency (EMA) and through publications available online. Inhaled medications were excluded from all analyses because the purpose was to assess systemically administered medicines.

A.2.2 Lung Accumulation Prediction

An indication of the degree to which candidate drugs are expected to accumulate in the lung (a presumed site of primary efficacy and for prevention of SARS-CoV-2 infection) was provided by calculation of unbound lung to plasma tissue partition coefficient (K_pU_{lung}) according to the methodology of Rodgers and Rowland (Rodgers et al., 2005; Rodgers & Rowland, 2006, 2007). Equations therein were implemented in the R programming environment (version 3.6.3). Briefly, the physicochemical properties of the drug (pKa, log P, classification as acid/base/neutral) and *in vitro* drug binding information (fraction unbound in plasma, blood to plasma ratio), in combination with tissue-specific data (lipid content, volumes of intra/extracellular water etc.) were used to predict tissue K_pU values. Measured log P and pKa values were used where available but substituted with calculated values where necessary and all parameter values used for the calculations for each drug, and their references/sources, are provided in Table B.9. K_pU_{lung} values were converted to K_{p_lung} by multiplying by fraction unbound in plasma to allow estimation of lung exposure from *in vivo* measurements of plasma C_{max} concentration. A similar analysis was conducted to assess the tissue distribution into other tissues. In the absence of observed tissue distribution data, the Rodgers and Rowland method is an accepted means to provide initial estimates of tissue partitioning for PBPK

modelling. However, there are known limits on accuracy with predicted K_pU by the Rodgers and Rowland method generally reported to be within 2-3-fold of observed tissue K_pU values (Rodgers et al., 2005; Rodgers & Rowland, 2006, 2007). This was confirmed for a limited number of drugs within the current dataset for which measure K_p values for lung were available from animal studies in the literature (see data analysis below). The lung accumulation prediction was performed by Henry Pertinez and Rajith Rajoli.

A.2.3 Data Analysis and Interpretation

Since in the majority of papers only an EC_{50} value was available, concentration-response data were digitised using the Web Plot Digitizer® software. Graphs were then replotted in SigmaPlot 14.0 (Systat Software, Inc.) and curves were fitted to confirm EC_{50} values and determine EC_{90} values. A C_{max}/EC_{50} and C_{max}/EC_{90} ratio was then calculated for each drug for which previous evidence of clinical use in humans and the availability of human pharmacokinetic data were available. Lung and other tissue K_pU values were used in combination with reported C_{max} values to derive an estimate of lung exposure at C_{max} for each drug. For a subset of molecules, the absence of available physicochemical or plasma protein binding parameters prohibited the derivation of a K_pU estimate. For the remaining drugs, a lung (or other tissue) C_{max}/EC_{50} and lung C_{max}/EC_{90} were calculated. Published plasma concentration-time data for the most promising candidates were then digitised (where available) and replotted to visually represent human pharmacokinetics relative to the calculated EC_{50} and EC_{90} data. Equivalence between values for the predicted lung K_p and those observed *in vivo* was undertaken for drugs with available animal lung and plasma concentration data. For this analysis, animal lung concentration data were available for anidulafungin (rat), bazedoxifene (rat), chloroquine (three albino rat studies), favipiravir (monkey), hydroxychloroquine (two albino rat studies), nitazoxanide (mouse), tamoxifen (rat), cyclosporine (rat), ritonavir (rat), azithromycin (mouse), dolutegravir (mouse), gilteritinib (albino rat), and lopinavir (rat) (Browning, 2014; Chandrasekaran et al., 2010; Damle, Stogniew, & Dowell, 2008; Gupta, Tulsankar, Bhatta, & Misra, 2017; Kawai, Mathew, Tanaka, & Rowland, 1998; Lien, Solheim, & Ueland, 1991; McChesney, Banks, & Fabian, 1967; Moss et al., 2015; PMDA, 2018; Rivulgo

et al., 2013). Agreement between the predicted and measured K_p was assessed by simple linear regression and by constructing Bland-Altman plots, the limits of agreement (mean ± 2 standard deviations) were included in these plots as previously described (Bland & Altman, 1986).

A.3 Results

A.3.1 Identified Papers and Methods

20 key studies that detailed the antiviral activity of 79 compounds were identified (Bojkova et al., 2020; Bukreyeva et al., 2020; Caly, Druce, Catton, Jans, & Wagstaff, 2020; Choy et al., 2020; Fintelman-Rodrigues et al., 2020; Nils C. Gassen et al., 2020; Ge et al., 2020; Gorshkov et al., 2020; S. Jeon et al., 2020; Jin et al., 2020; Ko, Jeon, Ryu, & Kim, 2020; Lo et al., 2020; Ohashi et al., 2020; Touret et al., 2020; M. Wang et al., 2020; Weston, Haupt, Logue, Matthews, & Frieman, 2020; T. Xu, Gao, Wu, Selinger, & Zhou, 2020; Yamamoto, Matsuyama, Hoshino, & Yamamoto, 2020; Yao et al., 2020; Zhijian et al., 2020). The majority of the *in vitro* SARS-CoV-2 infection experiments were performed in Vero E6 cells (ATCC 1586) maintained in either DMEM or MEM. Other studies utilised Vero-hSLAM cells, Calu-3, Vero E6 cells expressing TMPRSS2 and the CACO-2 cell line to cultivate the virus. The following SARS-CoV-2 strains were used across studies; WA-1 strain – BEI #NR-52281; Brazil/RJ-314/2020; C-Tan-nCoV Wuhan strain 01; Wuhan/WIV04/2019; USA-WA1/2020; nCoV-2019BetaCoV/Wuhan/WIV04/2019; BetaCoV/Hong Kong/VM20001061/2020; SARS-CoV-2 strain Munich; Australia/VIC01/2020; SARS-CoV-2/1/Human/2020/Frankfurt; βCoV/KOR/KCDC03/2020 and BavPat1/2020. Cells across all studies were infected with the virus with a multiplicity of infection (MOI) of 0.0005, 0.002, 0.01, 0.0125, 0.02, 0.05 and 0.1. Drugs were added at concentrations varying between 0.01µM - 500µM. A summary of the differences in methodologies between studies is presented in Table A.1. A ranking of included drugs based just on their EC_{50} and recalculated EC_{90} is presented in Figure B.11.

A.3.2 Identification of Candidates Achieving Plasma Concentrations Expected to Exert Antiviral Activity (C_{max}/EC_{50} Ratio)

Seventeen molecules had a reported C_{max} value greater than at least one of the reported EC_{50} values against SARS-CoV-2 and these were nelfinavir, chloroquine, remdesivir, lopinavir (ritonavir-boosted), eltrombopag, hydroxychloroquine, atazanavir (ritonavir-boosted), indomethacin, favipiravir, sulfadoxine, niclosamide, mefloquine, tipranavir (ritonavir-boosted), ritonavir, merimepodib,

anidulafungin and nitazoxanide. However, it should be noted that for amodiaquine, atazanavir, chloroquine, hydroxychloroquine, lopinavir, mefloquine, nelfinavir, remdesivir and toremifene, more than one EC_{50} value had been reported across the available literature and these were not always in agreement (Figure A.1a). Moreover, this variability in reported EC_{50} values sometimes resulted in C_{max}/EC_{50} ratios giving a different estimation of the likely value of the molecule. Meaning that for the same drug, the C_{max}/EC_{50} ratio could be above or below 1 (Figure A.1b). For amodiaquine and toremifene, all reported EC_{50} values were below their reported C_{max} and only for nelfinavir was the reported C_{max} value expected to exceed both reported EC_{50} values. For atazanavir, chloroquine, hydroxychloroquine, lopinavir, mefloquine and remdesivir, some EC_{50} values were above the C_{max} whereas others were below. This observation dramatically highlights the sensitivity of the current analysis of the reported antiviral activity data, and this should be taken into account when interpreting the data presented hereafter.

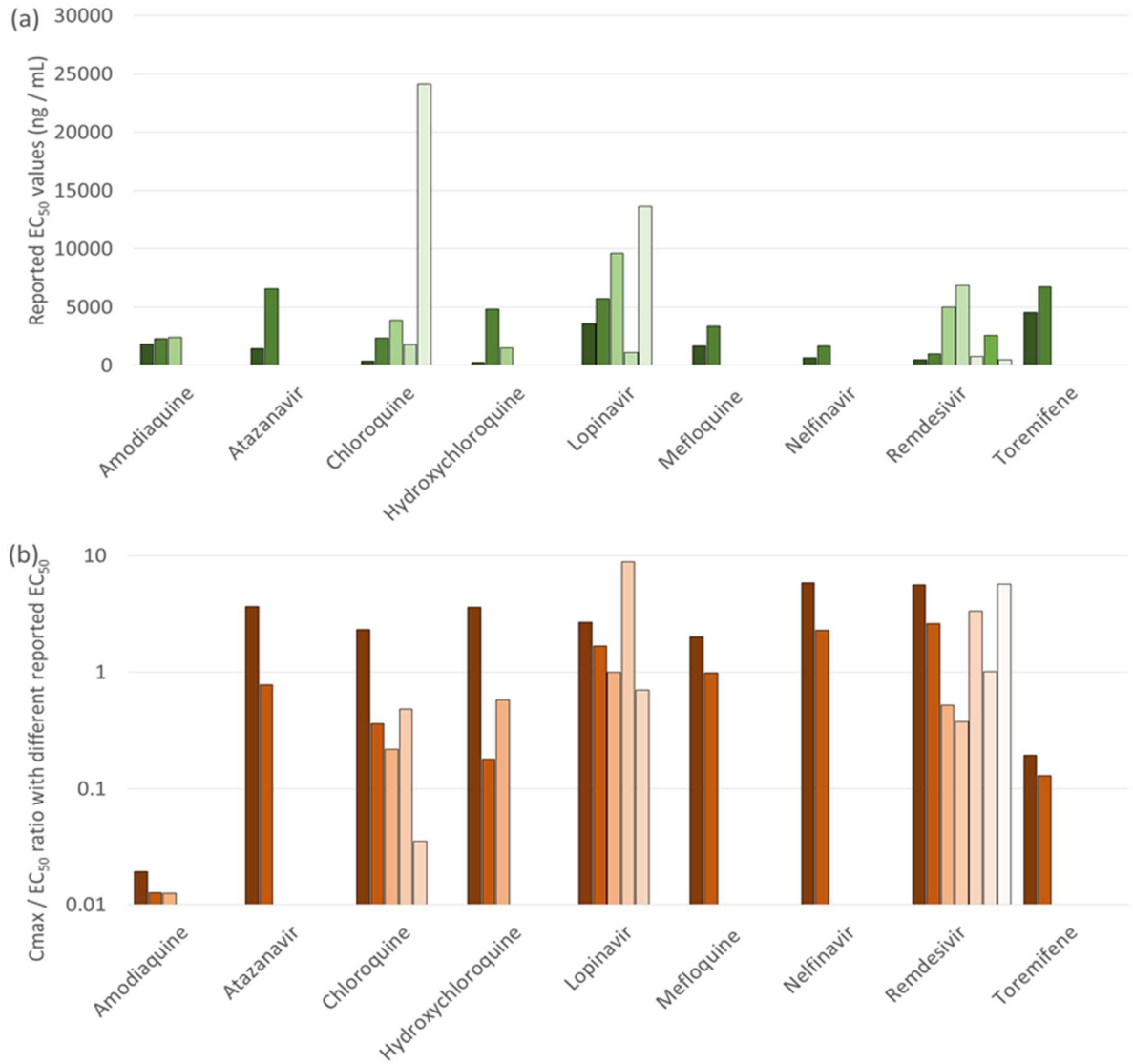

Figure A.1 Assessment of the variation in reported EC_{50} values for SARS-CoV-2 across the drugs for which more than one value was available in the literature **(a)**. The consequences of this variability in reported EC_{50} in terms of the C_{max}/EC_{50} ratio is also provided **(b)**. Amodiaquine and toremifene were estimated to exhibit sub-therapeutic pharmacokinetics irrespective of which EC_{50} value was used. Similarly, nelfinavir was estimated to have C_{max} value higher than its EC_{50} irrespective of which EC_{50} was used in the analysis. For the other drugs, interpretation was highly dependent upon which reported EC_{50} was utilised and this underscores the caution that should be taken in interpreting the available data.

A.3.3 Identification of Candidates Achieving Plasma Concentrations Exceeding the SARS-Cov-2 EC_{90} (C_{max}/EC_{90} Ratio)

For 66 of the reported antiviral activities, data covering a sufficient concentration range were available for digitisation and subsequent calculation of an EC_{90} value. For the remainder, it was not possible to calculate an EC_{90}. Drugs with an available EC_{90} were ranked according to their C_{max}/EC_{90} ratio (Figure A.2). Drugs with a value above 1.0 achieved plasma concentrations above the concentrations reported to inhibit 90% of SARS-CoV-2 replication. Only eltrombopag, favipiravir, lopinavir, remdesivir, nelfinavir, niclosamide, nitazoxanide and tipranavir were estimated to exceed at least one of their reported EC_{90} by 2-fold or more at C_{max} concentrations. Anidulafungin, chloroquine and ritonavir were also reported to exceed at least one of their reported EC_{90} values at C_{max} but by less than 2-fold. It was not possible to calculate an EC_{90} value for sulfadoxine or indomethacin.

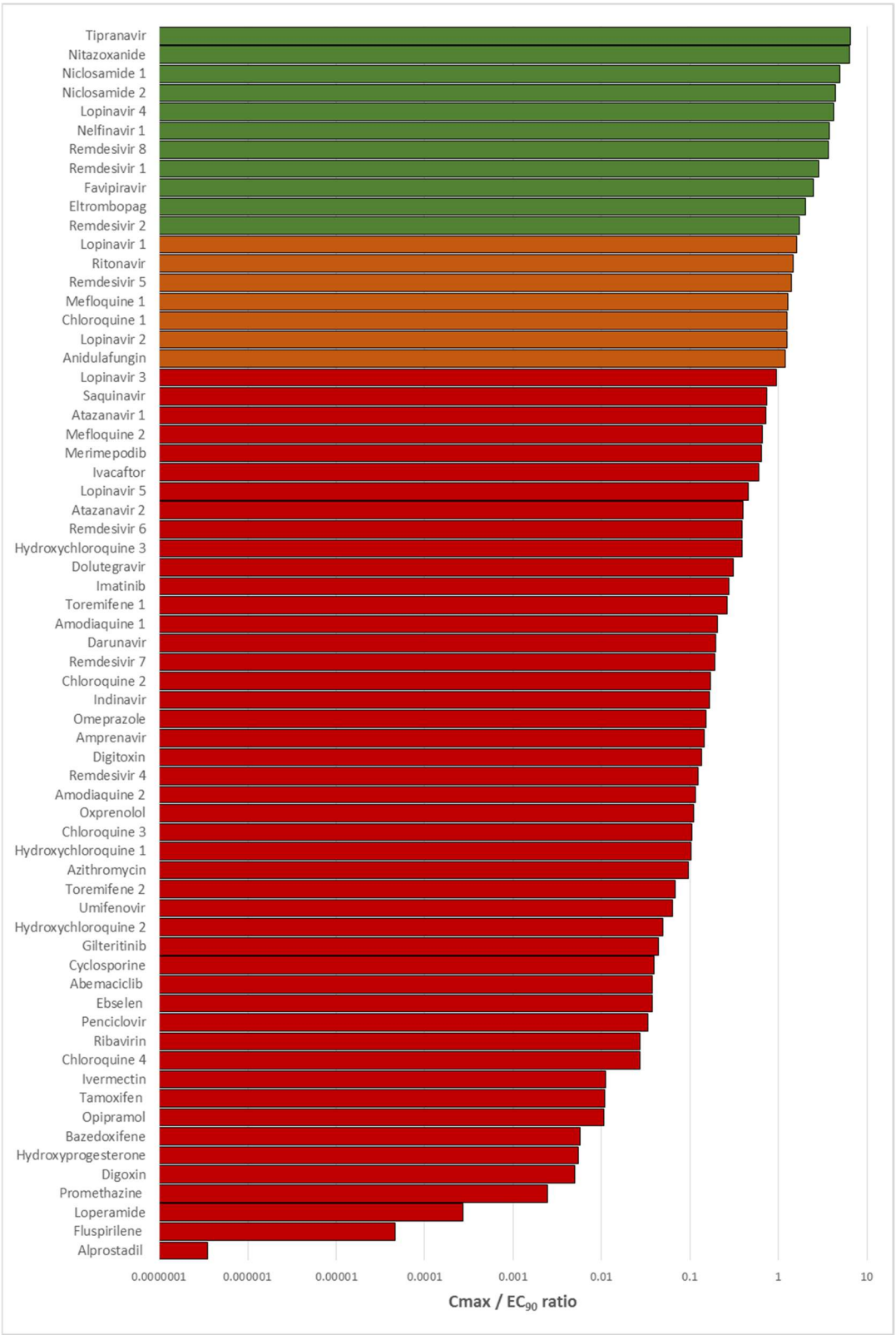

Figure A.2 A bar chart displaying C_{max}/EC_{90} ratio for compounds studied for in vitro antiviral activity against SARS-CoV-2 for which data were available to recalculate an EC_{90}. Drugs with a ratio below 1 were deemed not to provide plasma concentrations at their approved doses to exert sufficient systemic antiviral activity. Those drugs with a ratio above 1 (shown in orange) were deemed to have potential to provide plasma concentrations sufficient to exert at least some antiviral activity for at least some of their dosing interval at their approved dose. Drugs shown in green were predicted to exceed plasma concentrations over their EC_{90} by more than 2-fold.

A.3.4 Detailed Interrogation of the Plasma Pharmacokinetics in Relation to Reported Anti-SARS-Cov-2 Activity

For drugs, with C_{max} concentrations above at least one of their reported EC_{90} values that are not already in clinical trials for COVID-19, a detailed evaluation of concentrations across their approved dosing interval was undertaken. For this, published pharmacokinetic data were digitised and replotted relative to the calculated EC_{50} and EC_{90} data for SARS-CoV-2 (Figure A.3). For tipranavir (ritonavir-boosted), nelfinavir, sulfadoxine and nitazoxanide, plasma concentrations after administration of the approved dose remained above SARS-CoV-2 effective concentrations across the entire dosing interval. For remdesivir, anidulafungin, eltrombopag, lopinavir (ritonavir-boosted), mefloquine and chloroquine, C_{max} values were above EC_{90} at 1.15, 2-, 6-, 8- and 24-hours post-dose, respectively, but concentrations would be expected to dip below the EC_{50} at 1.3-, 3-, 8-, 10-, 72- and 120-hours post-dose, respectively, when given at approved doses and schedules. An overview of these drugs is presented in Table B.1

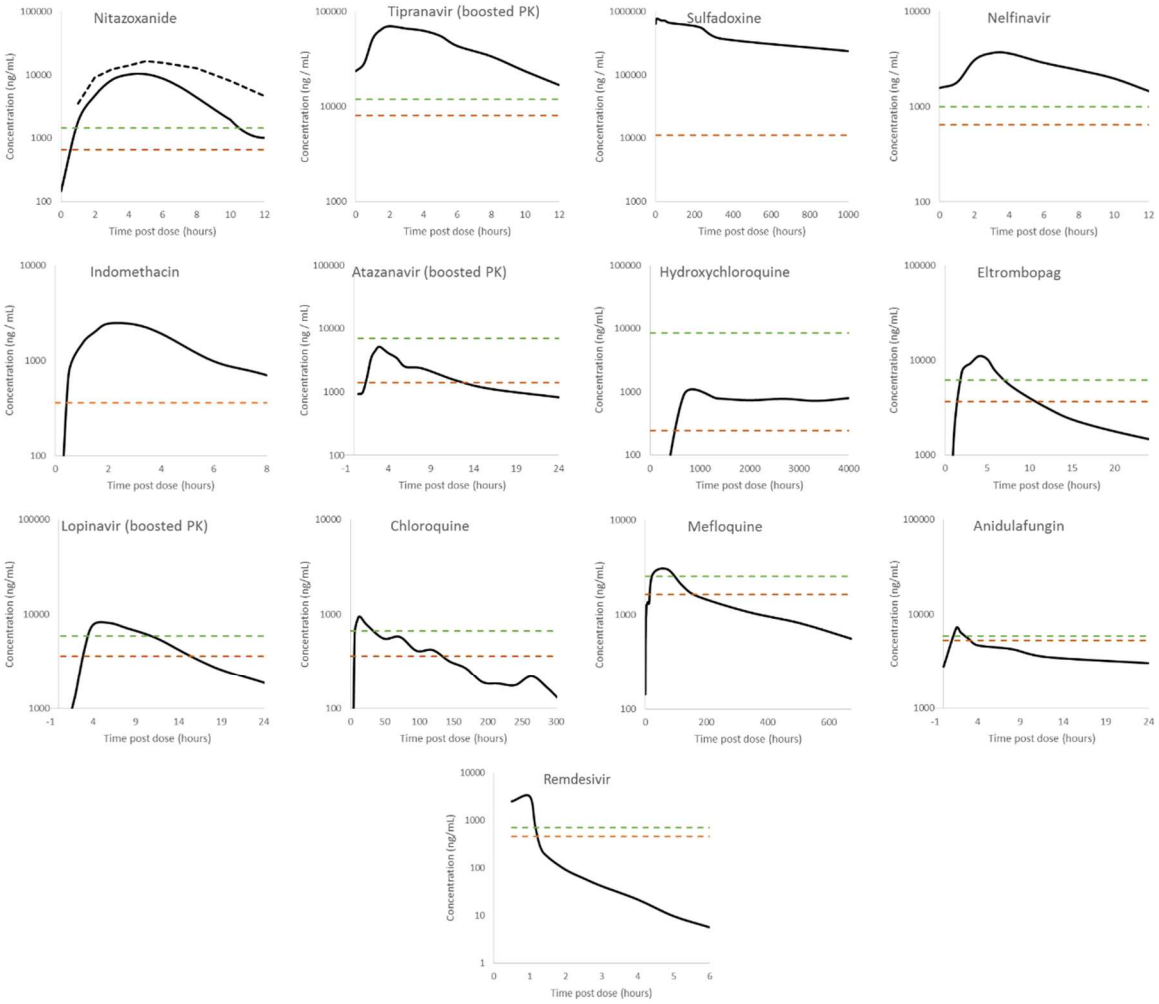

Figure A.3 Digitised pharmacokinetic interrogation of all drugs calculated to have a C_{max}/EC_{50} ratio above 1. The lowest reported SARS-CoV-2 EC_{50} (dashed orange lines) and associated recalculated EC_{90} (dashed green lines) are also highlighted. References for the utilised data are nitazoxanide 500mg BID and 1000mg BID (Fox & Saravolatz, 2005), tipranavir 500mg BID with 200mg ritonavir (la Porte, Sabo, Beique, & Cameron, 2009), sulfadoxine 1500mg with 75mg pyrimethamine (de Kock et al., 2017), nelfinavir 1250mg BID (Kruse et al., 2005), indomethacin 50mg TID (Rainsford et al., 1992), atazanavir 300mg QD with 100mg ritonavir (Burger et al., 2006), hydroxychloroquine 2000mg hydroxychloroquine sulfate/1550mg base administered over 3 days (Tett, Cutler, Beck, & Day, 2000), eltrombopag 75mg single dose (Shida, Takahashi, Nohda, & Hirama, 2011), lopinavir 400 mg with 100mg ritonavir (FDA, 2020), chloroquine 1500mg administered over 3 days (Na-Bangchang, Limpaibul, Thanavibul, Tan-Ariya, & Karbwang, 1994), mefloquine 1200mg over 3 days (Krudsood et al., 2010), anidulafungin 100mg QD (P. Liu et al., 2013) and remdesivir 150mg OD for 7 days (Humeniuk et al., 2020). Robust pharmacokinetic data were unavailable for niclosamide 500mg, ritonavir 600mg and merimepodib 300mg to conduct this digitised interrogation of these molecules.

Table A.1 Summary of the top leads identified

Drug	C_{max}: EC_{50}	C_{max}: EC_{90}	Approval	Indications	Route of administration	Dosage	Ref
Atazanavir & Ritonavir REYATAZ® (Bristol-Myers Squibb)	3.643	0.728	EMA FDA	HIV-1	Oral	300/100 mg	(Harrison & Scott, 2005; Raja, Lebbos, & Kirkpatrick, 2003)
Anidulafungin Eraxis®/Ecalta® (Pfizer)	1.323	1.192	EMA FDA	Invasive fungal infections	Intravenous infusion	200 mg QD + 100 mg QD	(Murdoch & Plosker, 2004)
Chloroquine Aralen® (Sanofi Aventis)	2.318	1.261	FDA	Malaria Extraintestinal amebiasis	Oral	1500 mg	(P. Goel & Gerriets, 2020)
Eltrombopag Promacta® /Revolade® (Novartis)	3.416	2.029	EMA FDA	Primary immune thrombocytopenia Acquired severe aplastic anaemia	Oral	75 mg QD	(Garnock-Jones, 2011)
Favipiravir Avigan® (Fujifilm Toyama Chemical Co)	6.326	2.469	PMDA - Japan	Influenza	Oral	600 mg BID	(PMDA, 2014)
Hydroxychloroquine Plaquenil® (Sanofi Aventis)	3.598	0.101	EMA FDA	Malaria	Oral	400 mg	(Ben-Zvi, Kivity, Langevitz, & Shoenfeld, 2012)
Indomethacin Indocin® (Merck & Co)	5.366	-	EMA FDA	Rheumatoid arthritis	Oral	50 mg TID	(Yeh, 1985)
Lopinavir & Ritonavir Kaletra® (AbbVie)	2.660 / 1.671	1.630 / 1.240	EMA FDA	HIV-1	Oral	400/100 mg BID	(Corbett, Lim, & Kashuba, 2002)

Mefloquine Lariam® (Roche)	1.350	1.284	EMA FDA	Malaria	Oral	250 mg	(R. N. Price et al., 1997)
Merimepodib (Vertex Pharmaceuticals)	1.629	0.638	Not clinically approved	HCV	Oral	300 mg TID	(McHutchison et al., 2005)
Nelfinavir VIRACEPT® (Roche)	5.849 / 2.287	3.755	EMA FDA	HIV-1	Oral	1250 mg BID	(James, 1997)
Niclosamide Yomesan® (Bayer)	8.286	4.936	EMA FDA	Infestation with tapeworms	Oral	2000 mg	(W. Chen, Mook, Premont, & Wang, 2018)
Nitazoxanide Alinia® (Romark Pharmaceuticals)	13.823	6.315	FDA	Diarrhoea caused by Giardia lamblia or Cryptosporidium parvum	Oral	1000 – 2000 mg BID	(Anderson & Curran, 2007)
Remdesivir (Gilead)	5.603 / 2.614	3.755 / 1.712	*Not clinically approved	Ebola	Intravenous	200 mg + 100 mg	(M. Wang et al., 2020)
Ritonavir Norvir® (AbbVie)	1.800		EMA FDA	HIV-1	Oral	600 mg	(Porche, 1997)
Sulfadoxine & pyrimethamine Fansidar® (Roche)	6.577		FDA - discontinued	Malaria	Oral	1500/75 mg	(K. D. Miller et al., 1986)
Tipranavir & Ritonavir Aptivus® (Boehringer Ingelheim Pharmaceuticals, Inc.)	9.647	6.559	EMA FDA	HIV-1	Oral	500/200 mg BID	(Orman & Perry, 2008)

*compassionate use programme

A.3.5 Simulated Exposure Relative to Reported Anti-SARS-Cov-2 Activity in Lung and Other Tissues

Lung K_pU was simulated for all molecules for which the necessary physicochemical properties and *in vitro* drug binding information were available. Regression and Bland–Altman plots were first used to assess the agreement between predicted lung K_p and that observed in previously published animal studies for drugs with available prior data. Good agreement was observed across the available drugs except for chloroquine. An r^2=0.86 was observed in linear regression when chloroquine was excluded but decreased to r^2=0.22 when included (Figure B.12A). Similarly, good agreement between measured and predicted Kp was observed by Bland-Altman analysis for all data points except for one chloroquine measurement (Figure B.12B). K_pU_{lung} was then used along with fraction unbound in plasma (Fu) and plasma C_{max} values to calculate a predicted C_{max}/EC_{50} (Figure A.4) and C_{max}/EC_{90} in the lung.

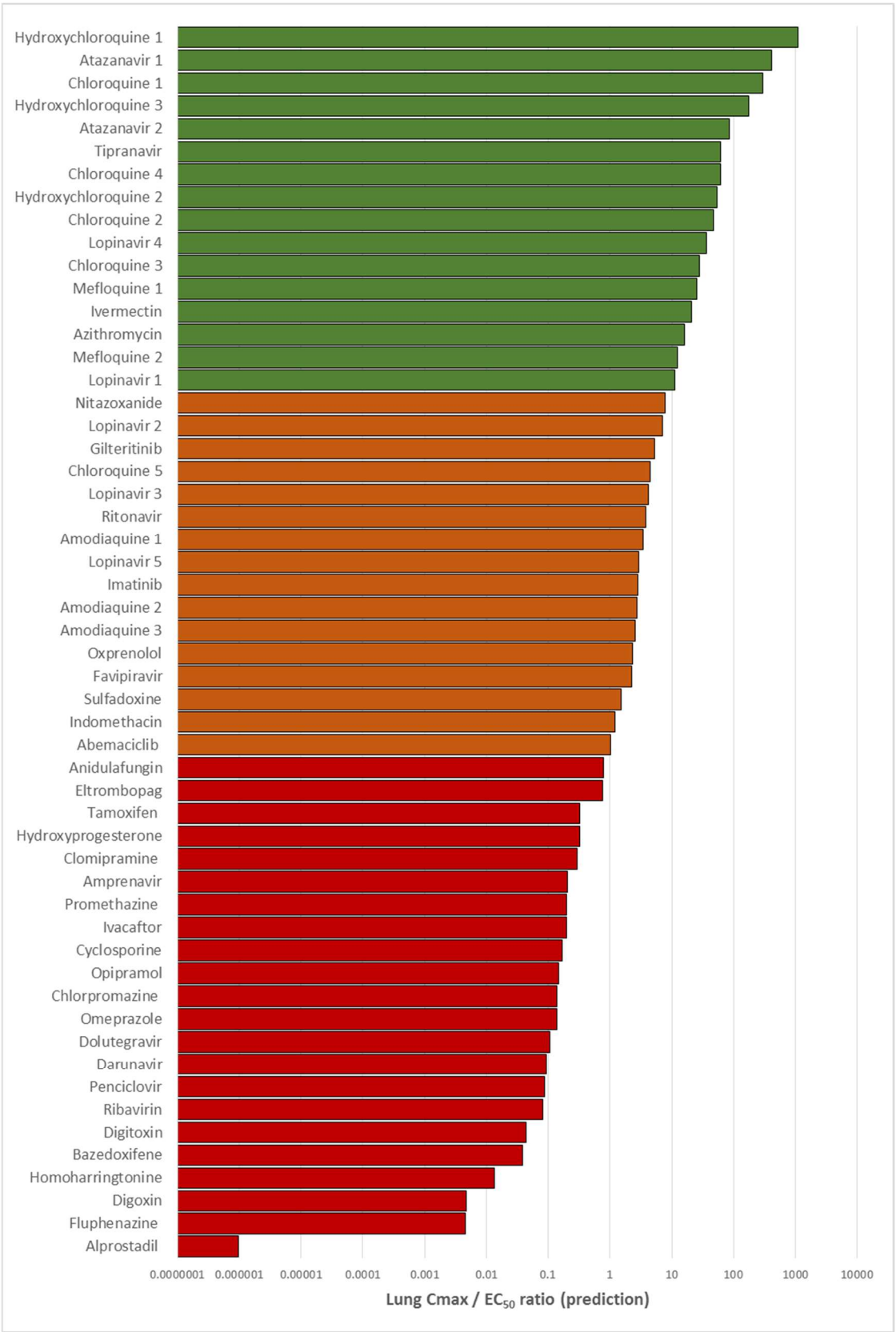

Figure A.4 A bar chart displaying the simulated lung C_{max}/EC_{50}. Drugs with a ratio below 1 were deemed not to provide lung concentrations at their approved doses to exert sufficient pulmonary antiviral activity for treatment or prevention strategies. Those drugs with a ratio above 1 (shown in orange) were estimated to provide lung concentrations sufficient to exert at least some antiviral activity at their approved dose. Drugs shown in green were predicted to exceed lung concentrations over their EC_{50} by more than 10-fold.

Tissue C_{max}/EC_{50} ratios are also shown for other tissues in Figure A.5. For 4 drugs, ebselen, merimepodib, niclosamide and remdesivir, the fraction unbound data were unavailable. For 6 other drugs, benztropine, indinavir, loperamide, nelfinavir, saquinavir and toremifene, the blood to plasma ratios were unavailable. For a further 4 drugs, camostat, emetine, fluspirilene and umifenovir, both fraction unbound and blood to plasma ratios were unavailable. Therefore, these drugs were excluded from the analysis. A total of 18 drugs with available data were predicted to give concentrations in lung above at least one of their reported EC_{50} against SARS-CoV-2 (Figure A.4) and 8 of these were predicted to exceed their EC_{50} by more than 10-fold. The rank order of lung C_{max}/EC_{90} ratio was chloroquine > hydroxychloroquine > atazanavir (ritonavir-boosted) > tipranavir (ritonavir-boosted) > lopinavir (ritonavir-boosted) > mefloquine > ivermectin > azithromycin > nitazoxanide > ritonavir > gilteritinib > amodiaquine > imatinib > oxprenolol (data excluded due to this analysis only being possible for 34 of the 57 drugs).

	Tissue Cmax/EC50 ratio											
	Lung	Kidney	Gut	Liver	Brain	Heart	Bone	Muscle	Pancreas	Skin	Spleen	Thymus
Abemaciclib	1.03	1.18	0.92	1.11	0.52	0.62	0.33	0.43	0.80	0.94	0.73	0.66
Alprostadil	0.00	0.00	0.00	0.00	0.00	0.00	0.00	0.00	0.00	0.00	0.00	0.00
Amodiaquine 1	3.42	4.38	2.13	3.98	0.41	1.99	0.61	1.38	1.50	1.18	2.80	2.04
Amodiaquine 2	2.73	3.50	1.70	3.18	0.33	1.59	0.49	1.10	1.20	0.94	2.23	1.63
Amodiaquine 3	2.59	3.32	1.61	3.02	0.31	1.51	0.46	1.04	1.14	0.89	2.12	1.55
Amprenavir	0.21	0.17	0.28	0.18	0.24	0.16	0.12	0.11	0.26	0.36	0.14	0.15
Anidulafungin	0.79	0.60	0.97	0.57	0.83	0.59	0.48	0.42	0.90	1.40	0.43	0.55
Atazanavir 1	406.68	311.68	665.21	333.28	638.29	269.42	288.61	196.51	693.93	994.19	166.69	315.87
Atazanavir 2	86.90	66.60	142.14	71.21	136.39	57.57	61.67	41.99	148.28	212.43	35.62	67.49
Azithromycin	16.04	20.26	10.59	18.50	2.85	9.45	3.23	6.63	7.85	6.72	12.96	9.77
Bazedoxifene	0.04	0.03	0.06	0.03	0.06	0.03	0.03	0.02	0.07	0.09	0.02	0.03
Chloroquine 1	300.78	386.01	187.12	350.74	35.03	174.47	53.46	120.52	131.88	103.54	245.72	179.19
Chloroquine 2	46.69	59.92	29.04	54.44	5.44	27.08	8.30	18.71	20.47	16.07	38.14	27.81
Chloroquine 3	28.32	36.35	17.62	33.03	3.30	16.43	5.03	11.35	12.42	9.75	23.14	16.87
Chloroquine 4	62.14	79.74	38.66	72.46	7.24	36.04	11.04	24.90	27.24	21.39	50.76	37.02
Chloroquine 5	4.50	5.78	2.80	5.25	0.52	2.61	0.80	1.80	1.97	1.55	3.68	2.68
Chlorpromazine	0.14	0.12	0.20	0.12	0.19	0.09	0.09	0.07	0.21	0.29	0.07	0.10
Ciclesonide	0.00	0.00	0.01	0.00	0.01	0.00	0.00	0.00	0.01	0.01	0.00	0.00
Clomipramine	0.29	0.37	0.21	0.34	0.07	0.17	0.06	0.12	0.16	0.15	0.23	0.18
Cyclosporine	0.17	0.13	0.26	0.14	0.25	0.12	0.11	0.08	0.27	0.38	0.08	0.13
Darunavir	0.09	0.08	0.11	0.09	0.07	0.08	0.04	0.04	0.08	0.12	0.09	0.06
Digitoxin	0.04	0.03	0.04	0.02	0.02	0.03	0.02	0.02	0.02	0.06	0.02	0.02
Digoxin	0.00	0.00	0.00	0.00	0.00	0.00	0.00	0.00	0.00	0.01	0.00	0.00
Dolutegravir	0.11	0.09	0.09	0.10	0.03	0.10	0.03	0.04	0.04	0.06	0.13	0.05
Eltrombopag	0.77	0.48	0.60	0.33	0.23	0.57	0.37	0.24	0.27	1.03	0.36	0.29
Favipiravir	2.22	1.80	1.92	1.43	1.36	2.00	1.04	1.30	1.33	2.40	1.61	1.42
Fluphenazine	0.00	0.00	0.01	0.00	0.01	0.00	0.00	0.00	0.01	0.01	0.00	0.00
Gilteritinib	5.28	6.79	3.27	6.16	0.57	3.04	0.92	2.07	2.28	1.81	4.29	3.11
Homoharringtonine	0.01	0.01	0.01	0.01	0.02	0.01	0.01	0.02	0.02	0.01	0.01	0.02
Hydroxychloroquine 1	1096.26	1408.93	678.16	1278.66	118.97	633.33	191.01	434.11	473.61	372.29	893.89	648.90
Hydroxychloroquine 2	54.69	70.29	33.83	63.79	5.94	31.60	9.53	21.66	23.63	18.57	44.59	32.37
Hydroxychloroquine 3	176.58	226.94	109.23	205.96	19.16	102.01	30.77	69.92	76.29	59.97	143.98	104.52
Hydroxyprogesterone	0.32	0.25	0.53	0.26	0.51	0.21	0.23	0.16	0.55	0.79	0.13	0.25
Imatinib	2.82	3.58	1.84	3.26	0.46	1.65	0.55	1.14	1.35	1.15	2.28	1.70
Indomethacin	1.18	0.74	0.92	0.50	0.33	0.88	0.57	0.37	0.39	1.57	0.55	0.44
Ivacaftor	0.20	0.13	0.18	0.10	0.09	0.14	0.10	0.07	0.11	0.29	0.09	0.09
Ivermectin	21.01	16.10	34.39	17.22	32.99	13.92	14.92	10.14	35.87	51.40	8.60	16.32
Lopinavir 1	11.18	8.59	18.07	9.20	17.21	7.49	7.83	5.39	18.73	26.83	4.80	8.61
Lopinavir 2	7.02	5.40	11.36	5.78	10.81	4.70	4.92	3.38	11.77	16.86	3.02	5.41
Lopinavir 3	4.20	3.22	6.78	3.45	6.46	2.81	2.94	2.02	7.03	10.07	1.80	3.23
Lopinavir 4	37.00	28.42	59.82	30.45	56.95	24.78	25.92	17.82	61.99	88.79	15.89	28.50
Lopinavir 5	2.95	2.27	4.77	2.43	4.54	1.98	2.07	1.42	4.94	7.08	1.27	2.27
Mefloquine 1	25.54	32.81	15.84	29.76	2.78	14.73	4.44	10.05	11.04	8.79	20.76	15.07
Mefloquine 2	12.51	16.07	7.76	14.58	1.36	7.22	2.18	4.92	5.41	4.31	10.17	7.38
Nitazoxanide (Tizoxanide)	7.80	5.57	10.20	5.25	8.43	5.42	4.85	3.31	9.26	15.73	3.39	4.90
Omeprazole	0.14	0.11	0.17	0.12	0.14	0.11	0.07	0.07	0.15	0.22	0.11	0.09
Opipramol	0.15	0.19	0.10	0.17	0.03	0.09	0.03	0.06	0.08	0.07	0.12	0.09
Oxprenolol	2.36	3.02	1.48	2.75	0.31	1.38	0.44	0.97	1.06	0.82	1.94	1.42
Penciclovir	0.09	0.08	0.08	0.08	0.08	0.08	0.05	0.08	0.08	0.08	0.08	0.08
Promethazine	0.20	0.25	0.14	0.23	0.04	0.12	0.04	0.08	0.10	0.10	0.16	0.12
Ribavirin	0.08	0.08	0.08	0.08	0.08	0.08	0.05	0.08	0.08	0.07	0.08	0.08
Ritonavir	3.85	2.97	6.10	3.19	5.73	2.62	2.63	1.83	6.25	8.96	1.78	2.92
Sulfadoxine	1.52	1.00	1.17	0.69	0.47	1.18	0.72	0.55	0.53	1.92	0.78	0.63
Tamoxifen	0.33	0.25	0.54	0.27	0.52	0.22	0.23	0.16	0.56	0.80	0.13	0.26
Tipranavir	62.52	47.80	101.73	50.96	97.29	41.45	44.22	30.07	105.80	152.20	25.62	48.28

Figure A.5 A heatmap displaying the simulated tissue C_{max}/EC_{50} values for all drugs with available data. Those drugs with a ratio above 1 (shown in orange) were estimated to provide tissue concentrations sufficient to exert at least some antiviral activity at their approved dose. Drugs shown in green were predicted to exceed tissue concentrations over their EC_{50} by more than 10-fold.

A.4 Discussion

The systematic development of mechanism-based inhibitors for key targets involved in viral replication or pathogenesis is likely to result in highly effective and safe medicines in the coming years. However, the repurposing of already approved medicines in antiviral treatment or chemoprevention strategies is undoubtedly the fastest way to bring forward therapeutic options against the urgent unmet need posed by SARS-CoV-2. A range of different drugs and drug classes have been demonstrated to display varying degrees of antiviral activity against SARS-CoV-2 *in vitro*, and many of these drugs are already licenced for use in humans for a range of indications. However, currently, the data emerging from global screening efforts are not being routinely benchmarked and prioritised against achievable concentrations after administration of doses proven to have acceptable safety profiles in humans.

The current analysis indicates that only 13 drugs with reported antiviral activity are likely to achieve plasma exposures above that required for an antiviral activity for at least some of their dosing interval. Notably, neither chloroquine, hydroxychloroquine nor lopinavir/ritonavir exhibited a sustained plasma concentration above their reported SARS-CoV-2 EC_{90} across their reported dosing interval. This did raise some concerns for ongoing trials with these drugs (chloroquine: NCT04323527; NCT04333628, hydroxychloroquine: NCT04316377; NCT04333225; NCT04307693 and lopinavir/ritonavir: NCT04331834; NCT04255017; NCT04315948). Of late, it has been shown that chloroquine, hydroxychloroquine and lopinavir/ritonavir failed to deliver benefits in randomised controlled trials for mild/moderate and severe disease (Cao et al., 2020; Tang et al., 2020). A lack of efficacy was seen for lopinavir/ritonavir, and toxicity and safety concerns were present for the investigation of hydroxychloroquine for prophylaxis (Borba et al., 2020; P. Yang, Tekwani, & Martin, 2020). This highlights the importance of systemic suppression (plasma exposure) as a prerequisite for a reduction in morbidity or mortality, and that predicted lung accumulation on its own does not provide any advantage as seen from the previous chemoprevention trials.

At least 8 of the 12 candidates achieving C_{max} above one of their reported EC_{50} and derived EC_{90} are already in clinical evaluation for the treatment of SARS-CoV-2. These include remdesivir (NCT04292730; NCT04292899; NCT04257656; NCT04252664; NCT04315948), favipiravir (NCT04310228; NCT04319900), niclosamide (NCT04345419; NCT04436458), mefloquine (NCT04347031), nitazoxanide (NCT04459286; NCT04441398; NCT04351347; NCT04406246) lopinavir/ritonavir and chloroquine. A recent trial for favipiravir demonstrated some success with an improvement over arbidol from 56% to 71% ($p = 0.02$) in patients without risk factors (but not critical cases or patients with hypertension and/or diabetes) (C. Chen et al., 2020). The results of compassionate use of remdesivir in severely ill patients and a randomised placebo-controlled trial were also recently reported, both of which serve as further validation of the other candidates presented here (Grein et al., 2020; Y. Wang et al., 2020). Of particular interest, nitazoxanide, tipranavir, sulfadoxine and nelfinavir may be expected to sustain their plasma pharmacokinetic exposure above their lowest reported EC_{50} and derived EC_{90} (where available) for the duration of their approved dose and dosing interval.

Nitazoxanide is an antiprotozoal drug that has previously been demonstrated to display broad antiviral activity against human and animal coronaviruses (Rossignol, 2016) as well as various strains of influenza (Haffizulla et al., 2014; D. Tilmanis, C. van Baalen, D. Y. Oh, J. F. Rossignol, & A. C. Hurt, 2017). Importantly, nitazoxanide is rapidly metabolised to tizoxanide in humans and this active metabolite is being investigated against SARS-CoV-2 (NCT04341493 and NCT04343248). Tizoxanide has been reported to exhibit similar activities to nitazoxanide for other viruses as well as other pathogens (Gekonge, Bardin, & Montaner, 2015; D. Tilmanis, C. van Baalen, D. Y. Oh, J.-F. Rossignol, & A. C. Hurt, 2017; Trabattoni et al., 2016). The mechanism of antiviral action is not fully understood for nitazoxanide, but it has been reported to affect viral genome synthesis, prevent viral entry and interfere with the N-glycosylation and maturation of the influenza hemagglutinin (Hickson, Margineantu, Hockenbery, Simon, & Geballe, 2018; Rossignol, 2014; Rossignol, La Frazia, Chiappa, Ciucci, & Santoro, 2009; Y. M. Wang et al., 2016). Notably, the SARS-CoV-2 spike protein is also highly

N-glycosylated (Y. Zhang et al., 2020). This drug has also been shown to elicit an innate immune response that potentiates the production of type 1 interferons (Clerici, Trabattoni, Pacei, Biasin, & Rossignol, 2011; Rossignol, 2014) and a phase 2b/3 clinical trial demonstrated a reduction in symptoms and viral shedding in patients with uncomplicated influenza (Haffizulla et al., 2014). The safety of nitazoxanide is well understood, but it has not been fully investigated during renal or hepatic impairment. The antiviral activity of nitazoxanide for SARS-CoV-2 requires further study but the existing data for this drug are encouraging. Niclosamide is another antiprotozoal drug that exhibits broad antiviral activity due to its ability to perturb the pH-dependent membrane fusion required for virus entry (Jurgeit et al., 2012), but it was reported to have no impact upon the attachment and entry of SARS-CoV-2 (X. W. Zhang & Yap, 2004). For MERS-CoV, niclosamide was observed to inhibit SKP2 activity impairing viral replication (N. C. Gassen et al., 2019). Niclosamide has been reported to be well-tolerated and does not influence vital organ functions (R. Li et al., 2013). However, it has low aqueous solubility and poor oral bioavailability (C. K. Lin et al., 2016) and, despite a higher reported SARS-CoV-2 potency (S. Jeon et al., 2020) than nitazoxanide (M. Wang et al., 2020), the C_{max}/EC_{90} ratio was slightly lower. There is a paucity of published pharmacokinetic data for niclosamide and this prohibited a thorough investigation of exposures concerning activity over its entire dosing interval. Both nitazoxanide and niclosamide have also been reported to be potent antagonists of TMEM16A, calcium-activated chloride channels that modulate bronchodilation (Miner et al., 2019).

Tipranavir and nelfinavir are HIV protease inhibitors (Lv, Chu, & Wang, 2015) and both drugs ranked highly in terms of their C_{max}/EC_{90} ratio. Moreover, a more in-depth analysis demonstrated that the concentrations across the dosing interval for both these drugs remained above the calculated EC_{90} values at approved doses and schedules. Unlike nelfinavir, tipranavir has to be co-administered with a low dose of ritonavir to boost its pharmacokinetics via CYP3A4 inhibition (Streeck & Rockstroh, 2007). Since ritonavir itself has been reported to exert anti-SARS-CoV-2 activity, this could be advantageous but would need to be balanced against the much higher risk of drug-drug interactions that could negatively impact patient management. The implications of drug interactions have already

been raised for this reason with lopinavir/ritonavir use for COVID-19 (Sanders, Monogue, Jodlowski, & Cutrell, 2020) and are likely to be exacerbated with the higher ritonavir dose needed for tipranavir. Moreover, tipranavir has a black box warning from the FDA for fatal and nonfatal intracranial haemorrhage as well as severe hepatotoxicity (Chan-Tack, Struble, & Birnkrant, 2008; Flexner, Bate, & Kirkpatrick, 2005; Amy C. Justice et al., 2008). The major route of metabolic clearance for nelfinavir is via CYP2C19 and this pathway generates the M8 metabolite that retains activity against the HIV protease (Hirani, Raucy, & Lasker, 2004). No data are available for inhibition of SARS-CoV-2 replication by the M8 metabolite but if active, this could provide an advantage for nelfinavir over tipranavir for COVID-19. Conversely, while the analysis of pharmacokinetics relative to potency of these molecules against SARS-CoV-2 is encouraging, it should be noted that the reported *in vitro* activity for HIV (Lv et al., 2015; K. E. Zhang et al., 2001) is far higher than that against SARS-CoV-2 and both drugs are highly protein-bound (King & Acosta, 2006; Motoya et al., 2006). Given that tipranavir and nelfinavir are associated with long-term toxicities (A. C. Justice et al., 2008; Lv et al., 2015; Markowitz et al., 2007; Unis et al., 2016), there will be concern over giving even short-term exposure for COVID-19.

Sulfadoxine is another antimalarial drug that is usually administered in combination with pyrimethamine as a folic acid antagonist combination (Lovegrove & Kain, 2008). Sulfadoxine inhibits the activity of dihydropteroate synthase within the malaria parasite, but its mechanism of action for SARS-CoV-2 is unclear. It should also be noted that the authors can find no data describing the antiviral activity of this drug against other viruses. Also, the concentrations used in the *in vitro* activity used in this analysis (Touret et al., 2020) were not high enough to reach or calculate an EC_{90} value. Therefore, like other molecules described in this manuscript, *in vitro* anti-SARS-CoV-2 activity should be repeated. Notwithstanding, sulfadoxine plasma concentrations far above the reported EC_{50} are maintained in patients receiving a single 1500mg dose (with 75mg pyrimethamine) for over 40 days (de Kock et al., 2017). Compared to some other reported molecules, sulfadoxine is not expected to have as high an accumulation in the lungs, but concentrations higher than its EC_{50} are estimated from the analysis of

its lung K_pU. Therefore, if the reported antiviral activity is confirmed, this drug may offer opportunities for therapy and/or chemoprophylaxis.

Indomethacin is an Non-Steroidal Anti-Inflammatory Drug (NSAID) that is indicated for rheumatoid arthritis, ankylosing spondylitis, osteoarthritis, acute painful shoulder or acute gouty arthritis. The recommended dose for acute gouty arthritis is 50mg three times a day and the pharmacokinetic exposure for this is shown in Figure A.3 relative to the reported EC_{50}. Indomethacin mechanism of action for SARS-CoV-2 remains elusive, but it was shown to inhibit translation of the vesicular stomatitis virus by activating protein kinase R leading to the phosphorylation of eukaryotic initiation factor-2 α-subunit (Amici et al., 2015). This abrogated viral protein translation, leading to a dramatic inhibition of viral replication and infectious viral particle production. The reported *in vitro* antiviral activity data for indomethacin were insufficient to calculate an EC_{90} and this activity requires confirmation in other studies (T. Xu et al., 2020). Furthermore, the drug has a black box warning for serious cardiovascular and gastrointestinal events from the FDA so its use should be managed with caution (Nalamachu & Wortmann, 2014).

Considering that most of the impact of the severe disease occurs in the lung and that this tissue may be a key site for transmission, the potential of candidate drugs to accumulate in lung tissue was considered. The lung K_p predictions were validated across 13 drugs for which previously reported animal plasma and lung concentrations were available and showed good agreement for all agents other than chloroquine. The poor fit for chloroquine does highlight that the predictions may not be accurate for all of the drugs listed and this should be considered in interpretation. Notwithstanding, the analysis of predicted lung C_{max}/EC_{50} ratio revealed more candidates expected to exceed the concentrations needed for antiviral activity in this tissue. Hydroxychloroquine, chloroquine, mefloquine, atazanavir (ritonavir-boosted), tipranavir (ritonavir-boosted), ivermectin, azithromycin and lopinavir were all predicted to achieve lung concentrations over 10-fold higher than their reported EC_{50}. All of these drugs were also predicted to exceed their EC_{90} in the lung by at least 3.4-fold. The

lung prediction was not possible for nelfinavir because insufficient data were available to calculate K_pU_{lung}, but nitazoxanide and sulfadoxine were also predicted to exceed their reported EC_{50} by 7.8- and 1.5-fold in the lung, respectively. Nitazoxanide was predicted to exceed its EC_{90} by 3.6-fold in the lung but an EC_{90} was not calculable from the available data for sulfadoxine.

Predictions for C_{max}/EC_{50} ratio were also made for other tissues and were generally in agreement with observations in the lung with some important exceptions. Gliteritinib, amodiaquine, imatinib, indomethacin, oxprenolol, and sulfadoxine were predicted to be subtherapeutic in the brain and bone, with indomethacin and sulfadoxine being predicted to be subtherapeutic across most of the tissues in which C_{max} was estimated.

During inflammation or injury, changes to the vascular microenvironment could have a profound effect on the ability of these drugs to accumulate in lung cells. Due to the recruitment of neutrophils and leaky endothelial cells (Pober & Sessa, 2007), the lung inflammatory microenvironment is characterised by increased body temperature, excessive enzymatic activity and, most importantly, a low interstitial pH (R. Zhang et al., 2019). In the case of chloroquine and hydroxychloroquine, these diprotic weak bases are exquisitely dependent on a pH gradient to drive lysosomal uptake as a mechanism of lung accumulation. It has been demonstrated that cellular chloroquine uptake is diminished 100-fold for every pH unit of external acidification (Geary, Divo, Jensen, Zangwill, & Ginsburg, 1990). This situation is likely to deteriorate further on mechanical ventilation, which also induces acidification of the lung tissue, independently of inflammation (Drachman et al., 2017; Pugin et al., 2008). Therefore, the benefits of lung accumulation for many of these drugs may be lost during the treatment of severe SARS-CoV-2 infection. Conversely, mefloquine is monoprotic and more lipophilic than chloroquine, which may make it much less reliant on the pH gradient to drive cellular accumulation in the lung. The charged form of the drug is likely sufficiently lipophilic to allow movement across biological membranes along a concentration gradient (Ginsburg, Nissani, & Krugliak, 1989). Only two studies have described mefloquine uptake into cells, one study suggested that

mefloquine uptake is not energy-dependent and the other suggested that mefloquine uptake is mediated by secondary active transport, rather than passive proton trapping (Fitch, Chevli, & Gonzalez, 1974; Vanderkooi, Prapunwattana, & Yuthavong, 1988). Mefloquine is known to cause severe psychiatric side effects in some patients and so the use of this drug should be managed with care (Ritchie, Block, & Nevin, 2013). Therefore, mefloquine may offer opportunities for treatment during severe disease that are not available with other drugs currently being tested for COVID-19 therapy. If the high lung exposures are proven empirically for the drugs on this list, then some may also prove to be valuable for chemoprevention strategies.

This study represents the first holistic view of drugs with reported activity against SARS-CoV-2 in the context of their achievable pharmacokinetic exposure in humans. While the analysis does provide a basis to rationally selected candidates for further analysis, there are some important limitations. Firstly, C_{max} was the only pharmacokinetic parameter that was universally available for all of the candidate drugs, but C_{min} values are generally accepted as a better marker of efficacy since they represent the lowest plasma concentration over the dosing interval. However, C_{max} was only used to assess whether plasma concentration would exceed those required at any point in the dosing interval, and this was followed by a more in-depth analysis of the most promising candidates.

Secondly, an EC_{50} value only equates to a concentration required to suppress 50% of the virus, and data were unavailable to calculate EC_{90} values for some of the drugs. EC_{90} values are a preferred marker of activity because the slope of the concentration-response curve can vary substantially between different molecules and between different mechanisms of action. Although EC_{90} values were not calculable for all drugs, molecules not achieving EC_{50} at C_{max} in this analysis were deprioritised. Thirdly, the reported antiviral activities were conducted under different conditions (Table B.10) and in several cases varied between the same molecule assessed in different studies (Figure A.1). Also, some of the studied drugs (e.g. nitazoxanide and amodiaquine) are rapidly metabolised such that the major species systemically is a metabolite that has not been investigated for anti-SARS-CoV-2 activity.

No mitigation strategy was possible for these limitations and the data should be interpreted in the context that the quality of the available data may profoundly impact the conclusions. *In vitro* activity should be confirmed for the promising candidates and/or relevant metabolites.

Fourthly, plasma protein binding can be an important factor in determining whether sufficient free drug concentrations are available to exert antiviral activity (Gonzalez, Schmidt, & Derendorf, 2013) and insufficient data were available across the dataset to determine protein binding-adjusted EC_{90} values. This is important because for highly protein-bound drugs the antiviral activity in plasma may be lower than reported *in vitro* activity because protein concentrations used in culture media are lower than those in plasma. Fifthly, robust pharmacokinetic data were not available for all the molecules and subtle differences have been reported in the pharmacokinetics in different studies. Where possible, this analysis utilised the pharmacokinetics described at the highest doses approved for other indications and checked them to ensure that profound differences were not evident between different studies. However, in some cases, higher doses and/or more frequent dosing has been investigated for some of the drugs mentioned so higher exposures may be available for some drugs with off-label dosing. Sixthly, the digitised pharmacokinetic plots presented represent the mean or median profiles depending on what was presented in the original manuscripts. Many of the drugs presented are known to exhibit high inter-individual variability that is not captured within the presented analysis and it is possible that even for promising candidates, a significant proportion of patients may have sub-therapeutic concentrations despite population mean/median being higher than the C_{max}. Advanced pharmacokinetics modelling approaches will be needed to unpick the exposure-response relationship and these studies are currently underway by the authors.

Seventhly, the presented predictions for lung accumulation may offer a basis for ranking molecules for expected accumulation in that organ, but the ultimate effectiveness of a chemoprophylactic approach will likely depend upon penetration into other critical matrices in the upper airways, for which there are currently no robustly validated methods of prediction. Also, while a generally

accepted method for assessing KpU was employed, the predictions were only validated for a subset of drugs for which previous animal lung accumulation data were available. Also, the KpU method assumes all the processes are passive and perfusion limited, and the complexity of pulmonary tissue pharmacokinetics is not captured in this analysis. The lungs include different structures including airways, bronchioles and alveoli with different blood flow perfusion and more detailed modelling validated through animal experiments will be required to capture this complexity.

Finally, this analysis assumes that drugs need to be active within the systemic compartment to have efficacy against SARS-CoV-2. Since current evidence suggests that the virus is widely disseminated throughout the body this is a logical assumption. However, the ultimate efficacy of any drug can only be demonstrated with robust clinical trial designs.

A.5 Conclusion

The current analysis reveals that many putative agents are never likely to achieve target concentrations necessary to adequately suppress SARS-CoV-2 under normal dosing conditions. Candidate medicines emerging from *in vitro* antiviral screening programmes must be considered in the context of their expected exposure in humans where possible. Clinical trials are extremely time-consuming and expensive, and only the best options must be progressed for robust analysis as potential mono- or combination therapy or prevention options. Finally, it would be highly beneficial for activity data for SARS-CoV-2 to be performed with a standardised protocol and with activity reported as EC_{90} values as a better marker of the concentrations required to suppress the virus to therapeutically relevant levels.

Appendix B

Table B.1 Origin, genetic and mutational characteristics of investigated human colorectal cancer cell lines

	DLD-1	**HCT116**	**LoVo**
Patient	Male	48-Year-Old Male	56-Year-Old Male
Site	Colon	Ascending Colon	Colon
Stage		Dukes' D	Dukes' C
Source	Primary Tumour	Primary Tumour	Left supraclavicular region
Microsatellite	Unstable	Unstable	Unstable
CIMP	+	+	-
CIN	-	-	-
KRAS	G13D	G13D	G13D; A14V
BRAF	WT	WT	WT
PIK3CA	E545K;D549N	H1047R	WT
PTEN	WT	WT	WT
TP53	S241F	WT	WT

Abbreviations: CIN, chromosomal instability pathway; CIMP, CpG island methylator phenotype; WT, wild type

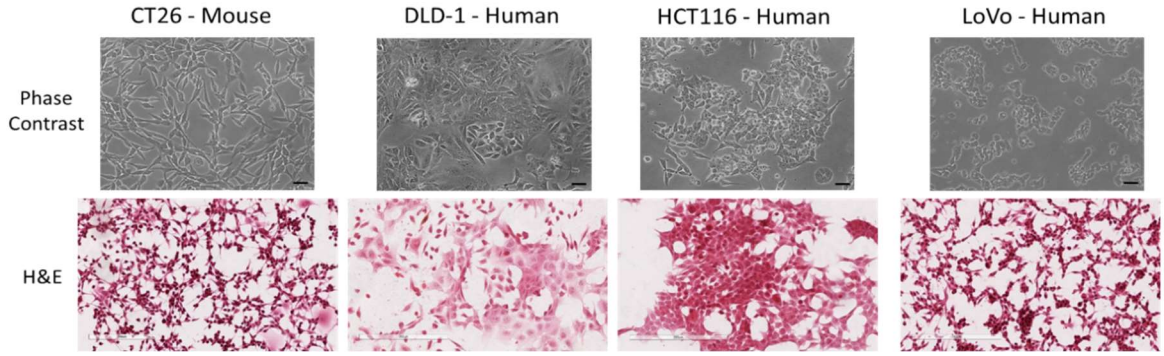

Figure B.1 Morphology and appearance of colorectal cancer cell lines in monolayer (2D). Representative images of HCT116 and CT26 cells. Phase-contrast images were taken at 10x magnification using a phase-contrast microscope (ECLIPSE TS100/100-F, Nikon) Images were captured using a digital camera head (DS-Vi1, Nikon) and a stand-alone controller and display unit (DS-L3, Nikon). Scale bars shown are 100µm. For H&E, cells were grown on coverslips, stained and scanned using the Leica Aperio CS2 Slide Scanner. Images were then processed using the ImageScope software. Scale bars shown are 200µm.

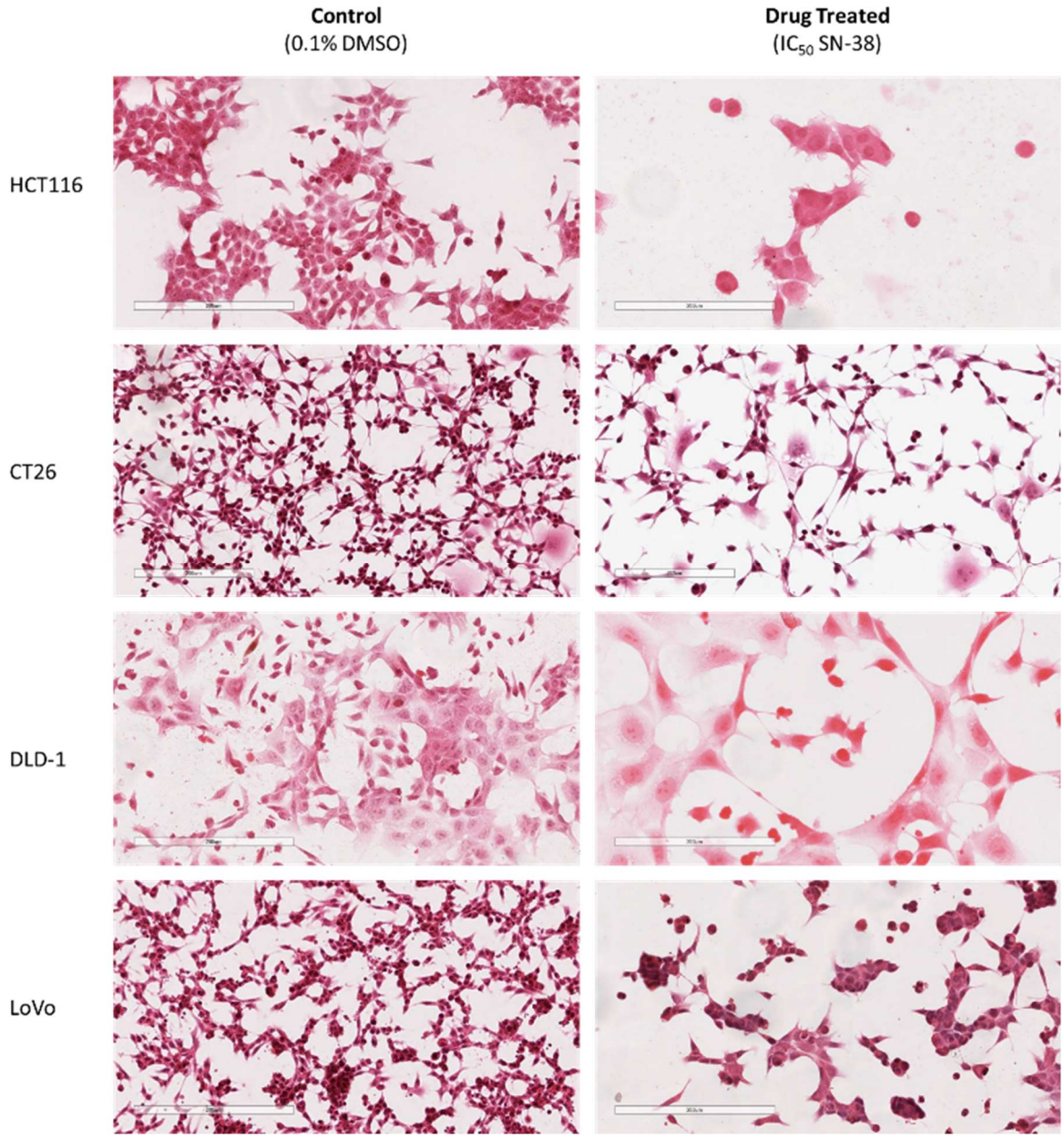

Figure B.2 Morphology of monolayer cells following drug treatment. Cells grown in monolayer on coverslips were treated with control (0.1% DMSO) or SN38 (predetermined IC_{50}) for 72 hours. Coverslips were then processed, stained with H&E and mounted onto slides before scanning them with the Leica Aperio CS2 Slide Scanner. Images were then processed using the ImageScope software. Scale bars shown are 200µm.

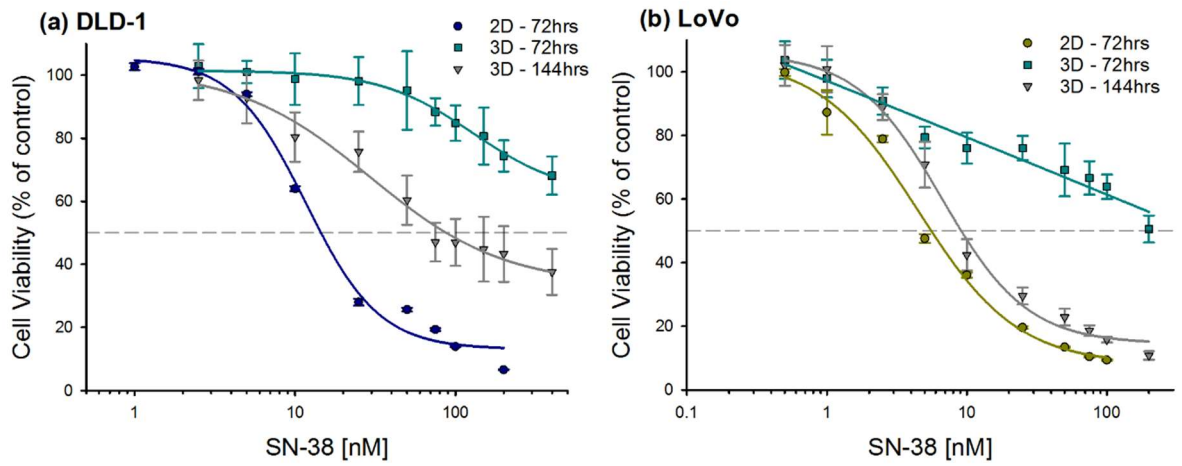

Figure B.3 Concentration-response curves for (**a**) LoVo and (**b**) DLD-1 cells grown in 2d vs. 3d. ATP levels were measured in following treatment with SN-38 [nM], for 72 hours in 2D and 72/144 hours in 3D (n=3 using 6 technical replicates, average ± %SD). Cell viability was calculated as a percentage of untreated vehicle control samples (DMSO – 0.1%). The dashed horizontal line represents the half-maximal inhibitory concentration (IC50).

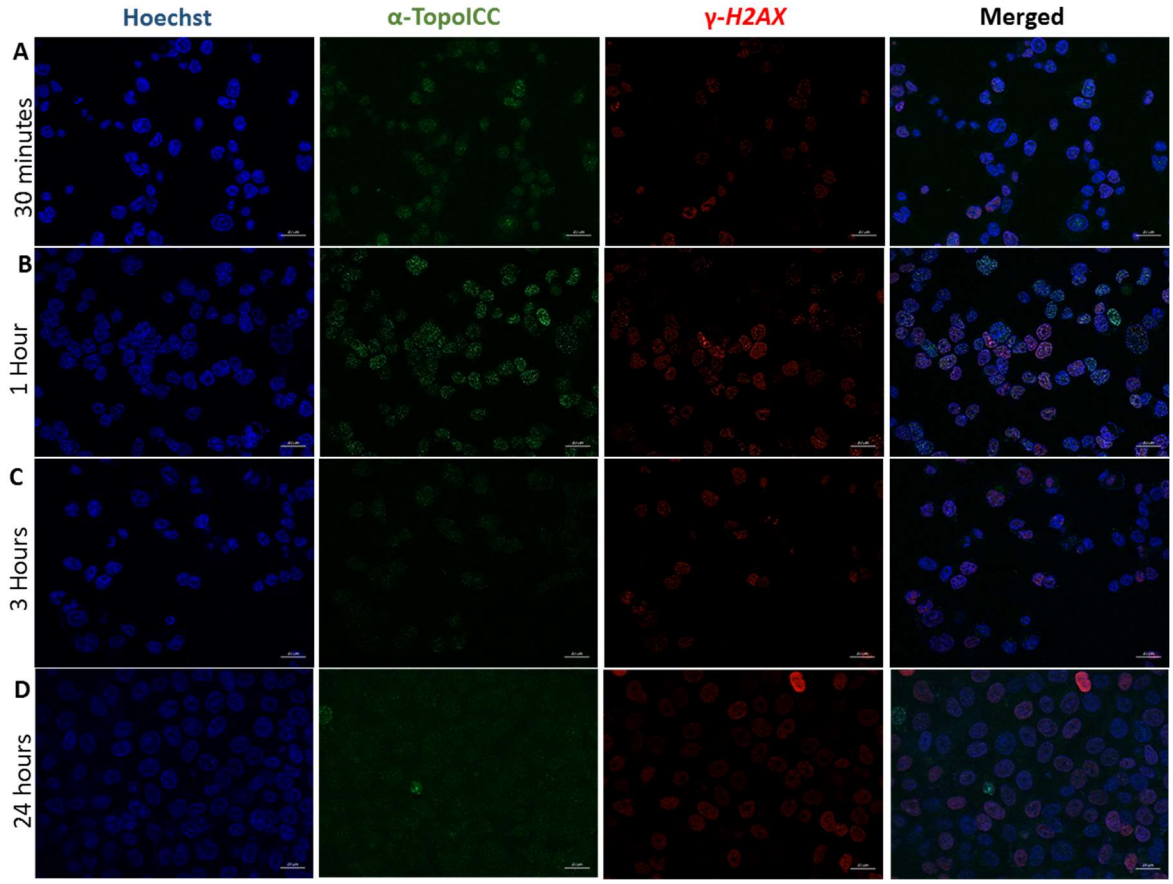

Figure B.4 Detection of topo I-DNA covalent complexes by fluorescence microscopy in HCT116 cells (2D). Time-course experiment after treatment with SN-38 at previously determined IC_{50} concentrations. HCT116 cells were fixed, permeabilised, incubated with SDS and stained with α-TopoIcc antibody (green), γ-H2AX (red) and Hoechst 33258 (blue). Images were taken on a Zeiss inverse Axio observer confocal microscope (Zeiss LSM 710, Carl Zeiss) using an x40 objective with apotome. Scale bars represent 20µm.

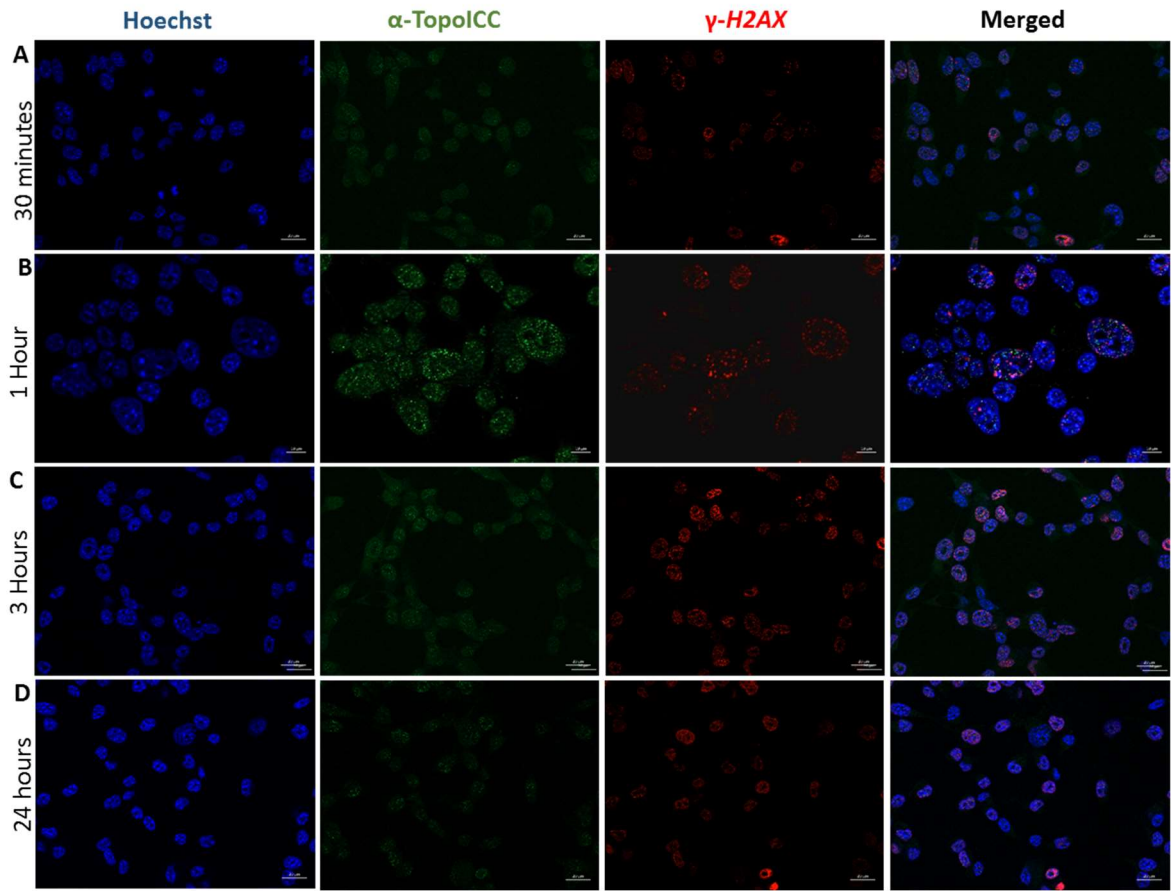

Figure B.5 Detection of topo I-DNA covalent complexes by fluorescence microscopy in CT26 cells (2D). Time-course experiment after treatment with SN-38 at previously determined IC_{50} concentrations. CT26 cells were fixed, permeabilised, incubated with SDS and stained with α-TopoIcc antibody (green), γ-H2AX (red) and Hoechst 33258 (blue). Images were taken on a Zeiss inverse Axio observer confocal microscope (Zeiss LSM 710, Carl Zeiss) using an x40 objective with apotome. Scale bars represent 20µm.

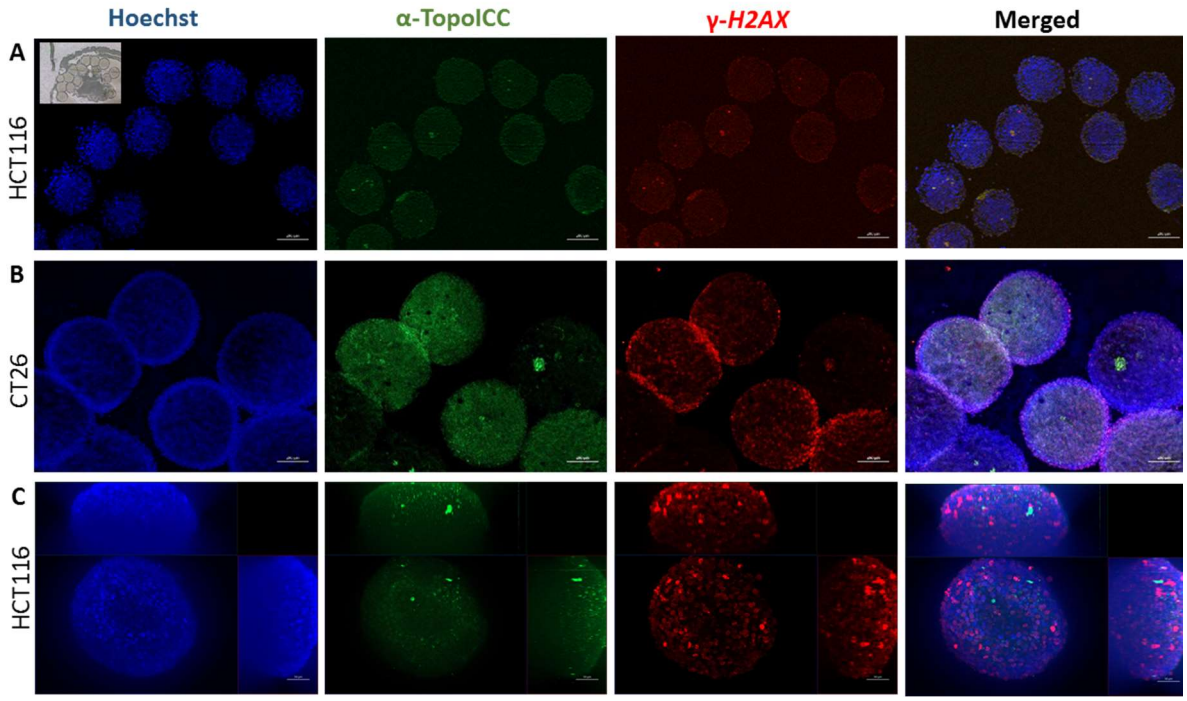

Figure B.6 Detection of topo I-DNA covalent complexes by fluorescence microscopy in microscopy following irinotecan treatment in 3D. After treatment for 24 hours with irinotecan at previously determined IC_{50} concentrations or a nominal concentration of 100µM (**A/C**) HCT116 and (**B**) CT26 spheroids were fixed, permeabilised, incubated with SDS and stained with α-TopoIcc antibody (green), γ-H2AX (red) and Hoechst 33258 (blue). Images A and B are spheroid sections and were taken on a Zeiss inverse Axio observer confocal microscope (Zeiss LSM 710, Carl Zeiss) using an x5 objective with apotome. Scale bars represent 100µm. For maximum intensity projection images were taken of a whole-mount spheroid using an x20 objective. Scale bars represent 50µm.

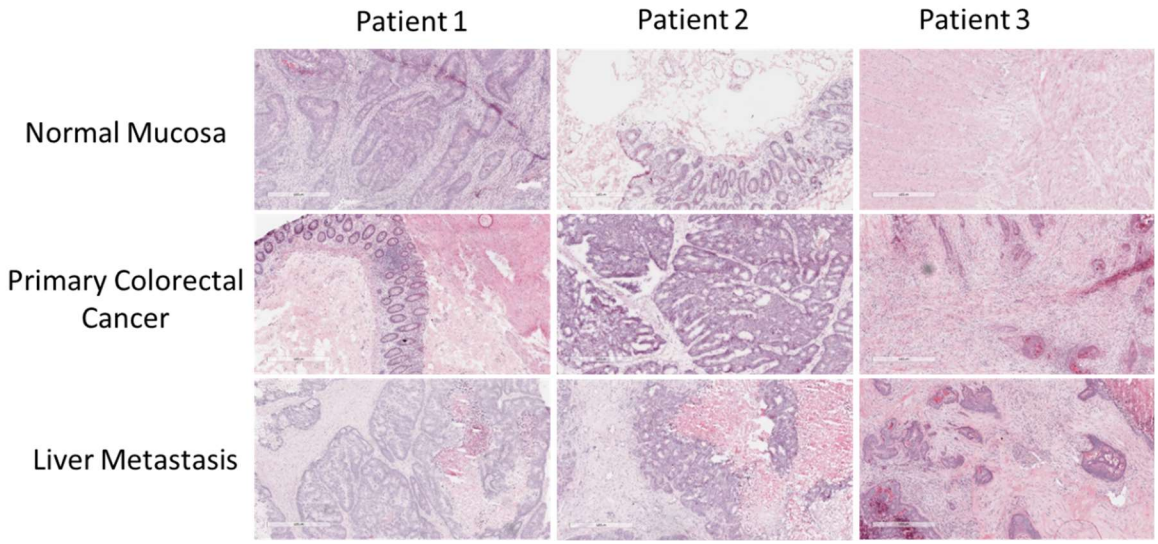

Figure B.7 Histological assessment of human tissue samples. Tissue samples from three patients were stained with H&E. Slides were scanned with the Leica Aperio CS2 Slide Scanner. Images were then processed using the ImageScope software. Scale bars shown represent 500µm.

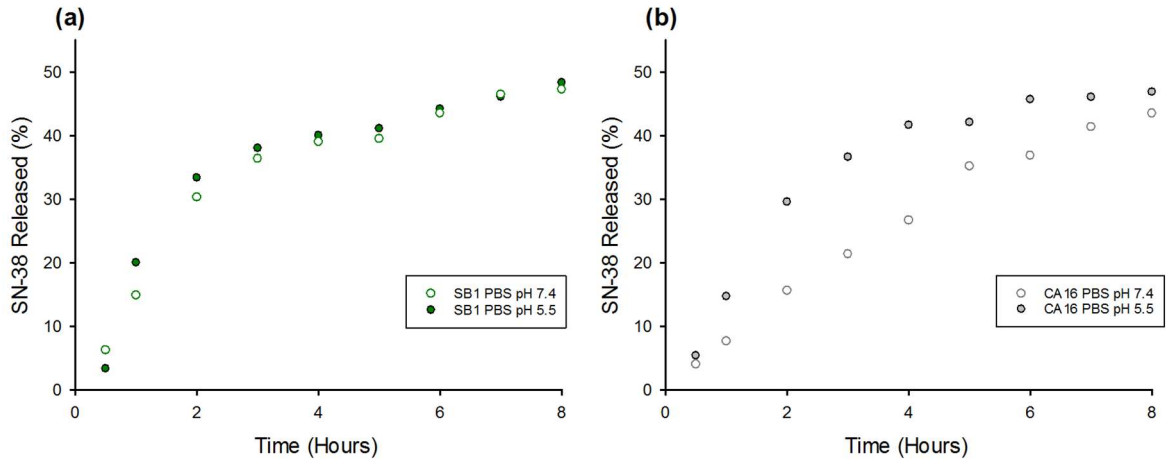

Figure B.8 Drug release profiles SN-38 loaded nanoparticles, **(a)** SB1 and **(b)** CA16, in phosphate-buffered saline at pH 5.5.

.

(a) SB1

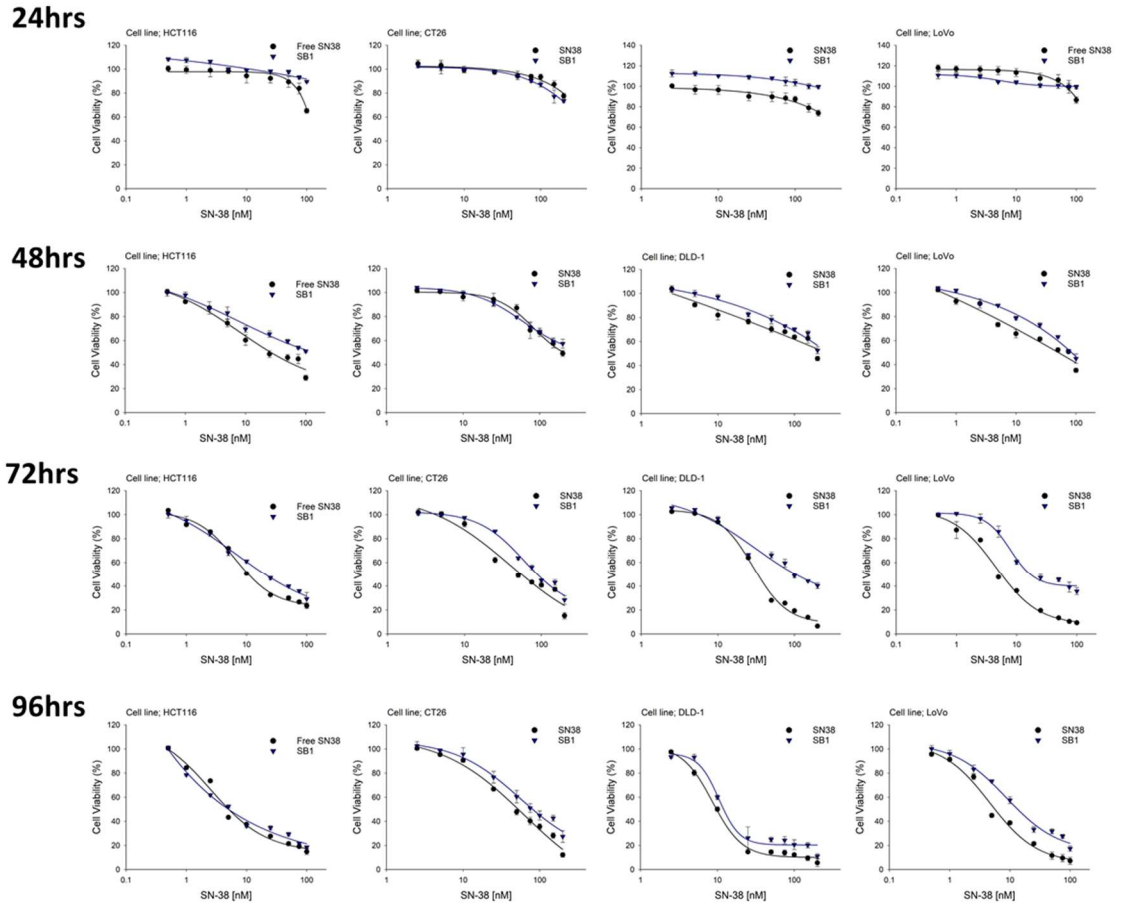
24hrs
48hrs
72hrs
96hrs
Cell line; HCT116
Cell line; CT26
Cell line; DLD-1
Cell line; LoVo
Free SN38
SN38
SB1
Cell Viability (%)
SN-38 [nM]

(b) SB2

24hrs

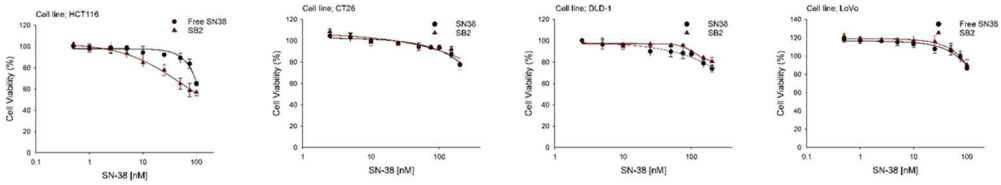

48hrs

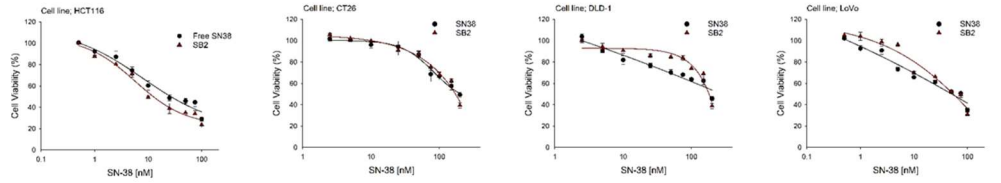

72hrs

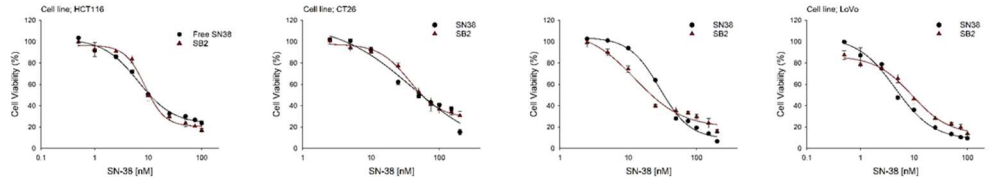

96hrs

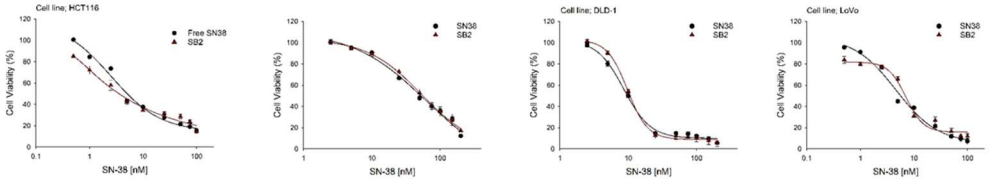

(c) SB3

24hrs

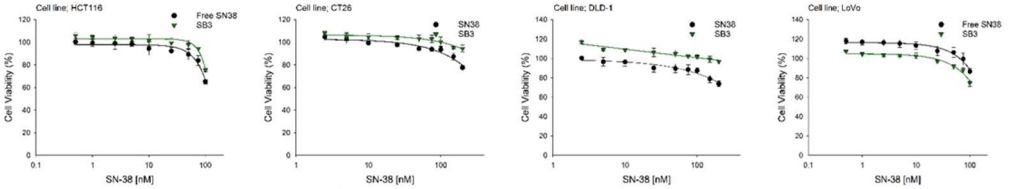

48hrs

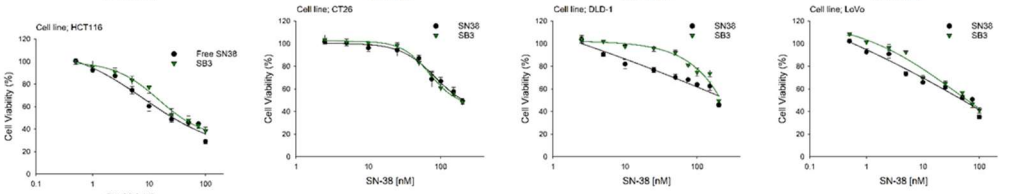

72hrs

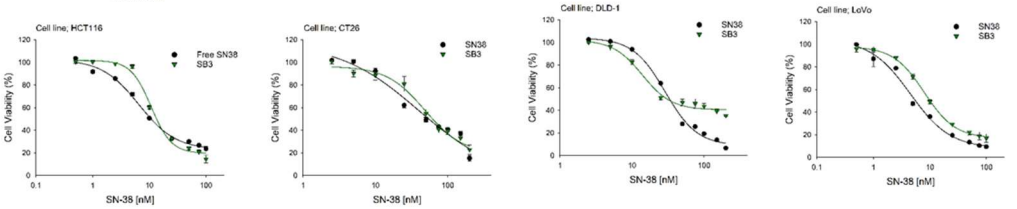

96hrs

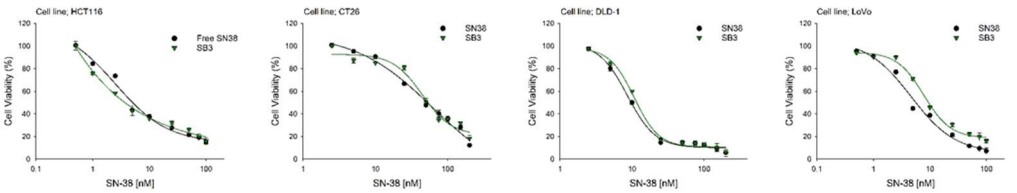

(d) SB7

24hrs

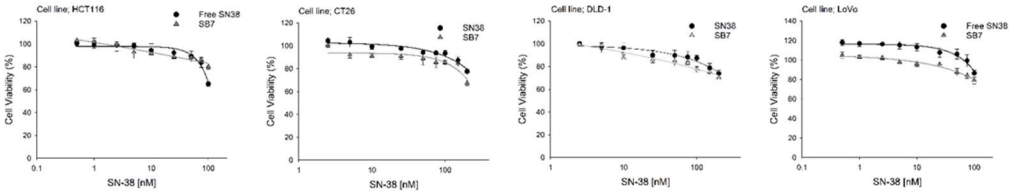

48hrs

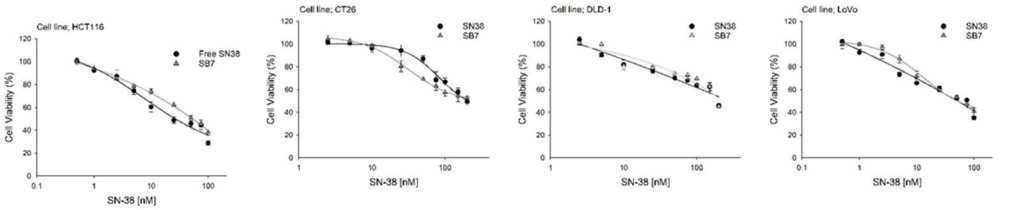

72hrs

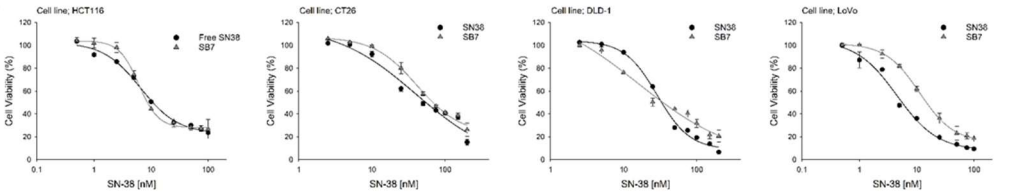

96hrs

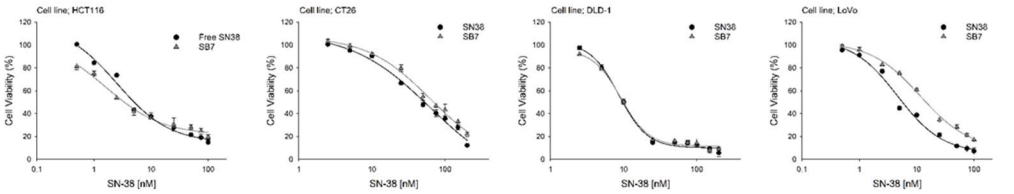

(e) SB8

24hrs

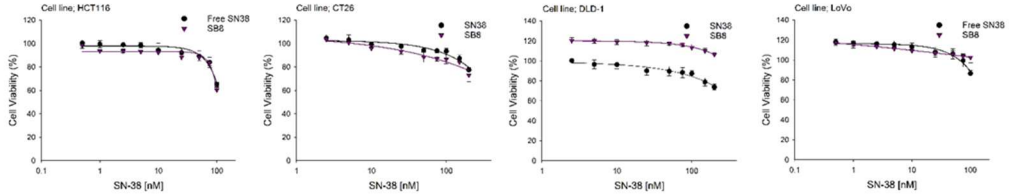

48hrs

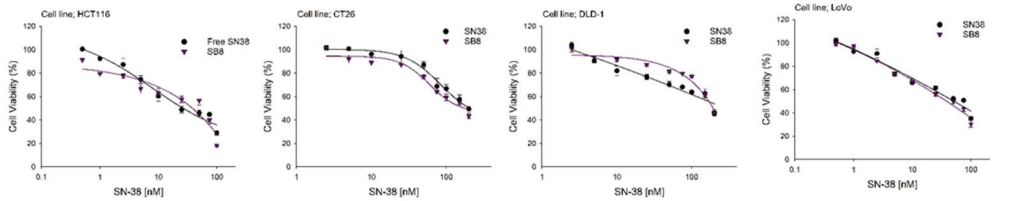

72hrs

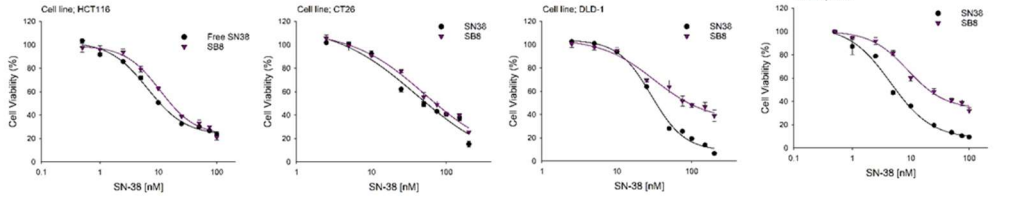

96hrs

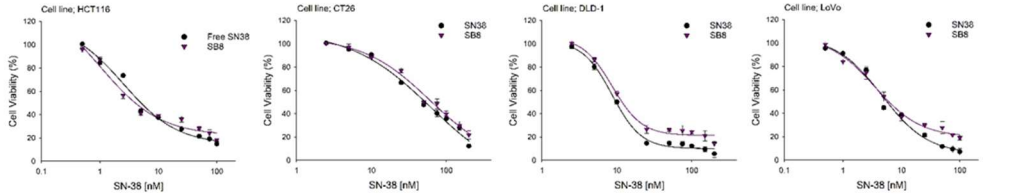

(f) CA1

24hrs

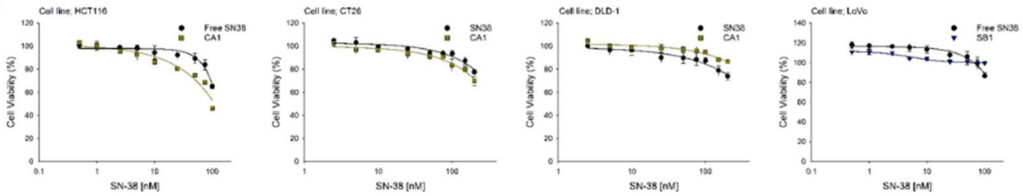

48hrs

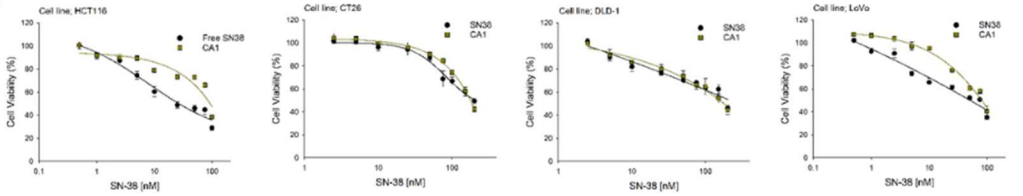

72hrs

96hrs

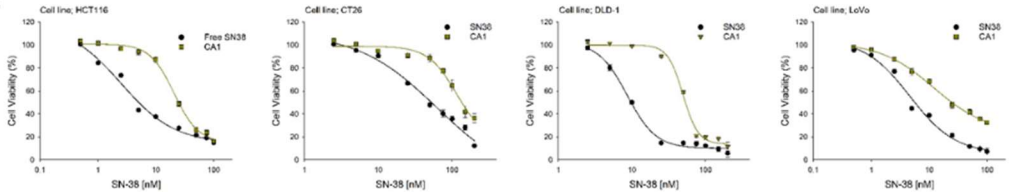

(g) CA14

24hrs

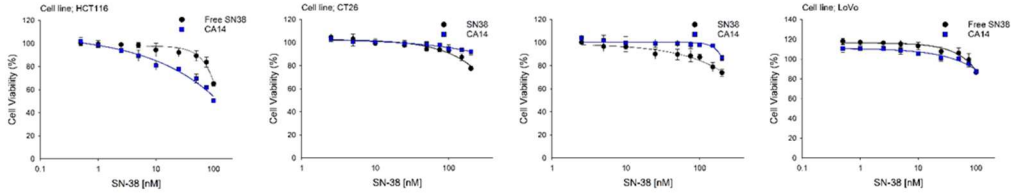

48hrs

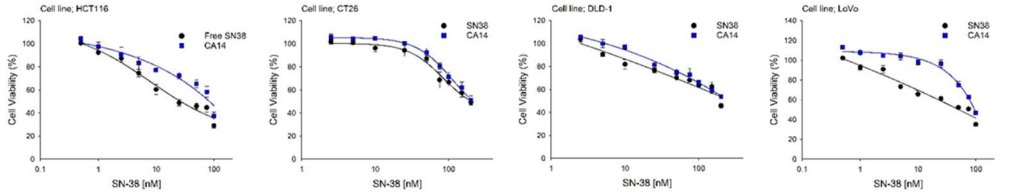

72hrs

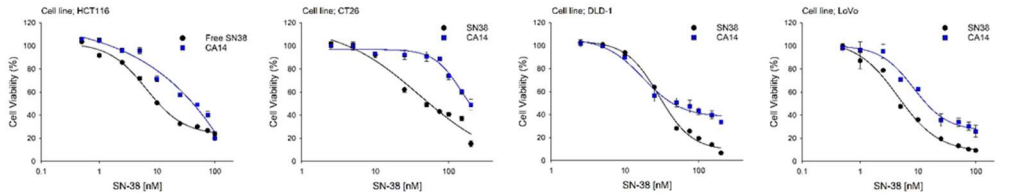

96hrs

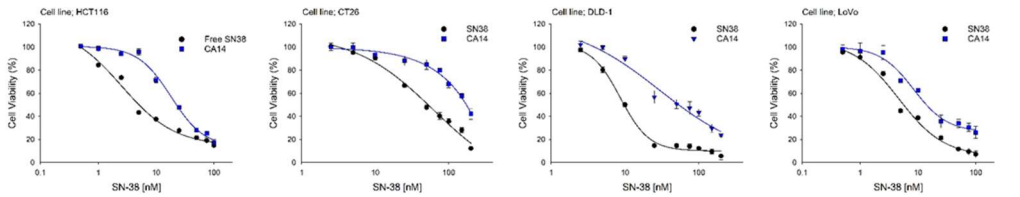

(h) CA16

24hrs

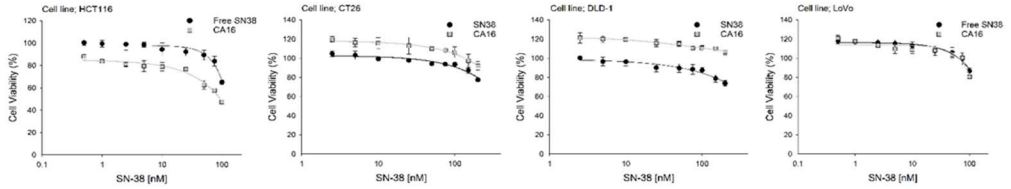

48hrs

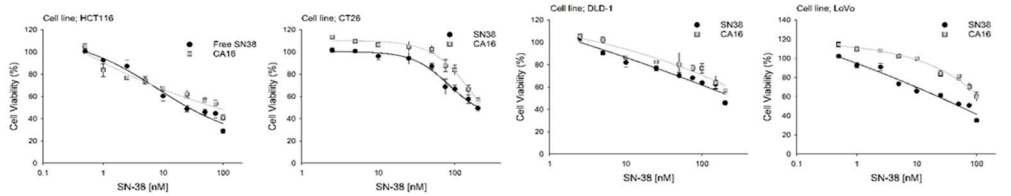

72hrs

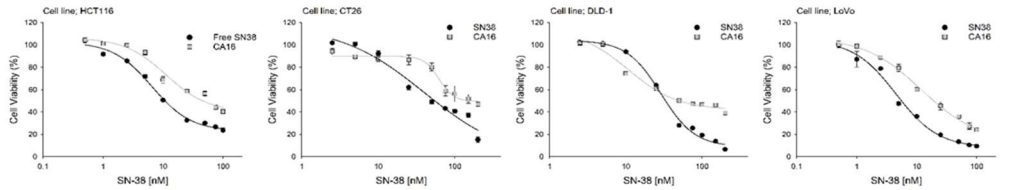

96hrs

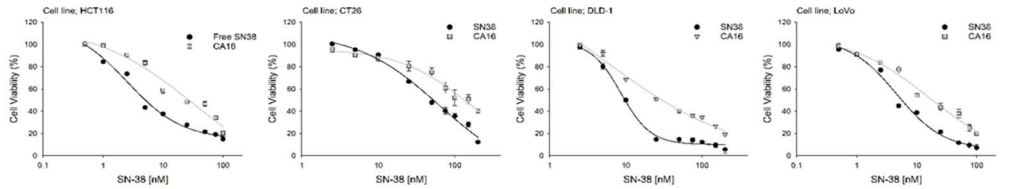

(i) CA18

24hrs

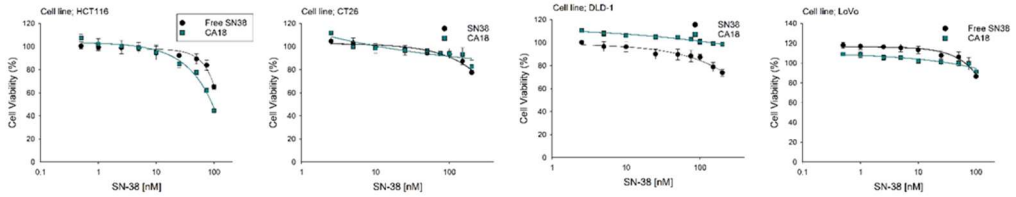

48hrs

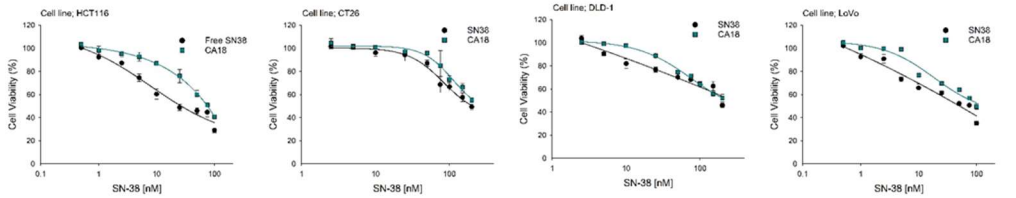

72hrs

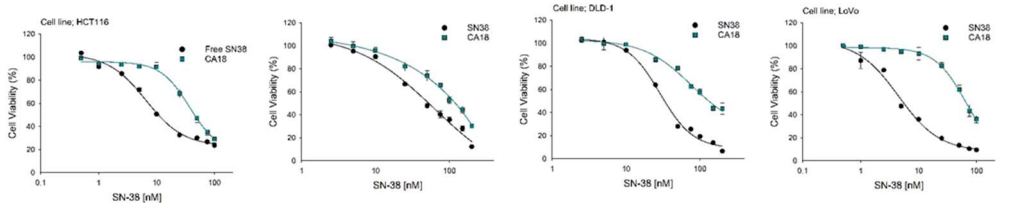

96hrs

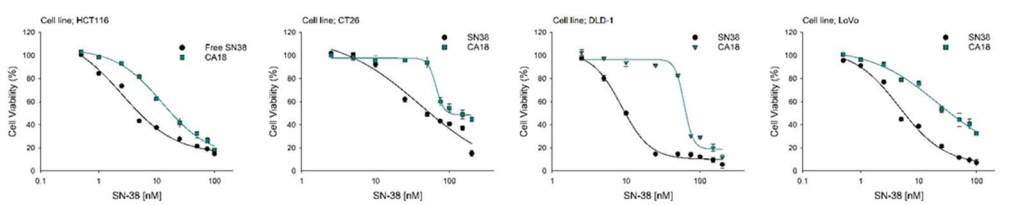

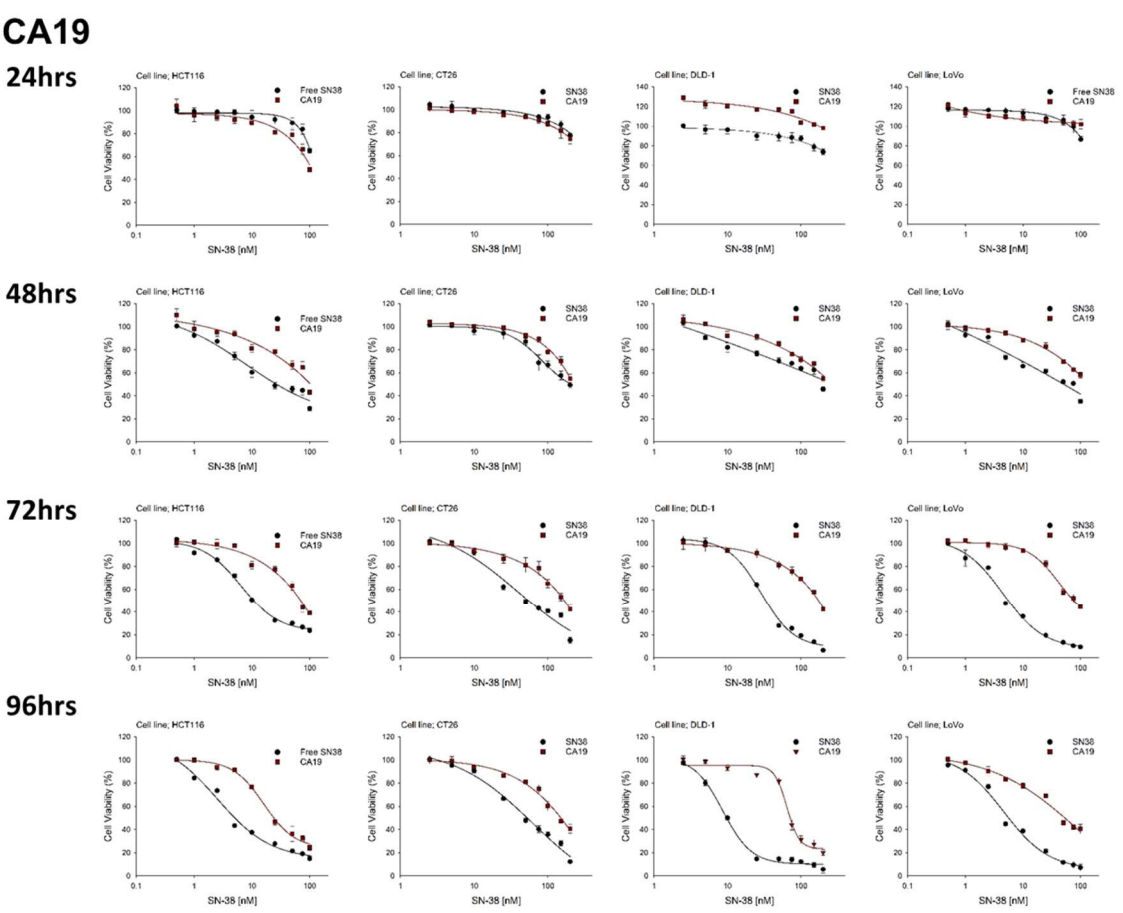

Figure B.9 Concentration-response curves for monolayer cells treated with select polymer nanomaterial's. ATP levels were measured in monolayer (2D) cells treated with **(a)** SB1, **(b)** SB2, **(c)** SB3, **(d)** SB7, **(e)** SB8, **(f)** CA1, **(g)** CA14, **(h)** CA16, **(i)** CA18 and **(j)** CA19 [nM], between 24-72 hours (n=3 using 6 technical replicates, Average ± %SD). Cell viability was calculated as a percentage of untreated vehicle control samples (blank nanoparticles in H_2O – 0.1%).

(a) SB2

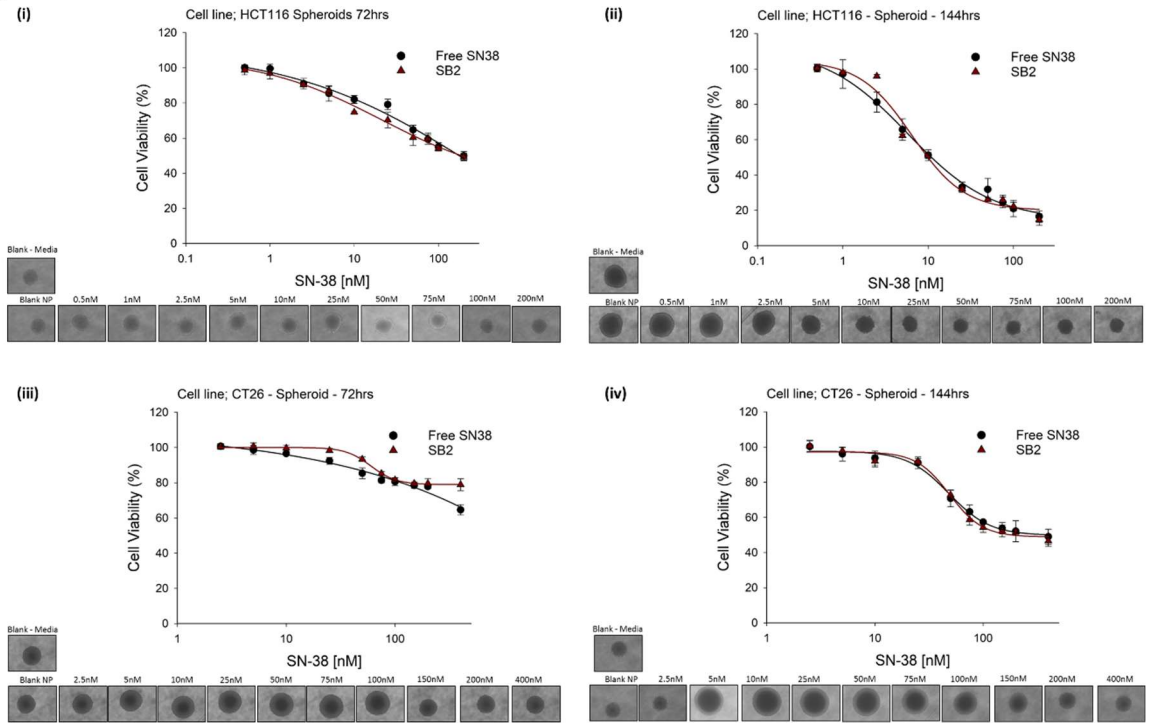
(i)
Cell line; HCT116 Spheroids 72hrs
Free SN38
SB2
Cell Viability (%)
SN-38 [nM]
Blank - Media
Blank NP
0.5nM
1nM
2.5nM
5nM
10nM
25nM
50nM
75nM
100nM
200nM
(ii)
Cell line; HCT116 - Spheroid - 144hrs
(iii)
Cell line; CT26 - Spheroid - 72hrs
150nM
400nM
(iv)
Cell line; CT26 - Spheroid - 144hrs

(b) SB3

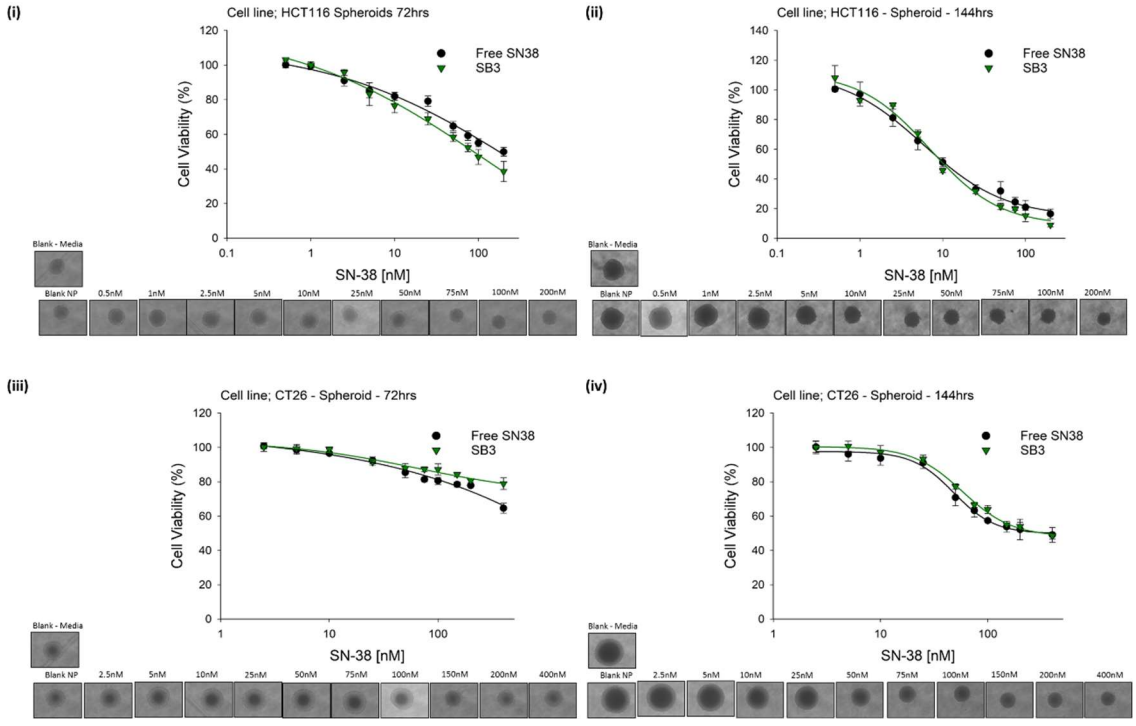
(i)
Cell line; HCT116 Spheroids 72hrs
Free SN38
SB3
Cell Viability (%)
SN-38 [nM]
Blank - Media
Blank NP
0.5nM
1nM
2.5nM
5nM
10nM
25nM
50nM
75nM
100nM
200nM
(ii)
Cell line; HCT116 - Spheroid - 144hrs
(iii)
Cell line; CT26 - Spheroid - 72hrs
150nM
400nM
(iv)
Cell line; CT26 - Spheroid - 144hrs

(c) SB7

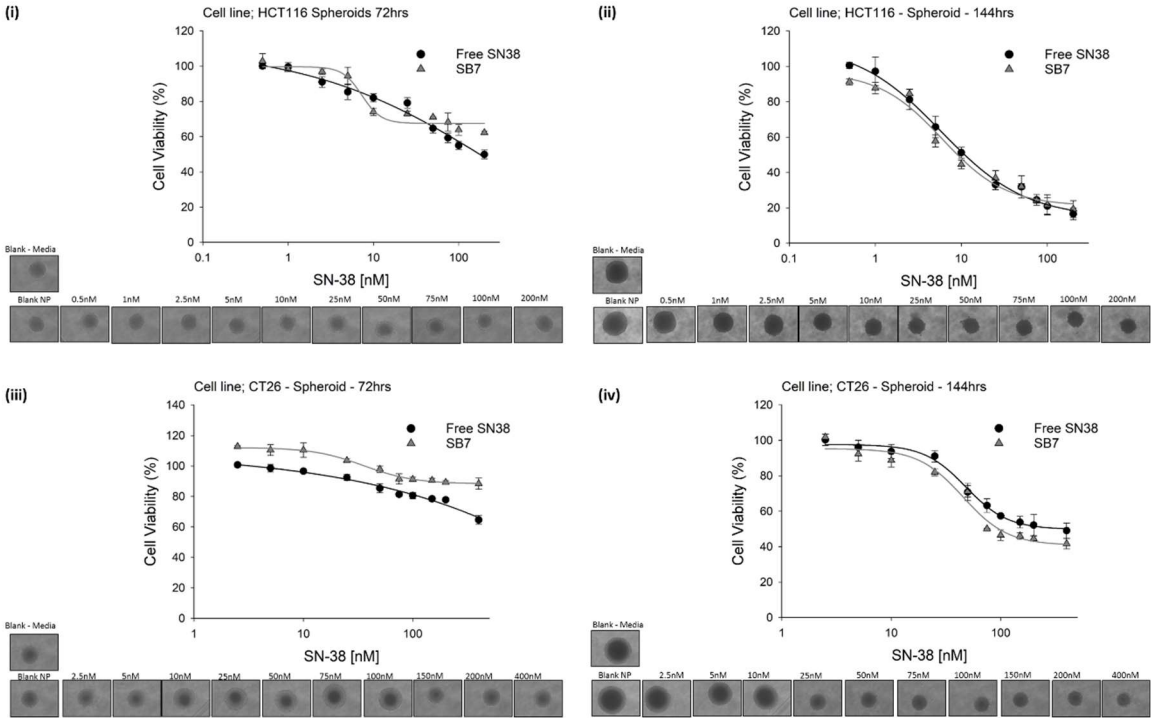
(i)
Cell line; HCT116 Spheroids 72hrs
Free SN38
SB7
Cell Viability (%)
SN-38 [nM]
Blank - Media
Blank NP
0.5nM
1nM
2.5nM
5nM
10nM
25nM
50nM
75nM
100nM
200nM
(ii)
Cell line; HCT116 - Spheroid - 144hrs
Free SN38
SB7
Cell Viability (%)
SN-38 [nM]
Blank - Media
Blank NP
0.5nM
1nM
2.5nM
5nM
10nM
25nM
50nM
75nM
100nM
200nM
(iii)
Cell line; CT26 - Spheroid - 72hrs
Free SN38
SB7
Cell Viability (%)
SN-38 [nM]
Blank - Media
Blank NP
2.5nM
5nM
10nM
25nM
50nM
75nM
100nM
150nM
200nM
400nM
(iv)
Cell line; CT26 - Spheroid - 144hrs
Free SN38
SB7
Cell Viability (%)
SN-38 [nM]
Blank - Media
Blank NP
2.5nM
5nM
10nM
25nM
50nM
75nM
100nM
150nM
200nM
400nM

(d) SB8

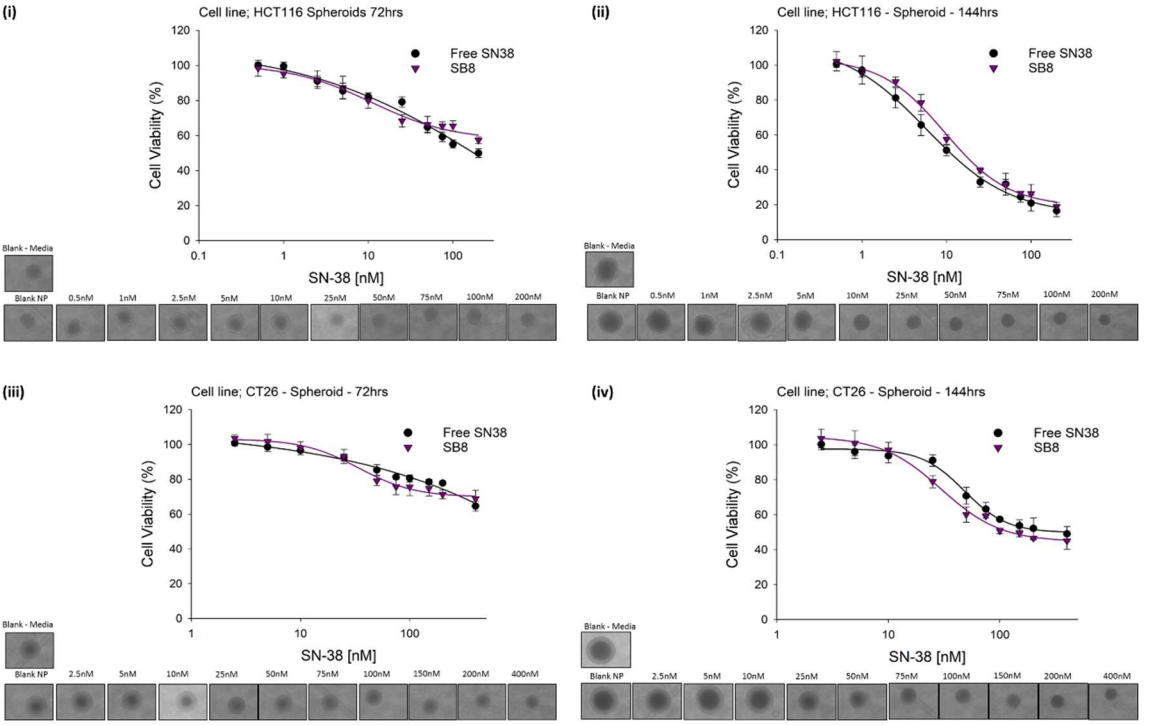
(i)
Cell line; HCT116 Spheroids 72hrs
Free SN38
SB8
Cell Viability (%)
SN-38 [nM]
Blank - Media
Blank NP
0.5nM
1nM
2.5nM
5nM
10nM
25nM
50nM
75nM
100nM
200nM
(ii)
Cell line; HCT116 - Spheroid - 144hrs
Free SN38
SB8
Cell Viability (%)
SN-38 [nM]
Blank - Media
Blank NP
0.5nM
1nM
2.5nM
5nM
10nM
25nM
50nM
75nM
100nM
200nM
(iii)
Cell line; CT26 - Spheroid - 72hrs
Free SN38
SB8
Cell Viability (%)
SN-38 [nM]
Blank - Media
Blank NP
2.5nM
5nM
10nM
25nM
50nM
75nM
100nM
150nM
200nM
400nM
(iv)
Cell line; CT26 - Spheroid - 144hrs
Free SN38
SB8
Cell Viability (%)
SN-38 [nM]
Blank - Media
Blank NP
2.5nM
5nM
10nM
25nM
50nM
75nM
100nM
150nM
200nM
400nM

(e) CA1

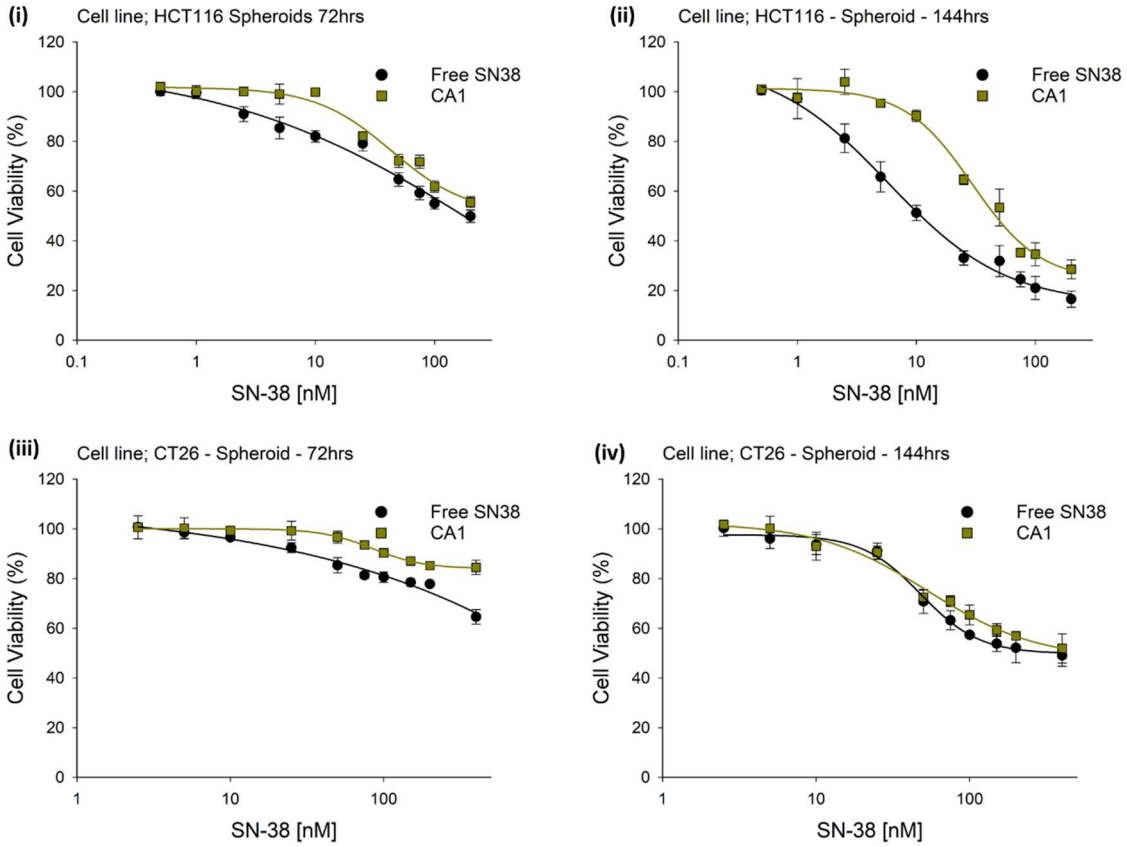
(i)
Cell line; HCT116 Spheroids 72hrs
(ii)
Cell line; HCT116 - Spheroid - 144hrs
(iii)
Cell line; CT26 - Spheroid - 72hrs
(iv)
Cell line; CT26 - Spheroid - 144hrs
Free SN38
CA1
Cell Viability (%)
SN-38 [nM]

(f) CA14

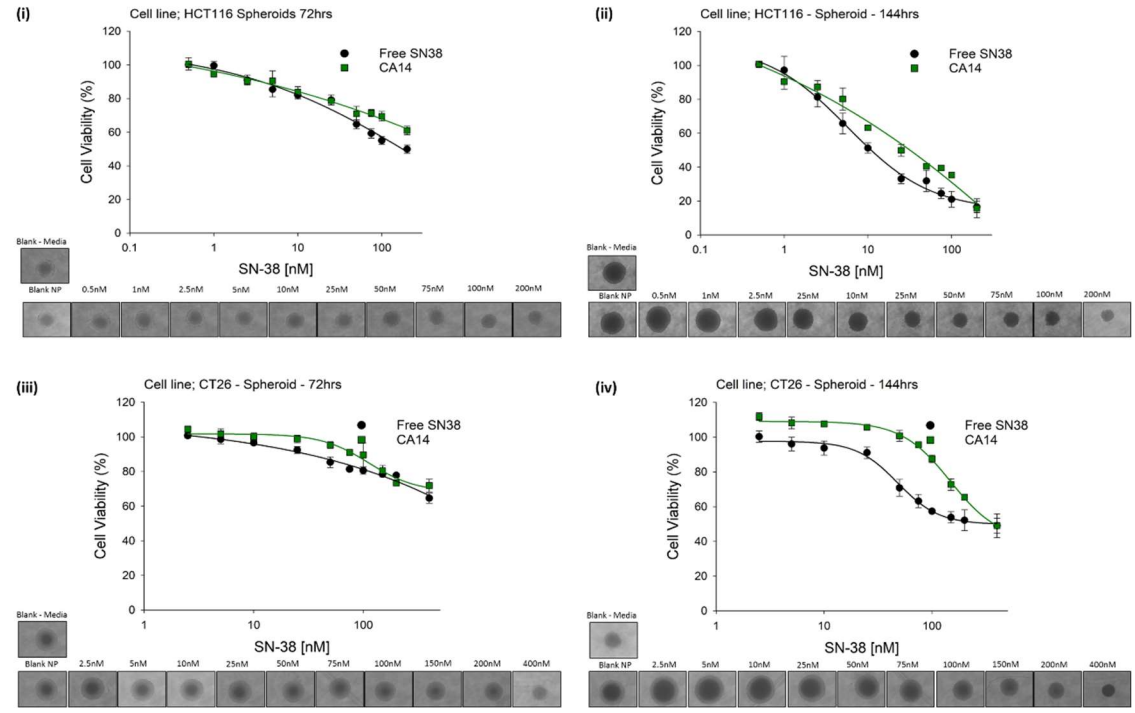
(i)
Cell line; HCT116 Spheroids 72hrs
(ii)
Cell line; HCT116 - Spheroid - 144hrs
(iii)
Cell line; CT26 - Spheroid - 72hrs
(iv)
Cell line; CT26 - Spheroid - 144hrs
Free SN38
CA14
Cell Viability (%)
SN-38 [nM]
Blank - Media
Blank NP

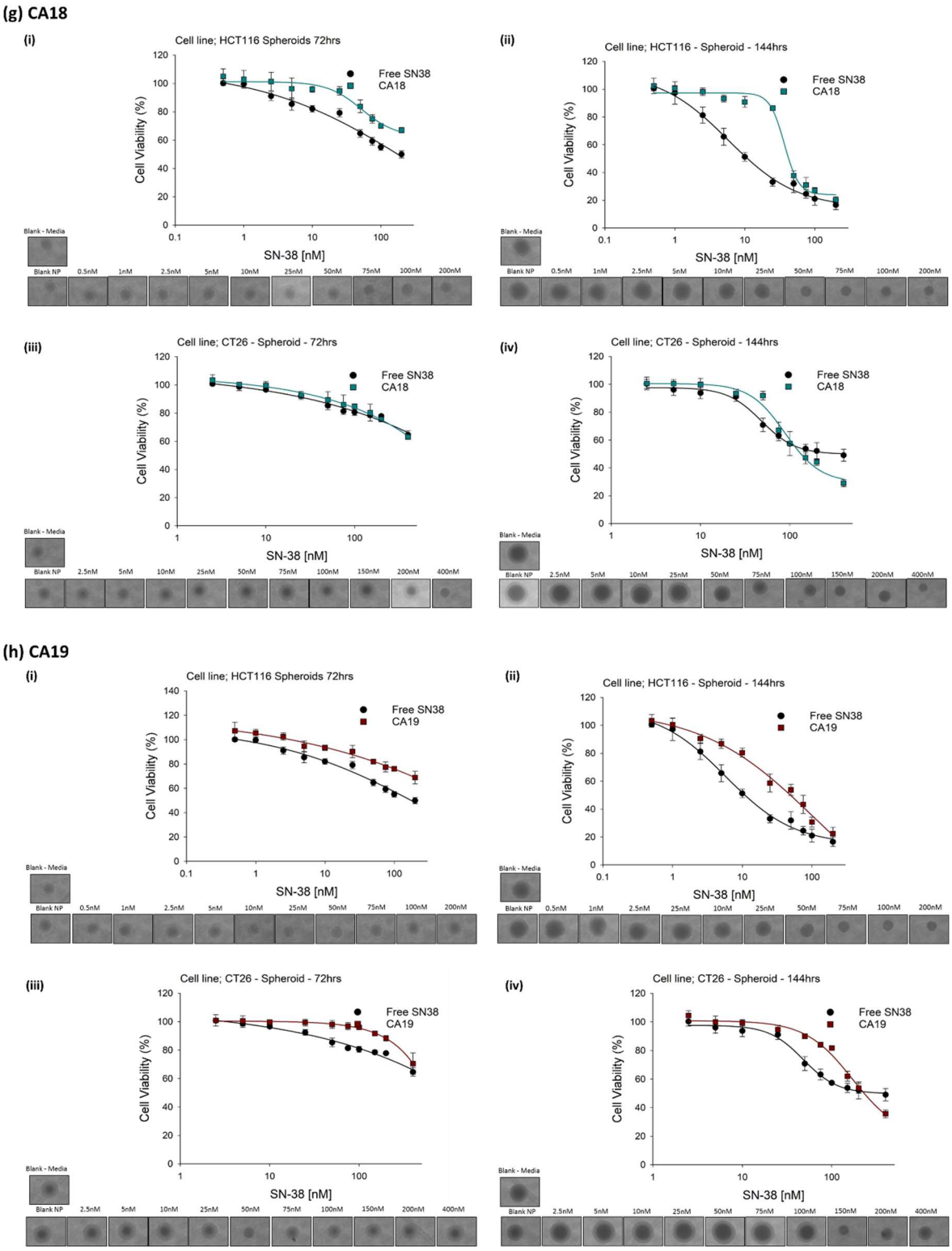

Figure B.10 ATP levels were measured in HCT116 and CT26 spheroids treated with SN-38 or **(a)** SB2, **(b)** SB3, **(c)** SB7, **(d)** SB8, **(e)** CA1 **(f)** CA14, **(g)** CA18 and **(h)** CA19 NPs, for 72 (**i** and **iii**) or 144 hours (**ii** and **iv**). Cell viability was calculated as a percentage of untreated vehicle control (DMSO – 0.1% or blank NP samples). Representative phase-contrast images (10x objective) are documented to capture spheroid integrity following treatment with SB1. Data points are means ± SD, with n=6 individual spheroids per condition.

Table B.2 SN-38 pharmacokinetic parameters after intravenous administration of irinotecan in BALB/c mice

Parameter	Unit	Value
Lambda_z	1/h	0.719390582
t1/2	h	0.963519954
Tmax	h	0.5
Cmax	ng/ml	1189.407127
C0	ng/ml	801.9322051
Clast_obs/Cmax		0.031903685
AUC 0-t	ng/ml*h	2478.134565
AUC 0-inf_obs	ng/ml*h	2530.882642
AUC 0-t/0-inf_obs		0.979158229
AUMC 0-inf_obs	ng/ml*h^2	3753.363652
MRT 0-inf_obs	h	1.483025562
Vz_obs	(mg/kg)/(ng/ml)	0.021969655
Cl_obs	(mg/kg)/(ng/ml)/h	0.015804763
Vss_obs	(mg/kg)/(ng/ml)	0.023438867

Table B.3 SN-38 pharmacokinetic parameters after intravenous administration of SN-38 in BALB/c mice

Parameter	Unit	Value
Lambda_z	1/h	0.346483553
t1/2	h	2.000519719
Tmax	h	0.08333
Cmax	ng/ml	7.410866071
C0	ng/ml	8.191211344
Clast_obs/Cmax		0.185840068
AUC 0-t	ng/ml*h	12.51392937
AUC 0-inf_obs	ng/ml*h	16.4888247
AUC 0-t/0-inf_obs		0.758933981
AUMC 0-inf_obs	ng/ml*h^2	52.02464282
MRT 0-inf_obs	h	3.155145606
Vz_obs	(mg/kg)/(ng/ml)	0.350072237
Cl_obs	(mg/kg)/(ng/ml)/h	0.121294273
Vss_obs	(mg/kg)/(ng/ml)	0.382701092

Table B.4 SN-38 pharmacokinetic parameters after intravenous administration of SB1 in BALB/c mice

Parameter	Unit	Value
Lambda_z	1/h	0.18494123
t1/2	h	3.747932144
Tmax	h	0.25
Cmax	ng/ml	388.6866014
C0	ng/ml	336.2519704
Clast_obs/Cmax		0.011463756
AUC 0-t	ng/ml*h	170.6280618
AUC 0-inf_obs	ng/ml*h	194.7211667
AUC 0-t/0-inf_obs		0.876268691
AUMC 0-inf_obs	ng/ml*h^2	266.1092272
MRT 0-inf_obs	h	1.366616849
Vz_obs	(mg/kg)/(ng/ml)	0.055537086
Cl_obs	(mg/kg)/(ng/ml)/h	0.010271097
Vss_obs	(mg/kg)/(ng/ml)	0.014036654

Table B.5 SN-38 pharmacokinetic parameters after intravenous administration of CA16 in BALB/c mice

Parameter	Unit	Value
Lambda_z	1/h	0.234685946
t1/2	h	2.953509535
Tmax	h	0.0833
Cmax	ng/ml	47.97942206
C0	ng/ml	122.0050613
Clast_obs/Cmax		0.067072534
AUC 0-t	ng/ml*h	37.00648474
AUC 0-inf_obs	ng/ml*h	50.71885842
AUC 0-t/0-inf_obs		0.729639544
AUMC 0-inf_obs	ng/ml*h^2	178.5947928
MRT 0-inf_obs	h	3.521269965
Vz_obs	(mg/kg)/(ng/ml)	0.168024821
Cl_obs	(mg/kg)/(ng/ml)/h	0.039433064
Vss_obs	(mg/kg)/(ng/ml)	0.138854465

Table B.6 SN-38 glucuronide pharmacokinetic parameters after intravenous administration of irinotecan in BALB/c mice

Parameter	Unit	Value
Lambda_z	1/h	0.367042549
t1/2	h	1.88846547
Tmax	h	0.5
Cmax	ng/ml	266.4015067
C0	ng/ml	186.1051998
Clast_obs/Cmax		0.131020915
AUC 0-t	ng/ml*h	521.2600514
AUC 0-inf_obs	ng/ml*h	616.3557543
AUC 0-t/0-inf_obs		0.845712963
AUMC 0-inf_obs	ng/ml*h^2	1503.670297
MRT 0-inf_obs	h	2.439614276
Vz_obs	(mg/kg)/(ng/ml)	0.176812158
Cl_obs	(mg/kg)/(ng/ml)/h	0.064897585
Vss_obs	(mg/kg)/(ng/ml)	0.158325075

Table B.7 SN-38 glucuronide pharmacokinetic parameters after intravenous administration of SB1 in BALB/c mice

Parameter	Unit	Value
Lambda_z	1/h	0.329293685
t1/2	h	2.104951331
Tmax	h	0.25
Cmax	ng/ml	435.353171
C0	ng/ml	328.8925898
Clast_obs/Cmax		0.043130541
AUC 0-t	ng/ml*h	266.9049856
AUC 0-inf_obs	ng/ml*h	323.9270865
AUC 0-t/0-inf_obs		0.823966246
AUMC 0-inf_obs	ng/ml*h^2	498.8347173
MRT 0-inf_obs	h	1.53995988
Vz_obs	(mg/kg)/(ng/ml)	0.018749916
Cl_obs	(mg/kg)/(ng/ml)/h	0.006174229
Vss_obs	(mg/kg)/(ng/ml)	0.009508065

Table B.8 SN-38 glucuronide pharmacokinetic parameters after intravenous administration of CA16 in BALB/c mice

Parameter	Unit	Value
Lambda_z	1/h	0.09433441
t1/2	h	7.347766103
Tmax	h	0.5
Cmax	ng/ml	15.38037915
C0	ng/ml	9.977672081
Clast_obs/Cmax		0.257717227
AUC 0-t	ng/ml*h	37.55547812
AUC 0-inf_obs	ng/ml*h	79.57395956
AUC 0-t/0-inf_obs		0.471956885
AUMC 0-inf_obs	ng/ml*h^2	724.6456589
MRT 0-inf_obs	h	9.106567813
Vz_obs	(mg/kg)/(ng/ml)	0.266433536
Cl_obs	(mg/kg)/(ng/ml)/h	0.02513385
Vss_obs	(mg/kg)/(ng/ml)	0.228883114

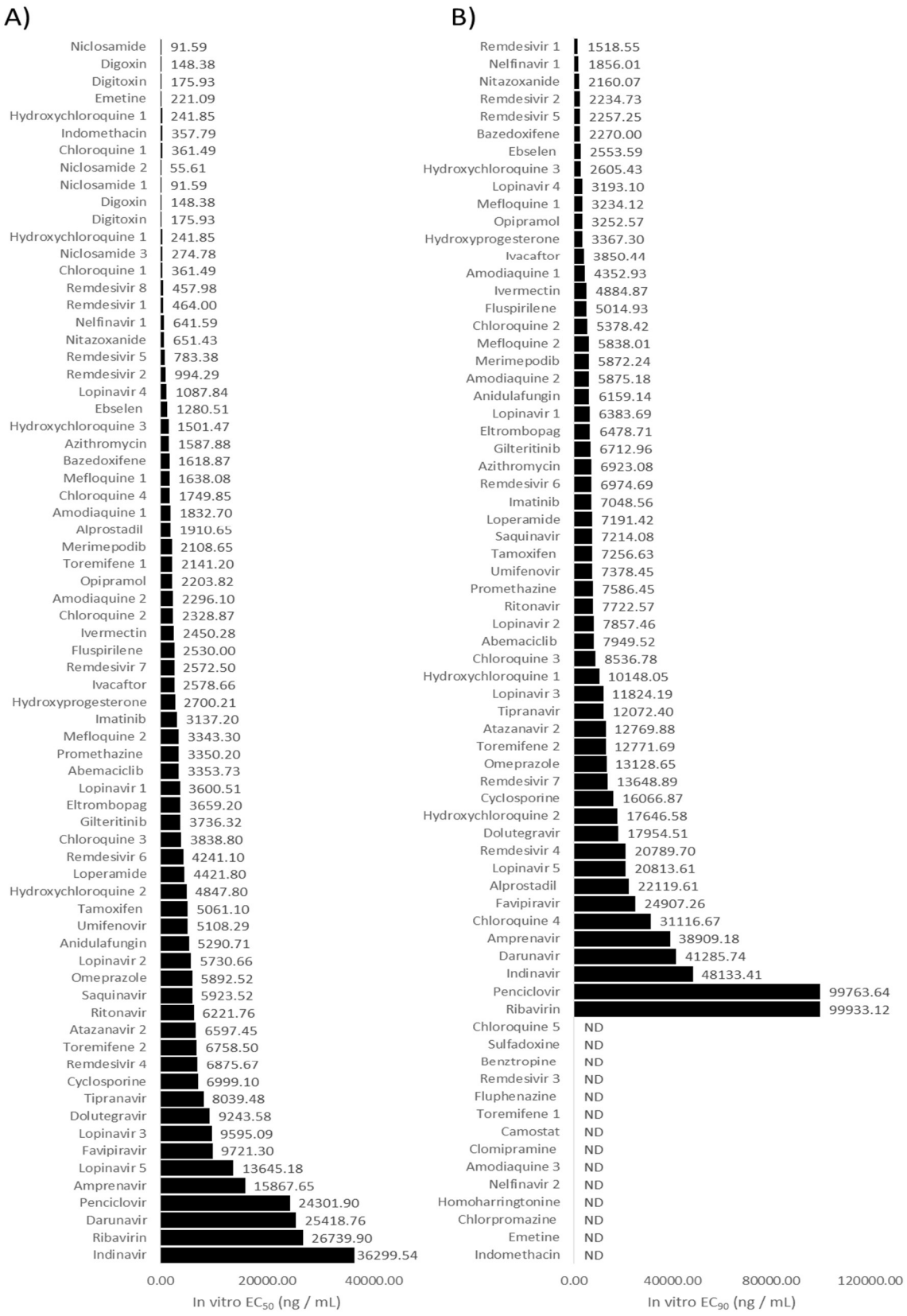

Figure B.11 Reported EC_{50} and EC_{90} derived from *in vitro* anti-SARS-CoV-2 activity data. **(A)** The reported EC_{50} values of various drugs against SARS-CoV-2 ranked from most potent to least potent **(B)** The recalculated EC_{90} values of various drugs against SARS-CoV-2 ranked from most potent to least potent.

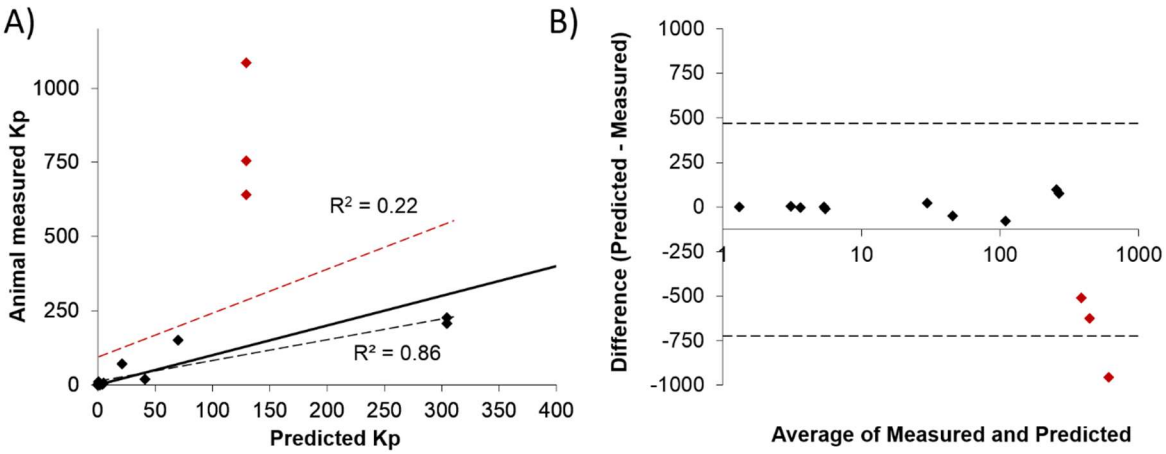

Figure B.12 (A) Scatter plot showing linear regression for predicted and measured lung K_p. Data are presented with (red) and without chloroquine (black). **(B)** A Bland-Altman plot displaying the relative differences of predicted and measured lung Kp for the 13 drugs for which previously reported animal lung concentrations were available. The 95% limits of agreement, defined as the mean difference plus and minus 2 times the standard deviation of the differences, are shown as dashed horizontal lines. The data points highlighted in red are for chloroquine.

Table B.9 Data used for deriving predicted Kp and KpU tissue concentrations

Drug name	pKa1	pKa2	logPow	logPvow	fu	BP ratio	Acid base type	Ref	Lung Kp	Kidney Kp	Gut Kp	Bone Kp	Brain Kp	Heart Kp	Liver Kp	Muscle Kp	Pancreas Kp	Skin Kp	Spleen Kp	Thymus Kp	Lung KpU	Kidney KpU	Gut KpU	Bone KpU	Brain KpU	Heart KpU	Liver KpU	Muscle KpU	Pancreas KpU	Skin KpU	Spleen KpU	Thymus KpU
Abemaciclib	8	NA	4.25	NA	0.035	1	monoprotic_base	Drugbank	11.62	13.30	10.39	3.71	5.86	6.98	12.45	4.87	9.03	10.58	8.19	7.45	331.93	379.87	296.84	105.94	167.35	199.38	355.81	139.10	257.90	302.27	234.04	212.94
Alprostadil	4.85	NA	3.2	NA	0.07	NA	monoprotic_acid	Drugbank	0.24	0.16	0.19	0.12	0.09	0.19	0.11	0.09	0.10	0.31	0.12	0.10	3.44	2.28	2.75	1.65	1.22	2.66	1.62	1.27	1.37	4.45	1.77	1.48
Amodiaquine 1	10.2	NA	2.3	NA	0.1	0.91	monoprotic_base	Drugbank, PubChem, LSTM internal determination	9.34	11.98	5.82	1.67	1.11	5.44	10.89	3.77	4.11	3.22	7.65	5.58	93.44	119.81	58.18	16.73	11.14	54.40	108.87	37.69	41.08	32.18	76.47	55.83
Amodiaquine 2	10.2	NA	2.3	NA	0.1	0.91	monoprotic_base	Drugbank, PubChem, LSTM internal determination	9.34	11.98	5.82	1.67	1.11	5.44	10.89	3.77	4.11	3.22	7.65	5.58	93.44	119.81	58.18	16.73	11.14	54.40	108.87	37.69	41.08	32.18	76.47	55.83
Amodiaquine 3	10.2	NA	2.3	NA	0.1	0.91	monoprotic_base	Drugbank, PubChem, LSTM internal determination (	9.34	11.98	5.82	1.67	1.11	5.44	10.89	3.77	4.11	3.22	7.65	5.58	93.44	119.81	58.18	16.73	11.14	54.40	108.87	37.69	41.08	32.18	76.47	55.83
Amprenavir	NA	NA	2.14	NA	0.1	NA	neutral	Drugbank	0.57	0.46	0.77	0.33	0.66	0.45	0.50	0.29	0.72	1.00	0.40	0.41	5.72	4.62	7.67	3.35	6.60	4.47	4.99	2.94	7.24	10.01	4.00	4.13
Anidulafungin	9.46	NA	1.87	NA	0.16	NA	monoprotic_acid	Drugbank. Neutral	0.59	0.46	0.73	0.36	0.63	0.45	0.43	0.31	0.68	1.06	0.33	0.42	3.71	2.85	4.59	2.26	3.93	2.80	2.70	1.97	4.25	6.60	2.04	2.60
Atazanavir 1	NA	NA	4.5	NA	0.14	NA	neutral	Drugbank	111.63	85.55	182.60	79.22	175.20	73.96	91.48	53.94	190.48	272.90	45.76	86.71	797.37	611.09	1304.26	565.86	1251.46	528.25	653.44	385.29	1360.57	1949.27	326.82	619.32
Atazanavir 2	NA	NA	4.5	NA	0.14	NA	neutral	Drugbank	111.63	85.55	182.60	79.22	175.20	73.96	91.48	53.94	190.48	272.90	45.76	86.71	797.37	611.09	1304.26	565.86	1251.46	528.25	653.44	385.29	1360.57	1949.27	326.82	619.32
Azithromycin	8.5	NA	3.02	NA	0.71	2.24	monoprotic_base	Drugbank	41.09	51.88	27.13	8.27	7.30	24.20	47.37	16.97	20.10	17.21	33.18	25.02	57.87	73.07	38.21	11.65	10.28	34.08	66.72	23.90	28.32	24.24	46.74	35.23
Baricitinib	NA	NA	1.08	NA	0.5	NA	neutral	Drugbank	0.63	0.57	0.70	0.36	0.65	0.57	0.58	0.48	0.68	0.75	0.56	0.55	1.26	1.14	1.40	0.71	1.30	1.14	1.15	0.96	1.37	1.51	1.12	1.09
Bazedoxifene	9.1	NA	6	NA	0.01	0.57	monoprotic_base	Drugbank	4.94	3.79	8.08	3.51	7.75	3.28	4.05	2.40	8.43	12.07	2.03	3.84	494.22	379.02	807.82	350.73	775.39	327.75	405.35	239.56	842.95	1206.53	203.33	384.34
Benztropine	10	NA	4.27	NA	0.05	missing	monoprotic_base	Drugbank	No B:P																							
Camostat	8.54	NA	1.88	NA	missing	missing	monoprotic_base	Drugbank	No Fu / No B:P																							
Chloroquine 1	10.1	8.1	4.63	NA	0.42	3.5	diprotic_base	LSTM internal assay/determination	129.75	166.51	80.72	23.06	15.11	75.26	151.30	51.99	56.89	44.66	106.00	77.30	308.93	396.46	192.18	54.91	35.98	179.19	360.24	123.78	135.45	106.35	252.37	184.04
Chloroquine 2	10.1	8.1	4.63	NA	0.42	3.5	diprotic_base	LSTM internal assay/determination	129.75	166.51	80.72	23.06	15.11	75.26	151.30	51.99	56.89	44.66	106.00	77.30	308.93	396.46	192.18	54.91	35.98	179.19	360.24	123.78	135.45	106.35	252.37	184.04
Chloroquine 3	10.1	8.1	4.63	NA	0.42	3.5	diprotic_base	LSTM internal assay/determination	129.75	166.51	80.72	23.06	15.11	75.26	151.30	51.99	56.89	44.66	106.00	77.30	308.93	396.46	192.18	54.91	35.98	179.19	360.24	123.78	135.45	106.35	252.37	184.04
Chloroquine 4	10.1	8.1	4.63	NA	0.42	3.5	diprotic_base	LSTM internal assay/determination	129.75	166.51	80.72	23.06	15.11	75.26	151.30	51.99	56.89	44.66	106.00	77.30	308.93	396.46	192.18	54.91	35.98	179.19	360.24	123.78	135.45	106.35	252.37	184.04
Chloroquine 5	10.1	8.1	4.63	NA	0.42	3.5	diprotic_base	LSTM internal assay/determination	129.75	166.51	80.72	23.06	15.11	75.26	151.30	51.99	56.89	44.66	106.00	77.30	308.93	396.46	192.18	54.91	35.98	179.19	360.24	123.78	135.45	106.35	252.37	184.04
Chlorpromazine	9.3	NA	5.4	NA	0.05	0.775	monoprotic_base		4.70	3.98	6.94	2.96	6.33	3.08	4.11	2.25	7.10	9.91	2.25	3.55	93.94	79.53	138.72	59.17	126.64	61.50	82.17	45.07	141.97	198.21	45.09	70.93
Clomipramine	9.2	NA	5	NA	0.025	1	monoprotic_base	Drugbank	12.40	15.43	8.66	2.67	2.75	7.24	14.12	4.97	6.58	6.27	9.70	7.50	496.05	617.30	346.41	106.87	109.99	289.48	564.78	198.82	263.32	250.95	388.03	300.05
Cyclosporine	NA	NA	2.9	NA	0.083	NA	neutral		1.85	1.44	2.89	1.25	2.70	1.28	1.54	0.91	2.94	4.19	0.90	1.41	22.30	17.32	34.76	15.10	32.56	15.46	18.58	10.94	35.48	50.48	10.83	16.99
Darunavir	NA	NA	1.89	NA	0.05	NA	neutral	Drugbank	0.30	0.24	0.33	0.14	0.23	0.25	0.27	0.14	0.26	0.36	0.27	0.19	5.90	4.85	6.61	2.77	4.62	5.08	5.38	2.81	5.26	7.26	5.48	3.71
Digitoxin	7.18	NA	1.85	NA	0.043	NA	monoprotic_acid	Drugbank	0.26	0.17	0.22	0.13	0.11	0.19	0.13	0.10	0.13	0.36	0.13	0.12	5.99	3.98	5.18	3.01	2.67	4.53	2.98	2.26	3.01	8.35	3.00	2.73
Digoxin	7.15	NA	1.26	NA	0.75	NA	monoprotic_acid	Drugbank	0.63	0.56	0.67	0.35	0.61	0.57	0.51	0.46	0.62	0.79	0.50	0.52	0.85	0.74	0.90	0.46	0.82	0.76	0.68	0.61	0.83	1.05	0.66	0.69
Dolutegravir	NA	NA	1	NA	0.01	NA	neutral	Drugbank	0.18	0.15	0.15	0.06	0.05	0.17	0.17	0.07	0.07	0.11	0.21	0.08	17.67	14.52	15.13	5.57	5.24	16.79	16.89	6.71	7.16	10.79	21.38	8.40
Ebselen	NA	NA	2.28	NA	missing	NA	neutral	Drugbank	No Fu																							
Eltrombopag	3.97	NA	5	NA	0.01	NA	monoprotic_acid	Drugbank	0.22	0.14	0.18	0.11	0.07	0.17	0.10	0.07	0.08	0.30	0.10	0.09	22.42	14.04	17.63	10.79	6.63	16.65	9.66	7.15	7.92	30.18	10.41	8.54
Emetine	9.1	NA	4.34	NA	missing	missing	monoprotic_base	Drugbank	No Fu / No B:P																							
Favipiravir	5.1	NA	0.37	NA	0.46	NA	monoprotic_acid	Drugbank	0.35	0.29	0.30	0.16	0.22	0.32	0.23	0.21	0.21	0.38	0.25	0.23	0.76	0.62	0.66	0.36	0.47	0.69	0.49	0.45	0.46	0.82	0.55	0.49
Fluphenazine	7.9	NA	4.36	NA	0.1	1	monoprotic_base	Drugbank. nmslabs report for B:P	13.99	10.75	22.82	9.93	21.92	9.31	11.50	6.84	23.82	34.02	5.82	10.92	139.94	107.54	228.17	99.25	219.17	93.11	115.00	68.40	238.22	340.16	58.20	109.15
Fluspirilene	9.31	NA	5.86	NA	missing	missing	monoprotic_base	Drugbank	No Fu / No B:P																							
Gilteritinib	8.47	NA	3.15	NA	0.06	3	monoprotic_base	Drugbank. EMA report "Xospata" 2019 for B:P	70.00	89.94	43.35	12.13	7.50	40.33	81.57	27.47	30.18	24.02	56.89	41.25	1166.60	1498.94	722.46	202.09	124.94	672.16	1359.46	457.83	502.95	400.33	948.12	687.58
Homoharringtonine	9.4	NA	1.99	NA	0.5	0.7	monoprotic_base	Drugbank B:P	0.74	0.75	0.75	0.49	0.87	0.74	0.81	0.85	0.91	0.58	0.83	0.87	1.47	1.50	1.51	0.98	1.75	1.47	1.61	1.70	1.82	1.17	1.66	1.73
Hydroxychloroquine 1	9.76	8.3	3.38	NA	0.5	7.2	diprotic_base	LSTM internal assay/determination	304.64	391.53	188.45	53.08	33.06	176.00	355.33	120.63	131.61	103.46	248.40	180.32	609.28	783.06	376.91	106.16	66.12	351.99	710.66	241.27	263.23	206.91	496.81	360.65
Hydroxychloroquine 2	9.76	8.3	3.38	NA	0.5	7.2	diprotic_base	LSTM internal assay/determination	304.64	391.53	188.45	53.08	33.06	176.00	355.33	120.63	131.61	103.46	248.40	180.32	609.28	783.06	376.91	106.16	66.12	351.99	710.66	241.27	263.23	206.91	496.81	360.65

Hydroxyprogesterone	NA	NA	5.3	NA	0.01	NA	neutral	Drugbank.	50.27	38.52	82.25	35.68	78.92	33.29	41.19	24.27	85.80	122.95	20.58	39.04	5026.86	3851.63	8225.24	3567.98	7892.05	3328.88	4118.97	2426.99	8580.42	12295.48	2057.91	3903.52
Imatinib	8.3	NA	3	NA	0.05	0.73	monoprotic_base	Drugbank	4.64	5.88	3.03	0.91	0.76	2.71	5.36	1.88	2.22	1.89	3.74	2.80	92.89	117.67	60.67	18.11	15.11	54.29	107.25	37.66	44.37	37.90	74.85	55.98
Indinavir	7.4	NA	2.9	NA	0.4	missing	monoprotic_base	Drugbank	No B:P																							
Indomethacin	4.5	NA	4.27	NA	0.01	NA	monoprotic_acid	Drugbank	0.22	0.14	0.17	0.11	0.06	0.16	0.09	0.07	0.07	0.29	0.10	0.08	22.08	13.78	17.07	10.55	6.08	16.43	9.38	6.99	7.33	29.35	10.28	8.28
Ivacaftor	6.57	NA	3.13	NA	0.01	NA	monoprotic_acid	Drugbank. Phenolic Acid assumed.	0.26	0.17	0.23	0.13	0.12	0.19	0.12	0.09	0.14	0.39	0.12	0.11	25.82	16.67	23.24	13.23	12.06	18.91	12.50	8.84	13.82	38.52	11.83	11.24
Ivermectin	NA	NA	5.83	NA	0.07	NA	neutral	Drugbank	1192.19	913.44	1950.82	846.22	1871.79	789.45	976.86	575.53	2035.07	2916.26	487.98	925.75	17031.32	13049.17	27868.91	12088.81	26739.86	11277.85	13955.10	8221.92	29072.36	41660.91	6971.21	13224.97
Loperamide	9.4	NA	5	NA	0.03	missing	monoprotic_base	Drugbank	No B:P																							
Lopinavir 1	NA	NA	3.91	NA	0.02	NA	neutral	Drugbank	4.20	3.23	6.79	2.94	6.47	2.81	3.46	2.02	7.04	10.08	1.80	3.24	210.10	161.37	339.64	147.14	323.37	140.70	172.89	101.19	351.94	504.15	90.21	161.81
Lopinavir 2	NA	NA	3.91	NA	0.02	NA	neutral	Drugbank	4.20	3.23	6.79	2.94	6.47	2.81	3.46	2.02	7.04	10.08	1.80	3.24	210.10	161.37	339.64	147.14	323.37	140.70	172.89	101.19	351.94	504.15	90.21	161.81
Lopinavir 3	NA	NA	3.91	NA	0.02	NA	neutral	Drugbank	4.20	3.23	6.79	2.94	6.47	2.81	3.46	2.02	7.04	10.08	1.80	3.24	210.10	161.37	339.64	147.14	323.37	140.70	172.89	101.19	351.94	504.15	90.21	161.81
Mefloquine 1	9.46	NA	3.9	NA	0.02	1	monoprotic_base	Drugbank	12.76	16.39	7.91	2.22	1.39	7.36	14.87	5.02	5.52	4.39	10.37	7.53	637.98	819.44	395.57	110.97	69.37	367.90	743.34	250.93	275.86	219.64	518.64	376.47
Mefloquine 2	9.46	NA	3.9	NA	0.02	1	monoprotic_base	Drugbank	12.76	16.39	7.91	2.22	1.39	7.36	14.87	5.02	5.52	4.39	10.37	7.53	637.98	819.44	395.57	110.97	69.37	367.90	743.34	250.93	275.86	219.64	518.64	376.47
Merimepodib	NA	NA	1.84	NA	missing	NA	neutral	Drugbank	No Fu																							
Nelfinavir 1	8.18	NA	6	NA	0.02	missing	monoprotic_base	Drugbank	No B:P																							
Nelfinavir 2	8.18	NA	6	NA	0.02	missing	monoprotic_base	Drugbank	No B:P																							
Niclosamide	6.89	NA	4.2	NA	missing	NA	monoprotic_acid	Drugbank	No Fu																							
Nitazoxanide	8.3	NA	3.2	NA	0.01	NA	monoprotic_acid	Drugbank, PubChem	0.56	0.40	0.74	0.35	0.61	0.39	0.38	0.24	0.67	1.14	0.25	0.35	56.40	40.28	73.80	35.11	60.99	39.18	37.95	23.92	66.99	113.77	24.50	35.41
Omeprazole	NA	NA	2.23	NA	0.05	NA	neutral	Drugbank	0.41	0.33	0.52	0.22	0.41	0.33	0.36	0.20	0.46	0.65	0.32	0.27	8.18	6.59	10.38	4.41	8.26	6.58	7.24	3.91	9.21	12.92	6.38	5.49
Opipramol	7.86	NA	3.13	NA	0.09	1	monoprotic_base	Drugbank,B:P 1 assumed	11.86	14.82	8.16	2.51	2.49	6.95	13.55	4.80	6.16	5.72	9.37	7.19	131.83	164.69	90.68	27.92	27.67	77.17	150.60	53.34	68.49	63.52	104.08	79.92
Oxprenolol	9.67	NA	2.1	NA	0.2	1	monoprotic_base	Drugbank, B:P 1 assumed	10.90	13.95	6.84	2.01	1.43	6.40	12.69	4.49	4.89	3.81	8.96	6.59	54.51	69.73	34.19	10.07	7.17	32.00	63.47	22.46	24.47	19.06	44.80	32.93
Penciclovir	8.01	NA	-1.1	NA	0.8	NA	monoprotic_acid	Drugbank	0.63	0.60	0.60	0.35	0.58	0.61	0.56	0.56	0.58	0.57	0.60	0.58	0.79	0.75	0.75	0.43	0.72	0.77	0.70	0.69	0.73	0.71	0.75	0.73
Promethazine	9.05	NA	4.81	NA	0.07	1.88	monoprotic_base	Drugbank, Pubchem	36.83	46.05	25.28	7.70	7.54	21.45	42.08	14.72	19.00	17.73	28.98	22.19	526.10	657.89	361.17	110.04	107.64	306.45	601.11	210.24	271.44	253.32	413.96	317.03
Remdesivir 1	10.2	NA	2.2	NA	missing	NA	monoprotic_acid	Drugbank, neutral	No Fu																							
Remdesivir 2	10.2	NA	2.2	NA	missing	NA	monoprotic_acid	Drugbank, neutral	No Fu																							
Remdesivir 3	10.2	NA	2.2	NA	missing	NA	monoprotic_acid	Drugbank, neutral	No Fu																							
Remdesivir 4	10.2	NA	2.2	NA	missing	NA	monoprotic_acid	Drugbank, neutral	No Fu																							
Ribavirin	NA	NA	-1.85	NA	1	NA	neutral	Drugbank	0.79	0.77	0.77	0.45	0.78	0.78	0.75	0.75	0.79	0.68	0.79	0.78	0.79	0.77	0.77	0.45	0.78	0.78	0.75	0.75	0.79	0.68	0.79	0.78
Ritonavir	NA	NA	3.9	NA	0.01	NA	neutral	Drugbank	2.14	1.65	3.39	1.46	3.18	1.46	1.77	1.02	3.47	4.98	0.99	1.62	213.92	164.71	339.13	146.35	318.12	145.70	177.20	101.92	347.01	497.59	98.76	161.98
Saquinavir	8.47	NA	3.8	NA	0.02	missing	monoprotic_base	Drugbank	No B:P																							
Sulfadoxine	6.12	NA	0.7	NA	0.06	NA	monoprotic_acid	Drugbank, antimicrobe.org for Fu	0.23	0.15	0.18	0.11	0.07	0.18	0.11	0.08	0.08	0.29	0.12	0.10	3.85	2.52	2.97	1.82	1.19	2.98	1.76	1.39	1.36	4.86	1.98	1.60
Tamoxifen	8.76	NA	6	NA	0.02	0.8	monoprotic_base	Drugbank	21.10	16.17	34.51	14.98	33.12	13.98	17.30	10.21	36.01	51.57	8.66	16.40	1055.02	808.69	1725.51	748.79	1655.89	699.09	864.85	510.26	1800.26	2578.40	432.85	819.80
Tipranavir	5.92	NA	6.9	NA	0.001	NA	monoprotic_acid	Drugbank	6.48	4.96	10.54	4.58	10.08	4.30	5.28	3.12	10.97	15.78	2.66	5.00	6480.40	4955.02	10544.57	4583.84	10084.78	4296.50	5282.28	3116.38	10966.89	15775.74	2655.81	5003.88
Toremifene 1	8.76	NA	6.8	NA	0.01	missing	monoprotic_base	Drugbank	No B:P																							
Toremifene 2	8.76	NA	6.8	NA	0.01	missing	monoprotic_base	Drugbank	No B:P																							
Umifenovir	9.87	6.01	4.36	NA	missing	missing	zwitterion	Drugbank	No Fu / No B:P																							

Table B.10 Drugs investigated for SARS-CoV-2 antiviral activity and experimental overview

Drug	Multiplicity of infection (MOI)	Cell type	Virus strain	Concentration range tested	Viral quantification method	Highest clinical dose approved	Indication	Population in which PK was assessed	C_{max} (ng/ml)
Abemaciclib	0.0125	Vero E6 cells (ATCC CCL-81)	βCoV/KOR/KCDC03/2020)	0.05– 50 uM	Immunofluorescence	200 mg BID	Cancer	Patients with BC, NSCLC, other solid tumours	298
Alprostadil	0.002	VeroE6 (ATCC CRL-1586)	BavPat1	0.6µM to 40µM	RT-PCR	360 ug QD (up to 500 ug for single topical use)	Induce vasodilatation/Erectile dysfunction	Healthy male volunteers - IV infusion	0.0077
Amodiaquine 1	0.0125	Vero E6 cells (ATCC CCL-81)	βCoV/KOR/KCDC03/2020)	0.05– 50 uM	Immunofluorescence	540 mg QD	Malaria	Healthy male Vietnamese volunteers	670.3
Amodiaquine 2	0.01	Vero E6 cells	WA-1 strain - BEI #NR-52281	0.4- 50 uM	plaque assay / TCID50/ qRT-PCR	10 mg/kg (single dose)	Malaria	Healthy Volunteers	670.3
Amodiaquine 3	0.01	Vero E6 cells	WA-1 strain - BEI #NR-52282	0.4- 50 uM	plaque assay / TCID50/ qRT-PCR	450 mg QD	Malaria	Healthy Volunteers	670.3
Amprenavir	0.01	VeroE6/TMPRSS2	No info	0.01-1000 uM	RT-PCR	600mg twice BID	HIV	HIV-1 infected patients	5710
Anidulafungin	0.0125	Vero E6 cells (ATCC CCL-81)	βCoV/KOR/KCDC03/2020)	0.05– 50 uM	Immunofluorescence	Loading of 200 mg QD and	Invasive candidiasis/candidaemia	Healthy volunteers	7000

						subsequent 100 mg QD			
Atazanavir 1	0.01	Vero E6	Brazil/RJ-314/2020	10- 1000 µM	RT-PCR	300/100 mg OD (with ritonavir)	HIV-1 infection	Healthy male volunteers	5135.7
Atazanavir 2	0.01	VeroE6/TMPRSS2	No info	0.01-1000 uM	RT-PCR	300/100 mg OD (with ritonavir)	HIV-1 infection	Healthy male volunteers	5135.7
Azithromycin	0.002	VeroE6 (ATCC CRL-1586)	BavPat1	0.6µM to 40µM	RT-PCR	500 mg QD	Used to treat a range of bacterial infections	Healthy male volunteers	620
Bazedoxifene	0.0125	Vero E6 cells (ATCC CCL-81)	βCoV/KOR/KCDC03/2020)	0.05– 50 uM	Immunofluorescence	40 mg QD	Treatment of osteoporosis in postmenopausal women	Healthy postmenopausal women	12.5
Benztropine	0.01	Vero E6 cells	WA-1 strain - BEI #NR-52284	0.4- 50 uM	plaque assay / TCID50/ qRT-PCR	1.5 mg QD	Parkinson's disease	Healthy Volunteers	2.5
Camostat	0.0125	Vero E6 cells (ATCC CCL-81)	βCoV/KOR/KCDC03/2020)	0.05– 50 uM	Immunofluorescence	200 mg TID	Pancreatitis	Can only find single dose PK	87.1
Chloroquine 1	0.05	Vero E6 cells (ATCC-1586)	Wuhan/WIV04/2022	1-1000	qRT-PCR/ NP expression, immunofluorescence	1500 mg over 3 days	Malaria	Healthy Thai subjects	838
Chloroquine 2	0.0125	Vero E6 cells (ATCC CCL-81)	βCoV/KOR/KCDC03/2020)	0.05– 50 uM	Immunofluorescence	1500 mg over 3 days	Malaria	Healthy Thai subjects	838
Chloroquine 3	0.05	Vero E6 cells (ATCC CCL-81)	βCoV/KOR/KCDC03/2020)	0.05– 50 uM	CPE	1500 mg over 3 days	Malaria	Healthy Thai subjects	838

Chloroquine 4	0.01	Vero cells	C-Tan-nCoV Wuhan strain 01	0.032 - 100 uM	RT-PCR	1500 mg over 3 days	Malaria	Healthy Thai subjects	838
Chloroquine 5	0.01	Vero E6 cells	WA-1 strain - BEI #NR-52285	0.4- 50 uM	plaque assay / TCID50/ qRT-PCR	1500 mg over 3 days	Malaria	Healthy Thai subjects	838
Chlorpromazine	0.01	Vero E6 cells	WA-1 strain - BEI #NR-52286	0.4- 50 uM	plaque assay / TCID50/ qRT-PCR	100 mg (single dose)	Antipsychotic	Healthy male volunteers	37.9
Clomipramine	0.01	Vero E6 cells	WA-1 strain - BEI #NR-52287	0.4- 50 uM	plaque assay / TCID50/ qRT-PCR	150 mg QD	Treatment of Obsessive-Compulsive Disorder	Healthy volunteers	63.37
Cyclosporine	0.0125	Vero E6 cells (ATCC CCL-81)	βCoV/KOR/KCDC03/2020)	0.05– 50 uM	Immunofluorescence	100 mg QD	Immunosuppressant	Healthy volunteers	635
Darunavir	0.01	VeroE6/TMPRSS2	No info	0.01-1000 uM	RT-PCR	600/100 mg BID (with ritonavir)	HIV	Adult patients Coinfected with Hepatitis C and HIV	8120
Digitoxin	0.0125	Vero E6 cells (ATCC CCL-81)	βCoV/KOR/KCDC03/2020)	0.05– 50 uM	Immunofluorescence	0.56 mg (single dose)	Cardiovascular/ Cancer	Healthy volunteers	30.1
Digoxin	0.0125	Vero E6 cells (ATCC CCL-81)	βCoV/KOR/KCDC03/2020)	0.05– 50 uM	Immunofluorescence	2 mg loading QD then 0.5 mg QD	Cardiovascular	Healthy volunteers	1.1
Dolutegravir	0.002	VeroE6 (ATCC CRL-1586)	BavPat1	0.6µM to 40µM	RT-PCR	50 mg BID	HIV	Healthy volunteers	5500

Ebselen	0.05	Vero cells (ATCC)	No info	0.4-100um	Plaque-reduction assay	1600 mg (single dose)	Prevention and treatment of noise-induced hearing loss	Healthy volunteers	83.4
Eltrombopag	0.0125	Vero E6 cells (ATCC CCL-81)	βCoV/KOR/KCDC03/2020)	0.05– 50 uM	Immunofluorescence	75 mg QD	Idiopathic thrombocytopenic purpura (ITP)	Healthy adult Japanese males	12500
Emetine	0.02	VeroE6 (ATCC CRL-1586)	BetaCoV/Hong Kong/VM20001061/2020,	No info	TCID50 assay/ qRT-PCR	30 ml syrup of Ipecac (single dose)	Not approved	Healthy volunteers, aged 18 - 45	9.6
Favipiravir	0.05	Vero E6 cells (ATCC-1586)	Wuhan/WIV04/2019	1-1000	qRT-PCR/ NP expression, immunofluorescence	600 mg BID	Ebola	Healthy volunteers	61500
Fluphenazine	0.01	Vero E6 cells	WA-1 strain - BEI #NR-52288	0.4- 50 uM	plaque assay / TCID50/ qRT-PCR	25 mg IM at SS	Antipsychotic	Patients receiving chronic neuroleptic maintenance	1.5
Fluspirilene	0.01	Vero E6 cells	WA-1 strain - BEI #NR-52289	0.4- 50 uM	plaque assay / TCID50/ qRT-PCR	2 mg IM dosed weekly	Antipsychotic	Healthy volunteers	0.2
Gilteritinib	0.0125	Vero E6 cells (ATCC CCL-81)	βCoV/KOR/KCDC03/2020)	0.05– 50 uM	Immunofluorescence	120 mg QD	Relapsed or refractory acute myeloid leukemia	Patients with relapsed or refractory AML	282

Homoharringtonine	0.02	VeroE6 (ATCC CRL-1586)	BetaCoV/Hong Kong/VM20001061/2020,	No info	TCID50 assay/ qRT-PCR	1.25 mg/m2 BID	chronic myeloid leukemia	Adult patients with a diagnosis of relapsed or refractory CML	25.1
Hydroxychloroquine 1	0.01	Vero cells	C-Tan-nCoV Wuhan strain 01	0.032 - 100 uM	RT-PCR	400mg daily	Rhuematoid arthritis	Patients with rhuematoid arthritis	870.3
Hydroxychloroquine 2	0.01	Vero E6 cells	WA-1 strain - BEI #NR-52290	0.4- 50 uM	plaque assay / TCID50/ qRT-PCR	400mg daily	Rheumatoid arthritis	Patients with rhuematoid arthritis	870.3
Hydroxychloroquine 3		Vero E6 cells	USA-WA1/2020	0.0029µM to 30µM	CPE	400mg daily	Rheumatoid arthritis	Patients with rheumatoid arthritis	870.3
Hydroxyprogesterone	0.0125	Vero E6 cells (ATCC CCL-81)	βCoV/KOR/KCDC03/2020)	0.05– 50 uM	Immunofluorescence	250 mg IM (single dose)	Reduces the rate of recurrent preterm birth	Pregnant women	17.3
Imatinib	0.01	Vero E6 cells	WA-1 strain - BEI #NR-52291	0.4- 50 uM	plaque assay / TCID50/ qRT-PCR	400mg BID	Cancer	Healthy volunteers	1907.5
Indinavir	0.01	VeroE6/TMPRSS2	No info	0.01-1000 uM	RT-PCR	800mg TID	HIV-1 infection	HIV-1 infected patients	8100
Indomethacin	5 ng pseudotyped virus	Vero E6	cDNA used to create a pseudotyped virus,	0.1-500uM	Luciferase labelled	50 mg TID	acute painful shoulder (bursitis and/or tendinitis)	Healthy male volunteers 20-32 yrs,	1920

			GenBank: MN908947.3					mostly Caucasian	
Ivacaftor	0.0125	Vero E6 cells (ATCC CCL-81)	βCoV/KOR/KCDC03/2020)	0.05– 50 uM	Immunofluorescence	150 mg BID	Cystic fibrosis	Healthy volunteers	1962
Ivermectin	0.1	Vero/hSLAM	Australia/VIC01/2020 isolate)	0.1-10 uM	RT-PCR	200microg/Kg (single dose)	Strongyloidiasis	Healthy volunteers (mainly male)	43.19
Loperamide	0.0125	Vero E6 cells (ATCC CCL-81)	βCoV/KOR/KCDC03/2020)	0.05– 50 uM	Immunofluorescence	8 mg (single dose)	Anti-diarrhoeal medication	Healthy Malaysian male volunteers aged 21-55	1.9
Lopinavir 1	0.01	VeroE6/TMPRSS2	No info	0.01-1000 uM	RT-PCR	400/100 mg Kaletra BID	HIV	Healthy male volunteers	9580
Lopinavir 2	0.0125	Vero E6 cells (ATCC CCL-81)	βCoV/KOR/KCDC03/2020)	0.05– 50 uM	Immunofluorescence	400/100 mg Kaletra BID	HIV	Healthy male volunteers	9580
Lopinavir 3	0.05	Vero E6 cells (ATCC CCL-81)	βCoV/KOR/KCDC03/2020)	0.05–50 µM	CPE	400/100 mg Kaletra BID	HIV	Healthy male volunteers	9580
Lopinavir 4	0.01	VeroE6/TMPRSS2		0.5-64uM	RT-PCR	400/100 mg Kaletra BID	HIV	Healthy male volunteers	9580
Lopinavir 5	0.1	Calu-3 (ATCC CCL-81)	βCoV/KOR/KCDC03/2020	0.1-50 µM	Immunofluorescence	400/100 mg Kaletra BID	HIV	Healthy male volunteers	9580
Mefloquine 1	0.0125	Vero E6 cells (ATCC CCL-81)	βCoV/KOR/KCDC03/2020)	0.05– 50 uM	Immunofluorescence	1250mg over 3 days	Malaria	Mostly Burmese male patients,	3279

								aged 17 - 50	
Mefloquine 2	0.01	Vero E6 cells	WA-1 strain - BEI #NR-52281	0.4- 50 uM	plaque assay / TCID50/ qRT-PCR	1250mg over 3 days	Malaria	Mostly Burmese male patients, aged 17 - 50	3279
Merimepodib	0.05	Vero	SARS-CoV-2 USA-WA1/2020	1493 - 4525 ng/ml		300mg TID	HCV / not currently approved	HCV+ patients, 18-70 years	3435
Nelfinavir 1	0.01	VeroE6/TM PRSS2 cells	No info	0.01-1000 uM	RT-PCR	1250mg BID	HIV	HIV+ patients, 62% male, mean age 49	3753
Nelfinavir 2	0.01	VeroE6/TM PRSS2	No info	0.01-1000 uM	RT-PCR	1250mg BID	HIV	HIV+ patients, 62% male, mean age 49	3753
Niclosamide 1	0.0125	Vero E6 cells (ATCC CCL-81)	βCoV/KOR/KCDC03/2020)	0.05– 50 uM	Immunofluorescenc	2000mg OD	Anthelmintic	Adult male, prostate cancer patient trial, aged 60-84	759
Niclosamide 2	0.0005	VeroFM cells	SARS-CoV-2 strain Munich	0 - 100 uM	Plaque assay	2000mg OD	Anthelmintic	Adult male, prostate cancer	759

								patient trial, aged 60-84	
Niclosamide 3	0.1	Calu-3 (ATCC CCL-81)	βCoV/KOR/KCDC03/2020	0.1-50 µM	Immunofluorescence	2000mg OD	Anthelmintic	Adult male, prostate cancer patient trial, aged 60-84	759
Nitazoxanide	0.05	Vero E6 cells (ATCC-1586)	Wuhan/WIV04/2020	0.1-100	qRT-PCR/ NP expression, immunofluorescence	500mg BID	Treatment of diarrhoea caused by Giardia lamblia	Healthy male volunteers, aged 25 - 45	9005
Omeprazole	0.002	VeroE6 (ATCC CRL-1586)	BavPat1	0.6µM to 40µM	RT-PCR	40mg QD	Gastric Ulcer	Adult, female caucasians, mean age 51	1979
Opipramol	0.002	VeroE6 (ATCC CRL-1586)	BavPat1	0.6µM to 40µM	RT-PCR	100mg TID	Somatoform disorders and generalised anxiety disorders	Adult healthy volunteers, aged 22 - 32	27.7
Oxprenolol	0.002	VeroE6 (ATCC CRL-1586)	BavPat1	0.6µM to 40µM	RT-PCR	320mg BID	Hypertension and angina pectoris	Healthy Volunteers	1320
Penciclovir	0.05	Vero E6 cells (ATCC-1586)	Wuhan/WIV04/2019	1-1000	qRT-PCR/ NP expression, immunofluorescence	500mg TID	Herpes zoster	Healthy Volunteers	3340

Promethazine	0.01	Vero E6 cells	WA-1 strain - BEI #NR-52292	0.4- 50 uM	plaque assay / TCID50/ qRT-PCR	25mg BID	Motion Sickness	Healthy volunteers	18
Remdesivir 1	0.05	Vero E6 cells (ATCC-1586)	Wuhan/WIV04/2022	0.1-100uM	qRT-PCR/ NP expression, immunofluorescence	200mg IV loading dose, then 100mg IV daily for 5-10 days	covid-19	Healthy Volunteers	2600
Remdesivir 2	0.002	VeroE6 (ATCC CRL-1586)	BavPat1	0.6µM to 40µM	RT-PCR	200mg IV loading dose, then 100mg IV daily for 5-10 days	covid-19	Healthy Volunteers	2600
Remdesivir 3	0.05	Vero cells (ATCC CCL-81)	SARS-CoV-2 (βCoV/KOR/KCDC03/2020	0.05–50 µM	CPE	200mg IV loading dose, then 100mg IV daily for 5-10 days	covid-19	Healthy Volunteers	2600
Remdesivir 4	0.0125	Vero cells (ATCC CCL-81)	SARS-CoV-2 (βCoV/KOR/KCDC03/2019	0.05–50 µM	Immunofluorescence	200mg IV loading dose, then 100mg IV daily for 5-10 days	covid-19	Healthy Volunteers	2600
Remdesivir 5	0.1	Calu-3 (ATCC CCL-81)	βCoV/KOR/KCDC03/2020	0.1-50 µM	Immunofluorescence	200mg IV loading dose, then 100mg IV daily for 5-10 days	covid-19	Healthy Volunteers	2600
Remdesivir 6		Vero E6 cells	USA-WA1/2020	0.0029µM to 30µM	CPE	200mg IV loading dose, then 100mg IV daily for 5-10 days	covid-19	Healthy Volunteers	2600
Remdesivir 7	0.05	Vero E6 cells (ATCC CRL-1586)	BetaCoV/Hong Kong/VM20001061/2020, SCoV2)	0.05-200µM	RT-PCR	200mg IV loading dose, then 100mg IV daily for 5-10 days	covid-19	Healthy Volunteers	2600

Remdesivir 8	0.01	Caco-2	SARS-CoV-2/1/Human/2020/Frankfurt	0.02 - 20 µM	immunofluorescence	200mg IV loading dose, then 100 mg IV daily for 5-10 days	covid-19	Healthy Volunteers	2600
Ribavirin	0.05	Vero E6 cells (ATCC-1586)	Wuhan/WIV04/2022	1-1000	qRT-PCR/ NP expression, immunofluorescence	1200mg OD	HCV	HCV+ patients	2748
Ritonavir	0.01	VeroE6/TMPRSS2	No info	0.01-1000 uM	RT-PCR	600mg BID	HIV	HIV+ adults	11200
Saquinavir	0.01	VeroE6/TMPRSS2	No info	0.01-1000 uM	RT-PCR	1000/100mg BID (with ritonavir)	HIV	HIV+ males, 83% white, mean age 33	5300
Sulfadoxine	0.002	VeroE6 (ATCC CRL-1586)	BavPat1	0.6µM to 40µM	RT-PCR	Sulfadoxine/pyrimethamine FDC (1500/75mg)	Malaria	Women post-partum	72,200
Tamoxifen	0.01	Vero E6 cells	WA-1 strain - BEI #NR-52293	0.4- 50 uM	plaque assay / TCID50/ qRT-PCR	20mg BID	Metastatic breast cancer	Breast Cancer Patients	78.7601
Tipranavir	0.01	VeroE6/TMPRSS2	No info	0.01-1000 uM	RT-PCR	500/200 mg BID (with ritonavir)	HIV	Healthy Male Volunteers, mainly white, age 21 - 58	77,562
Toremifene 1	0.05	Vero E6 cells (ATCC-1586)	Wuhan/WIV04/2023	1-1000	qRT-PCR/ NP expression, immunofluorescence	60mg OD	Metastatic breast cancer	70 patients with Breast cancer	879

Toremifene 2	0.01	Vero E6 cells	WA-1 strain - BEI #NR-52294	0.4- 50 uM	plaque assay / TCID50/ qRT-PCR	60mg OD	Metastatic breast cancer	70 patients with Breast cancer	879
Umifenovir	0.002	VeroE6 (ATCC CRL-1586)	BavPat1	0.6µM to 40µM	RT-PCR	200mg TID	Prophylaxis/treatment of influenza in Russia and China	Healthy Chinese subjects	467